

ASSESSMENT OF PHYSIOLOGICAL STATUS AND SPATIAL
DISTRIBUTION OF EMERGENT MACROPHYTES BASED ON
IMAGING SPECTROSCOPY

Thesis submitted for the degree of

Doctor of Philosophy

at the University of Leicester

by

Dimitris Stratoulas

Department of Geography

University of Leicester

2015

ABSTRACT

Wetlands are ecosystems encountered at the land-water ecotone and hence inheriting rich complexity and biodiversity. Emergent macrophytes are a prime example of this variability manifested by the co-occurrence of vegetation associations at a very fine spatial level. From 1960s onwards an abrupt deterioration of reed beds in Europe has been systematically observed and denoted as the 'reed die-back'. Since then, earth observation has been utilized mainly to map the extent of reed beds based on multispectral information. Hyperspectral remote sensing has frequently been employed in vegetation related studies, however the spectral information content of macrophytes has not been widely investigated. This study focuses on assessing the potential of imaging spectroscopy for assessing the ecophysiology of lake shore vegetation at leaf level and mapping macrophytes species associations from airborne imagery. Concurrently acquired spectroscopic, chlorophyll fluorescence and chlorophyll content information from field samples around Lake Balaton, Hungary are employed to identify spectral regions and propose narrowband indices which can aid the identification of reed ecophysiological status based solely on vegetation spectral characteristics. Macrophyte species as well as *Phragmites* in different phenological states have concretely separate spectral responses, however stable and die-back reed are not crucially different. Bathymetry regulates consistently the spectral response of *Phragmites*. Narrow band ratio 493/478 (0.65^{***}) correlates with the ETR, the latter being an indication of the photosynthetic activity of the plant, and hence the vegetation physiological status. Most indices correlating with fluorometric parameters are located in the optical domain. Based on R² graphs, the ratios 699/527 and 612/516 can be used to estimate Y(II) from AISA hyperspectral data. Estimation of the photophysiological parameters of a reed bed is possible based solely on airborne hyperspectral imagery. Simultaneously acquired airborne AISA Eagle, Hawk and discrete return LiDAR data are combined in order to stress out the potential of each dataset in classifying the reed bed in terms of species associations. An application of SVM on noise-reduced Eagle data, at the chlorophyll and near infrared absorption spectral regions, provides the most concrete results in terms of overall accuracy (89%). SVM outperforms ML and infrared sensors as well as LiDAR data do not improve the categorization of macrophyte classes. While airborne data inherit a superior spectral and spatial resolution, they are difficult to acquire in an operational context. Upcoming satellites will provide imagery with progressively higher spatial and spectral capabilities. A simulation of Sentinel-2 image over a reed bed in a nature protected area indicates the potential of satellite imagery in mapping macrophytes. Main classes can be distinguished, despite the fact that inter-class separability is becoming vague. Given the very large swath of Sentinel-2 (290km) an operational categorization of main macrophytes is foreseen achievable.

Acknowledgements

First, a big thank you to my mentors who have underpinned my endeavors during the last three years. Heiko and Viktor, I really thank you for your academic enlightenment, your educational spirit and friendly approach to all my concerns and hurdles. I am glad to have met you. My gratitude goes to the person who has been the reason of my appointment at the Balaton Limnological Institute in this lifetime unforgettable experience, without András this trip would have never started. My appreciation to my closest colleagues and supervisors during my secondments in Greece and Hungary is secondary to none, I really appreciated the guidance from and communication with Ifigenia, Olga, Peter and Csaba. I also express gratefulness to all the anonymous reviewers of submitted manuscripts in peer-reviewed journals for their fruitful remarks. A thank you goes to Paul also who has been generously sharing ideas and knowledge in our small hyperspectral sphere. Thanks go also to the colleagues and co-workers of the Balaton Limnological Institute of the Hungarian Academy of Sciences who eased my work and especially Magdi for her support always pleased to offer.

I owe to acknowledge the source of all the material used in this study and mainly the Airborne Research and Survey Facility vested in the Natural Environment Research Council for the collection and provision of the airborne dataset. The financial provisions from the European Commission through the Marie Curie Programme have been generous and appreciated. A thank you also to all people involved in GIONET, a fantastic educational idea that I was privileged to be part of.

Finally, a warm embrace to all the people around me who gave for support only patient and love, in the end this is what is all about. They will always be with me, my mother, my father, my siblings and Am.

This Thesis is dedicated to my father, who has supported me forever in fighting for the better. It takes some time to understand what role people hold in your life.

List of Contents

CHAPTER 1 INTRODUCTION	1
CHAPTER 2 BACKGROUND	3
2.1 IMPORTANCE OF WETLANDS	3
2.2 PHRAGMITES AUSTRALIS	5
2.3 THE REED DIE-BACK.....	6
2.4 LAKE BALATON.....	10
2.5 REMOTE SENSING OF WETLANDS.....	13
2.6 ENVIRONMENTAL POLICY FRAMEWORK	17
2.7 RESEARCH OBJECTIVES	19
CHAPTER 3 ANALYSIS OF MACROPHYTES <i>IN-SITU</i> SPECTRAL INFORMATION	23
3.1 INTRODUCTION	23
3.2 OBJECTIVES	24
3.3 FIELD CAMPAIGN AND SAMPLING DESIGN	25
3.3.1 <i>Spectroscopic data collection.....</i>	<i>25</i>
3.3.2 <i>Biophysical parameters and leaf hyperspectral concurrent measurements</i>	<i>29</i>
3.4 METHODOLOGY	32
3.5 RESULTS AND DISCUSSION	33
3.5.1 <i>Leaf spectral analysis of macrophyte species</i>	<i>33</i>
3.5.2 <i>Reed spectral analysis in regard to reed die-back.....</i>	<i>34</i>
3.5.3 <i>Canopy spectral analysis of reed's phenological status</i>	<i>38</i>
3.5.4 <i>Spectral analysis of sun and shade leaves of reed</i>	<i>38</i>
3.5.5 <i>The influence of inundation level on reed leaves stability.....</i>	<i>39</i>
3.6 CONCLUSIONS.....	43
CHAPTER 4 REMOTE SENSING OF REED ECOPHYSIOLOGY BY COUPLING CHLOROPHYLL FLUORESCENCE AND SPECTROSCOPIC INFORMATION	45
4.1 INTRODUCTION	45
4.2 STUDY AREA	49
4.3 DATA QUALITY ASSESSMENT	51
4.4 METHODOLOGY	52
4.4.1 <i>Optimizing leaf stress indication from spectroscopic data</i>	<i>53</i>
4.4.2 <i>Application on airborne imagery.....</i>	<i>56</i>
4.5 RESULTS AND DISCUSSION	58
4.5.1 <i>Complete-combination spectral indices for coupling with photophysiological parameters</i>	<i>58</i>

4.5.2	<i>Empirical indices for spectral assessment of photophysiological parameters</i>	66
4.5.3	<i>Estimation of Y(II) and ETR from RSI values</i>	68
4.5.4	<i>Application on airborne hyperspectral data</i>	74
4.6	LIMITATIONS	76
4.7	CONCLUSIONS	77
CHAPTER 5 AQUATIC VEGETATION MAPPING BASED ON AIRBORNE HYPERSPECTRAL AND LIDAR DATA		79
.....		
5.1	INTRODUCTION	79
5.2	CLASSIFICATION APPROACHES	81
5.2.1	<i>Data sources</i>	81
5.2.2	<i>Classification algorithms</i>	83
5.3	AREA OF STUDY	85
5.4	AIRBORNE REMOTELY SENSED DATA	85
5.4.1	<i>Hyperspectral imagery</i>	87
5.4.2	<i>LiDAR</i>	88
5.4.3	<i>Orthophotos</i>	89
5.5	DATA-PROCESSING	90
5.5.1	<i>Radiometric correction and bands exclusion</i>	92
5.5.2	<i>Atmospheric correction</i>	93
5.5.3	<i>Geometric correction</i>	96
5.6	TRAINING AND VALIDATION SET	97
5.7	METHODOLOGY	98
5.7.1	<i>Input layers</i>	98
5.7.2	<i>Reed bed masking and mosaicking</i>	102
5.7.3	<i>Classification</i>	103
5.7.4	<i>Accuracy assessment</i>	104
5.8	RESULTS AND DISCUSSION	105
5.9	CONCLUSIONS	114
CHAPTER 6 SENTINEL-2 IMAGE SIMULATION BASED ON AIRBORNE HYPERSPECTRAL DATA		116
.....		
6.1	INTRODUCTION	116
6.2	DATASET SPECIFICATIONS	118
6.3	METHODOLOGY	121
6.4	RESULTS AND DISCUSSION	123
6.5	CONCLUSIONS	127
CHAPTER 7 CONTRIBUTION TO SCIENCE		129
.....		
7.1	CONCLUSIONS	129

7.2 CONTRIBUTION TO KNOWLEDGE	132
APPENDIX 1: R LANGUAGE SCRIPT FOR PROCESSING OF THE FIELD DATA AND PRODUCTION OF CORRELATION MAPS	135
APPENDIX 2: CORRELATION OF <i>IN-SITU</i> FLUORESCENCE PARAMETERS AND LEAF HYPERSPECTRAL REFLECTANCE	146
APPENDIX 3: CORRELATION OF <i>IN-SITU</i> FLUORESCENCE PARAMETERS AND LEAF HYPERSPECTRAL TRANSMITTANCE.....	148
APPENDIX 4: ATMOSPHERIC CORRECTION INPUT PARAMETERS	150
REFERENCES	152

List of Tables

TABLE 3.1: INSTRUMENTS USED AND PARAMETERS MEASURED IN THIS FIELD CAMPAIGN.....	31
TABLE 4.1: EMPIRICAL INDICES PROPOSED FREQUENTLY IN REMOTE SENSING STUDIES OF VEGETATION.	50
TABLE 4.2: SPECTRAL BAND COMBINATION AND MAXIMUM VALUE OF COEFFICIENT OF DETERMINATION (R^2) FOR REFLECTANCE RSI AND NDSI IN REGARD TO THE PHOTOPHYSIOLOGICAL PARAMETER MEASURED IN-SITU. P: * \rightarrow p<0.05, ** \rightarrow p<0.01, *** \rightarrow p<0.001.....	61
TABLE 4.3: SPECTRAL BAND COMBINATION AND MAXIMUM VALUE OF COEFFICIENT OF DETERMINATION (R^2) FOR REFLECTANCE RSI AND NDSI IN REGARD TO THE PHOTOPHYSIOLOGICAL PARAMETER MEASURED IN-SITU. P: * \rightarrow p<0.05, ** \rightarrow p<0.01, *** \rightarrow p<0.001. A 3x3 FILTER HAS BEEN APPLIED IN ORDER TO REDUCE THE NUMBER OF BANDS FROM 600 TO 200.	65
TABLE 4.4: SPECTRAL BAND COMBINATION AND MAXIMUM VALUE OF COEFFICIENT OF DETERMINATION (R^2) FOR TRANSMITTANCE RSI AND NDSI IN REGARD TO THE PHOTOPHYSIOLOGICAL PARAMETER MEASURED IN-SITU. P: * \rightarrow p<0.05, ** \rightarrow p<0.01, *** \rightarrow p<0.001. A 3x3 FILTER HAS BEEN APPLIED IN ORDER TO REDUCE THE NUMBER OF BANDS FROM 600 TO 200.	66
TABLE 4.5: CORRELATION MATRIX BETWEEN THE MEASURED PHOTOPHYSIOLOGICAL PARAMETERS AND EMPIRICAL INDICES. P: * \rightarrow p<0.05, ** \rightarrow p<0.01, *** \rightarrow p<0.001, ALL THE NUMBER WITHOUT SIGNIFICANCE INDEXES ARE NOT SIGNIFICANT.	69
TABLE 4.6: MODEL PREDICTIONS FOR Y(II) FROM THE RSI REFLECTANCE DATASET.	71
TABLE 4.7: MODEL PREDICTIONS FOR ETR FROM THE RSI REFLECTANCE DATASET.....	73
TABLE 5.1: SPECIFICATIONS OF REMOTE SENSING INSTRUMENTS USED TO COLLECT SIMULTANEOUSLY HYPERSPECTRAL, LiDAR AND ORTHOPHOTOS DURING 21 ST – 26 TH AUG 2010 ON LAKE BALATON, HUNGARY UNDER CLEAR SKY CONDITIONS. 86	
TABLE 5.2: SOLAR ILLUMINATION CONDITIONS AT LAKE BALATON (LAT: 46.9127. LON: 17.8369) DURING TIME ACQUISITION AS CALCULATED FROM THE NATIONAL OCEANIC AND ATMOSPHERIC ADMINISTRATION (NOAA) SOLAR CALCULATOR (URL: HTTP://WWW.ESRL.NOAA.GOV/GMD/GRAD/SOLCALC).	92
TABLE 5.3: CONFUSION MATRIX ILLUSTRATING THE RESULTS OF THE CLASSIFICATION ON EAGLE DATA WITH MAXIMUM LIKELIHOOD (ML) AND SUPPORT VECTOR MACHINES (SVM) ALGORITHMS. ALL VALUES EXCEPT THE KAPPA COEFFICIENT ARE IN PERCENTAGES.	111
TABLE 5.4: CONFUSION MATRIX ILLUSTRATING THE RESULTS OF THE CLASSIFICATION ON HAWK DATA WITH MAXIMUM LIKELIHOOD (ML) AND SUPPORT VECTOR MACHINES (SVM) ALGORITHMS. ALL VALUES EXCEPT THE KAPPA COEFFICIENT ARE IN PERCENTAGES.	112
TABLE 5.5: CONFUSION MATRIX ILLUSTRATING THE RESULTS OF THE CLASSIFICATION ON INDICES DATASET WITH MAXIMUM LIKELIHOOD (ML) AND SUPPORT VECTOR MACHINES (SVM) ALGORITHMS. ALL VALUES EXCEPT THE KAPPA COEFFICIENT ARE IN PERCENTAGES.	113
TABLE 5.6: CONFUSION MATRIX ILLUSTRATING THE RESULTS OF THE CLASSIFICATION ON LiDAR FUSED DATASET WITH MAXIMUM LIKELIHOOD (ML) AND SUPPORT VECTOR MACHINES (SVM) ALGORITHMS. ALL VALUES EXCEPT THE KAPPA COEFFICIENT ARE IN PERCENTAGES.	114
TABLE 6.1: SIMULATED BANDS OF SENTINEL-2 (GREYED) AND SPECIFICATIONS OF INSTRUMENTS.	119

TABLE 6.2: CORRELATION BETWEEN THE SPECTRAL CHANNELS OF THE SIMULATED SENTINEL-2 IMAGE. BANDS IN BOLD
NUMBERS ARE WITH CORRELATION < 0.9. 124

List of Figures

FIGURE 2.1: ZONATION OF THE LAKE SHORE ENVIRONMENT. WETLANDS ARE ECOSYSTEMS RICH IN BIODIVERSITY AND ARE DIRECTLY ASSOCIATED WITH THE INUNDATION LEVEL, HENCE THE WATER AVAILABILITY.	4
FIGURE 2.2: REPRESENTATION OF MATURE PLANT OF SPECIES PHRAGMITES (ADAPTED FROM BRIX 1999A, DRAWING BY K. TIND) (UPPER LEFT), A TYPICAL DIE-BACK REED STAND IN LAKE BALATON, AS OBSERVED FROM THE WATERWARD SIDE (UPPER RIGHT) AND A STABLE VERY DENSE, STABLE AND TALL REED STAND (BOTTOM).....	9
FIGURE 2.3: AREA OF STUDY AT LAKE BALATON, HUNGARY AND THE DISTRIBUTION OF EMERGED MACROPHYTES ALONG THE SHORE. THE RELATIVE POSITION OF THE LAKE WITHIN EUROPE (LEFT) AND HUNGARY (RIGHT) ARE DEPICTED IN THE INSET IMAGES.	13
FIGURE 2.4: TYPICAL VEGETATION REFLECTANCE CURVE AND IMPORTANT FEATURES THAT CAN BE ESTIMATED THROUGH MAINLY SPECTROSCOPIC INFORMATION (AFTER HOFFER, 1978).	17
FIGURE 3.1: FIELD DATA COLLECTION AT DESIGNATED MACROPHYTE SITES ON LAKE BALATON, NAMELY SZIGLIGET BAY (LATITUDE 46.796965, LONGITUDE 17.405215), BOZSAI BAY (LATITUDE 46.918315, LONGITUDE 17.834720) AND KEREKEDI BAY (LATITUDE 46.967421, LONGITUDE 17.917029). 74% OF THE MACROPHYTE SITES LIE ON THE NORTH SHORE OF THE LAKE, WHILE ON THE SOUTH SHORE ONLY THIN SLIVERS OF VEGETATION ARE ENCOUNTERED. ...	28
FIGURE 3.2: PHOTOGRAPH ILLUSTRATING THE SETUP FOR COLLECTING CANOPY FIELD MEASUREMENTS FROM THE WATERWARD SIDE OF THE REED BED WITH THE AID OF A MOTORBOAT AT BOZSAI BAY IN LAKE BALATON, HUNGARY. THE SPECTRORADIOMETER IS ATTACHED VERTICALLY AT THE END OF A POLE AND IS POINTING DOWNWARDS AT THE TIME OF DATA ACQUISITION.	29
FIGURE 3.3: KEREKEDI BAY, LAKE BALATON AND LOCATION OF SAMPLING POINTS.	32
FIGURE 3.4: LEAF MEAN REFLECTANCE SPECTRA (CURVES) AND THE CORRESPONDING 95% CONFIDENCE INTERVALS (SHADED AREAS) FOR THE MACROPHYTES ASSOCIATIONS COLLECTED AT THE SZIGLIGET BAY IN LAKE BALATON. REED CATEGORIES REFLECTS STRONGER IN THE VISIBLE REGION AND ESPECIALLY AT THE CHLOROPHYLL ABSORPTION BANDS BETWEEN 560NM AND 670NM, WHILE IT REFLECTS WEAKER IN THE NEAR INFRARED, ASSOCIATED TO THE CELL STRUCTURE AS EXPLAINED IN	34
FIGURE 3.5: LEAF MEAN REFLECTANCE SPECTRA (CURVES) AND THE CORRESPONDING 95% CONFIDENCE INTERVALS (SHADED AREAS) FOR THE PHRAGMITES PLANTS COLLECTED FROM THE STABLE AND DIE-BACK REED STANDS AT THE WATERFRONT AREA OF THE KEREKEDI BAY IN LAKE BALATON.....	35
FIGURE 3.6: CANOPY MEAN REFLECTANCE SPECTRA (CURVES) AND THE CORRESPONDING 95% CONFIDENCE INTERVALS (SHADED AREAS) FOR PHRAGMITES PLANTS COLLECTED FROM STABLE AND DIE-BACK REED SAMPLES AT THE WATERFRONT AREA OF THE BOZSAI BAY IN LAKE BALATON.....	36
FIGURE 3.7: RED-EDGE INFLECTION POINT FOR LEAF AND CANOPY SCALE OF STABLE AND DIE-BACK REED SAMPLES. STATISTICALLY, IMPORTANT DIFFERENCES SEEM TO APPEAR ONLY AT LEAF SCALE.	37
FIGURE 3.8: SPECTRAL SURFACE RADIANCE (ATMOSPHERIC CORRECTION APPLIED) OF SAMPLE PURE PIXELS FROM AN AIRBORNE HYPERSPECTRAL SENSOR CORRESPONDING TO STABLE AND DIE-BACK REED FROM THE REED BED AT BOZSAI BAY, LAKE BALATON.....	37

FIGURE 3.9: CANOPY MEAN REFLECTANCE SPECTRA (CURVES) AND THE CORRESPONDING 95% CONFIDENCE INTERVALS (SHADED AREAS) FOR SAMPLES OF PHRAGMITES IN DIFFERENT PHONOLOGICAL STATES (REED WITH INFLORESCENCE, REED WITH DRIED RAMETS AND RECENTLY EMERGED REED) COLLECTED WITH AN ASD HANDHELD SPECTRORADIOMETER AT THE SZIGLIGET BAY, LAKE BALATON. RECENTLY EMERGED REED ABSORBS CONSIDERABLY HIGHER AT THE CCHLOROPHYLL ABSORPTION BANDS BETWEEN 560NM AND 690NM.....	38
FIGURE 3.10: LEAF MEAN REFLECTANCE SPECTRA (CURVES) AND THE CORRESPONDING 95% CONFIDENCE INTERVALS (SHADED AREAS) FOR SAMPLES OF REED UNDER SUNNY AND SHADED CONDITIONS COLLECTED AT THE KEREKEDI BAY, LAKE BALATON.....	39
FIGURE 3.11: MEAN REFLECTANCE SPECTRA (CURVES) AND THE CORRESPONDING 95% CONFIDENCE INTERVALS (SHADED AREAS) OF PHRAGMITES LEAF SAMPLES COLLECTED FROM THE TERRESTRIAL, SHALLOW WATER, DEEP WATER AND WATERFRONT PARTS OF THE REED STAND IN KEREKEDI BAY, LAKE BALATON. REED GROWING IN CATEGORIES WITH WATER HAVE A SLOPED INFRARED PLATEAU (750 – 1000NM), WHILE TERRESTRIAL REED HAS A STABLE REFLECTANCE VALUE ACROSS THESE WAVELENGTHS.....	41
FIGURE 3.12: CHANGES OF: (A) F, (B) Fm', (C) ETR, (D) Y(II) AND (E) CHLOROPHYLL CONTENT OF LEAVES OF PHRAGMITES AT THE TERRESTRIAL, SHALLOW WATER, DEEP WATER AND WATERFRONT OF THE REED BED AT THE STUDY SITE. N=27-55. THE COMPARISON WAS PERFORMED USING THE TUKEY-KRAMER TEST (PAIRWISE COMPARISONS FOR ONE-WAY LAYOUT DESIGN). BOXES ENCOMPASS THE 25% AND 75% QUANTILES OF ALL THE DATA FOR EACH SPECIFIC PART OF THE STUDIED AREA. THE CENTRAL SOLID LINE REPRESENTS THE MEDIAN, WHILE THE DASHED LINE REPRESENTS THE AVERAGE, BARS EXTEND TO THE 95% CONFIDENCE LIMITS, AND DOTS REPRESENT OUTLIERS. FIGURE REPRODUCED FROM STRATOULIAS ET AL. (2015).....	42
FIGURE 4.1: EXAMPLE OF REGRESSION FITTED FOR THE RSI COMBINATIONS AGAINST Fm' (A) AND Fs (B). THE RELATIONSHIP APPEARS TO BE LINEAR AND HENCE THE SQUARE OF THE PEARSON CORRELATION COEFFICIENT (R^2) WAS USED AS A MEASURE OF VARIANCE IN THE ASSUMED LINEAR RELATIONSHIP.....	54
FIGURE 4.2: COEFFICIENT OF DETERMINATION (R^2) (A) AND CORRESPONDING P VALUES (B) BETWEEN APPARENT FLUORESCENCE YIELD (Fs) AND RSI (Ri, Rj) MEASURED ON PHRAGMITES PLANTS AT THE DEEP WATER PART OF THE TRANSECT IN KEREKEDI BAY, LAKE BALATON. THE RSI WAS CALCULATED USING THE WHOLE SPECTRUM REFLECTANCE COMBINATIONS OF TWO WAVEBANDS AT I AND J.....	62
FIGURE 4.3: COEFFICIENT OF DETERMINATION (R^2) (A) AND CORRESPONDING P VALUES (B) BETWEEN MAXIMUM FLUORESCENCE YIELD (Fm') AND RSI (Ri, Rj) MEASURED ON PHRAGMITES PLANTS AT THE DEEP WATER PART OF THE TRANSECT IN KEREKEDI BAY, LAKE BALATON. THE RSI WAS CALCULATED USING THE WHOLE SPECTRUM REFLECTANCE COMBINATIONS OF TWO WAVEBANDS AT I AND J.....	62
FIGURE 4.4: COEFFICIENT OF DETERMINATION (R^2) FOR RSI (Ri, Rj) (A) AND NDSI (Ri, Rj) (B) BETWEEN Fs MEASURED ON PHRAGMITES PLANTS AT THE DEEPWATER PART OF THE TRANSECT IN KEREKEDI BAY, LAKE BALATON. RSI AND NDSI WERE CALCULATED USING THE WHOLE REFLECTANCE SPECTRUM COMBINATIONS OF TWO WAVEBANDS AT I AND J.....	64
FIGURE 4.5: COEFFICIENT OF DETERMINATION (R^2) FOR RSI (Ri, Rj) (A) AND CORRESPONDING P VALUE (B) RESULTS PRODUCED BY APPLYING THE R ALGORITHM ON AN INDEPENDENT DATASET COLLECTED IN THE AMAZON FOREST (WATER CONTENT VS REFLECTANCE SPECTRAL INDICES). AS EXPECTER, WATER CONTECT IS CORRELATING BETWEEN 900 NM AND 1000 NM.....	64

FIGURE 4.6: NON-FILTERED (A) AND 3X3 FILTERED (B) FOR REFLECTANCE RSI EXAMPLE	65
FIGURE 4.7: HIERARCHICAL CLUSTERING OF CORRELATION RELATIONSHIP BETWEEN THE SPECTRAL INDICES PROPOSED (GREY COLOUR), THE EMPIRICAL INDICES TESTED (BLACK COLOUR) AND THE BIOPHYSICAL PARAMETERS MEASURED IN-SITU (GREY COLOUR).....	70
FIGURE 4.8: LINEAR REGRESSION FOR F_s (A) AND F_m' (B) FOR THE REFLECTANCE RSIS WITH THE HIGHEST CORRELATIONS AT THE TERRESTRIAL PART OF THE TRANSECT IN KEREKEDI BAY, LAKE BALATON.	70
FIGURE 4.9: LINEAR REGRESSION OF THE MEASURED AND PREDICTED VALUES FOR $Y(II)$ OF PHRAGMITES PLANTS FROM THE TERRESTRIAL PART OF THE TRANSECT. PREDICTED VALUES CALCULATED BASED ON THE BEST CORRELATIONS FOUND FROM REFLECTANCE RSI FOR F_s AND F_m' (FIGURE 4.8).....	71
FIGURE 4.10: LINEAR REGRESSION FOR PAR (A) AND $Y(II)$ (B) FOR THE REFLECTANCE RSIS WITH THE HIGHEST CORRELATIONS AT THE WATERFRONT PART OF THE TRANSECT IN KEREKEDI BAY, LAKE BALATON.	72
FIGURE 4.11: LINEAR REGRESSION OF THE MEASURED AND PREDICTED VALUES FOR ETR OF PHRAGMITES PLANTS FROM THE WATERFRONT PART OF THE TRANSECT. PREDICTED VALUES CALCULATED BASED ON THE BEST CORRELATIONS FOUND FROM REFLECTANCE RSI FOR PAR AND $Y(II)$ (FIGURE 4.10).....	72
FIGURE 4.12: $Y(II)$ (A) AND ETR (B) ESTIMATION FROM THE HYPERSPECTRAL AIRBORNE DATASET OVER THE AREA OF STUDY AT KEREKEDI BAY, LAKE BALATON ACCORDING TO THE BEST CORRELATION FOUND IN THE REFLECTANCE RSI AT THE TERRESTRIAL PART OF THE TRANSECT (LEFT) AND PREDICTED VALUES CALCULATED FROM THE MAXIMUM CORRELATION OF F_s AND F_m'	75
FIGURE 5.1: FLIGHT LINES OF THE AIRBORNE CAMPAIGN UNDERTAKEN DURING AUGUST 2010 (MAIN IMAGE) AND SAMPLE OF THE CONCURRENTLY COLLECTED (A) HYPERSPECTRAL, (B) LIDAR AND (C) ORTHOPHOTOS DATASET (INSET IMAGE). ..	86
FIGURE 5.2: PRE-PROCESSING FLOWCHART OF THE HYPERSPECTRAL AND LIDAR DATASETS.....	91
FIGURE 5.3: COMPARISON OF THE SPECTRAL SIGNATURE OF A REED PIXEL FROM THE RAW DATA, QUICK ATMOSPHERIC CORRECTION (QUAC) AND FAST LINE-OF-SIGHT ATMOSPHERIC ANALYSIS OF SPECTRAL HYPERCUBES.....	95
FIGURE 5.4: RAW IMAGE AS DELIVERED BY THE DATA PROVIDER (A) AND GEOMETRICALLY REGISTERED IMAGE ON UTM 33N (B) DEPICTING THE EAST PART OF THE STUDY AREA.	97
FIGURE 5.5: WORKFLOW INDICATING THE PREPARATION OF INPUT LAYERS FOR THE CLASSIFICATION PROCESS BASED ON THE EAGLE, HAWK AND LIDAR PRE-PROCESSED DATASETS.	99
FIGURE 5.6: EIGENVALUES OF THE EAGLE IMAGE (A) AND DEPICTIONS OF THE MINIMUM NOISE FRACTION (MNF) TRANSFORMATION CORRESPONDING TO BANDS NUMBER 1 (B), 4 (C), 9 (D), 14 (E) AND 16 (F). NOISE IS CONSIDERABLY HIGHER THAN THE INFORMATION CONTENT AFTER BAND 14 AND HENCE ALL THE BANDS AFTER THIS THRESHOLD HAVE BEEN DROPPED.	100
FIGURE 5.7: EIGENVALUES OF THE HAWK IMAGE (A) AND DEPICTIONS OF THE MINIMUM NOISE FRACTION (MNF) TRANSFORMATION CORRESPONDING TO BANDS NUMBER 1 (B), 4 (C), 9 (D), 11 (E) AND 12 (F). NOISE IS CONSIDERABLY HIGHER THAN THE INFORMATION CONTENT AFTER BAND 11 AND HENCE ALL THE BANDS AFTER THIS THRESHOLD HAVE BEEN DROPPED.	102
FIGURE 5.8: WORKFLOW OF THE CLASSIFICATION SCHEME DEVELOPED THROUGH ITERATIVE CLASSIFICATIONS AND EVALUATIONS FOR MAPPING EMERGENT VEGETATION. THE TWO STEP APPROACH INVOLVES CLASSIFICATION OF THE IMAGE BASED ON THE MAIN MACROPHYTE SPECIES (PHRAGMITES, TYPHA, CAREX AND GRASSLAND) AND	

SUBSEQUENTLY ISOLATION OF THE PHRAGMITES CLASS AND CLASSIFICATION OF THE LATTER BASED ON THE DOMINANCE OF PHRAGMITES (DOMINANT, CO-DOMINANT AND SUB-DOMINANT) AND REED DIE-BACK. AT THE FINAL STAGE THE TWO CLASSIFICATION RESULTS ARE MERGED WITH THE PHRAGMITES-SPECIFIC CLASSIFICATION OVERLAID OVER THE MACROPHYTE SPECIES MAP. THE RESULT IS ASSESSED QUANTITATIVELY BASED ON EXPERT KNOWLEDGE AND CONCURRENTLY ACQUIRED ORTHOPHOTOS. 104

FIGURE 5.9: THEMATIC MAPS FROM THE ML CLASSIFICATION OF THE EAGLE (A), HAWK (B), INDICES FROM EAGLE (C) AND LIDAR COMBINED WITH EAGLE PCs OF THE MACROPHYTE MAIN SPECIES AND PHRAGMITES ASSOCIATIONS AT BOZSAI BAY, LAKE BALATON..... 109

FIGURE 5.10: THEMATIC MAPS FROM THE SVM CLASSIFICATION OF THE EAGLE (A), HAWK (B), INDICES FROM EAGLE (C) AND LIDAR COMBINED WITH EAGLE PCs OF THE MACROPHYTE MAIN SPECIES AND PHRAGMITES ASSOCIATIONS AT BOZSAI BAY, LAKE BALATON..... 110

FIGURE 6.1: STUDY AREA IN LAKE BALATON, HUNGARY AND THE WIDE SWATH (290 KM) OF SENTINEL-2. 120

FIGURE 6.2: RGB REPRESENTATION (665NM, 560NM, 490NM) OF THE SIMULATED SENTINEL-2 IMAGE. THE WHITE STRIPE INDICATES MISSING DATA DUE TO SYSTEMATIC DROPPING LINES OF THE HAWK SENSOR. INSETS: SUBSETS OF THE CENTRAL REED BED AREA OF THE MAIN IMAGE (BOTTOM) AND TRUE-COLOUR RGB AERIAL PHOTO (0.25 M) ACQUIRED CONCURRENTLY WITH THE HYPERSPECTRAL DATASET (TOP). 120

FIGURE 6.3: WORKFLOW OF THE METHODOLOGY, DERIVATION OF THE FOUR INPUT DATASETS FROM THE AISA AIRBORNE HYPERSPECTRAL IMAGERY. 122

FIGURE 6.4: A SPECTRAL PROFILE FROM A PIXEL OF PURE MONOSPECIFIC REED FROM THE COMBINED EAGLE AND HAWK DATA (GREY) AND THE SENTINEL-2 SIMULATED IMAGE (COLOUR). 124

FIGURE 6.5: CLASSIFICATION OF THE 4 PRODUCTS; HIGHLIGHTED ON THE LOWER RIGHT THE CLASSIFICATION RESULT DERIVED FROM THE SENTINEL-2 SIMULATED IMAGE..... 127

List of Abbreviations and Acronyms

AF	Absorption Factor
alpha	Maximum quantum yield for whole chain electron transport
ALS	Airborne Laser Scanning
ARI2	Anthocyanin Reflectance Index
ARSF	Airborne Research and Survey Facility
ASTER	Advanced Spaceborne Thermal Emission and Reflection Radiometer
BRDF	Bidirectional Reflectance Distribution Function
CH ₄	methane
CHL	chlorophyll
CO	carbon monoxide
CO ₂	carbon dioxide
CRI1	Carotenoid Reflectance Index
CRI2	Carotenoid Reflectance Index
D _i	Derivative value of radiance at i wavelength
DCM	Digital Canopy Model
DN	Digital Number
DSM	Digital Surface Model
DTM	Digital Terrain Model
ENMAP	Environmental Mapping and Analysis Program
ESA	European Space Agency
ETR	Electron Transport Rate
ETR _{max}	Maximum electron transport capacity
EU	European Union
EUREED	European Project on Reed Die-back and Progression
EUFAR	European Facility for Airborne Research
EVI	Enhanced Vegetation Index
FLAASH	Fast Line-of-sight Atmospheric Analysis of Spectral Hypercubes

Fm'	Maximum fluorescence yield
F _s	Apparent fluorescence yield
FWHM	Full-Width Half-Maximum
GMES	Global Monitoring for Environment and Security
GCP	Ground Control Point
GPS	Global Positioning System
HypIRI	Hyperspectral Infrared Imager
I _k	Light saturation intensity
IMU/GNSS	Inertial Measuring Unit/Global Navigation Satellite System
INS	Inertial Navigation System
IR	Infra-Red
KRC	Kernel based Re-Classification
LAI	Leaf Area Index
LiDAR	Light Detection And Ranging
mND705	modified Normalized Difference Index
mSR705	modified Simple Ratio Index
ML	Maximum Likelihood
MMS	Multimission Modular Spacecraft
MNF	Minimum Noise Fraction
NDSI	Normalized Difference Spectral Index
NDVI	Normalised Difference Vegetation Index
NDVI750	Red-edge Normalized Difference Vegetation Index
NERC	Natural Environment Research Council
NOAA	National Oceanic and Atmospheric Administration
N ₂ O	nitrous oxide
O ₂	molecular oxygen
OBIA	Object Based Image Analysis
p	Significance level (statistical measurement)
PAM	Pulse Amplitude Modulated
PAR	Photosynthetically Active Radiation

PC	Principal Component
PRI	Photochemical Reflectance Index
PS	Photosynthetic systems
PSII	Photosystem-II
PSRI	Plant Senescence Reflectance Index
QUAC	QUick Atmospheric Correction
r	Pearson product-moment correlation coefficient (statistical measurement)
R_i	Radiance value at i wavelength
R^2	Coefficient of determination (statistical measurement)
RGI	Red Green Index
RMSE	Root Mean Square Error
RSI	Ratio Spectral Index
SGI	Sum Green Index
SIPI	Structure Insensitive Pigment Index
SNR	Signal to Noise Ratio
SRF	Spectral Response Function
SRI	Simple Ratio Index
SD	Standard Deviation
SVM	Support Vector Machines
UAV	Unmanned Aerial Vehicles
UNFCCC	United Nations Framework Convention on Climate Change
UTC	Coordinated Universal Time
VOG	Vogelmann
WBI	Water Band Index
WFD	Water Framework Directive
Y(II)	Photosynthetic yield

Chapter 1

Introduction

During the 1960s in Europe reed beds started to deteriorate in several geographic regions simultaneously for unidentified reasons, resulting in a considerable reduction of reed surface coverage (Ostendorp 1989; Den Hartog et al. 1989; Van der Putten 1997; Brix, 1999a). The symptoms associated with reed decline and the consequences have been collectively denominated as the ‘reed die-back’ (Boorman et al. 1977). Whilst in European wetlands the phenomenon was sustained, in America reed needed to be restrained due to its aggressive growth, spread (McCormick et al. 2010) and ability to displace native aquatic vegetation. Operationally, in the U.S. the extent of reed stands was reduced by water level control, herbicide application, prescribed burn, etc. The problem has been reported widely in the literature to the point of considering the species as noxious (Leithead et al. 1976).

These two parallel observations stimulated a strong concern among scientific groups which sought ways to understand the cause underlying the phenomenon and the associated consequences. In parallel, legislative authorities developed strategies for sustainably tackling the problem in the framework of wetland ecosystem management. Land cover changes have a strong impact on biotic components of ecosystems, and therefore on human environment. Likewise, on a global scale the loss of biodiversity initiated a scientific interest in species distribution (biological invasion is the second most important reason for biodiversity loss after habitat fragmentation (Petrovskiy, S., inaugural lecture)), the associated environmental drivers and how they operate in different geospatial contexts (Turner et al. 2003). Part of the effort has been devoted to reporting qualitatively and quantitatively the coverage and condition of vegetation which, traditionally, was estimated based

on field visits and *in-situ* measurements. Only lately the scientific community started to entrust earth observation, to a degree driven by the abundance of remotely sensed data, the ever increasing technological improvements and the decreasing cost of purchasing imagery.

Imaging spectroscopy, commonly known as hyperspectral remote sensing, has been progressively employed in vegetation related studies. Plants inherit an immense variability in structure, composition and characteristics; fine spectral information is a key parameter to identify species, study the vegetation vigour or estimate biophysical parameters remotely in such complex scenes. Hyperspectral instruments record electromagnetic incoming radiation in hundreds contiguous spectral bands; this information can be translated to reflectance of the object of interest, which is directly associated to biophysical parameters and physiological status of the vegetation. For instance the stress condition of a leave is a direct consequence of the photosynthetic activity of the plant, the latter demonstrating specific spectral characteristics in the reflectance pattern which can be locate in the hyperspectral signature of the plant. Nevertheless and despite the fact that lately remote sensing has been rapidly advancing as a science, characterizing wetland vegetation with rich biodiversity has not been thoroughly investigated with hyperspectral data.

Chapter 2

Background

2.1 Importance of wetlands

Wetlands are multiple-value structures with a very high ecosystem significance covering approximately 4-6% of the world's terrestrial part and a “tentative minimum” global area of 12.8 million km² according to estimations from Finlayson et al. (1999). They are generally perceived as places where “water is the primary factor controlling the environment and the related plant and animal life” (Niering, 1985), and more strictly are defined according to the Article 1.1 of the Ramsar Convention (Ramsar Convention Secretariat, 2013) as “areas of marsh, fen, peatland or water, whether natural or artificial, permanent or temporary, with water that is static or flowing, fresh, brackish or salt, including areas of marine water the depth of which at low tide does not exceed six metres”. They serve important ecological functions and processes, despite the fact that are usually perceived by the general public in a negative context (Mitsch and Gosselink, 2000). At the ecosystem level, wetlands are functioning as means for providing habitat for a variety of organisms, erosion control, and water purification by recycling nutrients and sequestering pollutants. Their importance is stressed by the fact that they connect the terrestrial and water biotic and abiotic characteristics of the landscape, and as such they host a rich biodiversity of plant and animal species. Per se, the habitats encountered within wetlands are of a very dynamic nature and enclose rich diversity.

Lakeshore vegetation is such an ecosystem, and more specifically the ecotone where the terrestrial and aquatic ecosystems merge, hence the vegetation species biodiversity encountered in the buffer zone is intrinsically rich (Figure 2.1). Consequently wetlands are closely associated in the scientific context with biodiversity loss and environmental drivers (Turner et al. 2003). Likewise,

wetlands are areas profoundly susceptible to climate change both indirectly because of the biodiversity they house, and directly as they are fundamentally regulated by the water availability, which in essence is the inundation level of the water body. The fluctuation of water regime is expected to be a major consequence of anticipated global warming. Furthermore, wetlands sequester and release a large volume of fixed carbon in the biosphere and therefore are possibly an important component in global climate change (Mitsch and Wu, 1995). Finally, lately they have been of focal concern because of the growing anthropogenic pressure. The importance is further underpinned by the fact that the loss of wetlands through development, and the associated functions and values, is often irreversible.

Efficient management and conservation of wetlands and natural habitats has been increasingly a topic of investigation by several scientific groups during the last years (e.g. Spanhove et al. 2012). While the field is prevailed by

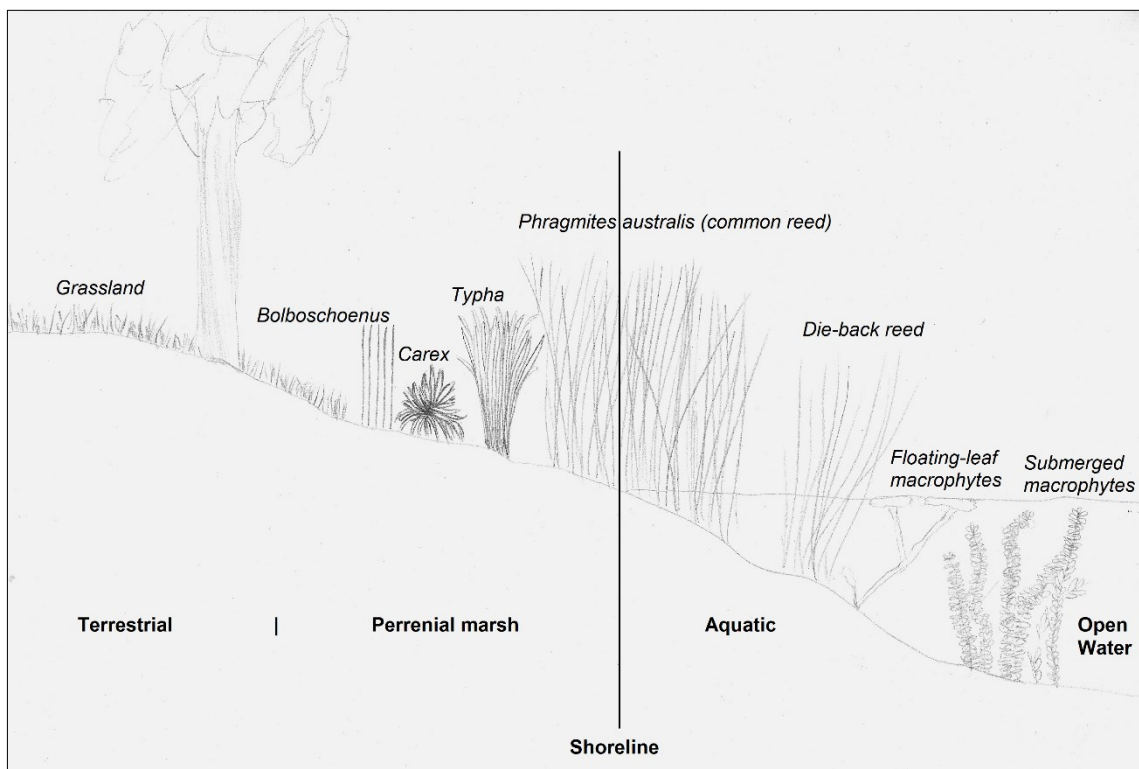


Figure 2.1: Zonation of the lake shore environment. Wetlands are ecosystems rich in biodiversity and are directly associated with the inundation level, hence the water availability.

biological and ecological oriented disciplines, earth observation data and associated techniques are progressively employed for mapping features of interest and indicators. This has urged the need to develop methodologies based on remotely sensed data and tailored to wetland characteristics.

2.2 Phragmites australis

Common reed (*Phragmites australis* (Cav.) Trin. ex Steud.) is a tall and rhizomatous perennial grass (Haslam, 1969; Leithead et al. 1976) (Figure 2.1). It is characterised as an herbaceous renascent aquatic plant typically encountered in wetland environments and more frequently in land-water interface zones (Tucker, 1990). Acting as a buffer zone between terrestrial and aquatic ecosystems (Brix, 1999b), it holds an important role as the key species of temperate wetlands and delivers valuable ecosystem services such as maintaining the shore stability (Engloner, 2009). It can tolerate certain amounts of salinity (<35‰ according to Lissner and Schierup (1997)) and therefore can expand into brackish waters as well. Although its ecological importance is significant, human disturbance has been a large threat for reed beds and subsequently the habitats they support (Wilcox, 1995; Meinesz, 1999).

Phragmites is one of the most widespread vascular plants on the Earth, growing in all continents except Antarctica (Tucker, 1990). Thus its appearance depends both on the environment and the genotype (Kühl et al. 1999; Brix, 1999b). Koppitz (1999) and Hansen et al. (2007) claim that *Phragmites* is a species with very high genetic variability, which accounts for the large differences between different clones. There is a considerable variation in the chromosome complement of *Phragmites* (Tucker, 1990; Hansen et al. 2007), however no correlation has been found in ploidy, habitat or geography between 40 European populations in a survey conducted by Raicu et al. (1972, as cited in Tucker, 1990). Bastlová et al. (2004) reported variation in *Phragmites* phenology as well as morphological and growth characteristics depending on

the geographical location; for instance plant height is decreasing with increasing latitude. This variability of characteristics is thought to be the differentiation of genotypes adapted to the local environment. Nevertheless, despite the importance of the findings from studies focusing on *Phragmites* from the ecological point of view, it is not uncommon to often reach contradictory results. For a more comprehensive description of *Phragmites* morphology, physiology and phenology the reader is suggested a review from 190 publications conducted by Engloner (2009).

Phragmites holds a significant role in wetlands as it provides a buffer zone between the terrestrial and aquatic ecosystems and therefore contributes to water quality stabilization. Its importance is particularly significant in shallow lakes since their ecological status depends on the abundance and composition of macrophytes (Hunter et al. 2010b). Furthermore, the maximum seasonal biomass of living shoots and rhizomes of *Phragmites* may exceed 170t dry weight per ha (Brix et al. 2001) in some places (e.g. Comana Lake, Romania), hence, on a global scale permanent reed beds can be considered as temporary greenhouse gas sinks. Moreover, reed is reducing considerably the erosion of the lake shoreline and contribute to long term geomorphological stability (e.g. Morris et al. 2015). From a commercial point of view, they are used for thatch, basketry and as a source of pulp for paper production especially in Eastern European countries (Tucker, 1990). Finally, reed formulates a dense stand occupying most part of the ecotone between the terrestrial and aquatic ecosystems and houses species from both sides. Therefore it is breeding, feeding and spawning zone and acts as an important sanctuary of wildlife.

2.3 The reed die-back

Since the beginning of the 1950's a sudden, widespread and escalating retreat of reed beds has been observed in parts of Europe (Ostendorp, 1989; Den Hartog et al. 1989). Typical indicative expressions reported include abnormal rhizome, root anatomy and low starch levels in rhizomes (Čížková et al. 2001),

weaker culms, gradual thinning, reduced size, formation of clumps, natural degeneration of the land-water ecotone and eventually retreat from relatively deep water (Van der Putten, 1997). These factors signifying an abrupt reduced stability are collectively reported in the literature as the 'reed die-back'. However, contrary to the typical stress manifestation in the leaf structure of most plants, identification of die-back conditions is not straightforward when using macroscopic visual assessment especially at an early stage, because of the connection of individual shoots by underground rhizomes allowing sharing of nutrients. Thus, while the entire plant may be in a state of die-back, the leaves do not necessarily show important phenotypic signs of deterioration.

Large scale reed die-back has been observed mainly in Central Europe (Krumscheid et al. 1989; Küshl and Kohl, 1992; Fogli et al. 2002) and to a lesser extent in Eastern and Northern Europe (Van der Putten, 1997). According to Ostendorp (1989) and Van der Putten (1997), the phenomenon was first reported 60 years ago by Hürlimann (1951). Since then an increasing scientific interest and environmental concern has been raised. Several national and international projects have been developed for studying and tackling the problem and awareness has been raised within the academic community.

Over the last decades various causative factors have been proposed, however a concrete assumption has not yet been agreed on. The conclusion of the 1993-1994 European Project on Reed Die-back and Progression (EUREED) is that stagnant water levels, due to changes in water table management practices, in combination with eutrophication is a key factor (Van der Putten, 1997; Brix, 1999a). Prolonged stabilized water levels have been reported from very early as a causal factor of emergent vegetation degradation (McDonald, 1955; Uhler, 1944; Harris and Marshall, 1963; Ostendorp, 1999). The first author pays attention to the rise of water level and refers to an early study by Oosting (1933) where a lake was filled up with water after a two-year dry

period and the emergent vegetation disappeared. The water level affects the reed growth, both on the amplitude of the fluctuation and the elevation. Deegan et al. (2007) found that *Phragmites* growth was actually enhanced by moderately fluctuating water level (± 30 cm) while Vretare et al. (2001) in their experiment found that increased or fluctuating water depth results in reduced plant growth. Weisner and Strand (1996) proposed that the sudden temporal increase in water depth is a critical aspect. They claim that *Phragmites* is a species well acclimated to water depth changes, however not to sudden temporal increases, which has consequences on the plants' rhizome architecture and oxygen supply. More specifically, due to inundation, oxygenation of rhizomes and roots, as well as the surrounding sediment, becomes less and less effective. As a result, hypoxic or even anaerobic conditions are formed which affect the sediment chemistry and create environments that could be tolerated by only certain plants.

Eutrophication was the major cause proposed in the early years as it coincided in time with reed die-back in several European Lakes. Boar et al. (1989) as well as Čížková-Končalová et al. (1992) refer to eutrophication as a condition affecting reed functionality indirectly in several ways. In the same paper it is suggested that wave action, generated by boats or drifting matter, makes reed more vulnerable. Complementary to this idea, Ostendorp (1989) suggested that waves loaded with floating rubbish, driftwood and wash of filamentous algae is a factor contributing to mechanical damage. However, Weisner (1987) reports more vigorous reed belts when macrophytes are exposed to waves than at sheltered sites. Algal wash can upset reed stands in eutrophic lakes. As indicated by Ostendorp (1992) in a lakeside reed belt the chemical influence of algae is not significant, however the mechanical impact is important as the stalks are broken from the algal masses. Other factors proposed to affect reed vigour are local disturbance such as mechanical mowing, the formation of toxic by-products of decomposing litter in anoxic environment (Van der

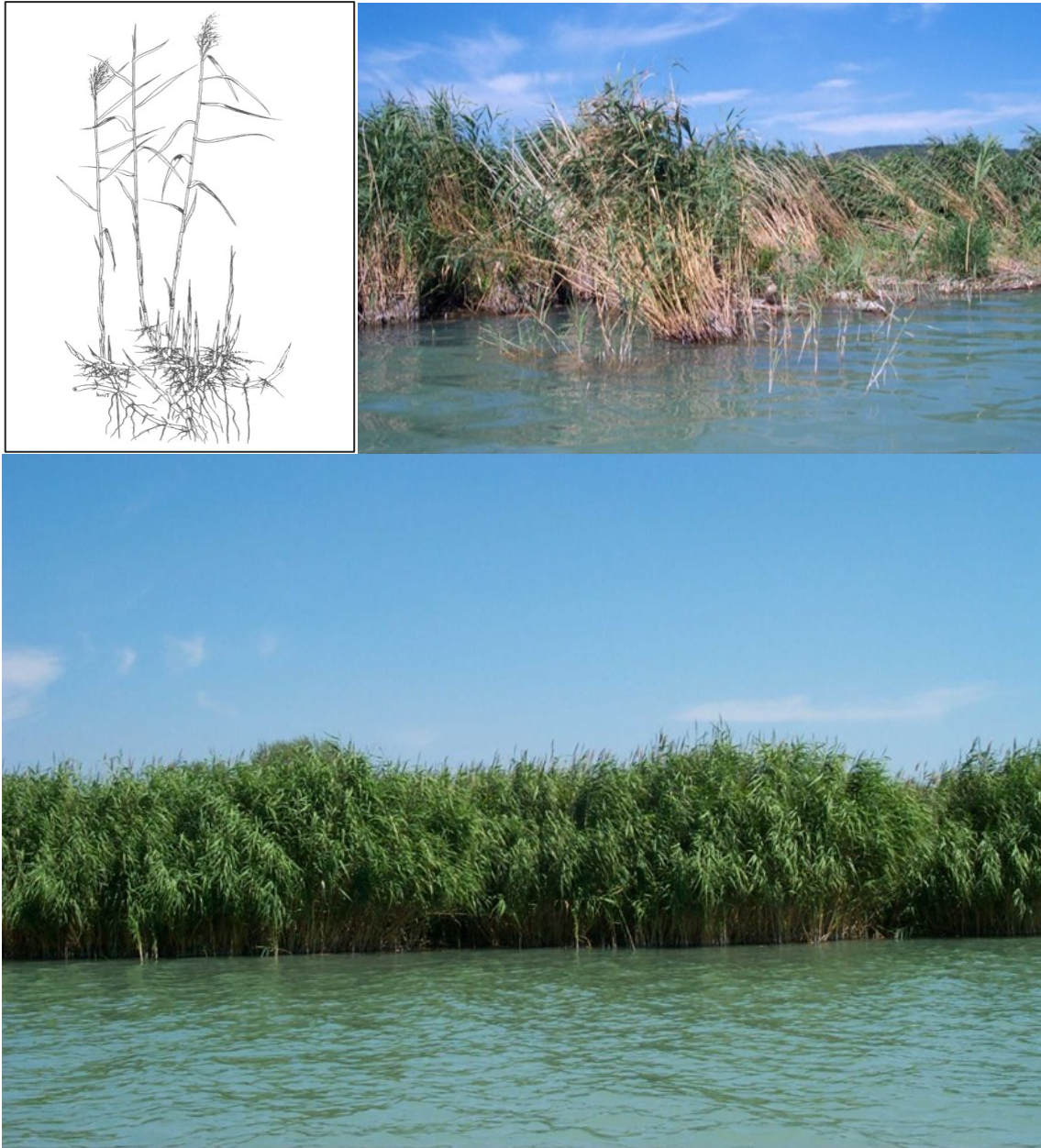


Figure 2.2: Representation of mature plant of species Phragmites (adapted from Brix 1999a, drawing by K. Tind) (upper left), a typical die-back reed stand in Lake Balaton, as observed from the waterward side (upper right) and a stable very dense, stable and tall reed stand (bottom).

Putten, 1997), premature senescence, insect bore holes and callus development (Armstrong et al. 1996), siltation, attacks by insects and organisms and damage by geese and muskrats (McDonald, 1955). Theories also include the carbon starvation hypotheses which is not a direct cause of reed die-back, but may be a gradual process preceding it (Van der Putten, 1997). Soil pore-water salinity was claimed by Fogli et al. (2002) to be a factor

affecting, directly or indirectly, the growth reduction in Denmark and the Mediterranean.

The reed die-back phenomenon has been a well-studied topic in limnology worldwide. Despite the potential capabilities of earth observation in vegetation-related studies, remote sensing techniques have only recently been encompassed in the framework of reed die-back and macrophytes species composition with representative examples presented by Liira et al. (2010), Hunter et al. (2010a), Onojeghuo and Blackburn (2011), Zlinszky et al. (2012) and Villa et al. (2013). The issue of 'reed die-back' may be important in various aspects such as habitat ecology or ecosystem conservation and remote sensing may be a vital tool for large scale assessment of physiological and biophysical parameters of reed vegetation.

2.4 Lake Balaton

Lake Balaton (Figure 2.3) is the largest (596 km²) freshwater shallow lake in Central Europe situated in the west part of Hungary (latitude 46.86026, longitude 17.75473) at 104.8 m above the Baltic Sea level. It has an average depth of 3.3 m and maximum depth 11 m and as such exhibits distinctive characteristics encountered at shallow lakes (e.g. rapid temperature changes). In general, wetlands encountered in such ecosystems are more sensitive to climate and human impact since small water level fluctuations are considerable in relative water depth terms (Korponai et al. 2010). Furthermore, in a very shallow lake wave action is effective over almost the entire lake depth, hence solid material does not accumulate (Bengtsson and Hellström, 1992) and resuspension becomes intense.

The Zala River is the main inflow of Lake Balaton among 50 smaller inputs from a catchment area of 5179 km². The only outflow existing is the artificial channel of Sió through which the water level is regulated and stabilized since the construction of the outlet sluice in 1863. In former times, due to the

absence of a temporary outflow, the water level was highly fluctuating and macrophytes were regulated according to changes in climatic conditions (Herodek, 1988a).

The Lake encompasses important natural conservation sites and plays a pivotal role in the greater region. Protection of water quality and maintaining the natural state of the lake has been of environmental, governmental and touristic importance (Szilassi (1999), cited in Jordan et al. 2005). Macrophytes are growing at the lakeshore, creating a long ecotone where the terrestrial and aquatic ecosystems merge. Large and continuous clusters of macrophytes appear along the north shore of the lake while in the south shore they are sporadically distributed in smaller and narrower reed beds.

According to the last survey conducted by the Hungarian Water Authorities within the lake boundary, 14.09 km² are covered by vegetation consisting mainly of 11.45 km² *Phragmites*, 0.93 km² quasi-natural vegetation (e.g. *Typha sp.*, *Carex sp.*, *Scirpus sp.*) and 1.79 km² other types of vegetation, mainly artificial trees, lawns etc. (Pomogyi, 2013). In essence, this is a large wetland area dominated by reed. Macrophytes in general stretch along 112 km of the 254 km of shoreline and particularly in the northern shore where they form large coherent and continuous stands.

From 1970s until mid-1990s and due to increasing nutrient load the lake transformed from mesotrophic to eutrophic and to hypertrophic (Cserny and Nagy-Bodor, 2000). In the 1970s and 1980s the lake faced environmental pollution, eutrophication and fish extinction, possibly due to redeposited soil masses containing fertilisers, pesticides and herbicides (Jordan et al. 2005). Especially during the 1980's the eutrophication intensified (Herodek, 1984) and in the summer of 1982 the water quality deteriorated sharply with the invasion of a long-lasting blooms of algae in the entire lake area (Herodek, 1988b) which caused severe environmental problems until the mid-1990's.

Attempts to restore the lake to its previous state and reverse the eutrophication were initiated in the mid-1980s (Padisák and Reynolds, 1998). The main actions taken were the construction of the Kis-Balaton water retention system with the aim of reducing the phosphorus load of the Zala River and construction of a drainage system around Lake Balaton that would deterred the treated sewage water from around the Lake directly into its outflow, the Sió Canal, i.e. outside the catchment area of the Lake (Somlyódy, 1998). Furthermore the water volume, and thus the water level of the lake, were adequately controlled by the operation of the Sió sluice (Virág, 1988). Water quality has been improved since early 1990s with wetland reconstruction and drainage and sewage infrastructure around the lake.

Reed die-back in the lake has been observed since the 1970s onwards (Kovács et al. 1989), a while after the eutrophication of the lake started. Eutrophication was consequently initially considered the primal reason of the reed die-back, however this theory was later on refuted as the die-back was essentially similar in the oligotrophic (eastern) and most hypertrophic (western) basins of the lake (Zlinszky et al. 2014). Several studies have focused on the reed die-back in lakes around Hungary. According to Van der Putten (1997) in the whole country die-back was apparent where reed has been harvested by heavy machinery. Positive correlation between die-back and litter accumulation can be typically found in lakes (Van der Putter, 1997). Felföldy et al. (1969) from very early reported water depth as factor of wave action, which is nowadays considered a crucial parameter in reed die-back. Čížková et al. (2001) while measuring carbohydrates reserves at the reed bed of Kis-Balaton found that the local reed stands are among stands with lowest values known to date, and suggest this might be the reason of vulnerability to shoot damage or removal.

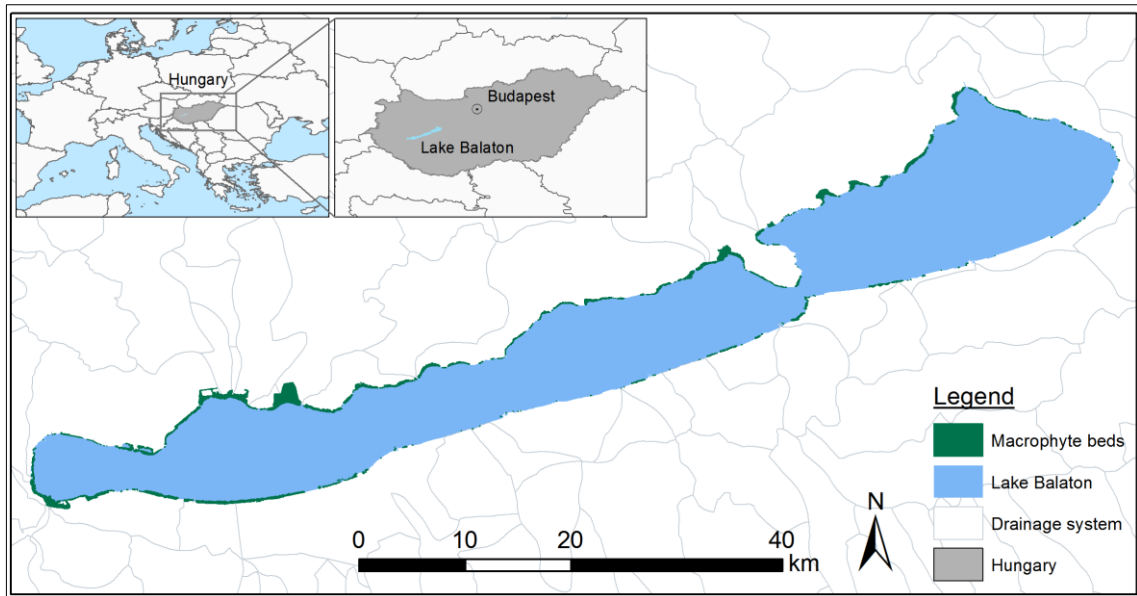


Figure 2.3: Area of study at Lake Balaton, Hungary and the distribution of emerged macrophytes along the shore. The relative position of the Lake within Europe (left) and Hungary (right) are depicted in the inset images.

The main reason suggested by scientists at the Balaton Limnological Institute, an Institute dedicated to studying the ecology of Lake Balaton, is the anaerobic state of the sediment caused from high and stable water level (Tóth V.R., personal communication; Zlinszky 2013). Since the creation of the Sió channel the water level is stabilized at 104.84 m above the Adriatic Sea level to prevent flooding in the area. As a consequence to the stabilization, the submerged sediment at the reed stands is not oxygenized properly; if the water level doesn't fluctuate, the anaerobic bacteria present in the sediment of the reed stands consuming reed litter create reductive conditions. As a result, reed deteriorates at depths deeper than 2 m where it becomes insufficiently oxygenized.

2.5 Remote sensing of wetlands

Optical and hyperspectral remote sensing is a valuable technique for vegetation related studies and its value has long been recognized. The spectral information from the optical and Infra-red (IR) domains is the key information when studying plants from distance; for this reason wetland studies are employing passive sensors and not so often radar, LiDAR or other

methods. Earth observation data have been used for mapping the distribution of wetland characteristics and later on for evaluating the condition of the vegetation from the late 1960's onwards in the form of aerial photos and satellite images since the advent of the Landsat Multimission Modular Spacecraft (MMS) (Bartlett and Klemas, 1980; Butera, 1983). Lately a growing number of monitoring reed habitats initiatives have started to emerge (e.g. Csaplovics and Schmidt, 2011; Pfeifer and Zlinszky, 2014).

However, traditionally wetland mapping has been relying on ground-based surveys undertaken by experienced ecologists. Large-scale conventional mapping methods based on *in-situ* measurements have been proven expensive, labour intensive, impossible at inaccessible areas, error prone and time consuming when covering large areas (Zhang, 1998). Spanhove et al. (2012) list the drawbacks of field mapping including budget restrictions for surveying large regions, inaccessibility of remote areas, slow speed of recording and processing field data and last but not least between-observer errors. For example, Cherrill and McClean (1999) in a study investigating the agreement between six independent surveyors report an average spatial agreement of 25.6%; the large disagreement is mainly attributed to classification errors. In the same study they suggest that the use of aerial photographs and maps before and during fieldwork could increase mapping precision. Aerial digital photos have been used as an alternative cost-effective methodology for spectral analysis on macrophyte cover as well (Anker et al. 2014). Several other papers have been acknowledging the contribution of earth observation data in assessing the conservation status of natural habitats (e.g. Turner et al. 2003; Kerr and Ostrovsky, 2003; Rebelo et al. 2009) as a non-destructive, time- and cost-benefit alternative.

Vegetation is one of the most studied characteristics of wetlands. Continuous advances in the spatial and spectral resolutions of sensors are offering a valuable tool for biodiversity monitoring, directly by identifying species (e.g.

Husson et al. 2014 map aquatic vegetation based on sub-decimeter images from Unmanned Aerial Vehicles (UAV)) as well as indirectly by deriving biophysical characteristics (Turner et al. 2003). For example, Spanhove et al. (2012) estimated fine-scale indicators by measuring coarse-scale parameters with remote sensing, hence providing indirectly information on ecological features. Bartlett and Klemas (1980) report that many important characteristics of wetland ecosystems may be inferred from the distribution of emergent macrophytes, such as chlorophyll absorption, percent green vegetation, total and green biomass and canopy height. Nevertheless, wetland mapping with earth observation data has been a challenging task for scientists and practitioners likewise. The large biodiversity encountered in this ecotone results in a complex spatial structure and composition. Additionally, the water level variability over time creates constantly changing conditions which are difficult to be monitored. The need to establish advanced methodologies for wetland vegetation mapping is prominent and several authors urge for developing and improving wetland specific methods using advanced remote sensing data from state-of-the-art sensors with enhanced capabilities (Rebelo et al. 2009). Turner et al. (2003) review the usefulness of remote sensing for biodiversity science and conservation and indicate great improvement of species detection and patterns of species richness with remotely sensed data. In the same paper they call for collaboration between remote sensing practitioners and biodiversity and conservation scientists.

As an example, the need to quantitatively determine the cover of reed on Lake Balaton is of significant importance and has been stressed from the very early years (Tóth, 1972). Similar conditions have been observed in several European wetlands with an increasing environmental and scientific interest. To date, most of the operational mapping takes place through field visits and visual evaluation to estimate the area covered and associated characteristics. Earth observation is undeniably a rich source of information for vegetation

mapping; yet equally importantly it can provide information on plants biophysical properties.

At leaf level, photons interact with vegetation by either absorption or scattering. When absorption occurs, the energy drives either the photosynthesis of the plant, either dissipates to the environment as heat, either is emitted back to the environment at different wavelength as chlorophyll fluorescence. Vegetation-specific processes such as photosynthesis can determine the spectral response of the plant. For instance, the dominant leaf pigments, chlorophyll a and b, a-carotene and xanthophyll, absorb collectively around 445 nm in the blue region and specifically chlorophyll (CHL) around 645 nm; as a result and according to widespread scientific perception, the photosynthetic activity is associated with the red-edge inflection point, the near-infrared region with the cell structure and the shortwave infrared with the water absorption of the plant (Figure 2.4). The optical part of the spectrum provides important information on the plant photosynthetic activity and manifestation of plant stress is expressed in this region. Especially the range 530-570 nm is suggested from Kotta et al. (2014) for species and larger taxonomic units separation. encompasses the important spectral characteristics of vegetation and rationalizes the necessity of using narrowband hyperspectral data in vegetation related studies.

Such accurate measurements are made with handheld spectroradiometers attached to leaves. The narrow bands of hyperspectral data can provide key information in regard to green vegetative cover (McGwire et al. 2000), species and vegetation associations (Schmidt and Skidmore, 2003), plant stress (Carter, 1993) and disease infection (Chen et al. 2008). Furthermore it is possible to estimate biophysical parameters remotely, such as with sensors attached onboard satellites, aircrafts or UAVs, however the interaction of the signal with the atmospheric elements and the capability of recording reflectance in pixel-sized areas can alter significantly the recorded values.

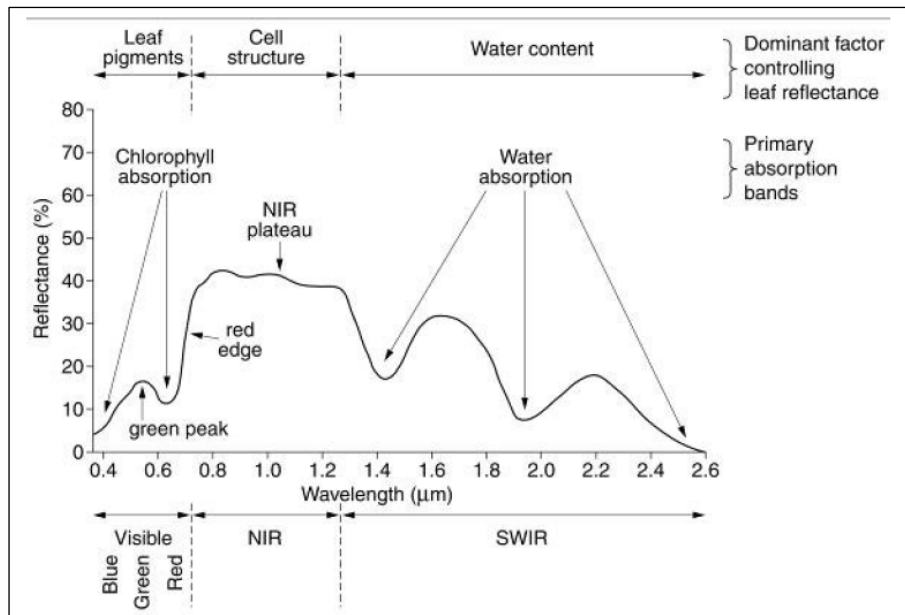


Figure 2.4: Typical vegetation reflectance curve and important features that can be estimated through mainly spectroscopic information (after Hoffer, 1978).

Satellite imagery has been the choice of most wetland mapping studies because it offers either very fine spatial resolution imagery (for instance WorldView-4 is planned to deliver images at 0.30m pixel size) or very high spectral resolution data (Hyspirci imaging spectrometer has 212 bands); yet currently no satellite in orbit offers both capabilities simultaneously. This can be accomplished at present only by hyperspectral sensors mounted on airplane platforms flying at low altitude.

For a complete overview of wetland mapping, Ozesmi and Bauer (2002) summarize the classification schemes used in remote sensing of wetlands, Rebelo et al. (2009) report on several recent initiatives using earth observation data to foster wetland inventorying, Adam et al. (2010) concentrate on the identification of wetland vegetation and Klemas (2011) compiles a comprehensive review of practical techniques.

2.6 Environmental policy framework

Legislative authorities have long realized the financial and social consequences of wetland degradation and developed strategies for monitoring and

inventorying natural habitats. The GlobWetland project coordinated by the European Space Agency (ESA) lasted from 2003 to 2008 in connotation with the Ramsar Convention on Wetlands established as early as 1971. GlobWetland II was the continuation programme run between 2009 and 2013, time during which approximately 200 wetlands were mapped in the Mediterranean region. In a similar effort, ESA and the Ramsar secretariat are launching the GlobWetland Africa project within 2014. This project will be established on satellite observations to support wetland management and its resources in Africa. Another important endeavour was the Millennium Ecosystem Assessment (2001-2005) (Finlayson et al. 2005), implemented to assist decision makers on the relationship between ecosystem change and human well-being, part of which is devoted to wetland mapping. In 2001 the Pan-Mediterranean Wetland Inventory was introduced (Fitoka and Keramitsoglou, 2008). Multi-scale Services for Monitoring NATURA 2000 Habitats of European Community Interest (2010-2013) mapped nature sites of community interest for fostering environmental legislation in Europe and reducing biodiversity loss. The “BIOdiversity multi-SOURCE Monitoring System: from space to species” is an ecological modelling system for monitoring habitats and particularly those exposed to pressure.

Another well-known project is NATURA 2000, a European Union (EU) wide network of nature protection areas established under the 1992 Habitat Directive and is the backbone of EU nature and biodiversity monitoring. One of the targets of EU strategy for 2020 is the better protection and restoration of ecosystems. It proposes the development of a framework for degraded ecosystems supported by relevant work for mapping and assessing its state.

The European Earth Observation programme Copernicus, previously known as Global Monitoring for Environment and Security (GMES), is a programme building on *in-situ* collected and earth observation data to provide reliable and up-to-date information to end users through 6 established services. GMES

was launched with the aim to provide reliable information to European public missions and successively establish a European observation capacity through an operational set of services. The objective was to develop a high-quality European Earth observation capability, which will benefit a broad range of European policies. Wetland ecosystems are part of the Copernicus land monitoring services.

Wetlands are vulnerable to changes and it is expected that climate change will have a pronounced effect on them (Erwin, 2009). Currently there is a lot of debate on the consequences of global warming and especially of sea level rise in the biosphere and the first indications are anticipated to be evident in wetland habitats. In this context, the United Nations Framework Convention on Climate Change (UNFCCC) was derived from Rio Earth Summit in 1992 and was entered into force on 21st March 1994 with the aim to address climate change. Quality of inland waters, which is part of wetland ecosystems and affects lakeshore vegetation, has been supported by the EU Water Framework Directive (WFD) and remote sensing can considerably contribute to water quality monitoring (Chen et al. 2004).

In regard to the reed die-back, the European Commission during the 1990s funded two consecutive research projects. The EUREED during 1993-1994 and the EUREED II from 1996 to 1999 were designed to provide the basis for co-ordinated research activities throughout Europe for studying the parameters affecting reed die-back.

2.7 Research objectives

The review of the previous scientific literature on the remote sensing of macrophytes has shown that wetland mapping, and specifically the case of lakeshore ecotones, is challenging especially when concerning large geographical areas. Earth observation plays an increasing role in ecology lately as it gains recognition while hyperspectral sensors are equipped with ever

increasing technical capabilities. In this application-oriented discipline, the need to research how and to which extent categorizing aquatic vegetation and estimate associated biophysical parameters based on remotely sensed imagery is prominent. Studies of mapping macrophytes with remote sensing are limited to delineating the reed bed and very few examples can be found which demonstrate species level categorization. Biophysical parameters are a more generic field in vegetation studies with many prime examples demonstrating precise estimation of nitrogen content, chlorophyll content and biomass for example, however these parameters are associated to plant stress only at an advanced stage.

This study is driven by the need to further develop remote sensing techniques for lakeshore vegetation applications, specifically delineating macrophytes classes of interest and estimating the stress condition of *Phragmites*. Studying the vegetation of ecosystems with rich biodiversity such as wetlands, requires *in-situ* measurements and fine scale imagery. The former allows for extracting site- and species-specific background data and results, while the latter is prerequisite for unveiling the complex structure of the ecosystem and the vegetation cover at species and association level. At this scale, distinguishing species assemblages or even individual species can become feasible (Turner et al. 2003). Towards this direction, a wide range of datasets was employed, from *in-situ* measurements to airborne data and simulated satellite imagery over Lake Balaton, Hungary in an attempt to investigate the potential of remote sensing for mapping macrophyte associations and stress conditions in the framework of the reed die-back phenomenon in a lakeshore environment.

More specifically, in this study the following objectives are addressed:

1. To study hyperspectral reflectance profiles of different macrophytes and *Phragmites* phenotypical states at leaf and canopy scale in order to differentiate between species and phenotype.

2. To study how the spectral response of *Phragmites* leaves associates with chlorophyll fluorescence parameters and hence with photosynthetic activity. Based on the results from the field data analysis, to further test whether reed die-back can be detected from hyperspectral remote sensing.
3. To search for classification schemes for lakeshore vegetation mapping with high spatial resolution airborne data and quantify their accuracies.
4. To simulate Sentinel-2 imagery from airborne data for assessing the expected potential of the satellite for lakeshore vegetation mapping and reed die-back detection as a possible application in the Copernicus programme.

The Thesis is structured accordingly in 4 remaining parts. Chapter 3 is dedicated to the analysis of hyperspectral responses collected from field samples on Lake Balaton over emergent macrophytes. The discrepancies in reflectance curves at the 400-1000nm spectrum between species and *Phragmites* stability conditions at leaf and canopy scale is investigated. Chapter 4 (together with sub-chapter 3.4.5) has been published at the time of this Thesis publication in the scientific journal of Remote Sensing of Environment (Stratoulas et al. 2015) and is an outcome of my personal scientific research. This chapter is dealing with finding appropriate narrowband indices which better represent reed's ecophysiology. This is accomplished on the basis of concurrently acquired hyperspectral and fluorescence data from the same leaf samples *in-situ* and by coupling spectral narrowband combinations with fluorometric parameters, the latter representing the physiological status of the plant. In the second part of this chapter the developed hyperspectral indices are applied on airborne imagery over the area of study in order to assess their performance from low-altitude airborne data. In chapter 5 an evaluation of classification algorithms and different airborne dataset inputs for mapping emergent macrophyte associations over a reedbed is presented. The

capabilities of hyperspectral sensors recording radiation at the 400-1000nm and 1000-2400nm spectral range and the joint classification of spectroscopic data with concurrently acquired airborne laser scanning data is discussed. Last, in chapter 6 a simulation of a Sentinel-2 image is presented based on the airborne hyperspectral data. A classification of the main classes is presented and the suitability of satellite data for operational mapping of lakeshore vegetation is discussed.

Chapter 3

Analysis of macrophytes *in-situ* spectral information

3.1 Introduction

The reed die-back has long been a subject of discussion in an endeavour to identify the causes and reveal its underlying mechanisms. Reed physiology and the associated aquatic environment have been extensively studied with regard to anatomy, chemical composition, biological processes and ecological behaviour. Imaging spectroscopy has lately been emerging as a promising technique for vegetation-related applications and scientific improvements are needed to sustain the potential for advancement in this field (Thenkabail et al. 2012). Despite the fact that the use of imaging spectroscopy has proven promising in similar fields such as precision agriculture and disease diagnostics, a detailed spectral analysis has not yet been compiled for the wetland vegetation at Lake Balaton. As an example, Chen et al. (2008) studied the spectral characteristics of a cotton canopy infected with *Verticillium* wilt in order to prepare the ground for utilizing remote sensing techniques. Given the fact that there is a strong theoretical background on the reed die-back, a similar spectral investigation and correlation of factors could provide useful techniques for mapping lake shore vegetation. For instance, nitrogen concentration has been identified as a factor related to reed disturbance; reed sequesters nearly twice the amount of nitrogen per unit area in living aboveground tissue compared to cattail (*Typha angustifolia*) (Findlay et al. 2002). Küshl and Kohl (1992) report a strong correlation between nitrogen accumulation and lower stability of the reed stands in 8 lakes in Germany.

Furthermore, the indications of reed die-back are generally not easily detectable with visual assessment. Reed plants (i.e. ramets) are interconnected with common rhizome and the phenotypical expression of a disease or disturbance is not easily distinguishable at the aboveground plant material.

The signs of stress are based on differences in density within the reed stand, the diameter and height of the stems, etc. Therefore, reed die-back is a general term expressing the phenomenon of deterioration at the plant community scale and not for individual ramets. As such, remote sensing could potentially provide a means to assess reed phenotype, which is difficult to accomplish otherwise.

On the other hand, unmanaged ecosystems have a richer number of species, phenotype, canopy structures, etc. which results in a large variability in chlorophyll content, leaf area, biomass, and photosynthetic functioning. As mentioned earlier, Lake Balaton, being the largest lake in central Europe, extends in a vast area and exhibits variability in water quality and ecological characteristics between eastern and western basins (Üveges et al. 2011), which results in higher morphological variability of species among different sites throughout the lake. *Phragmites* is a species with a wide phenotypic variability at Lake Balaton (Tóth and Szabó, 2012) and large differences in genetic variability (Engloner et al. 2010; Engloner and Major, 2011). The well-known morphological variability expressed in the chromosomes is transferred into the spectral signature of the plant material and the vegetation intra-variability might be considerably higher than the interspecific variations between plant associations or even species.

3.2 Objectives

This chapter focuses on the analysis of spectral samples collected on the northern shore of Lake Balaton in regard to vegetation classes of interest. The heterogeneity of vegetation is the pivotal point. The plasticity of the spectral response is discussed in regard to the species composition and the reed phenology on Lake Balaton. Specifically, the objectives are to:

1. Study the spectra of the main macrophyte associations of Lake Balaton

2. Investigate any differences existing between stable and die-back reed samples at leaf and canopy scale
3. Investigate differences in phenotype of reed canopy as appears in different growing stage
4. Study the differences between the sun and shade leaves of the reed plants
5. Examine the effect of inundation level on the reflectance and transmittance spectra of reed leaf samples as well as the chlorophyll fluorescence and chlorophyll content

3.3 Field campaign and sampling design

Spectra recorded non-destructively in the field are the most reliable source of information of vegetation's spectral signatures. Measurements on leaves have the advantage of providing pure spectral signal with no atmospheric interference, and hence uninfluenced by atmospheric interaction. On the other hand, spectra recorded with a field-of-view instrument over the canopy have little atmospheric interference and can provide local-specific spectra of a ground area analogous to the satellite's pixel resolution.

3.3.1 Spectroscopic data collection

A field campaign was carried out perimetrically of Lake Balaton during August 2012, coinciding with the biological productivity peak of reed stands. Data were obtained from 3 visits at different parts of the northern shore of Lake Balaton (Figure 3.1). The Szigliget, Bozsai and Kerekedi bays were selected as they are relatively large vegetated areas and include reed die-back patches.

At Szigliget bay (Figure 3.1) leaf reflectance spectra were collected based on the following main macrophytes associations of Lake Balaton (objective 1):

1. terrestrial reed (representing *Phragmites* growing on soil, hence not covered with water)
2. aquatic reed (*Phragmites* growing at sediment where at least 50cm is covered vertically with water)

3. *Typha sp.*
4. *Carex sp.*

21, 20, 19 and 10 samples were considered for terrestrial reed, aquatic reed, *Typha* and *Carex* respectively. Moreover, canopy spectra from reed samples in regard to different phenotype were collected (objective 3). The classes established were reed patches with inflorescence, reed with high dried content and recently emerged reed. All the above field samples were collected along transects perpendicular to the lake shore. A stratified random sampling (probabilistic method of sampling) was followed in the direction of the transect. This provides the benefit to minimize the variability between the different zones of the area. Samples were taken from fully mature leaves which receive sufficient solar radiation. Large leaves were selected for reasons of covering the whole area of the leaf-clip accessory instrument and avoiding illumination artefacts while recording *in-vivo*.

A morphological survey took place to investigate the separability of stable and die-back reed based on the hyperspectral signal at canopy scale (objective 2) at Bozsai bay (Figure 3.1). 6 location points were chosen for the stable samples and 7 points for the die-back sites. Bozsai bay is a natural protected site, therefore it is quasi-undisturbed from human activity and its biodiversity and complexity is higher than those of managed ecosystems. It encompasses a variety of macrophytes, trees and grasslands, however the main ecological focus is placed on *Phragmites* and a relatively smaller part covered with *Typha sp.* and *Carex sp.* This study area has the advantage of situated in the vicinity of the base Research Institute, providing easy access and assuring familiarity of the author and experienced researchers with the local vegetation.

Field data collection at Kerekedi bay was conducted between 2nd and 17th August 2012. The reed bed was covered by a stand of mostly monospecific *Phragmites*, although at the terrestrial part *Carex sp.* was co-dominant. The

western part of the reed bed has seen a regression of the reed fringe by 20 meters the last 10 years and is a characteristic case of die-back occurrence at the easternmost mesotrophic basin of Lake Balaton. Canopy measurements were collected in order to investigate the differentiation of stable and die-back reed samples. 7 location points were chosen for the stable samples and 11 points for the die-back sites. Furthermore leaf spectra were obtained in regard to stable and die-back reed conditions (objective 2). Sunny and shaded leaves were also collected and the spectra recorded from the middle of the leaves (objective 4).

Hyperspectral data from macrophytic samples from the three lake bays were recorded simultaneously with geolocation and floristic information appended. Access to waterfront parts of vegetation was accomplished by a boat (Figure 3.2), while access to the terrestrial part of macrophytes through narrow walkways and transects within the reed stand. A Hand-Held ASD portable FieldSpec 2 spectroradiometer (Analytical Spectral Devices Inc., Boulder, Colorado, U.S.A.) was used to record radiation intensity in 750 consecutive channels at the spectral domain 325-1075 nm with a spectral resolution less than 3nm at 700nm. Twenty consecutive measurements were acquired over the same sample leaf or canopy area. Integration time was 544 ms.

Canopy radiance was recorded between 11:00 and 15:00 local time (Central European Time) when sun is at zenith and irradiation is the highest of the day under clear sky conditions. This was accomplished by attaching the device to an extendable pole and placing it perpendicularly 50cm above the vegetation canopy (Figure 3.2). The field of view of the instrument in this configuration was 25°. The instrument was calibrated with a white reference panel every 10 min (Spectralon, Labsphere).

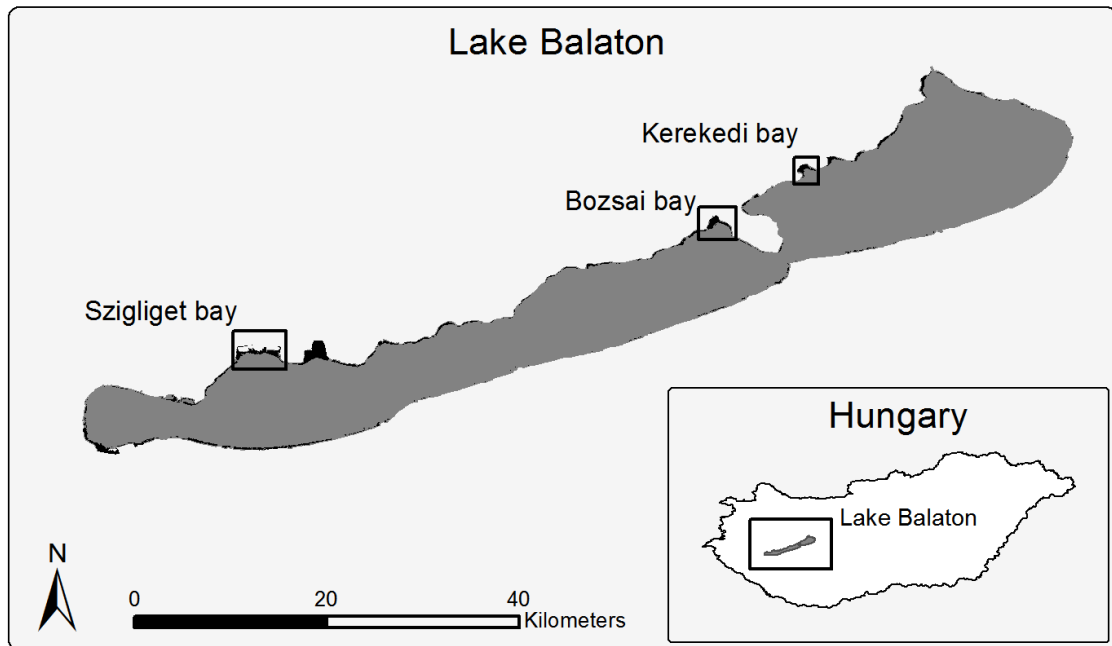


Figure 3.1: Field data collection at designated macrophyte sites on Lake Balaton, namely Szigliget bay (latitude 46.796965, longitude 17.405215), Bozsai bay (latitude 46.918315, longitude 17.834720) and Kerekedi bay (latitude 46.967421, longitude 17.917029). 74% of the macrophyte sites lie on the north shore of the Lake, while on the south shore only thin slivers of vegetation are encountered.

Leaf reflectance and transmittance values were collected through a leaf-clip attached to the device with an optical fiber. The light source in this experimental set-up is provided not by solar illumination conditions, but from an integrated light bulb in the leaf-clip. A white or a black panel is placed on the opposing side to record reflectance or transmittance values respectively as well as for calibration purposes.

Complementary, a Leica GS20 PDM handheld Global Positioning System (GPS) receiver was used to acquire the geolocation of the measurements accompanied by floristic information on the sampling point.



Figure 3.2: Photograph illustrating the setup for collecting canopy field measurements from the waterward side of the reed bed with the aid of a motorboat at Bozsai bay in Lake Balaton, Hungary. The spectroradiometer is attached vertically at the end of a pole and is pointing downwards at the time of data acquisition.

3.3.2 Biophysical parameters and leaf hyperspectral concurrent measurements

Hyperspectral, chlorophyll fluorescence and chlorophyll content were measured concurrently (Table 3.1) from reed leaves along a transect aligned perpendicular to the lake shore at the north-eastern part of the Kerekedi bay and according to different inundation categories (Figure 3.3) in regard to objective 5. A site where monospecific reed can be found was chosen to minimize inter-species heterogeneity. Some fragmentation in this area could be observed, but this inhomogeneity is a result of the vegetative growth of reed and can be considered natural and not a result of stress. There were no severely stressed plants at the edge of the reed bed since this was a relatively stable reed patch.

In-situ measurements were collected in the Kerekedi bay on August 14th, 2012 at the climax of the growing period in the area of study and under clear sky conditions between 11:00 and 13:00 local time (objective 5, further information provided at sub-chapter 3.2). Mid-morning period is the time of the day when signal levels are maximized in regard to stress identification

(Amoros-Lopez et al. 2008). The measurements were performed at the middle third of the youngest fully matured leaves of *Phragmites* in full sunlight conditions.

While the ecotone of the lakeshore is an environment in gradual transition, it is necessary to stratify it into meaningful categories for the sake of statistical analysis and interpretation. It is acknowledgeable that this crisp classification introduces errors and is a simplification of the ecotone environment, however it can provide meaningful results based on categories which can be identified as such in other parts of the Lake or even other Lakes. Taking into account the inundation level and the edge of the reed bed from the watershed side, four categories have been distinguished visually in the field:

1. Terrestrial
2. shallow water
3. deep water and
4. waterfront

In the terrestrial part of the transect sediment was not covered with water, in the shallow part the sediment was covered with up to 15 cm of water, at the deep part of the transect the plants were covered with more than 15 cm of water, while reed at depth of more than 140 cm and up to 5 meters in vicinity to the waterfront of the reed bed was considered as the waterfront category. The latter is receiving higher environmental pressure from wind, wave mechanical damage, litter accumulation and maneuvering from fishing boats docking between the reed stands. Measurements at 23, 55, 27 and 17 location points of the transect for the 4 categories respectively were collected.

Table 3.1: Instruments used and parameters measured in this field campaign.

<i>Data type</i>	<i>Instrument</i>
<i>Hyperspectral leaf reflectance</i>	<i>ASD FieldSpec-2 HandHeld spectroradiometer</i>
<i>Fluorescence yield</i>	<i>PAM-2500 fluorometer</i>
<i>Chlorophyll content</i>	<i>SPAD-502 chlorophyll meter</i>

Leaf chlorophyll content was estimated by a SPAD-502 chlorophyll meter (Konica Minolta, Inc., Japan), measurement which is based on the optical density difference at two wavelengths, 650 nm and 940 nm. Light adapted chlorophyll fluorescence data were acquired on site using a PAM-2500 fluorometer (Heinz Walz GmbH, Germany). For each sample the apparent (F_s) and the maximum (F_m') values of fluorescence yield and the Photosynthetically Active Radiation (PAR) (measured in $\mu\text{mol quanta m}^{-2} \text{s}^{-1}$) in the light-adapted state were measured. F_s is in essence the fluorescence yield under solar conditions (or under a constant actinic white light) while F_m' is the yield obtained when exposing the leaf to a saturating light pulse of high intensity ($3000 \text{ mmol m}^{-2} \text{s}^{-1}$). The nomenclature adapted in this study follows this from Genty et al. (1989).

The age difference between the leaf samples (of plants of the same age) due to the apical growth of Phragmites has been minimized by selecting only the apical first fully mature leaf.

Ground-based hyperspectral measurements were recorded contemporary using the Hand-Held ASD portable spectroradiometer from the same leaves as the biophysical parameters. The recording method was the same as already described.

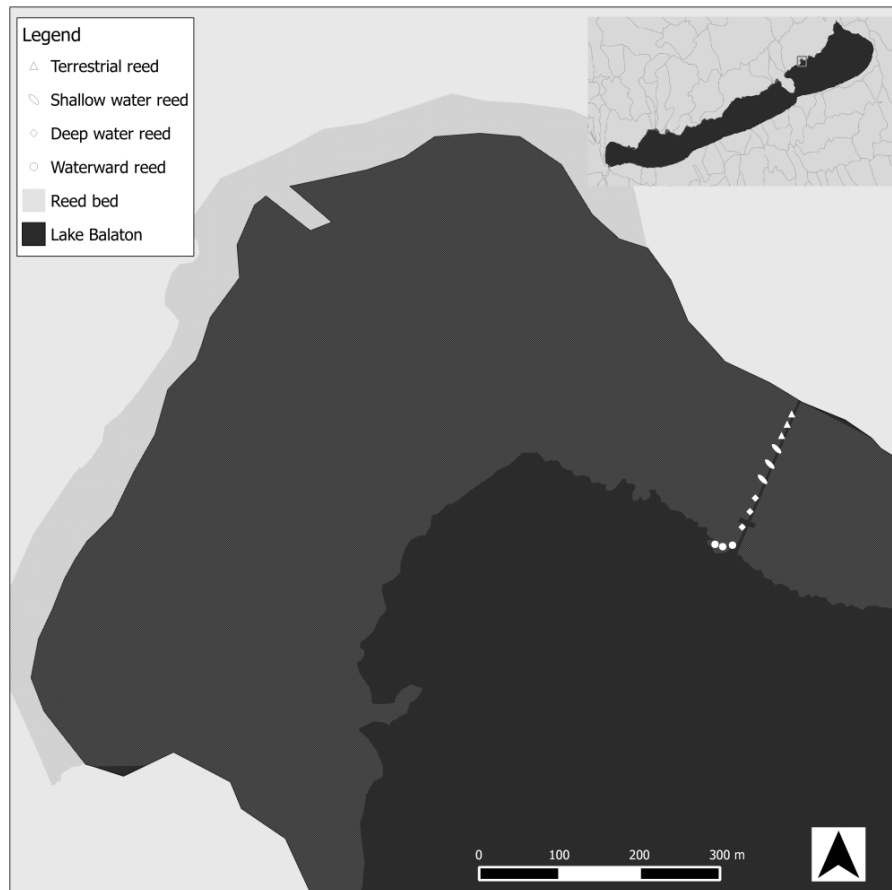


Figure 3.3: Kerekedi bay, Lake Balaton and location of sampling points.

3.4 Methodology

The methodology carried out for the analysis of the objectives follows a generic pattern as described below. The statistical analysis has been implemented mainly in the R language environment (R Core team, 2013). First the spectra were averaged to a mean value for the 20 occurrences after eliminating any outliers, which might have occurred especially in the first and last measurements due to the clip loose adjustment or the tilted orientation or low elevation of the instrument. The mean values were exported to an ascii file in ViewSpecPro 6.0 software in reflectance data format. Thereafter, the mean spectra and the associated standard deviation of the entire population of the samples were calculated. Each spectrum was subset to the region 400 – 1000 nm since the marginal wavelengths appeared to be highly unstable due to

error introduced by the instrument. Finally the mean value and the 95% confidence intervals were plotted for each experimental setup.

For the inundation level categories, the Tukey-Kramer Test (Pairwise Comparisons for One-Way Layout Design) was used to compare the photophysiological data collected from the fluorometer and the CHL meter for each category.

3.5 Results and discussion

3.5.1 Leaf spectral analysis of macrophyte species

Leaf reflectance spectra from the main macrophytes encountered at Lake Balaton were studied. The samples were collected from the Szigliget bay and categorized in four associations, namely terrestrial reed, aquatic reed, *Typha sp.* and *Carex sp.* The two reed categories show a distinguishing spectral curve comparatively to the other two species as they reflect stronger in the visible region (Figure 3.4). The difference is especially prominent in the region 560 – 670 nm, region which is regulated by the leaf pigments and indicates chlorophyll absorption as explained in . In the near-infrared domain reed categories reflect weaker, indicative of the different cell structure. Between terrestrial and aquatic reed small differences can be observed such as the gradually higher reflectance of the latter below 500 nm and above 800 nm (Figure 3.4). Spectral curves of *Carex* and *Typha* follow a similar pattern; nevertheless *Carex* demonstrates 10% relative lower reflectance throughout the spectrum (Figure 3.4).

The main macrophyte species encountered at Lake Balaton, and especially reed, have a high degree of separability at leaf scale. It is worth noting however that some species, such as *Carex* are rarely forming dominant patches in the study area; they are growing within other macrophytes patches and consequently such associations are more challenging to detect at canopy scale with non-proximate instruments. To add in the complexity of the scene when

studying macrophytes, consideration has to be given to the fact that reed also grows often in a mixture with other species, and its presence is not always dominant, especially in the terrestrial edge of the reed bed where drier sediment conditions become favorable to ruderal vegetation.

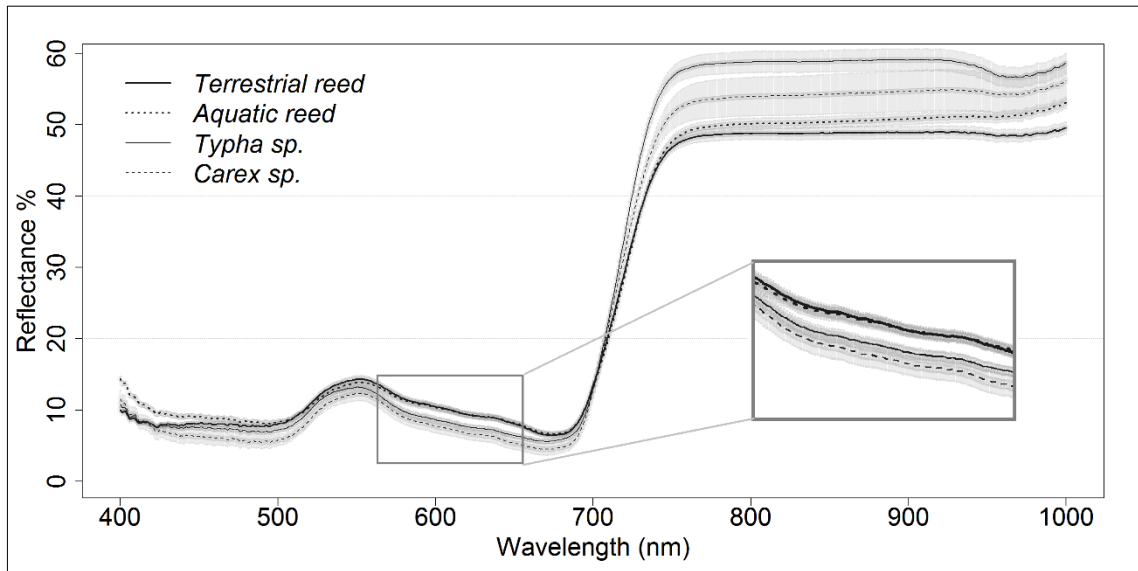


Figure 3.4: Leaf mean reflectance spectra (curves) and the corresponding 95% confidence intervals (shaded areas) for the macrophytes associations collected at the Szigliget bay in Lake Balaton. Reed categories reflects stronger in the visible region and especially at the chlorophyll absorption bands between 560nm and 670nm, while it reflects weaker in the near infrared, associated to the cell structure as explained in .

3.5.2 Reed spectral analysis in regard to reed die-back

Leaf reflectance spectra from stable and die-back reed plants were collected from the Kerekedi bay, Lake Balaton. Respectively, canopy reflectance spectra were obtained from the Bozsai bay at the waterward side of the lake.

The spectral responses at the leaf scale show statistically important discrepancies between plants from stable and die-back reed sites (Figure 3.5). First, the die-back reed has lower reflectance values in the visible wavelengths with the largest difference appearing at 560 nm. Furthermore, it exhibits a red-shift in the red-edge region, with the inflection point being shifted by 6 nm to longer wavelengths. In the near-infrared domain, the spectra appear to be very similar. In the red-edge region, differences in the reflectance at the inflection

point (Figure 3.7) are not large (0.45 (SD 0.027) for the stable and 0.49 (SD 0.017) for the die-back). Despite that statistically the differences are important, it should be noted that they are relatively small. Furthermore, the samples were taken from adjacent reed patches for each category, and thus the resemblance might also be attributed to the genetic similarity of the patch and not the die-back effect.

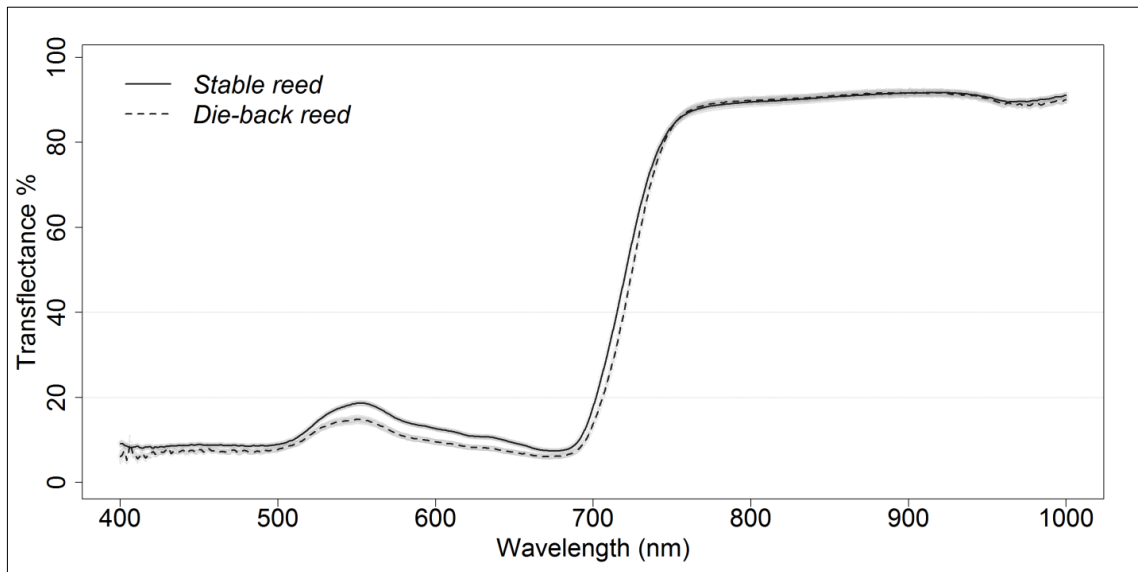


Figure 3.5: Leaf mean reflectance spectra (curves) and the corresponding 95% confidence intervals (shaded areas) for the *Phragmites* plants collected from the stable and die-back reed stands at the waterfront area of the Kerekedi bay in Lake Balaton.

At canopy-scale a 5% relative increase in reflectance is observed on the stable reed in comparison to the die-back reed (Figure 3.6). The spectra are similar in shape throughout the 400-1000 nm spectrum. High inter-variability is observed. The inflection point is found at 727 nm for the stable and 728 nm for the die-back. Differences in reflectance values are not large (0.22 (SD 0.03) for the stable and 0.22 (SD 0.04) for the die-back) (Figure 3.7). The 95% confidence intervals overlap and there are no crisp boundaries where separation between the two classes can be found throughout the spectrum. This variation is attributed to the vegetation material within the field of view as well as the illumination geometry of the scene; the radiance recorded by the

instrument with the field of view optics is a combination of reflectance from leaves, stalks, flowers and understory materials. Furthermore, the dense structure of the macrophytes as well as the orientation of the leaves create shadows and a generally complex scene which only little resembles the reflectance from the measurements at leaf scale. Variability in spectral response is also introduced by the viewing geometry between the incident light and the observer (Van der Meer and de Jong, 2002). Last but not least,

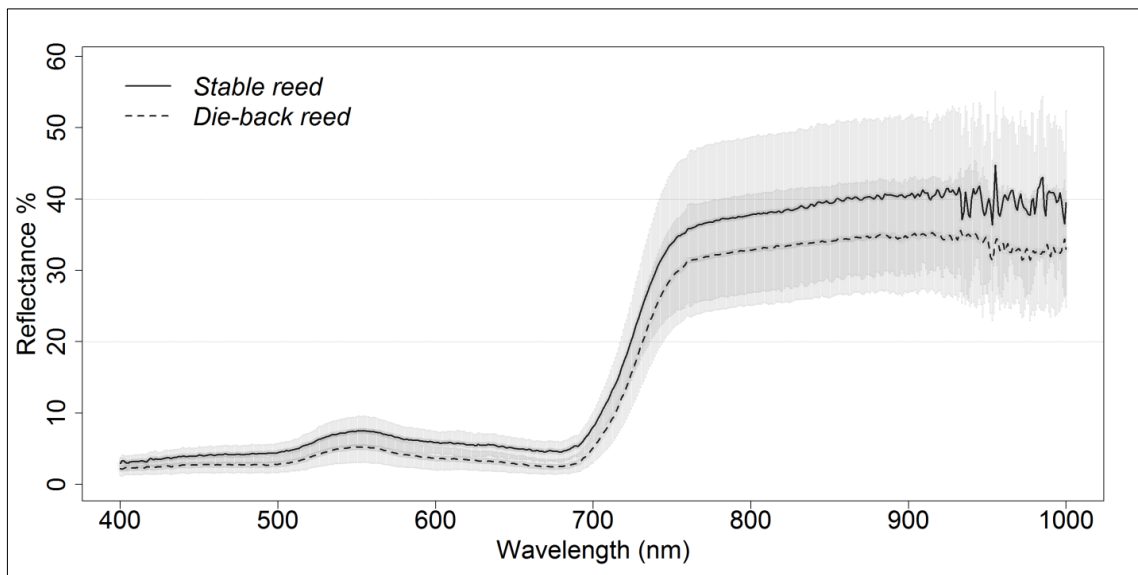


Figure 3.6: Canopy mean reflectance spectra (curves) and the corresponding 95% confidence intervals (shaded areas) for *Phragmites* plants collected from stable and die-back reed samples at the waterfront area of the Bozsai bay in Lake Balaton.

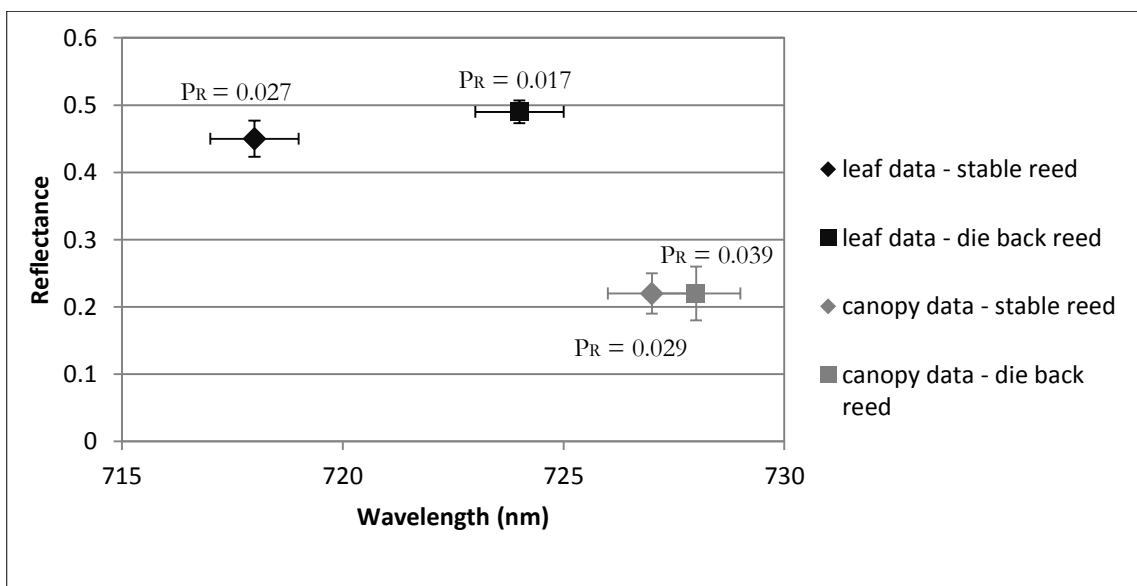


Figure 3.7: Red-edge inflection point for leaf and canopy scale of stable and die-back reed samples. Statistically, important differences seem to appear only at leaf scale.

and from an ecological point of view, the most important factor influencing the macrophytes canopy reflectance is the heterogeneity of the patches, since within the reed stand different patches may contain different species, different genotypes of the same species, and stalks of different age, height, dimension or structure; all these factors cumulatively assign a changeability in results of canopy values which is common in ecological studies.

Reflectance as recorded from the airborne sensor (Figure 3.8) shows contradictory results from the field measurements. A die-back reed pure pixel's indicative spectrum reflects stronger in the visible domain than the stable reed; however the opposite process takes place in the near-infrared domain. The signal recorded by sensors from distance are influenced by several factors, mainly the geometry and the structure of the material; in this case it is recognized that the orientation of the leaves, which differs in stable and die-back reed stalks, is playing a crucial role in the reflectance spectra.

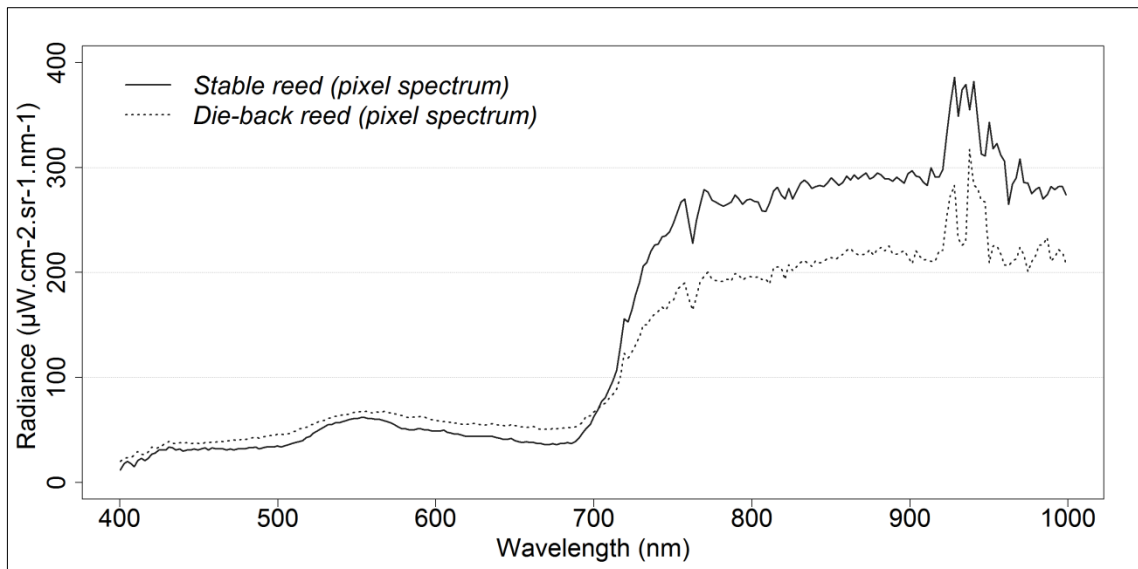


Figure 3.8: Spectral surface radiance (atmospheric correction applied) of sample pure pixels from an airborne hyperspectral sensor corresponding to stable and die-back reed from the reed bed at Bozsai bay, Lake Balaton.

3.5.3 Canopy spectral analysis of reed's phenological status

Reed patches with inflorescence (reed inflorescence), reed with dried ramets and recently emerged reed (reed) were studied from a stable reed bed at the Szigliget bay. Recently emerged reed shows lower values of reflectance throughout the whole spectrum, which is indicative either of the absence of reflecting materials, such as dried content and flowers encountered in the other two classes, either of the better light use efficiency or a combination of the two (Figure 3.9). Reed patches with dried ramets reflects higher probably because they contain dead reed stalks from previous years and therefore light utilization is at lower levels. Reed inflorescence has a gradually higher absorption from 590 to 690 nm and an overall higher reflectance at the near infrared domain, which indicates pigment absorption and high photosynthetic activity of the plant at this stage of growth.

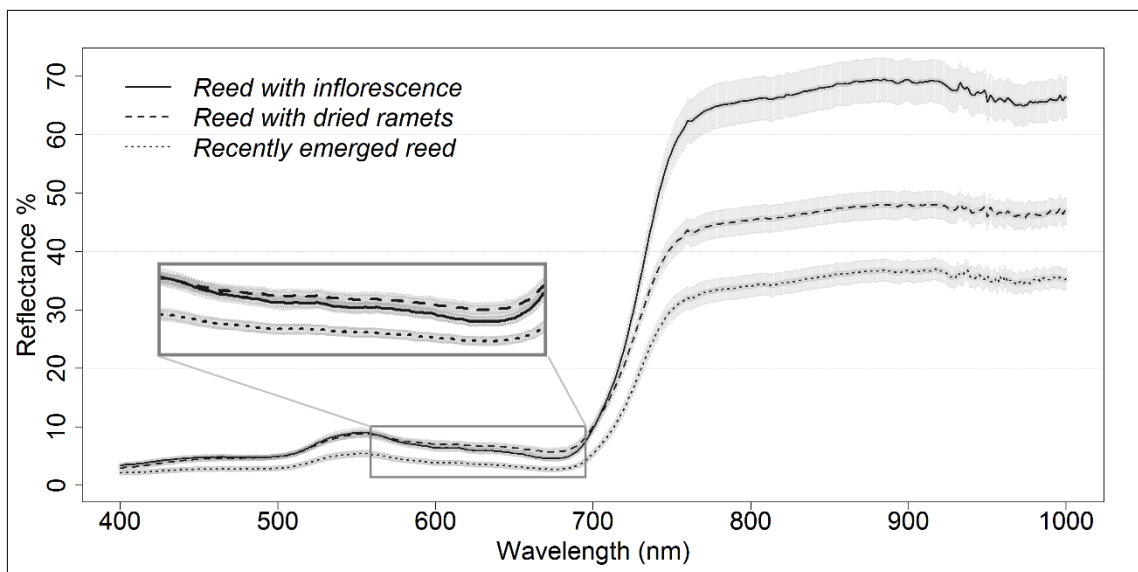


Figure 3.9: Canopy mean reflectance spectra (curves) and the corresponding 95% confidence intervals (shaded areas) for samples of *Phragmites* in different phenological states (reed with inflorescence, reed with dried ramets and recently emerged reed) collected with an ASD handheld spectroradiometer at the Szigliget bay, Lake Balaton. Recently emerged reed absorbs considerably higher at the chlorophyll absorption bands between 560nm and 690nm.

3.5.4 Spectral analysis of sun and shade leaves of reed

Leaves from the middle of the stem (shade) and from the top of the stem (sun) from Kerekedi bay were analyzed in order to investigate their spectral

response in connection with the leaf relative vertical position in the foliage.

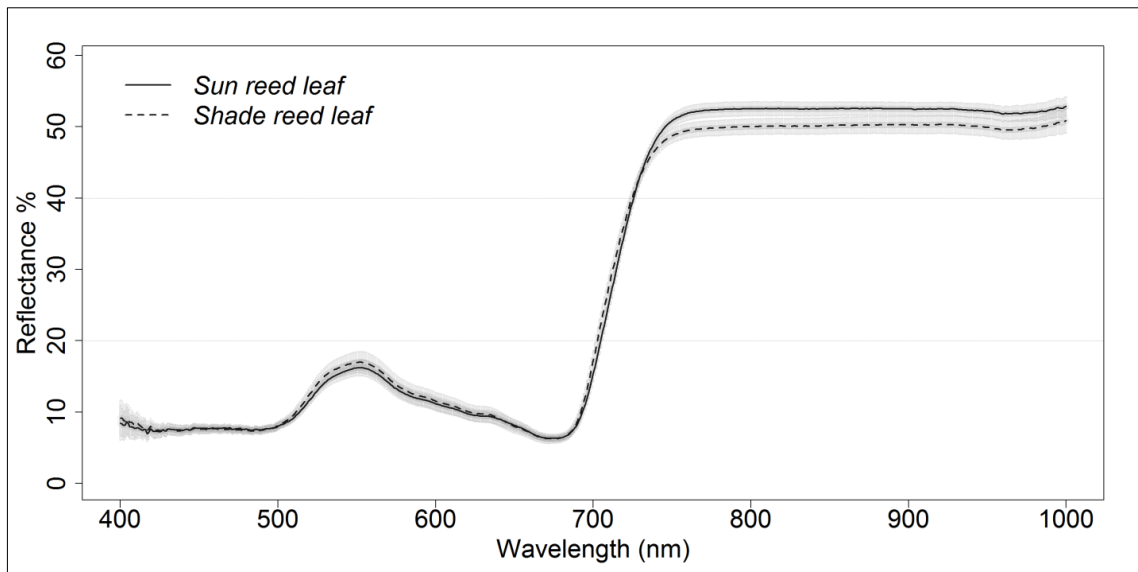


Figure 3.10: Leaf mean reflectance spectra (curves) and the corresponding 95% confidence intervals (shaded areas) for samples of reed under sunny and shaded conditions collected at the Kerekedi bay, Lake Balaton.

Sun leaves show a slightly higher reflectance in the infra-red region (Figure 3.10). The differences are insignificant, however this advocates that the addition of the relative position of the leaf in the foliage in perplexing the diverging spectral response by one more factor.

3.5.5 The influence of inundation level on reed leaves stability

In this part the concurrently acquired chlorophyll fluorescence parameters and spectral signatures from reed samples at different inundation categories are analyzed. Water level is a factor representing different environments where reed grows in, and its fluctuation has been an important aspect as reported in the literature (Paillisson and Marion, 2011; Tóth and Szabó, 2012). The study was conducted at a perpendicular to the shore transect of a stable reed bed of Kerekedi bay.

3.5.5.1 Spectral response of reed leaves in regard to the inundation environment

The results from the analysis of the four inundation classes indicate that the differences between categories are statistically important (Figure 3.11). To test

the hypothesis, a t-test for the bands at 500 nm and 800 nm which represent the optical and near-infrared domains was performed. For the terrestrial and deep water datasets the p value was lower than 0.001 for both wavelengths. The leaf reflectance curves of plants growing in terrestrial and shallow water conditions only show very small differences in the visible (<1%) and red-edge (<3%) domains of the spectrum. Their 95% confidence intervals partially overlap, which indicates that they cannot be distinguished based on the visible part but only in the infrared part of the spectrum. The reflectance curves from the deep water and the water's edge locations show differences of up to 5% in the visible and even >10% in the infrared domain when compared to the terrestrial and shallow locations. The vegetation spectra for the deep water and water's edge locations show that their 95% confidence intervals do not overlap with any of the other spectra. They are hence different and responsive to the inundation categories defined. Furthermore the plateau in the near-infrared region has an ascending trend in the categories with water substrate, while for the terrestrial the reflectance response is flat; this is associated to the cell structure as presented in and is attributed to role of the water level on the internal structure of the leaves.

It is important to note that the inundation categories define different ecotypes of the reed bed and hence different reed phenotypic categories. Tóth et al. (2012) suggest that morphology of *Phragmites* is influenced by site-specific environmental conditions rather than lake-scale factors. Some of these conditions are increased anaerobic bacterioflora due to litter accumulation in the reed stands, lack of oxygen in the sediment, anaerobic conditions in the sediment of stagnant waters and reed clones adapted to survive at deep water (lower redox). As a result from these local processes in the succession from the terrestrial to the deep water parts of the reed bed, different ecotypes of *Phragmites* can emerge. Hence the phenotypic variation is such an ecotone can be large, fact that is prominent in the spectral responses of the categories in

the experiment. shows clearly that ecosystem heterogeneity matters in the plants spectral response, in the sense that the same vegetation species (i.e. reed) has different reflectance curves for the terrestrial and shallow locations from the deep water and water edge locations.

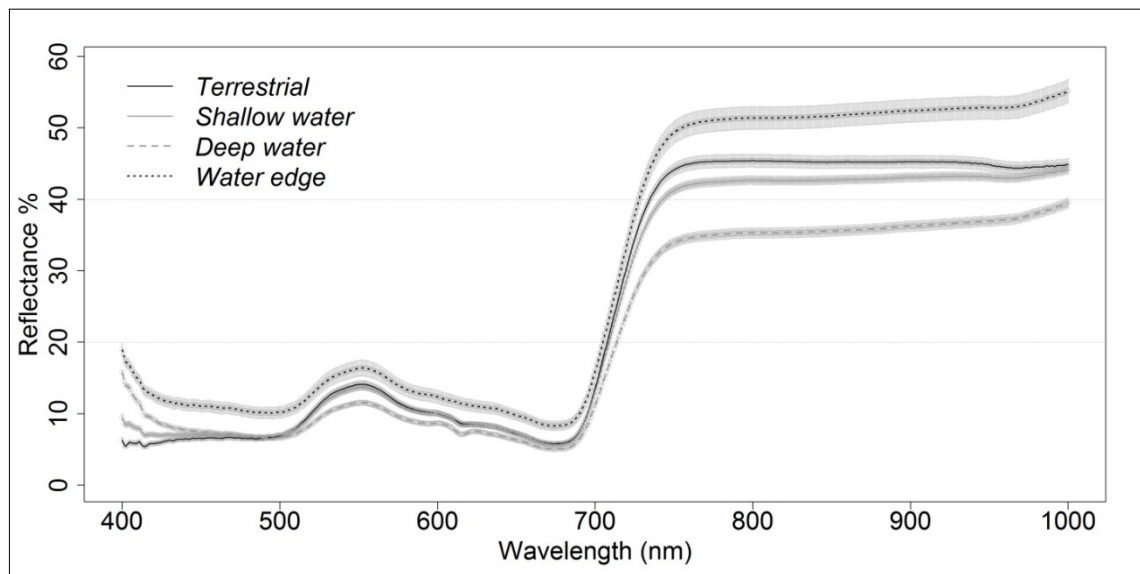


Figure 3.11: Mean reflectance spectra (curves) and the corresponding 95% confidence intervals (shaded areas) of *Phragmites* leaf samples collected from the terrestrial, shallow water, deep water and waterfront parts of the reed stand in Kerekedi Bay, Lake Balaton. Reed growing in categories with water have a sloped infrared plateau (750 – 1000nm), while terrestrial reed has a stable reflectance value across these wavelengths.

3.5.5.2 Photochemical response of reed leaves in regard to the inundation environment

The spectral response of leaves in regard to the bathymetric condition of the plants was investigated. The photophysiological data show a high degree of similarity (Figure 3.12). The ETR mean values changed throughout the transect between 173 and 222, although a small, but significant difference in the terrestrial part of the transect was observed. The chlorophyll content of the leaves was ca. 45 SPAD units, with a difference between the deep water and waterfront regions (Figure 3.12e). While on the basis of morphological parameters a special supra-individual ordinance was observed in the transects of the Kerekedi bay (Tóth and Szabó, 2012) and other experimental setups conducted in different lakes (Mauchamp et al. 2001; Vretare et al. 2001), the

different level of inundation does not affect the studied photochemical parameters, or this was masked by variability within the samples. The relatively high values of the Y(II) and ETR in comparison to earlier studies (Dulai et al. 2002; Mauchamp and Méthy 2004; Velikova and Loreto 2005; Nguyen et al. 2013) indicated that the studied plants were in stable condition (Figure 3.12c and Figure 3.12d). The water depth gradient did not affect these studied parameters, although the highest values of ETR and Y(II) were measured in the shallow and deep water part of the reed stand suggesting slightly better conditions for *Phragmites* in these parts of the transect.

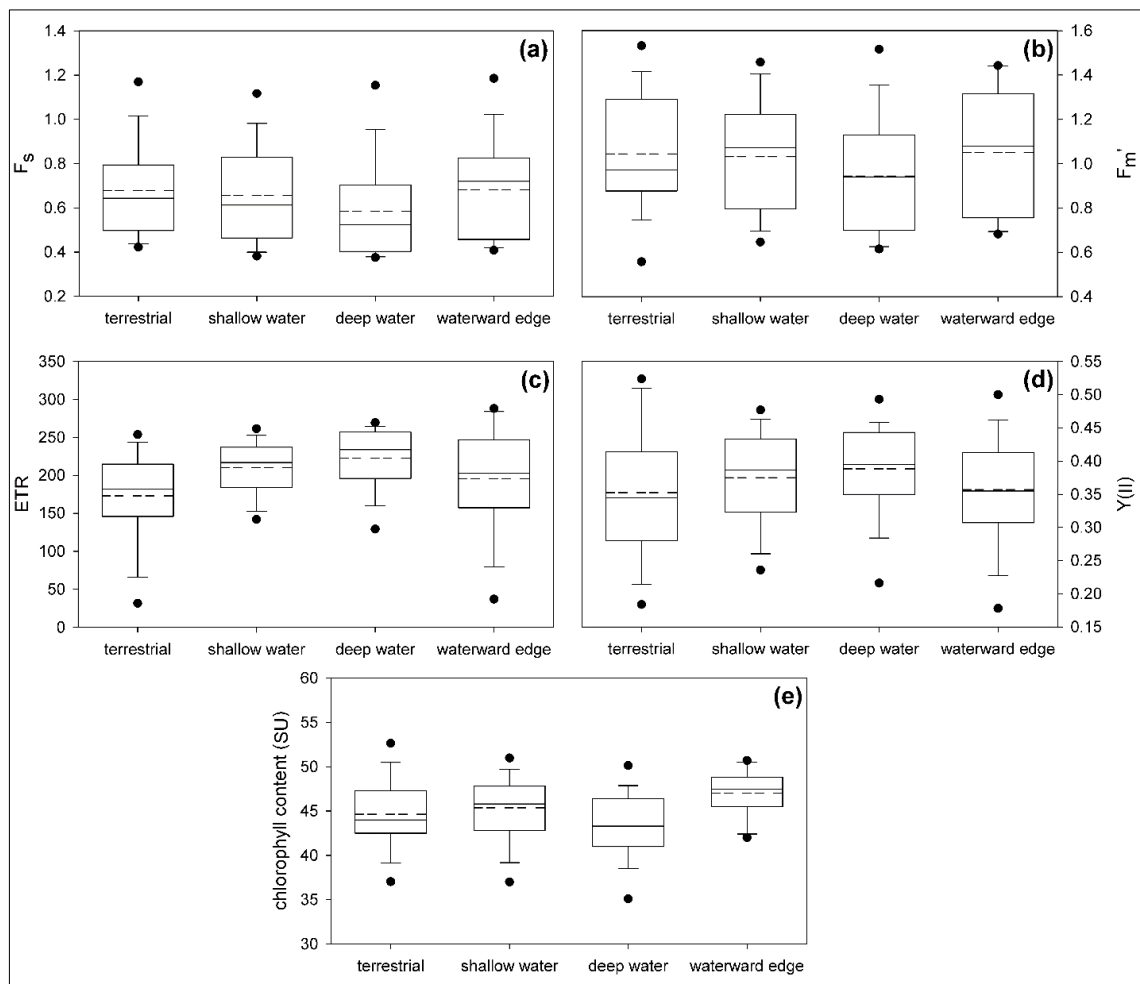


Figure 3.12: Changes of: (a) F_s , (b) F_m' , (c) ETR, (d) Y(II) and (e) chlorophyll content of leaves of *Phragmites* at the terrestrial, shallow water, deep water and waterfront of the reed bed at the study site. $n=27-55$. The comparison was performed using the Tukey-Kramer Test (Pairwise Comparisons for One-Way Layout Design). Boxes encompass the 25% and 75% quartiles of all the data for each specific part of the studied area. The central solid line represents the median, while the dashed line represents the average, bars extend to the 95% confidence limits, and dots

represent outliers. Figure reproduced from Stratoulías et al. (2015) based on data collected by D. Stratoulías and V.R. Tóth. This figure was produced by V.R. Tóth.

3.6 Conclusions

In-situ observations provide ground truthing for remote sensing as well as information not available by remote sensing (Christian 2008). While field imaging spectroscopy suffers from the drawbacks characterizing generally field data collection such as time and cost expenditures, in this study field spectral measurements have provided an insight into the physiological status of macrophytes at Lake Balaton. Under different experimental setups, the complexity and dependence of spectral signature of lakeshore vegetation to different environmental parameters affecting the leaf response was revealed.

Macrophyte species present diverging spectral signatures at leaf scale and can be strongly distinguished at the red and near infrared domains. Die-back reed samples presented a slight differentiation to stable samples; however this might be attributed to the fact that the sampling took place at neighboring areas for each class, and hence there is the possibility that clonal differences play a pivot role instead of the manifestation of die-back. Hence, local specific measurements might not represent the actual problem in such a highly dynamic nature of the lakeshore environment. Canopy analysis of the samples in terms of the die-back phenomenon did not present statistically sound results. Spectra from pure representative pixels of an airborne hyperspectral image are most probably associated with vegetation composition and canopy structure. Differences between canopy reflectance as measured in the field and from the airborne platform are strong and have been also reported in the literature. For instance Azaria et al. (2009) applied spectroscopic experiments on cannabis from different heights (i.e. short distance laboratory controlled conditions, 25m, 80m and airborne AISA) found that the spectral signal varies with distance from the sensor.

When examining *Phragmites* at different phenological states, it becomes obvious that flowering reed and reed with higher dried content (dead reed culms of previous years) reflects proportionally higher in the optical domain. Flowering reed also demonstrated a stronger absorption at the red region and a sharp red-edge curve, which is indicative of the high photosynthetic activity of the plant at this stage of growth. In an experiment comparing sunny and shaded leaves, the discrepancies were statistically small, with sunny leaves being slightly more vigorous indicated by a slight red-edge shift to longer wavelengths.

Spectral measurements on reed leaves in regard to bathymetry reveal a considerably different spectral behavior of reed samples. Despite the fact that no effect of inundation on photophysiological parameters (i.e. chlorophyll fluorescence parameters and chlorophyll content) across different water levels along a transect vertical to the lake shore has been found as described later in chapter 4, the spectral response diversifies significantly. It is a well-known fact that the phenotypic expression in regard to bathymetry is changing (Tóth and Szabó, 2012) as well as the DNA-fingerprint between land and water reeds (Engloner et al. 2010) also. The differences of reflectance profiles found for these levels of inundation can be attributed to the stress condition of the reed patch, the microenvironment in which the culms grow or even differences in genotype of the species growing in different environments.

All these fluctuations on reed spectra reflects the large phenotypic plasticity of *Phragmites* and the significant consequences in the phenotype of the shore vegetation. This study underpins the heterogeneity of lakeshore vegetation ecosystem inherited in the spectral response of the plants.

Chapter 4

Remote sensing of reed ecophysiology by coupling chlorophyll fluorescence and spectroscopic information

4.1 Introduction

Based on the results of the handheld spectral measurements presented in chapter 3, the following chapter will investigate the correlation between two concurrently measured datasets, the proximate spectroscopic information and chlorophyll fluorescence, with the aim to investigate to which extent spectral bands or spectral indices can represent chlorophyll fluorescence parameters and hence stress indications at leaf and subsequently canopy level.

Vegetation photosynthetic systems are very sensitive to environmental induced stress. Stress also manifests through reduced chlorophyll content in plants, green biomass, water absorption capacity and several other ways. Such properties are correlated strongly with spectral indices and have been widely studied in the literature with very high correlation coefficient values reported. However these alterations in properties are only the causalities succeeding in time the stress induction, and hence are the consequences of the process. As such, traditional indices correlating to vegetation vigor such as the Normalised Difference Vegetation Index (NDVI) might provide information on stress only when damage has already occurred (Meroni et al. 2008).

The first exhibition of leaf stress preceding morphological and other physiological changes will be reduced photosynthesis. Photosynthetic systems (PS) are the driving forces behind the biochemical and biophysical processes of photosynthesis. Any physiological process that affects the functioning, specifically the excitation and light quenching of the PS and especially the PSII, will have a detrimental effect on the photosynthesis. Besides the photosynthetic activity, chlorophyll fluorescence is one of the processes behind the de-excitation of the PSII, i.e. it can affect the process of reduction

in the reaction centers. The changes in processes of photosynthesis and consequently in chlorophyll fluorescence take place well before any measurable changes in chlorophyll content. It is a well-known fact that chlorophyll fluorescence is a direct indicator of the photosynthetic activity of the plant (Amoros-Lopez et al. 2008) and can be non-intrusively measured *in-situ*. Such photochemical parameters can provide an early diagnostic indicator of plants' stress and it is a well-studied fact that production of plants can be easily and non-intrusively estimated by chlorophyll fluorescence.

The most prevailing method to measure chlorophyll fluorescence is Pulse Amplitude Modulated (PAM) fluorescence. Photochemical parameters usually relate to the measured F_s and $F_{m'}$ values of fluorescence yield (Maxwell and Johnson, 2000). Genty et al. (1989) proposed a widely used formula to estimate changes in quantum yield defined as:

$$Y(II) = \frac{\Delta F}{F_{m'}} = \frac{F_{m'} - F_s}{F_{m'}} \quad (1)$$

where the photosynthetic yield $Y(II)$ represents the ratio of open (reduced) to closed (oxidized) PSII reaction centres at given irradiance, which is the proportion of energy potentially used for photosynthesis. More specifically it is a measurement of the transfer of electrons between photosystems within the process of photosynthesis. Since during photosynthesis 4 electrons must be transported for every assimilated carbon dioxide (CO_2) molecule, $Y(II)$ represents the potential possible driving force of photosynthesis. Therefore it relates to net photosynthesis at the given light intensity. From quantum yield, the Electron Transport Rate (ETR) could be calculated:

$$ETR = \frac{\Delta F}{F_{m'}} \times PAR \times AF \times 0.50 \quad (2)$$

where 0.50 accounts for distributing the energy between PSI and PSII and AF is the Absorption Factor for the monocotyledonous plant leaves which is assumed constant and equal to $AF=0.86$.

In chloroplasts the ETR within the PSII translates into production (Genty et al. 1989; Kitajima and Butler, 1975), parameter which provides significantly enhanced information in comparison to the photosynthetic activity at the given environmental conditions and time. It can be measured by PAM fluorometry, which *in-situ* is rapid, allowing determining hundreds of parameters within a short time span. When measured in a context of a correct methodological approach, it allows recording the apparent photosynthetic activity (PAR) estimating the photosynthetic efficiency (ETR). From PAR-ETR relation there is a possibility to calculate the maximum Electron Transport Capacity (ETR_{max}), the theoretical light saturation intensity (I_k) and the maximum quantum yield for whole chain electron transport (α), that are photophysiological characteristics to the specific plants grown at given light environment, and thus gives the opportunity to identify the acclimation shaping the photosynthetic processes. For a comprehensive explanation of chlorophyll fluorescence the reader is referred to Krause and Weis (1991) and Baker (2008).

Remote sensing applications for the mapping of reed condition in Europe have been reported in the literature but their function so far has been limited to a tool for assessing the distribution of vegetation species and sometimes the level of stress categorically; however quantification of reed stress physiological indicators has not been attempted. For example, Bresciani et al. (2009) used remotely sensed data to monitor reed physiological status represented by the Leaf Area Index (LAI) in three environmentally sensitive Italian lakes. Liira et al. (2010) estimated the macrophyte expansion in a eutrophic Lake based on a Landsat TM and ETM+ time series. Hunter et al. (2010a) mapped the distribution of macrophytes in a clear British shallow lake. Onojeghuo and Blackburn (2011) demonstrated the synergistic use of hyperspectral and Light Detection And Ranging (LiDAR) data for mapping reed bed habitats and Bresciani et al. (2011) estimated the LAI from field and

satellite data in the context of reed conservation. Lately, Zlinszky et al. (2012) used discrete return LiDAR to categorize aquatic vegetation and stressed reed in Lake Balaton, Hungary and Villa et al. (2013) presented an approach to monitor reed conservation status of Lake Garda in Italy with a variety of remotely sensed datasets. Remote sensing inherently has the capacity of species distribution mapping in lakeshore environments, however, macrophytes physiological status has not been yet investigated thoroughly from a remote sensing perspective. Despite the fact that chlorophyll fluorescence is one of the most powerful stress detection methods in plant ecophysiology (Maxwell and Johnson 2000), coupling with remote sensing has not yet been widely investigated. Only a few studies relate to the topic (e.g. Zarco-Tejada et al. 2002; Nauman et al. 2008; Zhang et al. 2011). Zarco-Tejada et al. (2002) suggest that fluorescence parameters can be derived solely from spectroscopic information by inverting the FRT-PROSPECT model.

Attempts to relate leaf spectral information with several physiological and morphological parameters have been widely reported in the literature, such as with chlorophyll, nitrogen, water, biomass content and leaf density. While some of these parameters have been proven to correlate highly with spectral indices, chlorophyll fluorescence provides significantly more information on the photosynthetic activity of plants than other physiological parameters.

The coupling between physiological parameters and spectral information is often established by building indices in the form of mathematical formulae integrating spectral bands. These spectral indices are typically developed on the basis of empirical observations or experimental processes as a proxy to vegetation characteristics (Table 4.1). For instance, Zarco-Tejada et al. (2001) proposed that the ratio of the reflectance of 750 nm (i.e. R_{750}) and 710 nm (R_{710}) is a good indicator of chlorophyll content at leaf level. Gitelson and Merzlyak (1996) suggest the indices R_{750}/R_{550} and R_{750}/R_{700} are highly proportional (correlation $R^2 > 0.95$) to chlorophyll concentration in leaves. In

a similar manner Vogelmann et al. (1993) propose R_{740}/R_{720} as well as the ratio of first derivative values D_{715}/D_{705} . Stagakis et al. (2010) in a thorough investigation of chlorophyll indices suggest that mNDVI (Sims and Gamon 2002), PSRI (Merzlyak et al. 1999) and SIPI (Peñuelas et al. 1995) perform well in chlorophyll estimation. Finally, Thenkabail et al. (2000) present a study on the relationship between vegetation indices and agricultural crop characteristics where they suggest that remarkably strong relationships are found in specific narrow bands.

This chapter presents the investigation of the potential of imaging spectroscopy for characterizing the ecophysiological status of reed in a lake shore environment based on fluorometric *in-situ* measurements. This is one of the first attempts to correlate chlorophyll fluorescence with spectroradiometry (in-situ and airborne) and investigate the correlation between these two aspects, and furthermore correlate spectral information with a more robust physiological parameter in regard to photosynthetic activity (i.e. chlorophyll fluorescence) than typical parameters used in similar studies such as chlorophyll, nitrogen, water or biomass content.

Statistical analysis was used to quantify the association between chlorophyll fluorescence kinetics and hyperspectral signatures of reed leaves. Spectral indices correlating significantly to fluorescence yield, and thus vegetation stability, were identified. An application of lake-shore vegetation status assessment based on hyperspectral airborne collected imagery demonstrates the potential of remote sensing for reed stability quantification.

4.2 Study area

This part of the study focuses on a monospecific reed bed at Kerekedi bay. The main objective is to couple fluorometric and spectroscopic data representing different inundation levels as described in the previous chapter (objective 5). The dataset used is the same as of section 3.4.5 and consists of

Table 4.1: Empirical indices proposed frequently in remote sensing studies of vegetation.

Index	Reference	Formula
<i>ARI2 (Anthocyanin Reflectance Index)</i>	<i>Gitelson et al. (2001)</i>	$R_{800} * \left(\frac{1}{R_{550}} - \frac{1}{R_{700}} \right)$
<i>CRI1 (Carotenoid Reflectance Index)</i>	<i>Gitelson et al. (2002)</i>	$\frac{1}{R_{510}} - \frac{1}{R_{550}}$
<i>CRI2 (Carotenoid Reflectance Index)</i>	<i>Gitelson et al. (2002)</i>	$\frac{1}{R_{510}} - \frac{1}{R_{700}}$
<i>EVI (Enhanced Vegetation Index)</i>	<i>Huete et al. (2002)</i>	$2.5 * \frac{R_{782} - R_{675}}{R_{782} + 6 * R_{675} - 7.5 * R_{445} + 1}$
<i>mND705 (modified Normalized Difference Index)</i>	<i>Sims and Gamon (2002)</i>	$\frac{R_{750} - R_{705}}{R_{750} + R_{705} - 2 * R_{445}}$
<i>mSR705 (modified Simple Ratio Index)</i>	<i>Sims and Gamon (2002)</i>	$\frac{R_{750} - R_{445}}{R_{705} - R_{445}}$
<i>NDVI (Normalized Difference Vegetation Index)</i>	<i>Tucker (1979)</i>	$\frac{R_{782} - R_{675}}{R_{782} + R_{675}}$
<i>NDVI750 (Red-edge Normalized Difference Vegetation Index)</i>	<i>Gitelson and Merzlyak (1994)</i>	$\frac{R_{750} - R_{705}}{R_{750} + R_{705}}$
<i>PRI (Photochemical Reflectance Index)</i>	<i>Gamon et al. (1997)</i>	$\frac{R_{531} - R_{570}}{R_{531} + R_{570}}$
<i>PSRI (Plant Senescence Reflectance Index)</i>	<i>Merzlyak et al. (1999)</i>	$\frac{R_{680} - R_{500}}{R_{750}}$
<i>RGI (Red Green Index)</i>	<i>Zarco-Tejada et al. (2005)</i>	$\frac{R_{690}}{R_{550}}$
<i>SGI (Sum Green Index)</i>	<i>Gamon and Surfus (1999)</i>	<i>Mean (R₅₀₀ to R₆₀₀)</i>
<i>SIPI (Structure Insensitive Pigment Index)</i>	<i>Peñuelas et al. (1995)</i>	$\frac{R_{800} - R_{445}}{R_{800} - R_{680}}$
<i>SRI (Simple Ratio Index)</i>	<i>Jordan (1969)</i>	$\frac{R_{800}}{R_{680}}$
<i>VOG1 (Vogelmann)</i>	<i>Vogelmann et al. (1993)</i>	$\frac{R_{740}}{R_{720}}$
<i>VOG2 (Vogelmann)</i>	<i>Vogelmann et al. (1993)</i>	$\frac{R_{734} - R_{747}}{R_{715} + R_{726}}$
<i>VOG3 (Vogelmann)</i>	<i>Vogelmann et al. (1993)</i>	$\frac{R_{734} - R_{747}}{R_{715} + R_{720}}$
<i>WBI (Water Band Index)</i>	<i>Peñuelas et al. (1993)</i>	$\frac{R_{900}}{R_{970}}$

contemporary acquired spectral and biophysical information recorded from the same leaves. For a detailed description of the dataset and the sampling design the reader is referred to section 3.2.2. Kerekedi bay is a managed ecosystem since reed is cut down in winter in contrast to the Boszai bay which is a protected area. Interventions in reed biomass such as slashing, burning and grazing practices for conservational purposes have a profound effect on reed structure and growth (Engloner, 2009). *Phragmites* is a species with an especially fast regenerating capability in comparison to other macrophytes. As such, in areas where anthropogenic interference occurs, it is expected that a monospecific stand of *Phragmites* would be present, in comparison to natural reserved ecosystems where heterogeneity shall be preserved and thus richer biodiversity encountered.

In addition to the field data, an airborne hyperspectral image from Eagle sensor is employed, acquired over the Kerekedi bay (Figure 3.1) collected on August 26th, 2010 at 15:17 Coordinated Universal Time (UTC). Further information on the image specifications is provided in chapter 5.

4.3 Data quality assessment

While this is a robust dataset for studying the ecophysiology and vegetation distribution at Lake Balaton, a critical issue has to be discussed; ideally field and airborne data should be collected concurrently, however this has not been logistically possible and there exists a gap between the airborne dataset (August 2010) and the field data (August 2012). Nevertheless, this two-year time difference does not introduce inconsistencies in the study for several reasons. First, the two groups of datasets are used for two different purposes; the indices developed from *in-situ* measurements are not time-specific in the sense that plants' chlorophyll fluorescence response is a physical phenomenon and hence the correlation with the spectral information cannot be affected by

time. As the temperature correlates with infrared signal independently of the acquisition year in vegetation, the spectral indices proposed are regarded in this study as a global index for fluorescence yield, and probably similar results would be yielded if repeating the experiments another year. The indices proposed should correlate similarly to the fluorescence any time they are applied (and probably anywhere). Secondly, regarding the reed die-back, it is a slow process and within 2 years the reed bed does not change substantially as currently the phenomenon is rather slow in comparison to the historically rapid occurrence in the 1970s. Furthermore, the field data have been used to identify optimal spectral indices, which presumably best represent the fluorescence yield, and not to classify the image, hence two datasets for two different purposes were used. Moreover, measurements have been taken to reduce the expected variability to minimum; both datasets are collected in August, period during which all emergent vegetation species at the geographical region of study are at climax. This means that the species' spatial distribution and proportional area coverage in mixed pixels will be representative of the real existence, hence eliminating seasonal (intra-annual) variability. Inter-annual variability is unavoidable, however has been minimal during 2010 and 2012 (Piroska Pomogyi, personal communication) since no physical or artificial disturbance occurred in Lake Balaton in general at the study site. For all the aforementioned reasons it is anticipated that the distribution of macrophytes has not changed considerably between the two years of interest.

4.4 Methodology

The overall methodology was based on identifying the optimal indices for characterizing the physiological status of reed from coupling the field spectroradiometer data with the fluorescence parameters; subsequently this method was transferred to the airborne dataset and apply the indices for

mapping the physiological status of a large part of the reed bed at Kerekedi bay.

Additionally, the effective quantum yield of photochemistry, i.e. the fraction of absorbed photons used by the photochemical systems (Y(II)) and the ETR were calculated on the basis of the former and according to the formulae (2).

4.4.1 Optimizing leaf stress indication from spectroscopic data

The methodological approach was established partly by taking as guidance the study presented by Inoue et al. (2012) on correlating hyperspectral data with canopy nitrogen content in paddy rice for diagnostic mapping. The collected hyperspectral *in-situ* data were exported using the bundled software ViewSpec Pro 6.0 (Analytical Spectral Devices Inc., USA) and the main processing was implemented in the R programming language (R Core Team, 2013). The R script used for processing the raw data and producing the graphs is provided in Appendix 1. While discrimination analysis can be performed in order to select the optimum bands, in this study the focus was on deriving the complete combination of spectral indices between all channels. The aim of spectral indices is to construct a mathematical combination of spectral band values for enhancing the information content in regard to the parameter under study. Many of the indices found in the literature are formed as a Ratio Spectral Index (RSI) of one band to another such as:

$$RSI(i, j) = \frac{R_i}{R_j} \quad (3)$$

Where R_i and R_j are the intensity values at wavelengths i and j respectively. The Normalized Difference Spectral Index (NDSI) is another transformation frequently used defined as:

$$NDSI(i, j) = \frac{R_i - R_j}{R_i + R_j} \quad (4)$$

A vegetation-specific representation of NDSI is the popular NDVI applied on a near-infrared and a red channel as reported first by Rouse et al. (1974).

Reflectance and transmittance data were used in a similar manner, nevertheless reflectance data are the backbone of the methodology since the results can be applied on remotely sensed imagery. RSI and NDSI for the hyperspectral spectra were calculated from complete combinations of the available bands, as in similar studies (e.g. Stagakis et al. 2010, Inoue et al. 2012). Multiple regressions and equations between samples of RSI and photophysiological parameters were fitted for several datasets. The general relationship between RSI (or NDSI) and Fm' and Fs appears to be linear (Figure 4.1). Thus it was assumed in this study that all the relationships were linear and the statistical moments of the relationship are indicative of the association between the spectral and the photophysiological parameters.

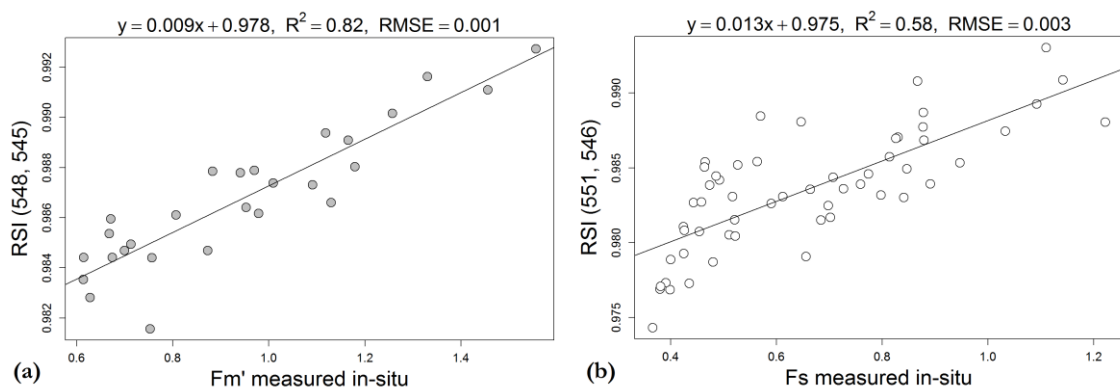


Figure 4.1: Example of regression fitted for the RSI combinations against Fm' (a) and Fs (b). The relationship appears to be linear and hence the square of the Pearson correlation coefficient (R^2) was used as a measure of variance in the assumed linear relationship.

For each photophysiological parameter and each environmental category the coefficient of determination (R^2) and the corresponding significance level (p) were calculated. More specifically the Pearson product-moment correlation coefficient was calculated by dividing the covariance of the two variables with the product of their standard deviations:

$$r = \frac{\sum_{i=1}^n (x_i - \bar{x}) \cdot (y_i - \bar{y})}{\sqrt{\sum_{i=1}^n (x_i - \bar{x})^2 \cdot \sum_{i=1}^n (y_i - \bar{y})^2}} \quad (5)$$

The square of the Pearson correlation coefficient (i.e. R^2), known as the coefficient of determination, represents the agreement level of the linear fit of the variance between the two variables. $R^2 = 1$ represents a perfect linear relationship while $R^2 = 0$ means that there is no linear relationship between the variables.

The results were visualized using raster maps of the coefficient of determination in increments of 0.1 and a complimentary map of the p value divided across the critical thresholds 0.050, 0.010 and 0.001. The optimum spectral index representing fluorescence yield is identified based on the highest R^2 between the *in-situ* hyperspectral and fluorescence measurements. This index is regarded as a global index for each inundation category which would sufficiently represent fluorescence yield, and hence photosynthetic activity, based on narrowband spectral channels. Finally, the same processing on the transmittance hyperspectral data was undertaken in order to investigate which radiance recorded from the sensor provides more accurate results. For the purposes of reducing computer processing time, the bands of the hyperspectra were averaged in increments of three channels and thus reducing the number of spectral bands from 600 to 200. The same filter was applied on the reflectance dataset for reasons of comparison retrospectively.

In the context of placing the findings in the framework of relevant studies, 18 narrowband empirical indices frequently reported in the literature (Table 4.1) were derived, and subsequently the coefficient of determination between the index and the photophysiological parameters. The performance of the empirical indices with the ones proposed from the presented hyperspectral analysis were compared based on the R^2 values and then cumulatively the

results were clustered in a hierarchical correlation relationship, indicating the performance of the indices studied.

4.4.2 Application on airborne imagery

Collaboratively with remote sensing techniques, efforts have been placed in coupling laboratory measurements with airborne imagery, however atmospheric interference in the later is affecting unevenly the wavelength dependent intensity and the overall signal to noise (including the atmospheric) ratio is not matched sufficiently. Typical wavelengths used in the laboratory are 663 nm for detecting chlorophyll a, 643 nm for chlorophyll b and 470 nm for carotenoids (Fogli et al. 2002).

An application of the findings from leaf to canopy level was attempted in order to investigate up-scaling of the application and the possibility to retrieve information on photosynthesis from remotely sensed data. The indices proposed from the field analyses that can be applicable to airborne imagery were identified. The 200-band correlation maps for reflectance were used since they have similar spectral resolution with the airborne (i.e. 3nm). The results were recomputed and the bands with optimal R^2 values located. However the choice of the optimal index for transferring the methodology to the airborne data depends on the nature of the latter; wavebands at the marginal available spectral range are dismissed since the airborne instrument noise and the water absorption from the atmosphere above 900 nm result in high levels of errors even after atmospheric correction. Additionally, many of the indices calculated from the raw data lie in a very small part of the spectrum, usually within one or a couple of pixels in the R^2 graphs, and wouldn't be adequate for the spectral resolution of the airborne image. Furthermore, indices based on adjacent bands were tested and provided unsatisfactory results, which can be attributed to the high signal correlation between adjacent bands recorded by the instrument. The optimal index for F_s and F_m' was selected based on the above criteria and searched for 2

wavelengths with a sufficient difference in the wavelength of more than 20nm, a wide waveband of more than 10nm and located outside the regions 300-400 nm and 900-1000 nm. The reflectance RSI with the highest R^2 for F_s and $F_{m'}$ from the terrestrial part of the transect was then used to plot the $Y(II)$ values calculated from the F_s and $F_{m'}$ indices according to equation (1) against the *in-situ* recorded measurements. In conjunction with the R , the Root Mean Square Error (RMSE) of the linear regression was taken into account to compare the behaviour of the calculated values and the estimated regression from the RSI index. RMSE is a frequently used measure of the difference between values predicted by a model and the values actually observed from the environment that is being modelled. The RMSE of a model prediction in regard to the observed values $X_{obs,i}$ and the estimated variable $X_{mod,i}$ is:

$$RMSE = \sqrt{\frac{\sum_{i=1}^n (X_{obs,i} - X_{mod,i})^2}{n}} \quad (6)$$

The best bands identified were isolated and the RSI index with the highest statistical significance was applied to the airborne hyperspectral images. The same procedure was carried out for the ETR parameter based on equation (2) and by using the result from the $Y(II)$ calculations as above and the best RSI for PAR. The leaf scale reflectance profiles were used as a representation of reed stability on the measurable leaf chemical and physiological properties.

The main aspect of this application was to investigate whether the methodology developed at the leaf level could be transferred to airborne imagery and to what extent the result is representative of the real $Y(II)$ and ETR values. For this task and since no accurate fieldwork at canopy level can present the values of $Y(II)$ and ETR, the results were visually interpreted by wetland ecologists at the Balaton Limnological Institute in Tihany to evaluate the information content in the vegetation index image. The performance of

the index in regard to reed condition in the study area is further assessed and discussed.

4.5 Results and discussion

4.5.1 Complete-combination spectral indices for coupling with photophysiological parameters

4.5.1.1 Reflectance data

Figure 4.2 and Figure 4.3 present an indicative subset of the results of the RSI relationship with F_s and F_m' respectively. The complete set of results is provided in Appendix 2. Graphs of RSI and NDSI correlations are an information source of significance of the wavelengths correlating to the physiological parameter under study and optimize the selection of the effective wavelength and bandwidth according to Inoue et al. (2008). With the increasing use of imaging spectroscopy, the need for standardized data processing techniques specifically for hyperspectral data has been prominent (Plaza et al. 2009). These case-specific optimization graphs provide ad-hoc information for the entire hyperspectrum. They are a prime example for analyzing the special properties of hyperspectral data and can be recommended as a process coupling ground data and hyperspectral information.

From a statistical point of view, the R^2 graphs represent the distribution of correlation between wavelength combinations and the physiological parameter under study. In essence, areas where the distribution is dense provide evidence of regions where information extracted from these spectral combinations can represent the physiological parameter. The p graph represents the confidence of the assumption made; the lower the p value the stronger the hypothesis we have built. A unique observation in the graph, or a cluster of observations, has to be studied synergistically in the R^2 and p graphs, optimization of the output is derived where R^2 will reach a maximum, and p is sufficiently low (in this study we seek for values $p = ***$). The results

of this analysis for all the physiological-spectral combinations investigated are summarized in

Table 4.2. The maximum R^2 values indicate a high correlation and thus a significant predictive ability when using the specific index as a proxy for the physiological parameter. Furthermore, the maps provide information on the effective wavelength bandwidth. For instance, bands with narrow width are appropriate in the context for hyperspectral data, while bands in the graph covering a wider spectrum are tailored to information which might be related to multispectral instruments.

Reflectance maximum values exhibit differently in regard to individual photophysiological parameters. F_s and F_m' correlation is very similar, which can be attributed to the fact that both F_s and F_m' represent fluorescence yield which is proportional to intensity of electromagnetic radiation and thus are directly related to the spectroradiometers' recorded values at specific wavelengths. On the other hand $Y(II)$ and ETR are calculated on the basis of the former. The correlation coefficient in this pair of parameters seems to be close in most cases (

Table 4.2). However, when measuring $Y(II)$ and ETR the reflectance values diverge. Radiance values correlate better in the deep water for F_s and F_m' while $Y(II)$, PAR, ETR and CHL present maximum R^2 at the waterfront part of the transect.

It is important to note the relatively low R^2 obtained for the combined dataset from the whole transect. This indicates that the environmental conditions at the given point of the transect affect essentially the spectral response of *Phragmites* and the inundation categories defined mark important differences between reed stands within a reed bed.

$Y(II)$ is representing the amount of used PSII systems, while ETR shows the actual activity at the given light intensity. Although ETR calculation is based

on Y(II), ETR and Y(II) appear to have different effective spectral regions. ETR performs slightly better than Y(II) in terms of maximum R^2 . ETR has the highest correlation $R^2 = 0.65$ at a narrow bandwidth of 3nm at (493, 478) for both RSI and NDSI at the waterfront category and a sufficient correlation window ($0.5 < R^2 < 0.6$) at 600-700 nm. This bandwidth is typical in multispectral sensors and information can be derived from a combination of bands within this spectral region, which several multispectral sensors contain. Hence, critical information for the ETR parameter is encountered at the red domain of the chlorophyll absorption region. Y(II) has a maximum $R^2 = 0.62$ at (473, 483) for RSI and NDSI.

4.5.1.2 Consistency between RSI and NDSI

Comparing the maximum values of R^2 for RSI and NDSI no important differences were found, however the wavelength combination as well as the shape of the spectral regions in the respective figures changes slightly in a few cases. For example, the RSI and NDSI for Fs in the deepwater category are presented in Figure 4.4. Both indices sustain similar highest R^2 value (0.76 and 0.75 respectively) at the same combination of wavelengths (633, 690) which is deemed to be significant, despite the very narrow width. Concerning wider wavebands, both indices seem to correlate in a homogeneous spectral area at the wavelengths 530-670 nm and a second region at 690-720 nm in which RSI correlates stronger ($0.6 < R^2 < 0.7$) around 700 nm. In the rest of the results in regard to the category and photophysiological parameter under study, minor differences can be located in the distribution of the RSI and NDSI maps, however they are insignificant. A comparison of the maximum of the combinations from Table 4.3 supports the very similar maximum R^2 values and wavelength combinations obtained when using the two indices. It is important to notice that the similarities between RSI and NDSI are sometimes intriguing. For this reason a quality assurance test was run in order to confirm that the R script used is faultless and delivered the anticipated results. The R^2

values for specific waveband pairs were calculated separately and compared with the results from the undertaken analysis, and the values were equal. Furthermore, RSI and NDSI values appear identical because they are rounded up to the second decimal point, for instance F_s for SI and NDSI is 0.67 for both cases in the revised table, however the actual values are 0.674408 for the SI and 0.673089 for the NDSI. To check the robustness of the algorithm, an application on a completely different dataset consisting of ASD measurements and water content as biophysical parameter collected in

Table 4.2: Spectral band combination and maximum value of coefficient of determination (R^2) for reflectance RSI and NDSI in regard to the photophysiological parameter measured in-situ. p : * $\rightarrow p < 0.05$, ** $\rightarrow p < 0.01$, *** $\rightarrow p < 0.001$.

	Terrestrial		Shallow water		Deep water		Waterfront		Combined dataset	
	R_i, R_j	R^2	R_i, R_j	R^2	R_i, R_j	R^2	R_i, R_j	R^2	R_i, R_j	R^2
$RSI = R_i / R_j$										
F_s	541, 549	0.67 ***	546, 551	0.58 ***	690, 633	0.76 ***	871, 861	0.60 ***	546, 551	0.47 ***
$F_{m'}$	544, 549	0.55 ***	539, 544	0.57 ***	545, 548	0.82 ***	904, 906	0.56 ***	539, 560	0.47 ***
$Y(II)$	803, 818	0.46 ***	663, 686	0.38 ***	908, 923	0.45 ***	473, 483	0.62 ***	659, 687	0.24 ***
P_{AR}	945, 941	0.48 ***	892, 889	0.25 ***	827, 825	0.48 ***	989, 997	0.71 ***	917, 922	0.09 ***
ETR	941, 945	0.52 ***	664, 685	0.47 ***	556, 564	0.48 ***	493, 478	0.65 ***	621, 692	0.25 ***
CHL	802, 800	0.51 ***	759, 764	0.57 ***	760, 764	0.50 ***	889, 924	0.63 ***	747, 748	0.14 ***
$NDSI = (R_i - R_j) / (R_i + R_j)$										
F_s	541, 549	0.67 ***	546, 551	0.58 ***	633, 690	0.75 ***	861, 871	0.60 ***	546, 551	0.47 ***
$F_{m'}$	544, 549	0.55 ***	539, 544	0.57 ***	545, 548	0.82 ***	904, 906	0.56 ***	539, 560	0.47 ***
$Y(II)$	803, 818	0.46 ***	663, 686	0.38 ***	908, 923	0.45 ***	473, 483	0.62 ***	659, 687	0.24 ***
P_{AR}	941, 945	0.48 ***	889, 892	0.25 ***	825, 827	0.48 ***	989, 997	0.71 ***	917, 922	0.09 ***
ETR	941, 945	0.52 ***	664, 685	0.47 ***	556, 564	0.48 ***	478, 493	0.65 ***	621, 692	0.25 ***

CHL	800, 802	0.51 ***	759, 764	0.57 ***	760, 764	0.50 ***	889, 924	0.63 ***	747, 748	0.14 ***
-----	----------	-------------	----------	-------------	----------	-------------	----------	-------------	----------	-------------

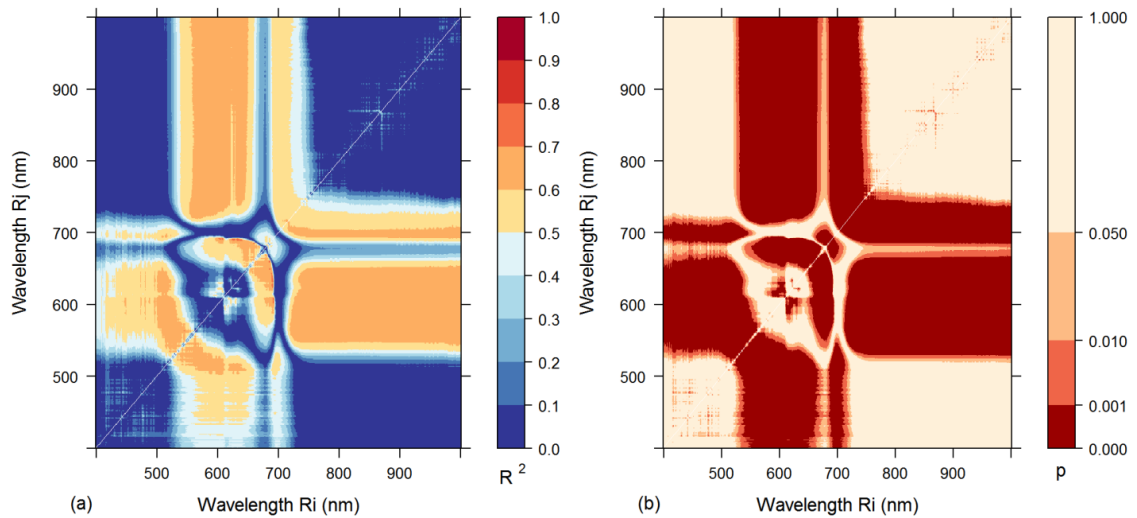


Figure 4.2: Coefficient of determination (R^2) (a) and corresponding p values (b) between apparent fluorescence yield (F_s) and RSI (R_i, R_j) measured on *Phragmites* plants at the deep water part of the transect in Kerekedi Bay, Lake Balaton. The RSI was calculated using the whole spectrum reflectance combinations of two wavebands at i and j .

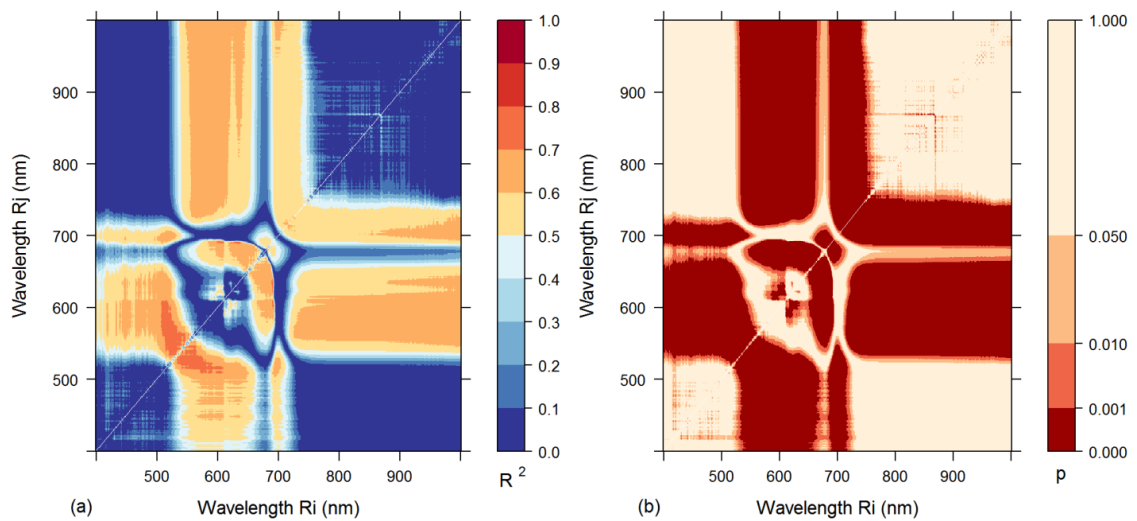


Figure 4.3: Coefficient of determination (R^2) (a) and corresponding p values (b) between maximum fluorescence yield ($F_{m'}$) and RSI (R_i, R_j) measured on *Phragmites* plants at the deep water part of the transect in Kerekedi Bay, Lake Balaton. The RSI was calculated using the whole spectrum reflectance combinations of two wavebands at i and j .

the Ecuadorian Amazon forest was conducted; the results show an expected output which is the correlation of the SI at the 940 nm according to the

literature (Figure 4.5). Similar consistency between RSI and NDSI is presented in results from Inoue et al. (2012) in a similar study for Nitrogen content in paddy rice. For these reasons it is suggested that the differences between RSI and NDSI are not crucial and the application of either is sufficient.

4.5.1.3 Transmittance data

The same methodology described above was applied on the transmittance and reflectance data again, this time with a 3x3 spectral filter to reduce the number of bands from 600 to 200 and hence computer requirements. A comparison between the results from the raw data and the filtered data does not reveal large differences (Figure 4.6). Transmittance and reflectance maximum values exhibit differently in regard to individual photophysiological parameters (Table 4.3 and Table 4.4). F_s and F_m' correlation is very similar, which can be attributed to the fact that both F_s and F_m' represent fluorescence yield which is proportional to intensity of electromagnetic radiation and thus are directly related to the spectroradiometers' recorded values at specific wavelengths. On the other hand $Y(II)$ and ETR are calculated on the basis of the former. The correlation in this pair of parameters seems to be proximate in most cases, with the exception of the transmittance in the waterfront category where there is a difference of 0.21 for the coefficient of determination (Table 4.4). However, when measuring $Y(II)$ and ETR the reflectance and transmittance values diverge. Reflectance values correlate better in the shallow water and terrestrial categories for $Y(II)$, PAR, ETR and CHL, while transmittance values for these parameters correlate better in the deep water and waterfront areas. It is important to note the relatively low R^2 values that were obtained for the combined dataset from the whole transect. This indicates that the environmental conditions (primarily water level) at the given point of the transect affected the reflectance of *Phragmites*, while the photophysiological parameters were not influenced as significantly.

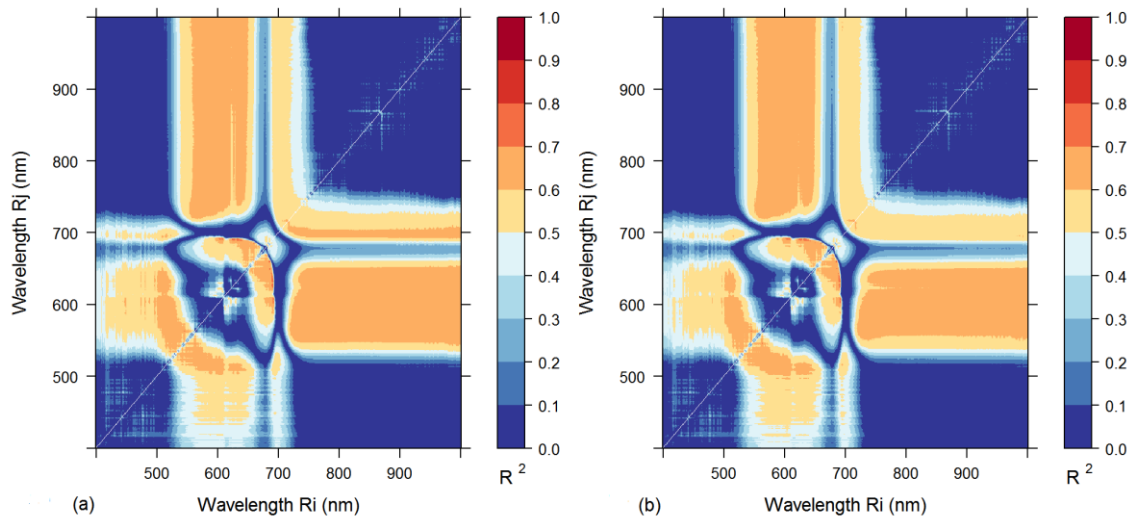


Figure 4.4: Coefficient of determination (R^2) for RSI (R_i, R_j) (a) and NDSI (R_i, R_j) (b) between F_s measured on *Phragmites* plants at the deepwater part of the transect in Kerekedi Bay, Lake Balaton. RSI and NDSI were calculated using the whole reflectance spectrum combinations of two wavebands at i and j .

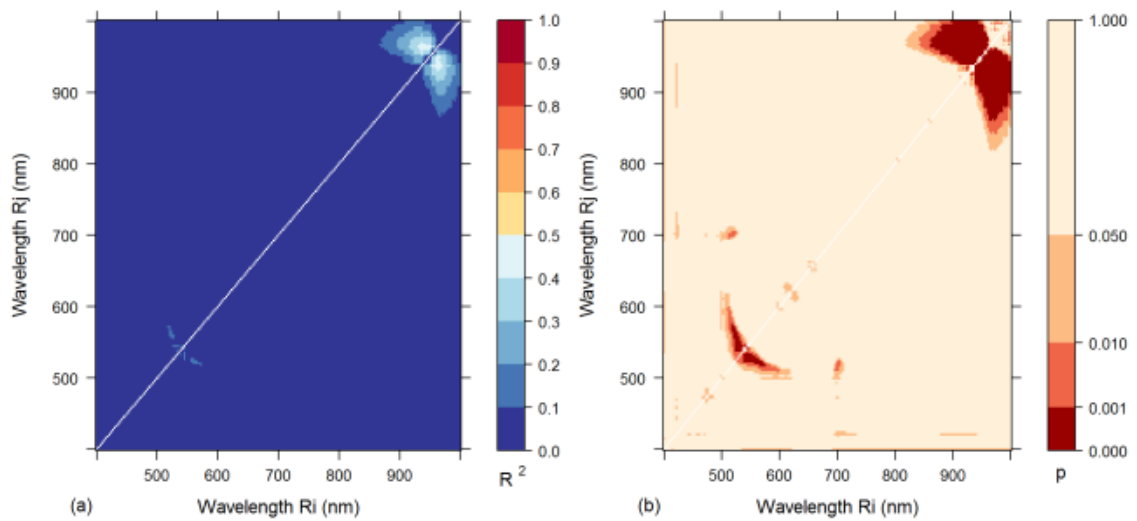


Figure 4.5: Coefficient of determination (R^2) for RSI (R_i, R_j) (a) and corresponding p value (b) results produced by applying the R algorithm on an independent dataset collected in the Amazon forest (water content vs reflectance spectral indices). As expected, water content is correlating between 900 nm and 1000 nm.

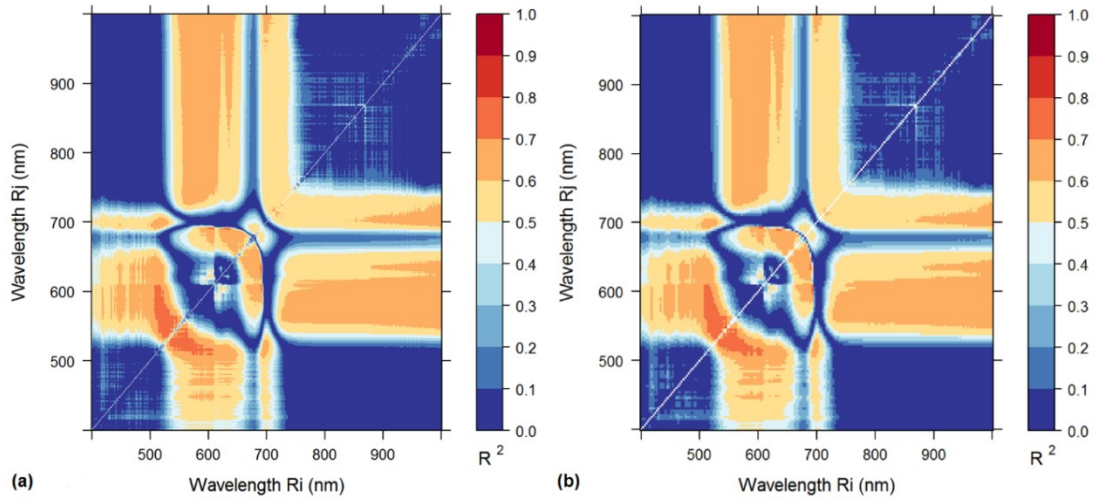


Figure 4.6: Non-filtered (a) and 3x3 filtered (b) for reflectance RSI example.

Table 4.3: Spectral band combination and maximum value of coefficient of determination (R^2) for reflectance RSI and NDSI in regard to the photophysiological parameter measured in-situ. p : * $\rightarrow p < 0.05$, ** $\rightarrow p < 0.01$, *** $\rightarrow p < 0.001$. A 3x3 filter has been applied in order to reduce the number of bands from 600 to 200.

	Terrestrial		Shallow water		Deep water		Waterfront edge		Combined dataset	
	R_i, R_j	R^2	R_i, R_j	R^2	R_i, R_j	R^2	R_i, R_j	R^2	R_i, R_j	R^2
$RSI_R = R_i / R_j$										
F_s	573, 525	0.65 ***	552, 546	0.53 ***	639, 690	0.72 ***	912, 909	0.48 **	552, 546	0.45 ***
$F_{m'}$	540, 561	0.52 ***	552, 540	0.55 ***	549, 546	0.80 ***	594, 600	0.38 **	561, 540	0.47 ***
$Y(II)$	462, 474	0.43 ***	687, 663	0.36 ***	924, 909	0.40 ***	492, 489	0.51 **	690, 651	0.23 ***
P_{AR}	462, 489	0.47 ***	888, 894	0.12 ***	885, 900	0.33 **	414, 429	0.52 **	996, 999	0.07 **
ETR	942, 945	0.41 **	663, 687	0.41 ***	912, 909	0.45 ***	480, 495	0.65 ***	693, 627	0.24 ***
CHL	711, 453	0.48 ***	765, 759	0.54 ***	612, 699	0.46 ***	417, 423	0.57 ***	756, 753	0.13 ***
$NDSI_R = (R_i - R_j) / (R_i + R_j)$										
F_s	552, 546	0.65 ***	552, 546	0.53 ***	690, 639	0.72 ***	912, 909	0.48 **	552, 546	0.45 ***
$F_{m'}$	561, 540	0.52 ***	552, 540	0.55 ***	549, 546	0.80 ***	600, 594	0.38 **	561, 540	0.47 ***
$Y(II)$	690, 651	0.43 ***	687, 663	0.36 ***	924, 909	0.40 ***	492, 489	0.51 **	690, 651	0.23 ***
P_{AR}	996, 999	0.46 ***	894, 888	0.12 **	900, 885	0.33 **	429, 414	0.51 **	399, 999	0.07 **
ETR	693, 627	0.41 **	687, 663	0.40 ***	912, 909	0.45* **	495, 480	0.65** *	693, 627	0.24***
CHL	756, 753	0.47 ***	765, 759	0.54 ***	699, 612	0.46* **	423, 417	0.57** *	756, 753	0.13***

Table 4.4: Spectral band combination and maximum value of coefficient of determination (R^2) for transmittance RSI and NDSI in regard to the photophysiological parameter measured in-situ. p : * $\rightarrow p < 0.05$, ** $\rightarrow p < 0.01$, *** $\rightarrow p < 0.001$. A 3×3 filter has been applied in order to reduce the number of bands from 600 to 200.

	Terrestrial		Shallow water		Deep water		Waterfront edge		Combined dataset	
	T_i, T_j	R^2	T_i, T_j	R^2	T_i, T_j	R^2	T_i, T_j	R^2	T_i, T_j	R^2
$RSI_T = T_i / T_j$										
F_s	576, 525	0.65 ***	681, 672	0.51 ***	603, 516	0.72 ***	534, 528	0.61 ***	564, 537	0.44 ***
$F_{m'}$	558, 543	0.50 ***	582, 528	0.52 ***	585, 525	0.79 ***	459, 453	0.40 **	564, 537	0.45 ***
$Y(II)$	510, 651	0.41 **	681, 672	0.29 ***	663, 687	0.36 **	471, 492	0.79 ***	690, 654	0.23 ***
P_{AR}	462, 486	0.46 ***	930, 933	0.10 *	738, 408	0.50 ***	411, 543	0.45 **	492, 681	0.07 **
ETR	693, 624	0.40 **	684, 669	0.40 ***	645, 690	0.59 ***	447, 462	0.66 ***	624, 693	0.34 ***
CHL	705, 552	0.32 **	762, 759	0.50 ***	702, 564	0.51 ***	975, 966	0.72 ***	759, 756	0.11 ***
$NDSI_T = (T_i - T_j) / (T_i + T_j)$										
F_s	576, 525	0.65 ***	681, 672	0.51 ***	603, 516	0.71 ***	534, 528	0.61 ***	564, 537	0.44 ***
$F_{m'}$	558, 543	0.50 ***	561, 549	0.52 ***	585, 525	0.79 ***	459, 453	0.40 **	564, 537	0.45 ***
$Y(II)$	651, 510	0.40 **	681, 672	0.29 ***	687, 663	0.35 **	492, 471	0.79 ***	690, 654	0.23 ***
P_{AR}	486, 462	0.46 ***	933, 930	0.10 *	735, 429	0.49 ***	543, 411	0.43 **	681, 498	0.07 **
ETR	693, 624	0.40 **	684, 669	0.40 ***	690, 645	0.59 ***	462, 447	0.65 ***	693, 624	0.34 ***
CHL	705, 552	0.32 **	762, 759	0.50 ***	702, 564	0.51 ***	975, 966	0.72 ***	759, 756	0.11 ***

4.5.2 Empirical indices for spectral assessment of photophysiological parameters

18 frequently used empirical indices derived from the *in-situ* spectral measurements according to the 4 inundation categories are presented in Table 4.5. It is obvious that the best correlations ($R^2=0.71$) were obtained from the basic photophysiological parameters (F_s and $F_{m'}$), while the derived parameters (i.e. ETR and $Y(II)$) decrease the number of significant correlations found. For F_s and $F_{m'}$ the highest and more significant correlation was obtained in the deep water part of the transect, while the

waterfront of the studied transect had smaller and less significant correlations. This difference in F_s and F_m' correlation could be explained by high homogeneity of the deep water reed stand and the heterogeneity of the studied *Phragmites* in the terrestrial (sporadic appearance of the co-dominant *Carex* and other ruderal species) and waterfront (plants of different ages and physical conditions) of the stand. The Photochemical Reflectance Index (PRI) = $(R_{531} - R_{570}) / (R_{531} + R_{570})$ (Gamon et al. (1997)) has outperformed the other indices and reached R^2 values equal to 0.65 and 0.71 for F_s and F_m' respectively at the deep water category.

Contrary to F_s and F_m' results, for ETR and Y(II) high coefficient correlations are observed in the waterfront category ($R^2 = 0.57^{***}$ and 0.36^* respectively) and are represented better by the narrowband NDVI. The reed standing at the edge of the reed bed is assumed to be under higher environmental pressure relatively to the inner part of the reed bed; therefore diverse physiological states can be encountered and linear correlation with indices representing photosynthetic activity can be optimized.

A comparison of R^2 values between the optimized indices derived from the complete combinations (Table 4.3) and the empirical indices (Table 4.5), reveals that the R^2 values of the proposed narrowband indices are significantly higher than the best performed empirical indices. For instance, regarding F_s in the deep water category, the RSI and NDSI band combinations (690, 633) result in $R^2 = 0.76^{***}$ for RSI and $R^2 = 0.75^{***}$ for NDSI while the best empirical index PRI reaches 0.65^{***} . For F_m' in the same category, the combination (544, 548) gives $R^2 = 0.82^{***}$ for RSI and NDSI while PRI = 0.71^{***} . In the waterfront category, $R^2 = 0.62^{***}$ for Y(II) when calculated from RSI and NDSI while from NDVI $R^2 = 0.36^{***}$. In a similar manner and for ETR, $R^2 = 0.65^{***}$ for RSI and NDSI while for NDVI $R^2 = 0.57^{***}$. The results are in some way anticipated, at least concerning PRI and NDVI; these two empirical indices are each a specific case of NDSI and the result from

their calculation has been already accounted for in the complete combination bands. PRI has been proposed also by Meroni et al. (2008) to detect stress at an early stage, in contrast with NDVI which provided stress-related information only when the damage has occurred. Comparing the PRI band combination (531, 570) with the optimized one for Fs in the terrestrial part (541, 549), it is noticeable that these two indices lay in the same 2-dimensional spectral region, and hence the results are expected to be similar. By testing the complete combination bands, the exact bands which provide optimum coefficient correlation were identified for a specific case study. This becomes obvious in Figure 4.7 where the relationship between all spectral indices in the form of correlation clusters for the shallow water part category is visualized. It is worth noting that mathematically more complicated empirical indices such as EVI didn't perform satisfactorily. This fact in combination with the observation that RSI and NDSI are very similar can lead to the conclusion that the importance of constructing a spectral index lies in the band selection and not the mathematical formulae.

4.5.3 Estimation of Y(II) and ETR from RSI values

4.5.3.1 Y(II) estimation

For the maximum values of the correlations found between the photophysiological parameters F and Fm' and the corresponding RSIs, the linear regression was calculated on the dataset collected at the terrestrial part of the transect according to equation (1) (Figure 4.8 and Table 4.6). Based on the values of F and Fm' for each measurement, the Y(II) was calculated and the linear regression between the latter modelled Y(II) and the *in-situ* measurement for Y(II) recorded was investigated for each category. The R² of the model predictions was for most cases considerably lower than the calculated from the RSI. Only the terrestrial modelling prediction is

Table 4.5: Correlation matrix between the measured photophysiological parameters and empirical indices. p :
 $*$ → $p<0.05$, $**$ → $p<0.01$, $***$ → $p<0.001$, all the number without significance indexes are not significant.

Index	F_s	F_m'	$Y(II)$	PAR	ETR	CHL	F_s	F_m'	$Y(II)$	PAR	ETR	CHL
	Terrestrial						Shallow water					
ARI2	0.3**	0.33**	0.01	0.03	0.02	0.22*	0.18**	0.24***	0.04	0	0.07	0.03
CRI1	0.07	0.06	0.03	0.02	0.12	0.25*	0.1*	0.06	0.13**	0.03	0.09*	0.01
CRI2	0.12	0.11	0.03	0.01	0.09	0.29**	0.14**	0.11*	0.14**	0.02	0.11*	0.01
EVI	0.4**	0.32**	0.08	0.03	0	0.02	0.01	0.02	0	0.01	0.01	0.23***
mND₇₀₅	0.25*	0.31**	0	0.02	0.02	0.23*	0.15**	0.21***	0.02	0	0.02	0.23***
mSR₇₀₅	0.26*	0.3**	0.01	0.01	0.02	0.23*	0.16**	0.21***	0.02	0	0.03	0.19***
NDVI	0	0	0	0.05	0.12	0.15	0.04	0.07*	0	0.03	0.01	0
NDVI₇₅₀	0.22*	0.28**	0	0.01	0.01	0.1	0.18**	0.26***	0.01	0	0.02	0.24***
PRI	0.62***	0.45***	0.22*	0	0.17	0.03	0.48***	0.52***	0.22***	0	0.26***	0
PSRI	0	0.01	0.04	0.15	0.07	0.01	0.04	0.03	0.07	0	0.08*	0.03
RGI	0.01	0.03	0	0.15	0.17	0.18*	0	0	0	0.03	0.01	0.2***
SGI	0.08	0.06	0.01	0	0	0.01	0.08*	0.14**	0	0.01	0.01	0.06
SIPI	0	0	0.04	0.17*	0.1	0.08	0	0	0	0	0	0
SRI	0	0	0.01	0.05	0.14	0.15	0.03	0.07	0	0.04	0.01	0.01
VOG1	0.18*	0.25*	0	0.02	0.01	0.14	0.17**	0.24***	0.02	0	0.02	0.31***
VOG2	0.14	0.21*	0	0.02	0	0.16	0.15**	0.22***	0.01	0	0.01	0.35***
VOG3	0.14	0.22*	0	0.02	0	0.16	0.15**	0.22***	0.01	0	0.01	0.35***
WBI	0.13	0.07	0.05	0	0.01	0.01	0	0	0	0	0	0
Index	F_s	F_m'	$Y(II)$	PAR	ETR	CHL	F_s	F_m'	$Y(II)$	PAR	ETR	CHL
	Deep water						Waterfront					
ARI2	0.39***	0.4***	0.08	0.01	0.14	0.13	0.02	0	0.03	0.06	0.09	0.31*
CRI1	0.38***	0.46***	0.04	0.01	0.09	0.15*	0.07	0.03	0.14	0.15	0.24*	0.28*
CRI2	0.43***	0.5***	0.05	0.01	0.11	0.16*	0.05	0.03	0.1	0.1	0.17	0.36*
EVI	0.01	0.07	0.05	0.04	0.01	0.1	0.05	0	0.26*	0.19	0.41**	0.42**
mND₇₀₅	0.57***	0.61***	0.1	0	0.1	0.14	0.01	0	0.11	0.34*	0.35*	0.01
mSR₇₀₅	0.65***	0.63***	0.17*	0	0.17*	0.1	0.01	0	0.08	0.26*	0.27*	0.01
NDVI	0.21*	0.16*	0.16*	0.01	0.12	0	0.17	0.04	0.36*	0.31*	0.57***	0.1
NDVI₇₅₀	0.56***	0.58***	0.13	0	0.11	0.17*	0.04	0	0.22	0.38**	0.5**	0.04
PRI	0.65***	0.71***	0.14	0.04	0.27**	0.02	0.05	0.06	0.03	0.03	0	0.33*
PSRI	0.08	0.14	0	0.2*	0.1	0.01	0	0	0.02	0.04	0.04	0.4**
RGI	0.09	0.12	0	0.04	0.02	0.21*	0.19	0.11	0.17	0.03	0.18	0.01
SGI	0.28**	0.27**	0.08	0	0.09	0	0.01	0	0.07	0.37**	0.31*	0.13
SIPI	0.1	0.13	0.01	0.04	0.05	0.03	0	0.01	0.02	0.02	0.02	0.44**
SRI	0.21*	0.16*	0.16*	0.01	0.12	0	0.12	0.03	0.3*	0.27*	0.5**	0.13
VOG1	0.56***	0.58***	0.12	0.01	0.1	0.21*	0.02	0	0.21	0.36*	0.47**	0.05
VOG2	0.55***	0.56***	0.12	0.01	0.09	0.23*	0.01	0.01	0.2	0.32*	0.44**	0.06
VOG3	0.55***	0.57***	0.13	0.01	0.09	0.23*	0.01	0.01	0.2	0.32*	0.43**	0.06
WBI	0.04	0.02	0.04	0.03	0.01	0.14	0.01	0.06	0.05	0.02	0.06	0.2

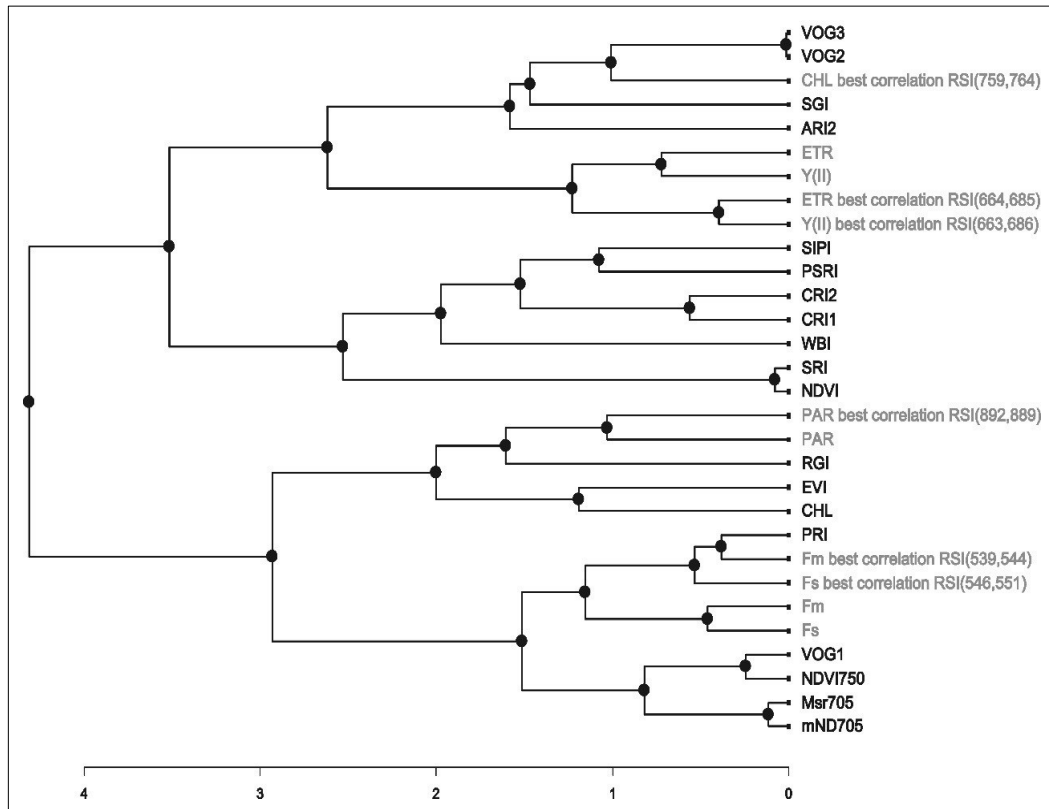


Figure 4.7: Hierarchical clustering of correlation relationship between the spectral indices proposed (grey colour), the empirical indices tested (black colour) and the biophysical parameters measured in-situ (grey colour).

distinguished by providing a correlation of 0.35 (Figure 4.9) while the estimated correlation from the best *in-situ* RSI was 0.46. The corresponding RMSE was found to be 0.057.

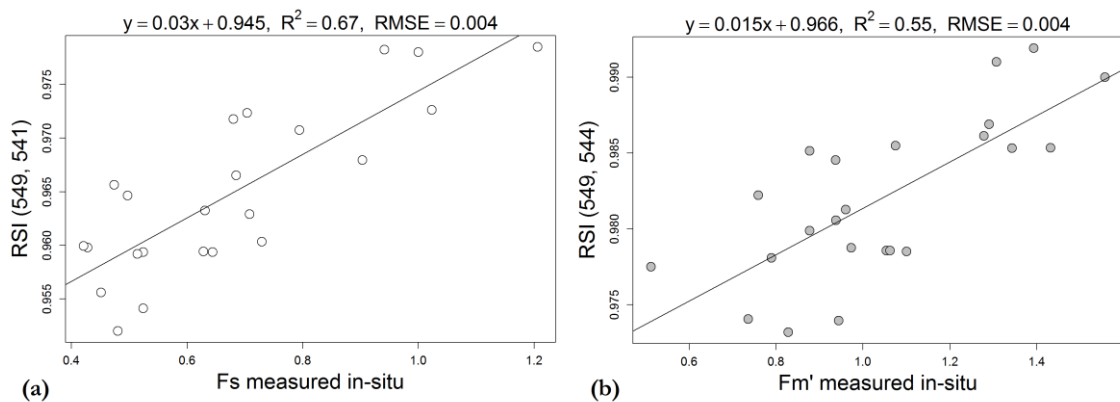


Figure 4.8: Linear regression for F_s (a) and $F_{m'}$ (b) for the reflectance RSIs with the highest correlations at the terrestrial part of the transect in Kerekedi Bay, Lake Balaton.

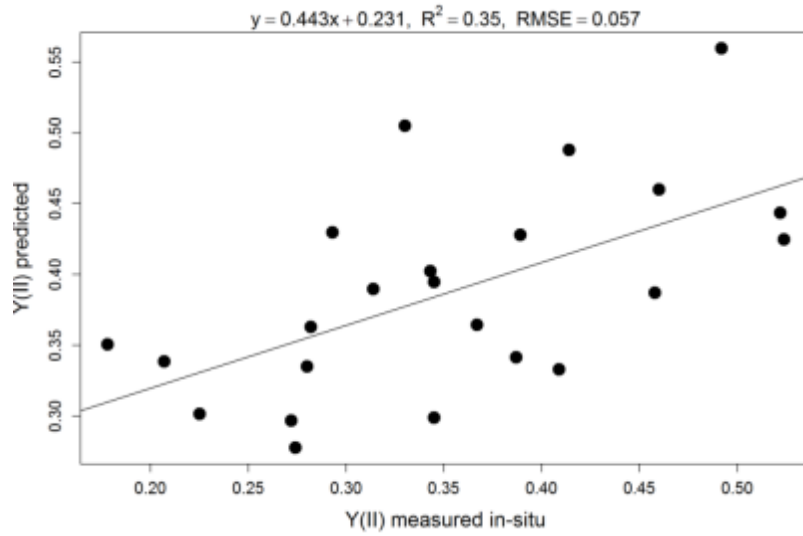


Figure 4.9: Linear regression of the measured and predicted values for Y(II) of *Phragmites* plants from the terrestrial part of the transect. Predicted values calculated based on the best correlations found from reflectance RSI for F_s and F_m' (Figure 4.8).

Table 4.6: Model predictions for Y(II) from the RSI reflectance dataset.

	<i>Equation</i>	<i>RMSE</i>	<i>R² from predicted Y(II)</i>	<i>R² from best RSI for Y(II) – Table 4.1</i>
Terrestrial	$y = 0.443x + 0.231$	0.057	0.35 (Figure 4.9)	0.46
Shallow water	$y = 0.873x + 0.074$	0.167	0.12	0.38
Deep water	$y = 0.456x + 0.236$	0.131	0.05	0.45
Waterfront	$y = 1.395x - 0.200$	0.180	0.27	0.62
Combined dataset	$y = 0.513x + 0.180$	0.334	0.01	0.24

4.5.3.2 *ETR estimation*

In a similar manner the ETR for the reed on the waterfront part of the transect was calculated on the basis of the maximum RSI values for PAR and Y(II) (Figure 4.10). The predicted R^2 value was found to be 0.72 (Figure 4.11) while the R^2 value from the *in-situ* ETR correlation with the best RSI was 0.65. This indicated that the modelled prediction based on the equation (2) provides slightly higher R^2 values for ETR. The corresponding RMSE was 49.707. The results for the other parts of the transect (Table 4.7) indicate that the

predicted R^2 value is always lower than the measured, however the differences are not significant. In comparison to the prediction of $Y(II)$, prediction in ETR seems to perform better in terms of the coefficient of determination values.

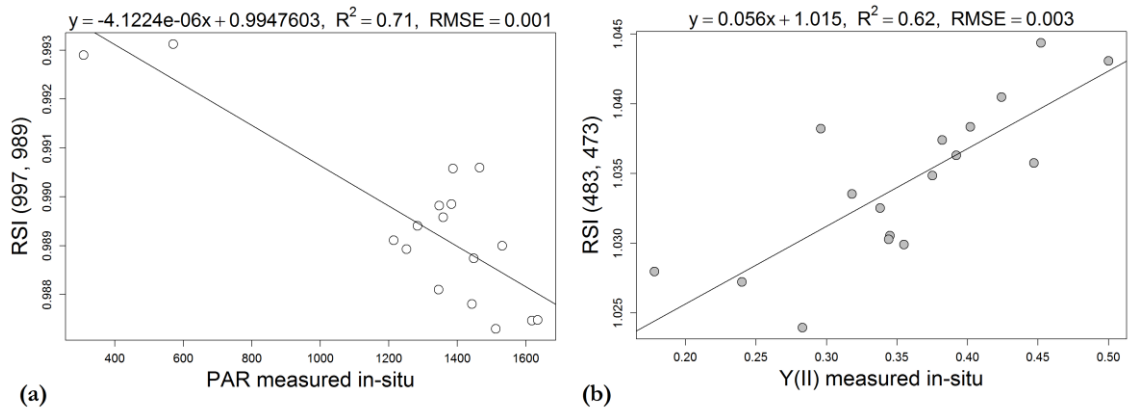


Figure 4.10: Linear regression for PAR (a) and $Y(II)$ (b) for the reflectance RSIs with the highest correlations at the waterfront part of the transect in Kerekedi Bay, Lake Balaton.

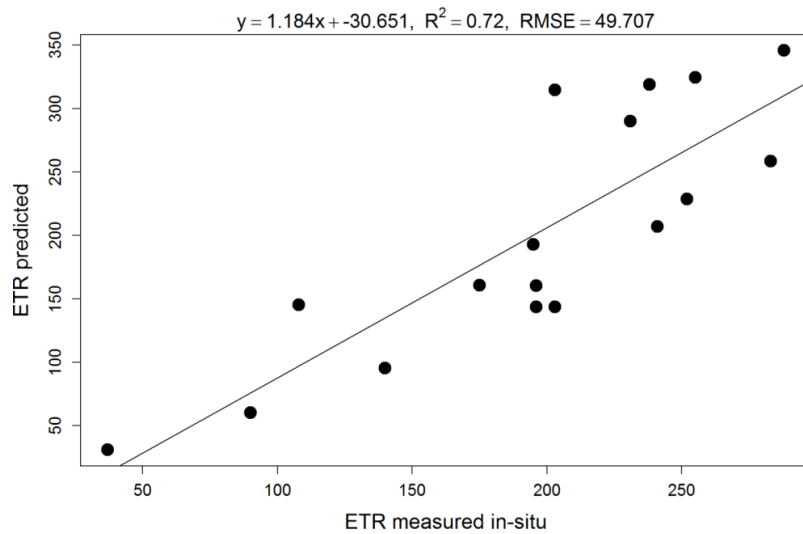


Figure 4.11: Linear regression of the measured and predicted values for ETR of *Phragmites* plants from the waterfront part of the transect. Predicted values calculated based on the best correlations found from reflectance RSI for PAR and $Y(II)$ (Figure 4.10).

Table 4.7: Model predictions for ETR from the RSI reflectance dataset.

	<i>Equation</i>	<i>RMSE</i>	<i>R² from predicted Y(II)</i>	<i>R² from best RSI for Y(II) – Table 4.1</i>
<i>Terrestrial</i>	$y = 1.098x - 55.703$	66.329	0.48	0.52
<i>Shallow water</i>	$y = 1.247x - 43.055$	58.587	0.38	0.47
<i>Deep water</i>	$y = 1.024x + 12.544$	52.96	0.37	0.48
<i>Waterfront</i>	$y = 1.184x - 30.651$	49.707	0.72 (Figure 4.11)	0.65
<i>Combined dataset</i>	$y = 1.247x - 37.723$	134.89	0.17	0.25

The experimental design introduces some unavoidable limitations in correlation and therefore generally cannot lead to exceptionally high R² values. The paired dataset is acquired from two different scientific electronic instruments with different set up, operation and associated errors. Furthermore, while measurements were made on the same area of each leaf, the overlap due to the users' operation accuracy is not certain, as well as the measuring surface is not identical in the two instruments and neither could be compensated. An additional source of variability is the heterogeneity of reed vegetation coming both from microhabitat differences of the study area and genetic patchiness of the reed stands. Finally Y(II) is a measurement of the light capture efficiency of PSII, while ETR is a proxy of the gross rate of carbon fixation, the latter is assumed to represent photosynthesis (Maxwell and Johnson 2000). A high correlation is found under laboratory conditions between these relationships, however when measured in the field, Y(II) and CO₂ fluxes can be affected by temperature (Fryer et al. 1998). All the above errors are introduced and propagate through the experiment, thus the correlation coefficient estimated is not as high as in similar studies investigating direct morphological and physiological aspects (i.e. stem density, dry biomass, chlorophyll and nitrogen content with laboratory methods) which are more accurate to measure; nevertheless coupling with fluorescence

data provides a direct measurement of photosynthetic activity of the plant and an indirect estimation of environmental stress.

4.5.4 Application on airborne hyperspectral data

The optimal index for the application on the airborne dataset was defined as the band combination with the highest R^2 value from the filtered 3x3 results, a corresponding confident p value, the lowest RMSE and also covers an adequate broad spectrum to contain the remote sensors bandwidth at the specific wavelength. This has been identified as the band combinations RSI(612, 516) (0.63***) for F_s , (699, 527) (0.51***) for F_m' and (463, 488) (0.47***) for PAR based on the terrestrial category. The Y(II) and ETR maps resulting from transferring the field methodology to the airborne imagery is presented in Figure 4.12. The Y(II) calculated on the basis of F_s and F_m' parameters reveals the photophysiological homogeneity over the stable reed and is sufficient for estimation of the Y(II) value based on remotely sensed data. This becomes obvious when comparing the map with the actual Y(II) measurements *in-situ* (Figure 3.12). The terrestrial and waterfront sides of the stand have slightly lower Y(II) values, while the reed stands in the middle of the reed bed contain higher values (and Figure 4.12). The calculated Y(II) values are lower by 15-20% compared to the *in-situ* actual data, but insertion of a correction factor could compensate for the final output. In spatially more heterogeneous environments, such as the waterfront and terrestrial edges, the potential photosynthetic capacity is lower than in the more homogeneous environment in the middle of the reed bed. This is probably in connection with disturbances that the plant is encountering at less homogeneous patches. Moreover in these sites the possibility of appearance of adventive species is significantly higher, thus different ETR and Y(II) signals could be originated from the abundance of other species within a single pixel. Furthermore, the waterfront of the reed stands contains plants of significant age differences (Tóth and Szabó, 2012) which affects the photophysiological parameters too,

while the interior of the stands has a more homogeneous age distribution and thus more reliably measured by remote sensing. Thus, while during the *in-situ* fluorescence measurements usually the average and fully grown plants were measured, the airborne data contains the spectral response from a very diverse pool of *Phragmites* plants including the very strong signal from young shoots.

In summary, it is proposed that the photosynthetic activity can be estimated from hyperspectral airborne imagery. The images have to be radiometrically and atmospherically corrected in order to assure consistency between the remotely sensed and leaf data. This methodology has been successfully demonstrated when applied to high spectral and spatial resolution airborne imagery. Based on the reflectance spectral indices (band1, band2: 612, 516) (0.63^{***}) for Fs, (699, 527) (0.51^{***}) for Fm' and (463, 488) (0.47^{***}) and the equations (1) and (2) estimation of Y(II) and ETR is feasible qualitatively. When applying a linear regression to fit the spectral indices to the *in-situ* observations according to the equations in Table 4.6 and Table 4.7, quantitative estimation of Y(II) and ETR is possible. While the study area comprised mainly of stable reed, reed areas receiving environmental pressure appear at marginal values. This methodology could be used to map the physiological status of reed beds based solely on hyperspectral imagery.

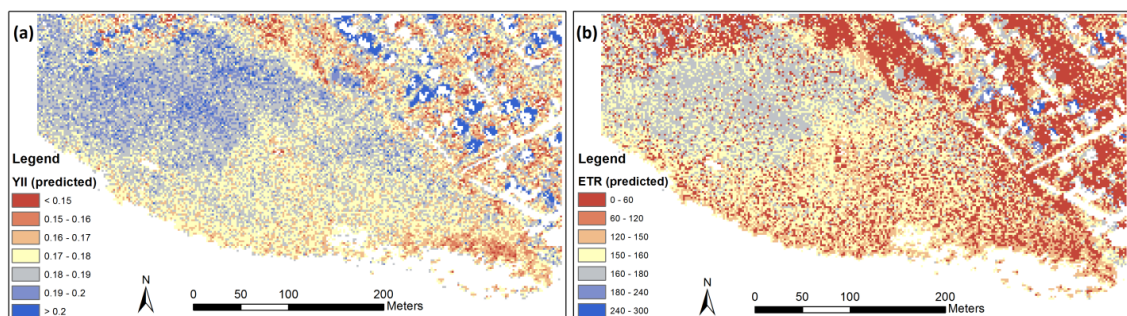


Figure 4.12: Y(II) (a) and ETR (b) estimation from the hyperspectral airborne dataset over the area of study at Kerekedi Bay, Lake Balaton according to the best correlation found in the reflectance RSI at the terrestrial part of the transect (left) and predicted values calculated from the maximum correlation of Fs and Fm'.

4.6 Limitations

When the findings from the leaf scale are used for interpretation of airborne imagery, some confounding factors need first to be considered. This is a limitation of a direct application of the findings from the field spectroradiometry to canopy level airborne imagery. Airborne reflectance measurements are made at a coarser scale and tend to average over a very large number of leaves, which may include healthy and diseased leaves, stems or even leaves from different species. Furthermore, shadows caused by the vegetation and orientation of the leaves are largely affecting the illumination conditions of canopy reflectance. In addition, in sparse vegetative conditions understory vegetation, ground or water signal can add in to the radiant exitance within a pixel.

Spectra of similar materials are recorded differently from the ASD and AISA sensors due to the fact that airborne remote sensing systems measure the amount of radiation reflected by an object which varies depending upon the sensitivity of the instrument, the wavelengths sampled, lighting geometry and atmospheric conditions (Roberts and Herold 2004) rather than reflectance. Another source of variation is the Bidirectional Reflectance Distribution Function (BRDF) which can be measured only indirectly (Schaepman-Strub et al. 2006). Although a compensation for that has not been attempted in the lack of multi-directional data, this might have introduced variations in the illumination of the area. Additionally, the spectral resolution of the airborne instrument was set to maximum (i.e. < 3 nm) during the acquisition of the data, which resulted to suboptimal Signal-to-Noise Ratio (SNR). Consequently, the marginal spectral regions will be noisy and the indices proposed from the field analysis that lay in these areas will not be applicable. Especially in regard to estimating biophysical parameters in optically complex waters, errors associated only to SNR can account as high as 80% for space borne hyperspectral sensors as demonstrated by Moses et al. (2012).

Furthermore, low radiometric resolution means high correlation between adjacent channels, and application of indices to the airborne data based on these channels will provides a noisy output. Hence the selection of the F_s and F_m' was based on the highest correlation among the indices which are not encountered in the regions 400-450 nm and 900-1000nm and they have a sufficient spectral difference of 10nm.

4.7 Conclusions

Spectroradiometric leaf reflectance and photophysiological parameters were measured *in-situ* over reed leaves in different inundation categories at vegetation peak in the mesotrophic Kerekedi bay. Despite the fact that correlation coefficient values are not as high as the correlation of spectral information with chlorophyll content or other directly measured biophysical parameters, chlorophyll fluorescence is the most representative measure of photosynthetic activity and therefore stress condition of the plant, and the R² was found to be statistically sufficient to support the estimation of leaf stress based solely on spectroscopic data. A strong correlation between narrowband spectral indices and chlorophyll fluorescence parameters has been found. This indicates the potential of *in-situ* hyperspectral data in assessing plant condition in real time, in agreement with Meroni et al. (2008). In this study it is suggested that for *in-situ* hyperspectral leaf measurements, the index (690, 633) provides the best coefficient correlation (0.76^{***}) for F_s in the stable deep water part of the transect and (545, 548) (0.82^{***}) for the F_m'. In the waterfront category, Y(II) correlates better with the band combination (473, 483) (0.62^{***}) and ETR with (493, 478) (0.65^{***}).

While these indices are spectrally very narrow and can be applied only when the instrument has a very high spectral resolution of 1nm, maps of the coefficient of determination can aid locating indices tailored to other remote sensing instrument. An application of the findings from the field data analysis to the airborne hyperspectral imagery on a study area at Lake Balaton,

Hungary presents actual estimation of Y(II) and ETR values over the reed bed under study. The indices identified were Fm': (699, 527) and Fs: (612, 516) for calculating Y(II) and PAR: (463, 488) for calculating ETR on the basis of mathematical equations (1) and (2). Hence the representation of photosynthesis from airborne hyperspectral image is feasible. It is worth mentioning that the indices proposed are largely found in the optical domain; this comes in contrast with a related study from Zarco-Tejada et al. (2002) who suggests an RSI index based on the red-edge domain for stress detection after analyzing information from inverting a radiative transfer model.

This research underpins the development of methods for estimating photophysiological parameters on *Phragmites* based solely on imaging spectroscopy and proposes optimal indices for evaluating the ecological status of reed based on spectroscopic data. Future work based on the findings could encompass samples from reed populations comprising of stable and die-back reed, which will provide die-back specific spectral indicators. Furthermore research on spectral indices beyond the 400-1000 nm spectrum would provide information on leaf-water absorption bands and lignin-cellulose features, which can also associate with environmental stress in aquatic vegetation.

Chapter 5 Aquatic vegetation mapping based on airborne hyperspectral and LiDAR data

5.1 Introduction

In chapter 4 it became apparent that proximate and field spectroscopic data are a reliable source of information at species and canopy level, however such a sample collection over large geographic areas, such as Lake Balaton, is cumbersome at frequent intervals. In chapter 5 we scale up the problem of detecting macrophytes and reed die-back categories from airborne imagery. Earth observation data is essentially the only way to monitor a large wetland, synergistically with field measurements. Nevertheless, classification of wetlands from remotely sensed imagery is a challenging task for scientists and practitioners alike. The high biodiversity encountered in the ecotone between the terrestrial and the aquatic ecosystems results in a complex spatial structure and a lack of concrete boundaries between habitat types. Typically, all available image sources and steps during the classification process have to be investigated and minor changes, for instance in the selection of the training set or the classification set-up, can alter the final outcome noticeably.

A pivotal role in vegetation mapping has been assigned to hyperspectral remote sensing, mainly due to the ability to discriminate vegetation types based on the spectral characteristics, which are largely correlated with vegetation species and cannot be easily differentiated with multispectral sensors. The importance of spectral reflectance in vegetation mapping has been realised as early as the 1970's (Carter and Anderson, 1972). Shive et al. (2010) report this advantage in a study trying to identify various types of wetland frog habitats, which is typically formed of ponds and lakes during June and July within areas of emergent vegetation. Burai et al. (2010) in a similar to my study effort separated 7 main vegetation classes in a wetland in

Hungary with overall accuracy 78% and kappa coefficient 0.63. In the same paper they stress the need to develop wetland specific spectral libraries.

LiDAR information has also been used mainly in forestry due to the ability to penetrate in the canopy cover and extract height and volumetric distribution of trees (e.g. Miller, 2001; Pedergrana et al., 2011; Puttonen et al., 2010; Jones et al., 2010). In low vegetation and habitat identification LiDAR capabilities are restricted, however efforts are continuing mainly by integrating LiDAR as auxiliary data. Anderson et al. (2010) have stressed the usefulness of LiDAR data in habitat architecture in a range of ecosystems by capturing fine spatial patterns.

Finally, aerial photos have been employed successfully in mapping the expansion of emergent vegetation (e.g. Weisner 1991) especially in the ages when space- and airborne spectrometers were not available. For instance, in the framework of reed die-back Krumscheid et al. (1989) attempted to locate reed regression through interpretation of aerial photographs. Object-based image analysis is prevailing lately in image processing of very high spatial resolution images, however most of the studies in the literature are employing satellite data and not much research has been done with airborne imagery which expands pixel resolution capabilities to less than 20 cm. Recently, sub-decimetre resolution UAV imagery was successfully used to identify aquatic vegetation in a lake site with 95.1% overall accuracy (Husson et al. 2014).

In this chapter the focus is on the classification scheme for mapping lakeshore vegetation with high spatial resolution data. An evaluation of the degree in which the different remotely sensed datasets (sources) are providing accurate information on the vegetation classes of interest is presented as well as a comparison of two popular classification algorithms in wetland mapping, namely Maximum Likelihood (ML) and Support Vector Machines (SVM).

5.2 Classification approaches

The advent of very high resolution imagery revealed new capabilities in earth observation, as well as challenges. One of the main complications associated with high spatial resolution is that the homogeneity of land cover, as it appears in pixels of medium resolution satellite images, is lost (Ehlers et al. 2003); as the spatial resolution of the image increases, individual scene elements are appearing and the spectral response of the scene becomes more varied, hence the representation of each class less consistent (Barnsley and Barr, 1996). Blaschke and Strobl (2001) state that when the pixel size becomes smaller than the size of the object, the derived object is made up of several pixels and the value of an individual pixel relates not to the character of the object but to its components. Therefore fine resolution provides high structural detail but also high contrast between neighboring pixels. This might lead to confusion on selecting representative spectra for the classification. Gong et al. (1992) and Johnsson (1994) reckon that classification of such high spatial resolution data does not necessarily translate into better results. For instance, Barker and King (2012) report that pixel-based classification produced more heterogeneous classes than the object based image approach when using orthophotographic imagery. As a consequence, it is still a challenge to investigate the means with which information at high spatial resolution can be transformed to accurate information on the ground.

5.2.1 Data sources

With data been available at increasing resolutions and decreasing cost, there is a tendency in the literature for fusing data types in order to increase accuracy in classification problems. Dalponte et al. (2008) provide a justified reason for fusing hyperspectral and LiDAR data in vegetation related studies and urge the need to develop advanced classification systems which will fruitfully exploit information provided by these two sources. The idea behind this assumption is that different data types acquired from different sensors

provide different sort of information, which to an extent are complimentary to each other. Hyperspectral sensors for instance record the spectral dimension which is sensitive for discrimination of species and surface types, while LiDAR is providing information on the dimensionality and structure of geometric surface properties (Koetz et al. 2007). Several sources have reported increased classification accuracy as a result of integration of data from multiple sensors. Jones et al. (2010) in a study mapping 11 tree species in a coastal region report an increase of user's accuracy when fusing data by 8.4% – 18.8% in comparison to solely hyperspectral classification. Johansen et al. (2010) present an automatic feature extraction of biophysical properties from LiDAR data and suggest that similar applications can be employed from natural resource management agencies. Swatantran et al. (2011) conclude that these two data types have many potential applications in ecological and habitat studies. Klemas (2011) recommends that the combined use of LiDAR and hyperspectral imagery can improve the accuracy of wetland species discrimination. Finally, Onojeghuo and Blackburn (2011) optimise the synergistic use of LiDAR and AISA hyperspectral for mapping reed bed habitats and report a significant improvement by 11% when a mask based on LiDAR dataset was incorporated.

With regards to the spectral information, plant pigment absorption is demonstrated at the spectral region of the visible domain and the red-edge; hence most vegetation studies are concentrating at this region. Nevertheless, the near infrared domain is associated to information on the plants cell structure and water content (figure 1.4) which is directly related to macrophytes environmental conditions. A few studies have been using synergistically the two datasets (e.g. Hunter et al. 2010a; Onojeghuo and Blackburn, 2011; Mewes et al. 2011; Lausch et al. 2013). Peerbhay et al. (2013) suggest that inclusion of near-infrared spectrum might provide increased potential in vegetation species mapping.

5.2.2 Classification algorithms

With the increasing availability of earth observation data, there comes a large vault of source information in offer; however, more data does not necessarily translate into better analysis (Fernandez-Prieto et al. 2006) as long as the schemes to extract the information are not optimized. Appropriate image processing is an essential aspect of any classification of remotely sensed data to a meaningful categorical map (Lu and Weng, 2007).

Pixel based classifiers have traditionally been the means to classify remote sensing imagery from very early years. These classifiers are making categorical judgments based solely on the spectral information of each individual pixel (Gong and Howarth, 1990). Unsupervised classification algorithms are implemented on the assumption that no knowledge of the study area exists; hence the result is spectrally consistent, however the thematic categories assigned after classification are not necessarily associated to real classes of objects. Supervised classification on the other hand relies on the indication of representative polygons to be used for the classification from the user. The most widely used supervised classifier in remote sensing has probably been the ML which assumes however that the statistical function of each class in each band follows the Gaussian distribution. SVM developed by Vapnik (1995) is a supervised non-parametric statistical learning technique that has become popular the last years due to increasing citation in scientific literature (e.g. Brown et al. 2000; Keramitsoglou et al. 2006; Chi et al. 2008). SVM performs well in cases with a small number of training samples, which is one of the problems encountered often in remote sensing classifications. Mountrakis et al. (2011) review the use of SVM in remote sensing and stress the superiority of the classifier over most of the traditional algorithms. Several papers have confirmed the superiority of SVM over alternative classifiers applied on hyperspectral data (Melgani and Bruzzone, 2004; Pal and Mather, 2004; Camps-Valls and Bruzzone, 2005; Oommen et al. 2008; Dalponte et al.

2008; Hunter et al. 2010a; Kuo et al. 2010; Bahria et al. 2011) and in land use/land cover classification schemes (Pal and Mather, 2005; Boyd et al. 2006; Keramitsoglou et al. 2006; Dixon and Candade, 2008; Dalponte et al. 2009). Yang et al. (2008) reports on the suitability of SVM when comparing the application of six classifiers on airborne hyperspectral imagery for the detection of giant reed. Furthermore, SVM seems to eliminate the Hughes effect (the predictive power reduces as the dimensionality increases), which is crucial for high-dimension hyperspectral data (i.e. Hughes phenomenon: (Hughes, 1968)) (Pal and Mather, 2004; Oommen et al. 2008).

Classification integrating the textural information of a scene has also been widely used. Object Based Image Analysis (OBIA) (Lang and Blaschke, 2006; Blaschke 2010) is a sub-discipline of GIS devoted in partitioning imagery into meaningful objects (Hay and Castila, 2006) embracing information extracted from the spatial relationship of the image elements. Barker and King (2012) and Elatawneh et al. (2012) are some examples of studies reporting superiority of OBIA methodology. Kernel based Re-Classification (KRC) is a texture-based algorithm developed by Barnsley and Barr (1996) taking into consideration the frequency and the spatial arrangement of the class labels of the pixels and has provided accurate results in fine scale habitat mapping with fine resolution imagery (Keramitsoglou et al. 2005).

Nevertheless, while other vegetation canopies (e.g. trees) are composed of plants which vary by species, height, size and texture, macrophytes are encountered most often in assemblages of species with more homogeneous spatial characteristics, leaving no other option of discrimination other than their spectral response. Hyperspectral information is the main pillar of information for such discrimination. In the context of reed mapping, Gilmore et al. (2009) report high classification accuracies due to unique high near-infrared reflectance in the early fall. However there still exists the need to

investigate the algorithms best suited to map macrophytes with high spatial resolution data.

5.3 Area of study

A large data pool of airborne imagery, is available for the complete shore line of Lake Balaton. However, due to inconsistencies in date acquisition, flight orientation, atmospheric conditions, data size and processing time it was deemed impossible to combine the whole dataset in one image and define as the area of study the whole Lake. It was decided to follow a site-specific approach for applying the classification approaches and focus on the Bozsai bay, described in chapter 3.2.1 and its relative position to Balaton Lake is depicted in figure 3.1. Two adjacent hyperspectral scenes comprise the reed bed and neighbouring grasslands, open fields, roads, settlements, potato farmlands and trees.

5.4 Airborne remotely sensed data

Airborne platforms are a means for acquiring remotely sensed imagery offering advanced capabilities in comparison to the satellite operational systems. Their main advantage is the flexibility to operate in time and space; therefore ideal atmospheric and illumination conditions at the time of image acquisition are assured, and the availability of data depends only on the weather conditions, unlike satellite systems which are following an established orbit. Functional operation of an airborne remote system can be rapid, making it ideal for emergency situations and unexpected events, such as floods, earthquakes and landslides. Furthermore, the low altitude from which imagery is acquired translates into high spatial resolution, the magnitude of which depends on the absolute altitude of the aircraft. Likewise, atmospheric interaction is restricted at the lowest part of the atmosphere and hence radiometric resolution is typically higher than satellite systems. Malthus and George (1997) suggested from very early that airborne remote sensing has a strong potential for monitoring freshwater macrophyte species.

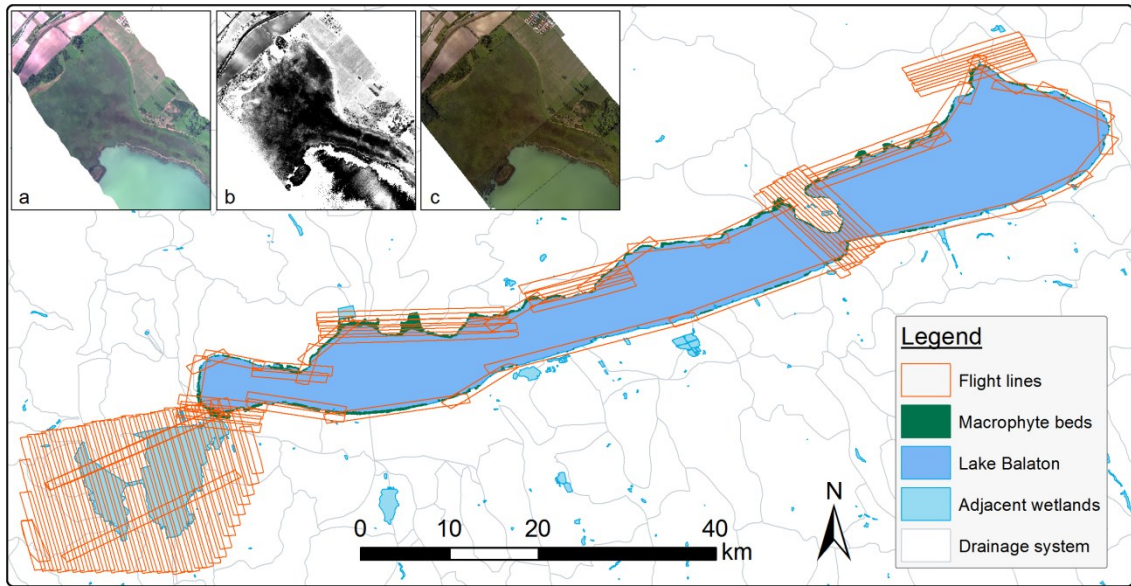


Figure 5.1: Flight lines of the airborne campaign undertaken during August 2010 (main image) and sample of the concurrently collected (a) hyperspectral, (b) LiDAR and (c) orthophotos dataset (inset image).

Table 5.1: Specifications of remote sensing instruments used to collect simultaneously hyperspectral, LiDAR and orthophotos during 21st – 26th Aug 2010 on Lake Balaton, Hungary under clear sky conditions.

Data type	<i>Hyperspectral</i>	<i>Hyperspectral</i>	<i>Discrete return LiDAR</i>	<i>RGB photography</i>
Instrument	<i>AISA Eagle</i>	<i>AISA Hawk</i>	<i>Leica ALS50-11</i>	<i>Leica RCD105</i>
Ground pixel size at 1550 m absolute altitude	<i>1.05 m</i>	<i>2.10 m</i>	<i>4 returns maximum (resampled)</i>	<i>17.5 cm</i>
Swath at 1550 m relative altitude (1445 true altitude)	<i>992m (38° fov)</i>	<i>614m (24° fov)</i>	-	<i>948 m</i>
Spectral domain	<i>400 – 970 nm</i>	<i>970 – 2450 nm</i>	<i>1064 nm</i>	<i>Visible</i>
Number of bands	<i>253</i>	<i>256</i>	<i>Maximum four discrete returns</i>	<i>3</i>
Spectral resolution	<i>3.3 nm</i>	<i>8.5 nm</i>	-	<i>RGB</i>
FWHM	<i>2.20 – 2.44</i>	<i>6.31</i>	-	-
Radiometric resolution	<i>12 bit</i>	<i>14 bit</i>	-	<i>16 bit</i>
Signal to Noise Ratio (SNR)	<i>1250:1 (max)</i>	<i>800:1 (max)</i>	-	-

An extensive EUFAR airborne campaign was undertaken between August 21st and 26th 2010 by the Airborne Research and Survey Facility (ARSF, Gloucester, U.K.) vested in the Natural Environment Research Council (NERC). The platform used was a Dornier 228-101 research aircraft able of

flying up to 15000 ft altitude at a maximum speed of 160 knots true air speed when performing scientific operations. The aircraft flew at 1550m true altitude and was equipped with an Inertial Measuring Unit/Global Navigation Satellite System (IMU/GNSS) providing information on the aircrafts' position and orientation respectively. The survey covered the whole Lake Balaton and the Kis Balaton, an adjacent wetland on the south west of the main Lake (Figure 5.1). The dataset (Table 5.1) comprises of concurrently recorded hyperspectral (400-2500 nm), discrete return LiDAR and orthophotos (Zlinszky et al. 2011).

5.4.1 Hyperspectral imagery

Hyperspectral reconnaissance mapping systems inherit a considerably higher spectral resolution in comparison to conventional spaceborne sensors. They have been suggested for vegetation related projects in several studies (Shive et al. 2010; Dalponte et al. 2008) based on the fact that the fine segmentation of the sensors' spectral response is able to provide suitable information for discriminating vegetation attributes at associations and species level. Currently most remotely sensed data are acquired from sensors carried on aircrafts. Only two hyperspectral space-borne imagers are orbiting around the earth, namely CHRIS on PROBA-1 and Hyperion on Earth Observing-1, but more will become available in the near future, such as the Environmental Mapping and Analysis Program (ENMAP), Prisma and the Hyperspectral Infrared Imager (HyspIRI). With the launch of missions setting in orbit state-of-the-art multispectral and hyperspectral sensors, imaging spectroscopy dataset are gradually becoming wider available.

The hyperspectral imagery was collected from an airplane-mounted Specim's AISA dual system (Spectral Imaging Ltd., Oulu, Finland) incorporating the nadir-looking sensors Eagle and Hawk as in similar studies (Artigas and Yang, 2005; Jensen et al. 2007; Dalponte et al. 2008; Shafri and Hamdan, 2009; Yang and Artigas, 2009; Burai et al. 2010; Onojeghuo and Blackburn, 2011). The sensors recorded incoming radiation cumulatively in 509 bands from 400 to

2450nm with Full-Width Half-Maximum (FWHM) 2.20 – 2.44 and 6.32 for Eagle and Hawk respectively and delivered a spatial resolution of 1.5m at 1550m true altitude (Table 5.1). The angle between the line of sight of the sensors and the zenith was 180° since they are nadir looking instruments. The data were delivered in 1b ENVI BIL data format with metadata attached in HDF4.

5.4.2 LiDAR

Airborne Laser Scanning (ALS), widely known as LiDAR, is the technique of estimating the range of objects from the sensor with the use of pulsed laser. LiDAR systems can deliver either discrete-return pulses or full-waveform. In discrete-return typically one pulse from the top of the object and a second from the bare ground are reflected, based on which the Digital Surface Model (DSM) and the Digital Terrain Model (DTM) respectively can be calculated. In full-waveform systems, a more detailed representation of the canopy structure can be achieved. Downward-looking LiDAR from airplane platforms has lately been used in the context of wetlands for discriminating vegetation species from marsh components (Rosso et al. 2006), classifying wetland elements based solely on LiDAR data (Brennan and Webster, 2006), estimating the inundation level below forest canopy based on the amplitude of the LiDAR signal (Lang and McCarty, 2009), synergistically with high resolution satellite data to improve wetland distinction (Maxa and Bolstad, 2009) and categorizing vegetation species in Lake Balaton, Hungary (Zlinszky et al. 2012).

A maximum of 4 discrete-returns of an 83kHz (1064 nm) pulse were recorded from a Leica ALS50 compact laser scanning system and delivered in ASCII point cloud format. At the last calibration before the 2010 campaign LiDAR data were judged against Ground Control Points (GCPs) and a mean error of 3.1 cm and SD of 2.2 cm at an altitude of 1350 m was estimated. Further

information on the LiDAR system specifications can be found at Zlinszky et al. (2012).

5.4.3 Orthophotos

Aerial photography allows for very high spatial resolution depiction of land characteristics in a manner that is used extensively by practitioners to visualize stereoscopically species and classes of interest (Caylor, 2000). Orthophotos were one of the first techniques used to map macrophytes (e.g. Malthus et al. 1987; Ferguson et al. 1993; Rutchey and Vilchek, 1999), nevertheless photo-interpretation is a subjective application and can become time- and consequently cost-consuming in an operational context (Jensen et al. 1986).

True-colour images were recorded from a 39 megapixel Leica RCD105 medium format digital camera. The CCD instrument of the camera recorded radiation in three channels in the visible domain and delivered images in 16-bit TIFF format, with approximate ground resolution of 17.5 cm from 1550 m aircraft true altitude. In the specific setup, the data were extracted via two separate channels from the camera; due to the sensitivity of the instruments to temperature a discontinuity of spectral response at the centre of the image is noticeable. For this reason the data provider considered the image pixel data values not appropriate to use for scientific radiometric measurements. Furthermore, the main disadvantage of aerial photography is the need to mosaic the individual photos to cover a larger area (Carleer and Wolff, 2004), especially considering the relatively small area covered in images acquired from low-altitude flights. This pre-processing step results to further radiometric degradation.

A total of 1940 aerial images were collected and archived. Geometric registration on a UTM projection was implemented by the Vienna University of Technology. This dataset was used synergistically with expert knowledge for selecting training and validation sets from the hyperspectral images in the

processes of classification and accuracy assessment respectively, while the use of radiometric values has been dismissed.

5.5 Data-processing

Remote sensing sensors record incoming radiation in the form of a Digital Number (DN). Nevertheless from the DN to the actual quantitative information about features on the earth's surface, there are numerous factors that can alter the value of the electromagnetic signal. First the DN values are calibrated to radiance values, which is the quantitative representation of the incoming radiation at the sensor. This procedure account for sensor defects, system noise and variations in the scan angle of an airborne system and is accomplished by applying a gain and offset to the DN values, according to the specification of the instrument.

The second and most significant factor for hyperspectral sensors is the influence from the atmosphere, which absorbs and scatters unequally for different wavelengths. Above wetlands, the effect of the water vapour is most prominent. Radiance image contains the overall radiation reaching the sensor, including radiation reflected from the surface of the earth, the clouds, the atmosphere directly and through scattering and is affected by the solar radiation intensity properties. In the lack of concurrently acquired field data, the ideal way to isolate the surface reflectance signal is by removing the unwanted atmospheric and illumination effects through the application of correction models, which require information on the atmospheric conditions at the time of acquisition.

The third contribution in distorting the image information is influence from the solar illumination dependencies, terrain roughness and the BRDF. Atmospheric correction as implemented in various commercial packages will account for the first two factors when integrating a DEM in the calculations.

Geometry is reconstructed based on flight information collected concurrently with the image.

This pre-processing of airborne imagery is a time and effort consuming procedure and requires specialized software and user skills, however is critical for the quality of the final product. The processing order of the adjustments does not affect considerably the output image according to Xu and Wu (2012). An approach for correcting the artefacts apparent in the specific images to compensate for radiometric, atmospheric and geometric inaccuracies was followed (Figure 5.2). First, cross-track illumination correction was applied to remove the glitter found in several images. Then atmospheric correction was implemented based on a radiative transfer model. The geometric registration was applied integrating a DEM derived from the concurrently acquired LiDAR data. Finally the water pixels were removed and the two images were subset and mosaicked around the reed bed at the Bozsai bay.

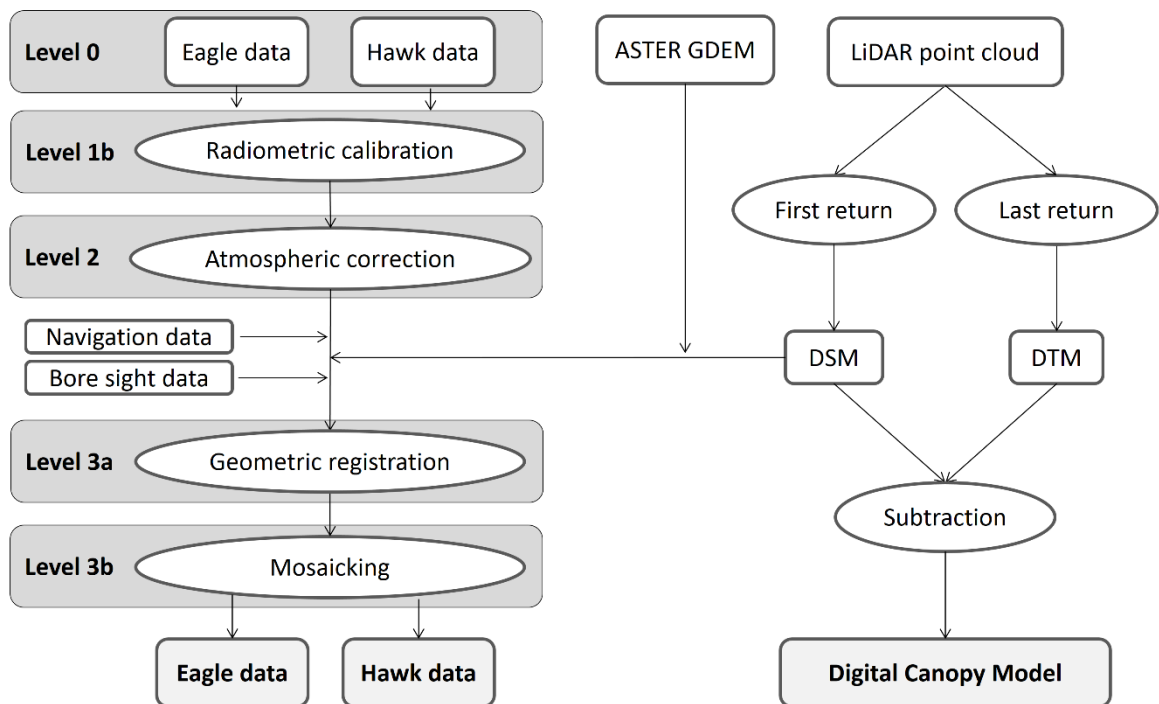


Figure 5.2: Pre-processing flowchart of the hyperspectral and LiDAR datasets.

5.5.1 Radiometric correction and bands exclusion

Radiometric correction is necessary to compensate for the effects of the atmosphere, off-nadir surface reflection and glint. Vignetting effects, instrument scanning, off-nadir view angle and sun reflection as well as other illumination effects can affect the image non-uniformly and are generally regarded as cross-track illumination effects (ITT Visual Information Solutions, 2009). In the used dataset the main contributor has been the sun reflection when solar azimuth was diverging from the aircraft orientation (Table 5.2) and illumination conditions have therefore not been isotropic. As a result, a glitter at the edge of the images is apparent in several images and especially in the flight with North-South orientation such as this above Tihany peninsula (Figure 5.1).

Table 5.2: Solar illumination conditions at Lake Balaton (lat: 46.9127. lon: 17.8369) during time acquisition as calculated from the National Oceanic and Atmospheric Administration (NOAA) Solar calculator (url: <http://www.esrl.noaa.gov/gmd/grad/solcalc>).

<i>Flight number (Julian day)</i>	<i>Date (dd/mm/yyyy)</i>	<i>Time (GMT)* (hh:mm)</i>	<i>Solar noon</i>	<i>Solar azimuth (in degrees)</i>	<i>Solar elevation (in degrees)</i>
233	21/08/2010	13:40 - 14:18	12:52	200.16 – 214.55	53:71 – 50:71
234	22/08/2010	13:31 - 14:28	12:52	196.51 – 217.89	53:85 – 49:37
235	23/08/2010	12:56 - 14:02	12:51	181.97 – 208.53	54:48 – 51:47
238b	26/08/2010	10:25 - 11:38	12:50	127.95 – 151.32	42:30 – 50:38
238d	26/08/2010	14:29 - 15:29	12:50	217.70 – 235.52	47:91 – 40:45

*Local time is +1 hour from the GMT and observes the Daylight Saving Time.

The quality of the available data degrades at the low and high wavelength edges of both Eagle and Hawk sensors. The bands for Eagle were restricted to the bandwidth 450-900 nm and for Hawk to 1000-2400 nm. Along-track mean values were then calculated and plotted to stress the variation in illumination differences across the image lines. Cross-track illumination correction was applied on the samples of each image. A 2nd order polynomial function and an additive correction method were fit. The output of the

process (i.e. .bsq file) was converted to a .bil file format which is an acceptable format for the atmospheric correction plug-in.

5.5.2 Atmospheric correction

As solar electromagnetic radiation propagates through the earth's atmosphere, it interacts with gases and aerosols through absorption, reflection and scattering. This process is wavelength dependent and therefore is especially noticeable in hyperspectral imagery. Below 290 nm almost the entire incoming solar radiation is attenuated by molecular oxygen (O_2) and ozone (O_3). In the optical spectral region atmosphere does not absorb considerably, while in the infrared radiation is absorbed moderately by water vapour (Seinfeld et al. 2012) at bands centred at 940 nm, 1140 nm, 1380 nm and 1880 nm, as well as by molecular oxygen (O_2) at 760 nm, CO_2 at 2010 nm and 2080 nm and other gases such as carbon monoxide (CO), nitrous oxide (N_2O) and methane (CH_4) (Van der Meer, 2001). Apart from gases, tropospheric aerosols contribute to reflection. However and contrary to the atmospheric gases, their spatial and temporal distribution fluctuates strongly as a consequence of their week-long lifetime (Kaufman et al. 2002).

To add in the complexity, the adjacency effect also affects recorded radiation, a term referring to the occurrence of optical path interference between reflectances from adjacent surface materials (Burazerović et al. 2013), with a prominent example being that of coastlines, where existence of water and land, two materials with different spectral behavior, are merging. More specifically, a proportion of photons reflected from the one surface will be dispersed in the air due to atmospheric backscattering, and thus can be deflected in the radiance path of the second material, as recorded by the instrument. This spectral contamination is prominent especially at short wavelengths in scenes containing large reflectance contrast (Richter et al. 2006). Such a case is macrophytes growing in Lake Balaton, the water of which is characterized by high reflectivity in the optical domain due to the

suspended sediment, submerged macrophytes and high chlorophyll concentration. Several studies have attempted to develop algorithms for correcting the phenomenon (i.e. Santer and Schmechtig, 2000, Sanders et al. 2001, Sterckx et al. 2011) nevertheless popularly the effect is accounted for in established atmospheric correction models.

The correction is deemed necessary if the radiation reflected by the target material on the ground is to be estimated. Atmospheric correction was implemented in the Fast Line-of-sight Atmospheric Analysis of Spectral Hypercubes (FLAASH), which is part of the ENVI atmospheric correction module (ITT Visual Information Solutions, 2009). FLAASH is a first-principles atmospheric correction tool based on a modified version of the MODTRAN4 radiation transfer code (Matthew et al. 2000) to correct wavelengths in the visible through near-infrared and shortwave infrared regions up to 3 μ m. MODTRAN is a well-established atmospheric radiance transfer code reported to outperform other radiation transfer codes (Staenz et al. 2002) and on which the major atmospheric correction commercial software is based on (i.e. FLAASH and ATCOR-4). Another atmospheric correction method considered was the QUick Atmospheric Correction (QUAC) which is a more automated and approximate method than FLAASH in the sense that the algorithm does not feed on information from the user about the illumination conditions but rather derives it from within the scene. QUAC also does not account for the adjacency effect neither scene average visibility and requires several material to be encountered in the scene, including a dark pixel. QUAC yielded similar results (Figure 5.3), however due to the simplicity of the underlying theory, it was decided to implement the more sophisticated FLAASH algorithm. After taking into account the time period of the airborne campaign and the geographical position of the study area, the mid-latitude summer atmospheric model was used. No aerosol model was accounted for as in the scene there is a lack of dark pixels, which is necessary for the

implementation of aerosol integration (Kaufman et al. 1997). Instead, the aerosol amount was estimated by the visibility which was set to 50 km in agreement with the atmospheric conditions on the day of the acquisition and confirmed by the local METAR report. The CO₂ mixing ratio was set to 404 ppm. Spectral polishing was used with a width of 9 spectral channels. The ground elevation at the Lake is approximately 80 m above sea level and can be assumed constant for the purpose of atmospheric correction as the terrain around the Lake is in principle flat. The rest of the input for FLAASH was taken from the navigation file recorded during the flight campaign for each individual scene. A list of the parameters used and further explanation is provided in Appendix 4.

A total of 188 images were corrected with water absorption intensity calculated from each individual image from bands including the 820 nm and 1135 nm wavelength for eagle and hawk instruments respectively. Overall the atmospheric correction provided typical spectral responses for the

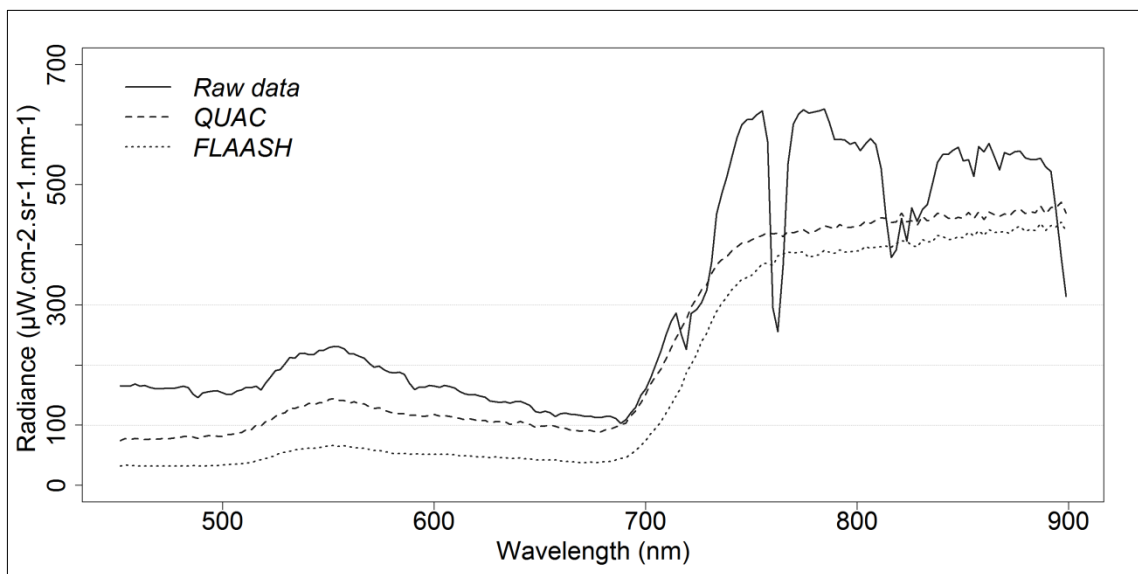


Figure 5.3: Comparison of the spectral signature of a reed pixel from the raw data, *QUick Atmospheric Correction (QUAC)* and *Fast Line-of-sight Atmospheric Analysis of Spectral Hypercubes (FLAASH)*

vegetation contained in the image (Figure 5.3). No artefacts were apparent, due to the clear sky conditions at the time of image acquisition and the lack of open water absorbing bodies around the mesotrophic Kerekedi bay.

5.5.3 Geometric correction

Airborne collected data differ from satellite products in the sense that during image acquisition the airplane is moving through the atmosphere and small fluctuations in the motion of the aircraft can result in large distortions in the raw image. For this reason, simultaneous acquisition of the aircraft's motion variables is necessary in order to place the measurements into a precise geographical reference (Bange et al. 2013). These variables include altitude, attitude (yaw, pitch and roll angles), position and velocity of the aircraft and are acquired from on board integrated IMU/GNSS devices. Furthermore, the comparatively short distance between the aircraft and the target introduces systematic distortion in the image as well as unsystematic depending on the terrain roughness, which deems necessary to take into account the topography of the area if geodetic accuracy is to be achieved.

The geometric registration was applied with the open-source Airborne Processing Library software v3.1.4 (Warren et al. 2014). The algorithm is designed to geographically register the raw imagery by taking into account bore-sight information recorded during the flight. The DSM extracted from the concurrently acquired LiDAR dataset with missing values filled-in from the Advanced Spaceborne Thermal Emission and Reflection Radiometer (ASTER) Global DEM (NASA LP DAAC, 2001) was used to increase the geometric precision. The two images were registered at the Projected Coordinate System UTM (Zone 33N) of the WGS 1984 Datum in a 1.5m x 1.5 m grid (Figure 5.4).

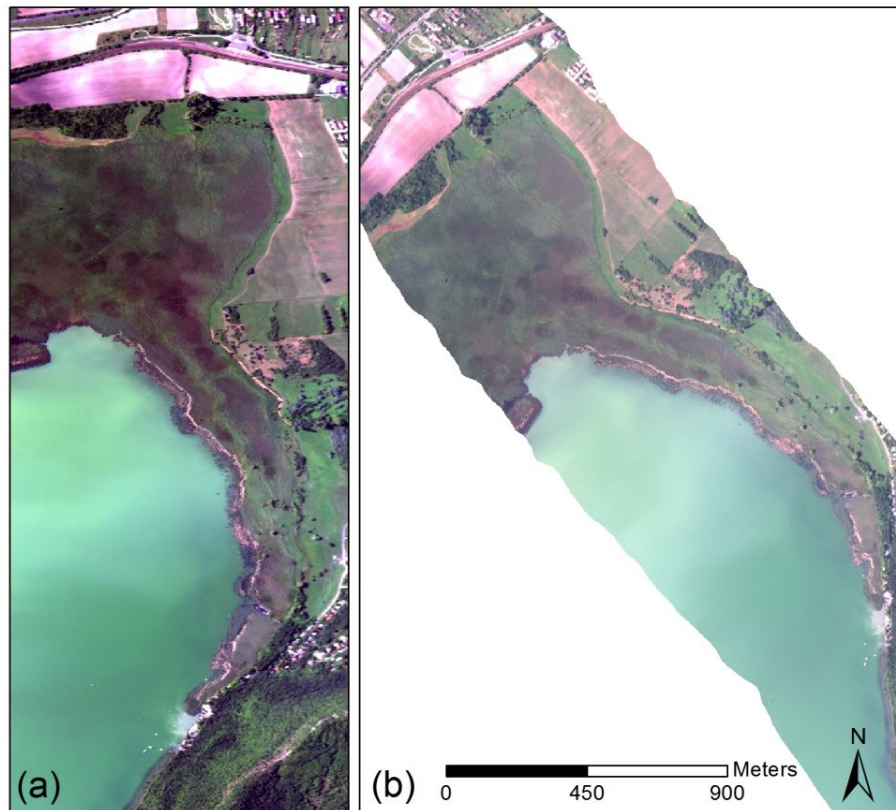


Figure 5.4: Raw image as delivered by the data provider (a) and geometrically registered image on UTM 33N (b) depicting the east part of the study area.

5.6 Training and validation set

Chen and Stow (2002) make a thorough comparison of common training strategies for classification used in the literature and reckon that the training approach can affect the classification result. Moreover, they claim that the training has a higher influence on the result when applied on fine rather than coarse resolution images. Information on vegetation species and geolocation of pure areas formed the basis for selecting the training and validation sets. For the reed-specific categories, close collaboration was established with ecologists with experience of the study area. A set of polygons was selected on the hyperspectral image representing 7 emergent-vegetation classes of interest. A stratified random sampling (probabilistic method of sampling) was followed for the reason of minimizing variability within different zones of the image area. The sampling area was divided in large zones and each one was assigned a number of sample units proportional to its area. The position of the units

then was defined randomly and the size of the samples was proportional to the size of the class they represent. The concurrently acquired aerial photography was used to assure coherency of the polygons. The set was divided in two groups, one used for training the classifier and the other for validating the results.

5.7 Methodology

5.7.1 Input layers

The input layers for the classification process have been prepared based on the Eagle, Hawk and LiDAR data sources as of Figure 5.5. The first input layer was extracted from the Eagle dataset by removing the noise from the hyperspectral images. The second input layer was created in a similar manner from the Hawk data. The third image input for the classification is a layer stack of indices as identified from previous chapters and others employed frequently in the literature. Finally the last input layer is based on the 3 PCs of the Eagle image and the DCM as extracted from the LiDAR data. PCs were used as representative bands inheriting most of the information from the raw image and was preferred over the MNF eigenvalues as MNF main function is to reduce the noise rather than compacting the information of data. The steps for each of the 4 datasets is described in detail in the sub-chapters below.

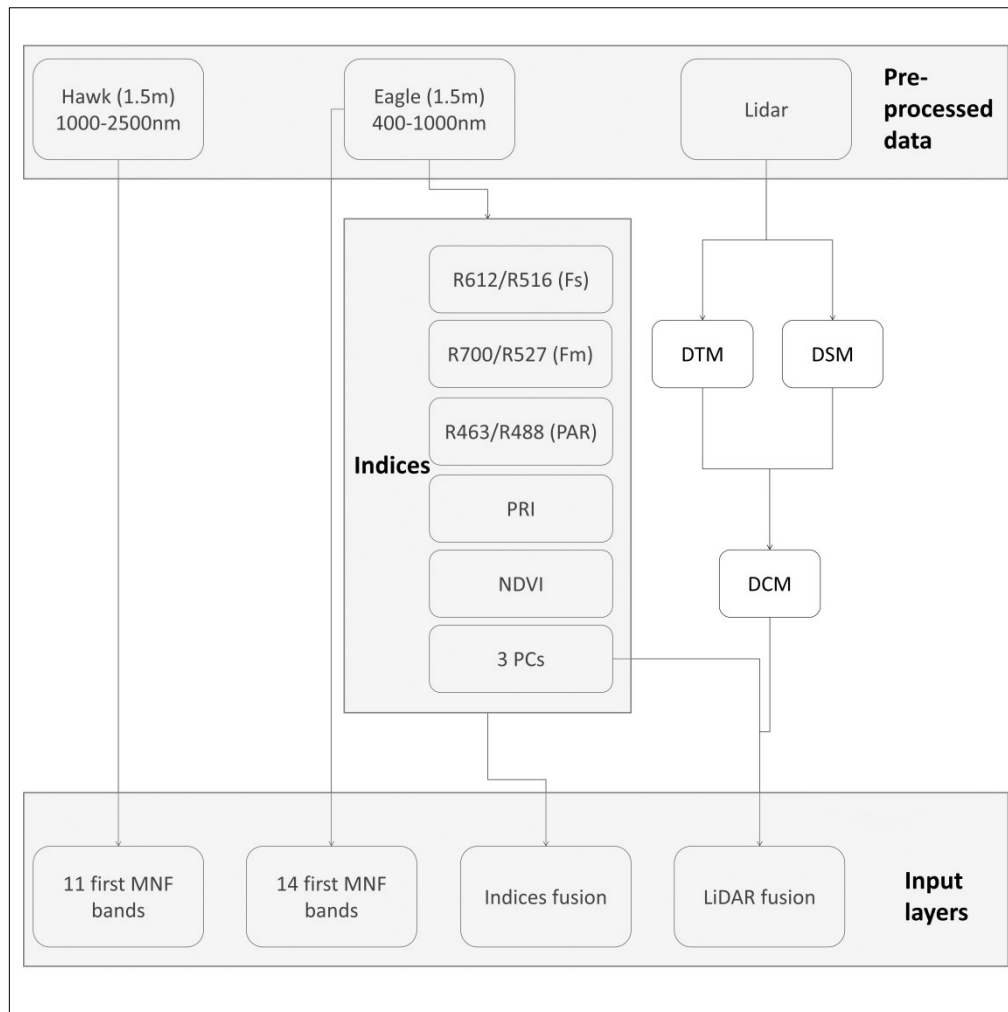


Figure 5.5: Workflow indicating the preparation of input layers for the classification process based on the Eagle, Hawk and LiDAR pre-processed datasets.

5.7.1.1 Eagle data

Due to the nature of hyperspectral data, the spectral bands are highly correlated and the dataset in whole contains a large degree of redundancy. A Minimum Noise Fraction (MNF) transformation (Green et al. 1988) can be applied to eliminate the noise, reduce the dimensionality of the data and hence the computational requirements without important loss of information. Subsequently, the components (i.e. eigenvalues) of the transformation which are unaffected from noise can be inversed back to the real hyperspace. Nevertheless, these transformations are not improving the performance, but just speed up the classification, as indicated by Musci et al. (2008) who found no considerable differences when classifying AISA hyperspectral imagery

based on the original scene, the forward MNF and the inversed MNF. Controversially, Pandey et al. (2014) in a study using similar data found that the classification accuracy improves in case ML algorithm is applied on the MNF in comparison to the total number of bands.

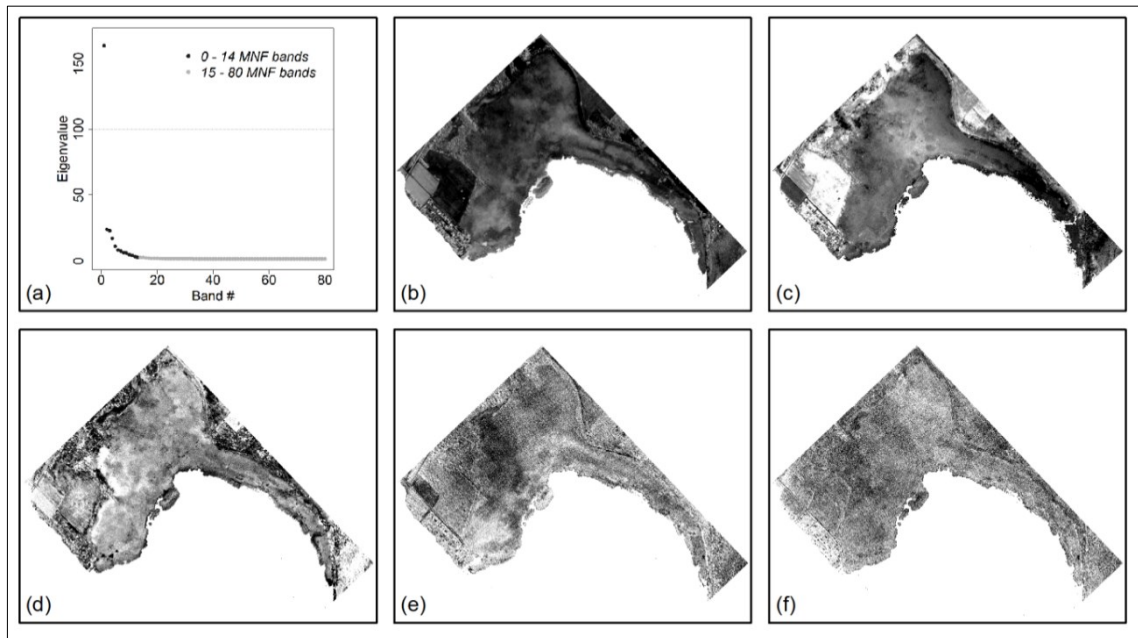


Figure 5.6: Eigenvalues of the Eagle image (a) and depictions of the Minimum Noise Fraction (MNF) transformation corresponding to bands number 1 (b), 4 (c), 9 (d), 14 (e) and 16 (f). Noise is considerably higher than the information content after band 14 and hence all the bands after this threshold have been dropped.

Forward MNF transformation was applied on the Eagle image. Based on the eigenvalues and the corresponding MNF bands, the first 14 transformed bands were selected as the threshold where information is still more prominent in the image in comparison to noise (Figure 5.6).

5.7.1.2 Hawk data

Hawk data have been provided along with the Eagle imagery; nevertheless the coverage of the whole reed bed is not complete due to its narrower swath and adjacent images do not overlap. This appears as a wide missing stripe at the edge of the individual images. Furthermore, Hawk suffers from regular dropped frames, resulting in missing lines in the image. The integration of the Hawk data in the methodology was attempted provided the best results and

evaluate the usefulness of the infrared spectral domain in wetland vegetation mapping. A similar methodology as for Eagle data was followed for processing the Hawk data. Bands between 1336-1462nm and 1791-1967nm have been excluded as they are largely affected by atmospheric absorption. The MNF was then calculated and the first 11 eigenvalues selected in a similar procedure as described in the previous part (Figure 5.7).

5.7.1.3 Joint classification of LiDAR and Eagle data

LiDAR data can indirectly provide information on height and structure of the canopy, which is an independent and complimentary to spectroscopy source of information for classes on the ground. In this part the difference of the first and last LiDAR returns, representing the material height, was used with the hyperspectral data to classify the area of interest. In a similar attempt Dalponte et al. (2008) merged hyperspectral information with elevation and intensity channels from LiDAR resulting to a slight increase in classification accuracy.

First and last discrete LiDAR returns were used to extract the DSM and DTM respectively. Subsequently the Digital Canopy Model (DCM) was calculated by subtracting the DTM from the DSM at a 2.5m raster grid. Despite the fact that the DCM derived from moderate-density LiDAR data underestimates the canopy height (Zlinszky et al. 2012), it is however associated to the canopy height characteristics. Thereafter the DCM of the two adjacent stripes were mosaicked and resampled to 1.5m pixel size. Finally the first 3 Principal Components (PCs) from the Eagle image were extracted and combined with the DCM to enhance the information content.

5.7.1.4 Indices fusion

A classification scheme based on products derived from the hyperspectral image was attempted. The first three PCs from the Eagle image were calculated. The narrowband empirical indices NDVI and PRI (table 4.2) were

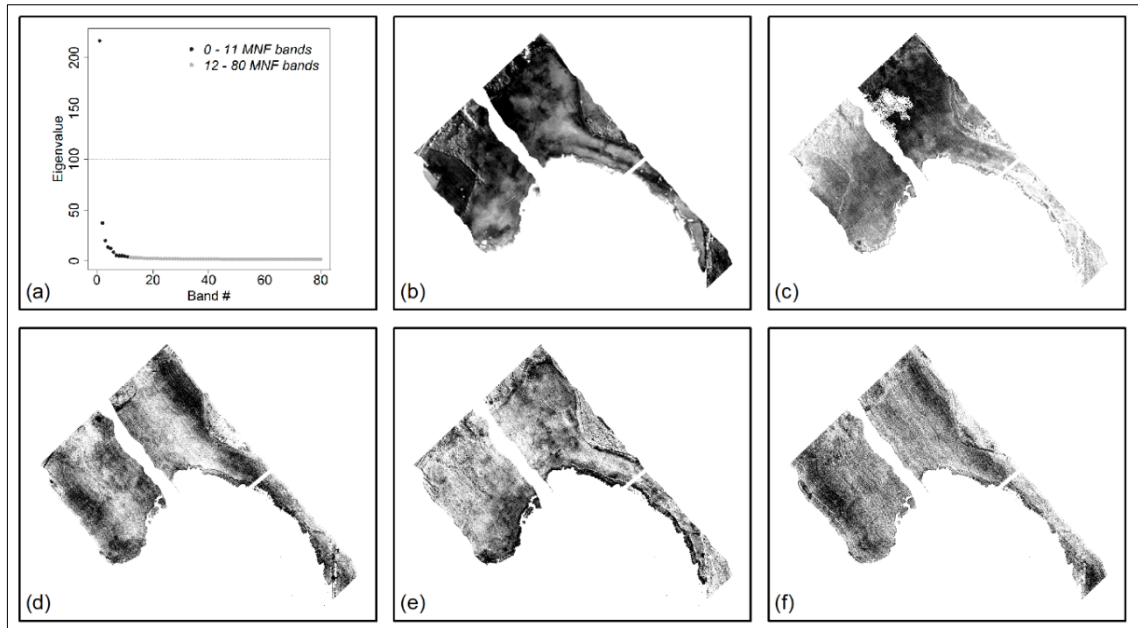


Figure 5.7: Eigenvalues of the Hawk image (a) and depictions of the Minimum Noise Fraction (MNF) transformation corresponding to bands number 1 (b), 4 (c), 9 (d), 11 (e) and 12 (f). Noise is considerably higher than the information content after band 11 and hence all the bands after this threshold have been dropped.

extracted.

These are indices heavily used in vegetation related studies as they are associated to vegetation characteristics. Furthermore, the band ratios representing the F_s , F_m and PAR per findings of the fluorescence analysis in chapter 4 were derived. The individual layers were combined in a composite image.

5.7.2 Reed bed masking and mosaicking

The interest of this study lays in the reed bed of the Bozsai bay. The macrophytes encountered in this natural reserve inherit a diverse and complex structure, and it was decided to narrow the focus on the emergent macrophytes of this area rather than a more broad vegetation types on the lake shore. In essence trees, lake water, bare ground and manmade materials, some of which are part of the natural reserve, were excluded however and scientifically speaking it is not challenging as identification of trees and other

generic classes has already been demonstrated widely in the literature successfully.

A mask from the DCM was derived by selecting all pixels with values between 0.3 and 3m, range which represents typical macrophytic vegetation. The hyperspectral image was subset with the mask to isolate pixels of macrophytes. Finally, a mosaicking procedure was undertaken to stitch together the two images. No colour balancing was used and a feathering distance of 100 pixels was assumed.

5.7.3 Classification

Several processing steps were iteratively tested and concluded to the methodological workflow presented in Figure 5.8. The classification procedure was conducted identically for the 4 different input layers developed and using the same training dataset. For each case, a two-step classification was followed. The image was first classified based on the main macrophytes encountered in the area, namely *Phragmites*, *Typha*, *Carex* and grassland. The *Phragmites* class was used to subset the original input layer again, and this subset image was then classified based on the dominance of *Phragmites* in the patch according to the classes of dominant, co-dominant, sub-dominant and reed die-back. Subsequently, the two classification products were merged with the sub-classes of *Phragmites* substituting the generic class *Phragmites* in the main classification. This scheme was applied twice, first based on the ML algorithm and a second time based on SVM for each input layer. Expert knowledge and the concurrently acquired orthophotos during the field campaign were used to conduct the accuracy assessment based on an error matrix. Image processing and classification were realized with the software ENVI 5.0 (Exelis Visual Information Solutions). The cartographic production was carried out in ArcMAP 10.0 (Environmental Systems Research Institute, Inc.).

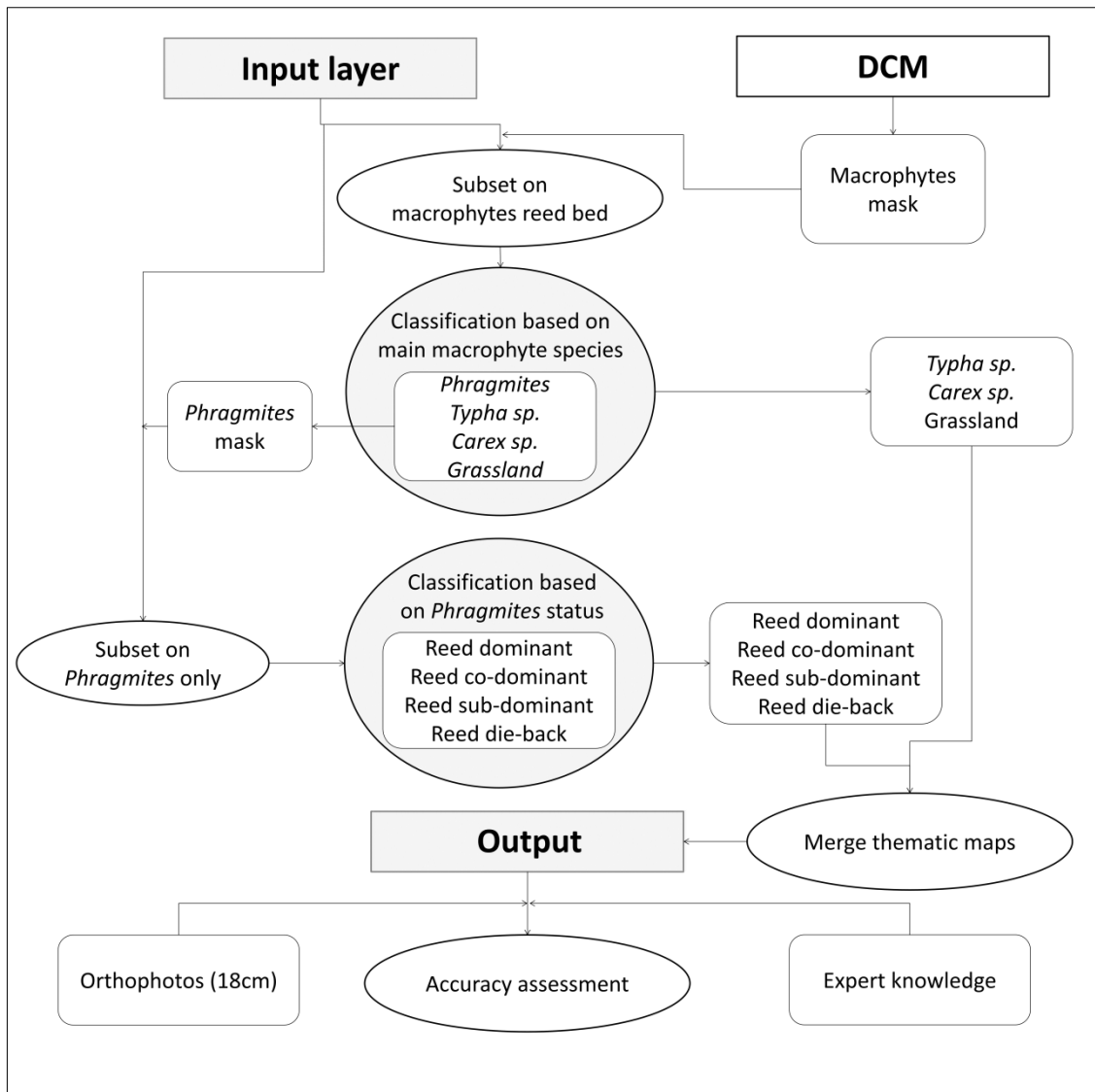


Figure 5.8: Workflow of the classification scheme developed through iterative classifications and evaluations for mapping emergent vegetation. The two step approach involves classification of the image based on the main macrophyte species (*Phragmites*, *Typha*, *Carex* and grassland) and subsequently isolation of the *Phragmites* class and classification of the latter based on the dominance of *Phragmites* (dominant, co-dominant and sub-dominant) and reed die-back. At the final stage the two classification results are merged with the *Phragmites*-specific classification overlaid over the macrophyte species map. The result is assessed quantitatively based on expert knowledge and concurrently acquired orthophotos.

5.7.4 Accuracy assessment

Remotely sensed imagery is especially suitable for vegetation mapping purposes, however the output of the classification procedure has no credibility unless its accuracy is assessed and quantified (Chen et al. 2004). A mainstream methodology for accuracy assessment was followed based on an error matrix

(contingency table) as suggested by Congalton (1991). An approach presented by Dalponte et al. (2008) in a study employing similar data has been adapted. As already mentioned, *in-situ* floristic information synergistically with the concurrently acquired high resolution ortho-photos and expert knowledge were combined to create the validation polygons. More specifically, based on the validation set collected as described in section 5.6, the validation polygons were overlaid on the high resolution ortho-photos. The latter was used together with expert-knowledge to decide on the class information for the polygon; Given the homogeneity of the polygon, which was taken into account when designing the sample polygons, the ascribed classes were considered are the truth data. The accuracy assessment was carried out thereafter comparing in essence the resultant thematic map with the truth data.

5.8 Results and discussion

Figure 5.9 and Figure 5.10 present the results of the classification based on ML and SVM algorithms respectively and for each data source. Table 5.3, Table 5.4, Table 5.5 and Table 5.6 present the error matrix of the accuracy assessment for each data source independently. The maps contain solely classes of emergent macrophytes typically encountered around Lake Balaton. The overall accuracy ranges from 41.79% for the LiDAR dataset with ML classification to 88.64% for the Eagle dataset with SVM. In general SVM provides better results than ML, a fact which is also observed in a similar study mapping submerged macrophytes by Hunter et al. (2010a). Some errors exist between the different classes of reed and especially the classes encountered at the edge of the reed bed, i.e. reed die-back and sub-dominant reed.

Reed in the central part of the reed bed was classified as co-dominant and botanical surveys support this finding, while at the edges (both terrestrial and waterward) of the reed bed and especially in the thin sliver at the west reed

seems to compete with other macrophyte species. The main class (i.e. *Phragmites*) typically grows in the same environment with other macrophyte species and grasses, and hence the dominant class in all classification results is reed co-dominant which occupies the main reed bed. Co-dominant reed is very accurately classified by SVM in the cases of Eagle and Indices layers with 96% and 97% producer accuracy. Pure reed (i.e. reed dominant) is encountered at a small part of the Lake shore east of the *Typha* island, part which is correctly classified with both ML and SVM in all data sources except LiDAR; in the case of SVM this part is only slightly containing reed dominant pixels while with ML a large part of the image is classified as reed dominant which is incorrect. The canopy structure information contained in the LiDAR does not assist in the classification of this class. SVM shows a higher accuracy for Eagle and Indices data sources (84% and 68% respectively) in comparison to ML, however when classifying Hawk data ML has an advantage of producer accuracy 60% over 40% for SVM. It is worth noting that reed dominant has the lowest accuracy across macrophytes, as homogeneous and pure patches of *Phragmites* are not frequently encountered in the Bozsai bay and to an extent they always contain a degree of other macrophyte species within a pixel. Reed sub-dominant contains reed as a minority within other macrophytes, and is encountered at the edge of the reed bed, where terrestrial vegetation and grass grow in favorable conditions. ML and SVM are classifying the east part of the reed bed as reed sub-dominant as well as fringe areas of the reed bed. One important difference is found on the north part of the reed bed where there is a sliver of grassland as indicated by SVM classifications of Eagle image and the Indices image, however ML classifies this part mainly as reed subdominant which is incorrect. ML always provide better producer accuracy than SVM, while the opposite is realized for the case of user accuracy; in essence this means that SVM results show a realistic map of sub-dominant reed, however several pixels from the validation set have not

been labeled correctly by SVM and therefore some pixels of this class are misclassified as other classes on this map.

Reed die-back is encountered at the waterward edge of the north-east part of the reed bed mainly as fragmented patches of water reed. Reed die-back is confused mainly with reed sub-dominant and to a less extent with *Typha*, as it is mainly neighboring with the first and the fringe of the *Typha* island is misclassified as die-back in several cases in regard to the latter. This also means that spectrally, and at 1.5m spatial resolution, die-back is different than the more homogeneous classes of dominant and co-dominant reed. SVM overestimates the extent of reed die-back in the case of Eagle data in comparison to the ML results, while the opposite is the case for the Indices composite image. LiDAR data in the case of ML presents an unrealistic result while SVM indicates realistically the extend of the die-back reed; this might be attributed to the fact that ML is not performing well when classifying multi-source images while SVM is not confused with this approach. In overall ML seems to perform weaker when classifying datasets of different data types, such as the LiDAR or the Hawk data integration with Eagle imagery.

It is worth commenting that the literature is controversial on the capability of imaging spectroscopy on mapping vegetation stress. Swatantran et al. (2011) for example mention that hyperspectral data can provide information such as stress on canopy state, while Leckie et al. (2005) attempted unsuccessfully to include unhealthy classes of species in a classification of old growth temperate conifer forest canopies. In this study representative polygons of reed die-back areas were selected, however reed die-back is a dynamic phenomenon characterizing the physiological condition of a plant and not a vegetation category with concrete boundaries. As such reed die-back areas are indicated by the fragmentation of the reed patch rather than the physiological status of the plant in this classification scheme. For a more representative estimation of the physiological status, spectral indices can show the degree to which the area

is stable as it was demonstrated in chapter 4. However when integrating the die-back class in a macrophytes classification scheme, it provides an indication of fragmented and sparse reed patches which are under unfavourable environments at the period of image acquisition and hence potentially associated to reed die-back conditions.

Typha, occupying the small island in the centre of the image, is correctly classified by all ML results, however in the cases of the indices and LiDAR layers several *Typha* patches are indicated in the reed bed. In the SVM classification the Eagle classification provides similar to the ML results, the Indices and LiDAR layers indicate the outer buffer zone as reed co-dominant. *Typha* is often confused with other assemblages of *Phragmites*, fact which is also reported in a similar study from Maheu-Giroux and de Bloisa (2005) in a similar study using colour aerial photography. *Carex* is encountered at the west of the reed bed, classified correctly only in the case of Eagle data for both algorithms with 82% and 94% user accuracy respectively; however when using the Hawk data ML does not classify any pixel as *Carex* and instead replace it with *Typha*. SVM on the other hand presents an area restricted in size. In the case of Indices and LiDAR, there is a fragmented distribution in other parts of the image as well for the ML classification, while SVM does not classify *Carex* pixels. Again the most representative source for pure macrophytes species is coming from Eagle.

Grassland is a class differing in the height of the foliage and hence it would be expected to be distinguished from the LiDAR composite image, however this is not the case for ML (producer accuracy 6%); SVM only partially classifies the sliver on the north part of the image (producer accuracy 39%). ML in all cases does not perform satisfactorily in the case of grassland as it is most often classified as reed sub-dominant. This fact in some very parts is true as the transition from the reed bed to the grassland does not have a concrete boundary, however it is a smooth transition occupying a buffer zone where

the two species co-exist in different proportions. SVM applied on the Eagle dataset is outperforming considerably for the grass class with 92% producer accuracy and 97% user accuracy.

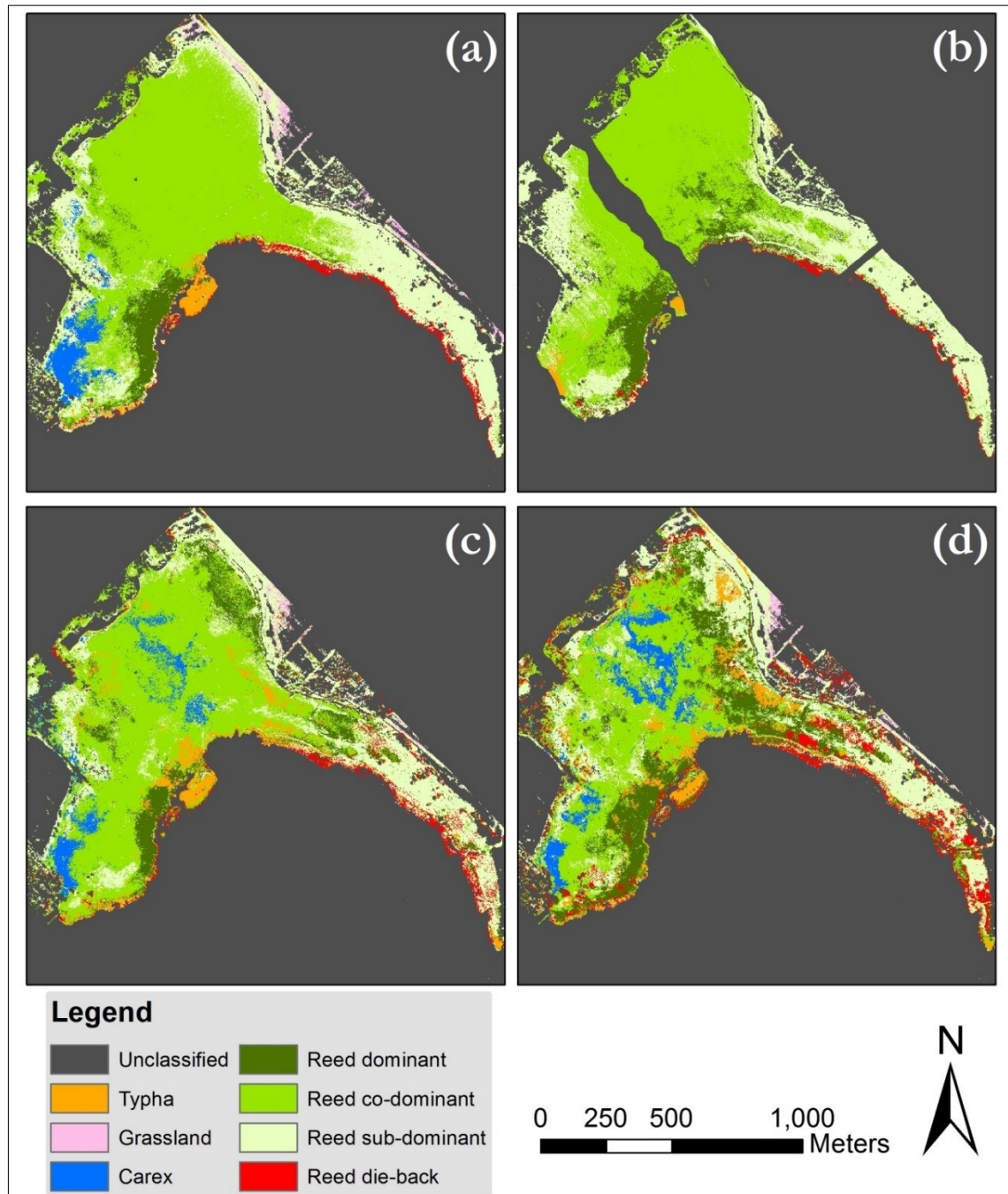


Figure 5.9: Thematic maps from the ML classification of the Eagle (a), Hawk (b), Indices from Eagle (c) and LiDAR combined with Eagle PCs of the macrophyte main species and Phragmites associations at Bozsai bay, Lake Balaton.

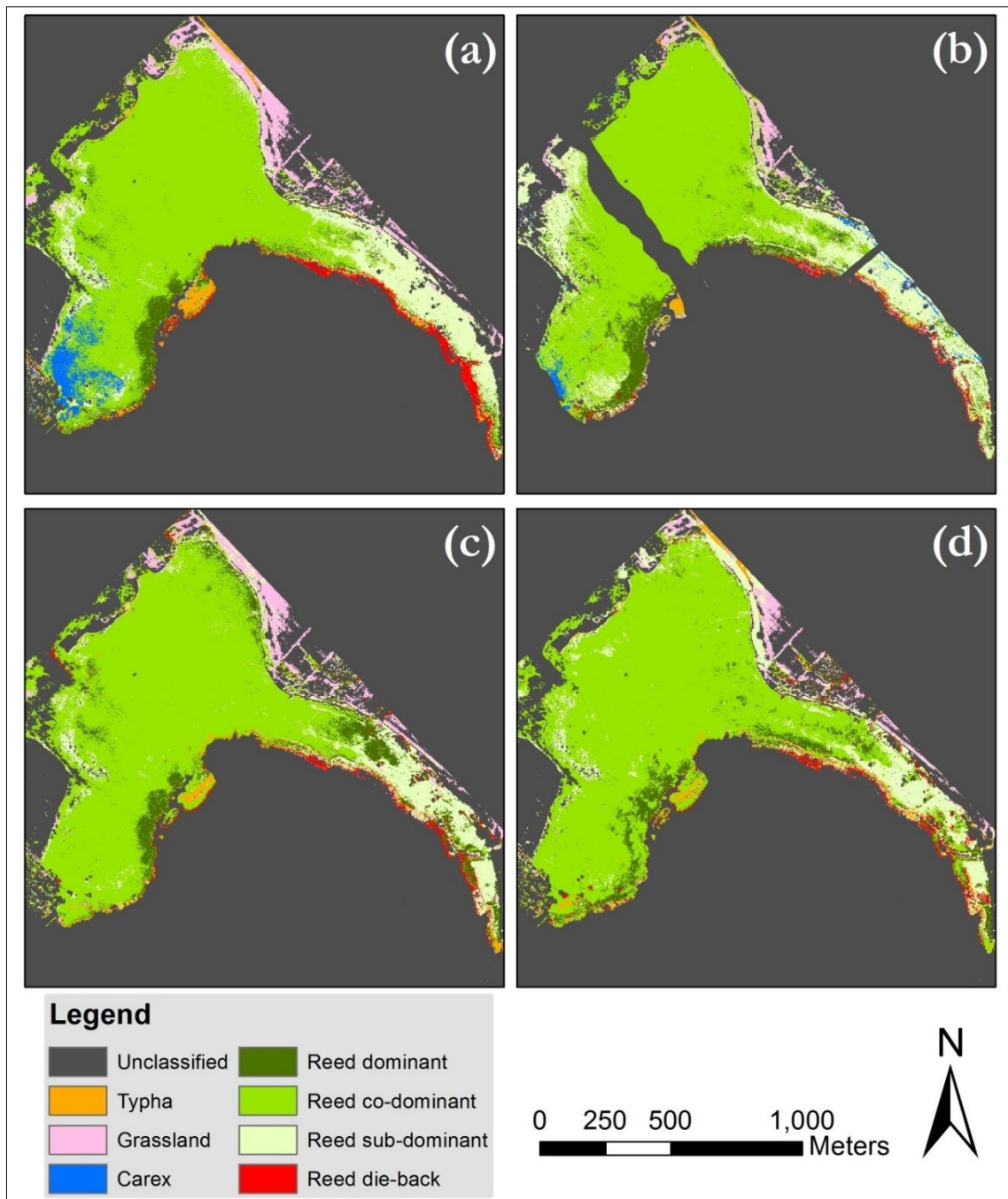


Figure 5.10: Thematic maps from the SVM classification of the Eagle (a), Hawk (b), Indices from Eagle (c) and LiDAR combined with Eagle PCs of the macrophyte main species and Phragmites associations at Bozsai bay, Lake Balaton.

Table 5.3: Confusion matrix illustrating the results of the classification on Eagle data with Maximum Likelihood (ML) and Support Vector Machines (SVM) algorithms. All values except the Kappa coefficient are in percentages.

	<i>Typha</i>		<i>Grassland</i>		<i>Carex</i>		<i>Reed dominant</i>		<i>Reed co-dominant</i>		<i>Reed sub-dominant</i>		<i>Reed die-back</i>		<i>User Accuracy</i>	
	<i>ML</i>	<i>SVM</i>	<i>M</i> <i>L</i>	<i>SV</i> <i>M</i>	<i>M</i> <i>L</i>	<i>SV</i> <i>M</i>	<i>M</i> <i>L</i>	<i>SV</i> <i>M</i>	<i>M</i> <i>L</i>	<i>SV</i> <i>M</i>	<i>M</i> <i>L</i>	<i>SV</i> <i>M</i>	<i>M</i> <i>L</i>	<i>SV</i> <i>M</i>	<i>M</i> <i>L</i>	<i>SV</i> <i>M</i>
<i>Typha</i>	95	54	-	-	-	-	6	1	0	0	0	1	1	5	81	75
<i>Grassland</i>	-	-	25	92	-	-	-	-	-	0	-	0	-	1	10	97
<i>Carex</i>	-	-	-	-	95	84	-	-	0	0	3	0	-	-	82	94
<i>Reed dominant</i>	-	19	-	0	-	-	65	84	6	2	0	2	-	3	43	65
<i>Reed co-dominant</i>	-	10	3	1	1	14	0	11	86	96	4	14	-	1	98	92
<i>Reed sub-dominant</i>	1	2	69	6	4	1	24	0	7	2	89	75	26	13	71	92
<i>Reed die-back</i>	4	15	2	-	-	-	3	2	1	-	2	6	68	72	49	37
<i>Producer accuracy</i>	95	54	25	92	95	84	65	84	86	96	89	75	68	72		
<i>Overall Accuracy</i>	83.22 %	88.64 %														
<i>Kappa Coefficient</i>	0.72	0.8														

Table 5.4: Confusion matrix illustrating the results of the classification on Hawk data with Maximum Likelihood (ML) and Support Vector Machines (SVM) algorithms. All values except the Kappa coefficient are in percentages.

	<i>Typha</i>		<i>Grassland</i>		<i>Carex</i>		<i>Reed dominant</i>		<i>Reed co-dominant</i>		<i>Reed sub-dominant</i>		<i>Reed die-back</i>		<i>User Accuracy</i>	
	<i>ML</i>	<i>SVM</i>	<i>M</i> <i>L</i>	<i>SV</i> <i>M</i>	<i>M</i> <i>L</i>	<i>SV</i> <i>M</i>	<i>M</i> <i>L</i>	<i>SV</i> <i>M</i>	<i>M</i> <i>L</i>	<i>SV</i> <i>M</i>	<i>M</i> <i>L</i>	<i>SV</i> <i>M</i>	<i>M</i> <i>L</i>	<i>SV</i> <i>M</i>	<i>M</i> <i>L</i>	<i>SV</i> <i>M</i>
<i>Typha</i>	63	59	3	0	29	-	0	0	0	0	0	0	-	2	44	79
<i>Grassland</i>	-	15	-	69	-	-	-	3	-	0	-	1	-	4	-	79
<i>Carex</i>	-	-	-	-	-	30	-	0	-	0	-	4	-	-	-	56
<i>Reed dominant</i>	4	4	-	-	-	-	60	40	22	8	0	1	9	26	15	23
<i>Reed co-dominant</i>	29	20	46	26	38	57	14	42	63	85	2	3	5	1	87	89
<i>Reed sub-dominant</i>	4	1	50	5	33	12	13	8	15	6	94	86	20	8	63	82
<i>Reed die-back</i>	-	1	-	-	-	-	12	5	-	-	1	2	41	34	43	46
<i>Producer accuracy</i>	63	59	-	69	-	30	60	40	63	85	94	86	41	34		
<i>Overall Accuracy</i>	64.44%	79.49%														
<i>Kappa Coefficient</i>	0.45	0.65														

Table 5.5: Confusion matrix illustrating the results of the classification on Indices dataset with Maximum Likelihood (ML) and Support Vector Machines (SVM) algorithms. All values except the Kappa coefficient are in percentages.

	<i>Typha</i>		<i>Grassland</i>		<i>Carex</i>		<i>Reed dominant</i>		<i>Reed co-dominant</i>		<i>Reed sub-dominant</i>		<i>Reed die-back</i>		<i>User Accuracy</i>	
	<i>ML</i>	<i>SVM</i>	<i>M</i> <i>L</i>	<i>SV</i> <i>M</i>	<i>M</i> <i>L</i>	<i>SV</i> <i>M</i>	<i>M</i> <i>L</i>	<i>SV</i> <i>M</i>	<i>M</i> <i>L</i>	<i>SV</i> <i>M</i>	<i>M</i> <i>L</i>	<i>SV</i> <i>M</i>	<i>M</i> <i>L</i>	<i>SV</i> <i>M</i>	<i>M</i> <i>L</i>	<i>SV</i> <i>M</i>
<i>Typha</i>	57	20	-	-	-	-	23	10	10	1	2	1	3	3	12	26
<i>Grassland</i>	-	-	7	68	-	-	-	-	-	0	-	0	-	4	10 0	97
<i>Carex</i>	-	-	-	-	81	-	-	-	4	-	0	-	-	-	57	-
<i>Reed dominant</i>	7	9	1	1	-	-	55	68	2	0	13	20	2	7	33	34
<i>Reed co-dominant</i>	30	68	3	9	13	97	5	18	74	97	8	21	1	1	93	83
<i>Reed sub-dominant</i>	-	-	84	18	6	3	8	0	9	1	70	54	31	37	63	84
<i>Reed die-back</i>	6	3	5	3	-	-	7	2	-	0	5	2	58	43	32	45
<i>Producer accuracy</i>	57	20	7	68	81	-	55	68	74	97	70	54	58	43		
<i>Overall Accuracy</i>	69.0 5%	77.69 %														
<i>Kappa Coefficient</i>	0.52	0.59														

Table 5.6: Confusion matrix illustrating the results of the classification on LiDAR fused dataset with Maximum Likelihood (ML) and Support Vector Machines (SVM) algorithms. All values except the Kappa coefficient are in percentages.

	<i>Typha</i>		<i>Grassland</i>		<i>Carex</i>		<i>Reed dominant</i>		<i>Reed co-dominant</i>		<i>Reed sub-dominant</i>		<i>Reed die-back</i>		<i>User Accuracy</i>	
	<i>ML</i>	<i>SVM</i>	<i>M</i> <i>L</i>	<i>SV</i> <i>M</i>	<i>M</i> <i>L</i>	<i>SV</i> <i>M</i>	<i>M</i> <i>L</i>	<i>SV</i> <i>M</i>	<i>M</i> <i>L</i>	<i>SV</i> <i>M</i>	<i>M</i> <i>L</i>	<i>SV</i> <i>M</i>	<i>M</i> <i>L</i>	<i>SV</i> <i>M</i>	<i>M</i> <i>L</i>	<i>SV</i> <i>M</i>
<i>Typha</i>	41	8	1	-	0	-	17	1	11	0	3	2	2	6	9	14
<i>Grassland</i>	-	-	6	39	-	-	-	-	-	-	-	0	-	0	10	96
<i>Carex</i>	-	-	-	-	73	-	-	-	4	-	1	-	-	-	54	-
<i>Reed dominant</i>	33	7	0	-	0	-	63	51	38	10	17	7	3	6	9	20
<i>Reed co-dominant</i>	2	80	1	4	17	95	13	44	31	87	5	35	-	4	88	76
<i>Reed sub-dominant</i>	5	0	92	57	8	5	1	1	13	2	65	50	29	28	56	73
<i>Reed die-back</i>	19	5	-	0	1	-	4	1	3	0	7	3	60	49	18	45
<i>Producer accuracy</i>	41	8	6	39	73	-	63	51	31	87	65	50	60	49		
<i>Overall Accuracy</i>	41.79%	68.72%														
<i>Kappa Coefficient</i>	0.26	0.43														

5.9 Conclusions

A set of classification results derived from the application of ML and SVM algorithms on 4 different airborne data sources has been presented. Hyperspectral Eagle, Hawk and LiDAR data have been used independently and synergistically to map emergent macrophytes at a nature protected area on Lake Balaton. A detailed representation of most classes under study is achieved, a result which can be attributed to the concurrent very high spectral and spatial resolution of the imagery.

Significant pre-processing is required to be applied on the airborne hyperspectral data before undertaking classification, which might prove to be time and effort consuming when handling large datasets. While classification techniques can be automated given the availability of a training set, pre-processing is site- and image-specific and the intervention of the user is essential. Field data are an important part of mapping aquatic vegetation; a classification based solely on the airborne imagery and without the contribution of information on the ecological status of the training samples would provide incomprehensible results in this study.

Phragmites is growing in the same environment with other macrophytes and grasses, especially in the terrestrial part of the reed bed. Hence, there is an abundance of reed within a pixel. In this study a categorical approach of reed abundance and other macrophytes species as well as grass was adhered. The reed sub-classes show a high degree of separability, with the most prominent class (i.e. co-dominant reed) exhibiting 96% producer accuracy and 92% user accuracy (SVM applied on Eagle data). Reed die-back is the most challenging case of vegetation mapping and unique since it refers to a state of deterioration of the vegetation species rather than species or association of species. Nevertheless, fragmentation at the edge of the reed bed is associated to the consequences of the die-back conditions and hence the extent to which the reed bed is affected. SVM outperforms ML, mainly in regard to the class of grassland and provides higher overall accuracy in all data sources, reaching an 89% for Eagle data. The joint classification of LiDAR data with the first 3 PCs from the Eagle image did not perform satisfactorily (overall accuracy 69%, kappa coefficient 0.43). Macrophytes associations and species encountered in a typical reed bed on Lake Balaton are identified using the MNF transformation of high spatial resolution hyperspectral data, and especially in the visible and near-infrared spectrum.

Chapter 6 Sentinel-2 image simulation based on airborne hyperspectral data

6.1 Introduction

As the previous chapters have shown, airborne and handheld hyperspectral systems provide the opportunity to study in detail the ecophysiology of a lakeshore environment. This chapter is examining what might be achieved from a satellite platform and more specifically from the upcoming Sentinel-2 superspectral mission.

Airborne and handheld hyperspectral systems deliver the capability of acquiring imagery with fine spatial, spectral and radiometric characteristics; nevertheless, the financial cost per unit area is high and routine provision of information over large geographic areas can become expensive. Moreover, airborne systems lack a consistent viewing geometry as the recorded DN values are affected by the airplane's relative orientation to the sun. For example Griffin and Burke (2003) when studying AVIRIS scenes acquired at different times during a flight found that for a two-hour flight centred in time at solar noon, the retrieved reflectance errors exceeded ± 0.10 at visible wavebands. With regard to the image's spatial aspect, orientation relative to the earth surface can introduce considerable nonlinear geometric distortions. Finally, data products for scientific applications are commonly delivered in low level format, inheriting the above misrepresentations and requiring a tedious pre-processing procedure. Especially in the case of hyperspectral imagery, it is critical to compensate for radiometric, atmospheric, geometric and terrain distortions (Perry et al. 1998).

For the aforementioned reasons airborne data are not regularly employed for operational purposes; instead satellite images have been commonly used for earth observation. Reduced pre-processing, artefacts and expense to acquire satellite products are the main reasons of popularity amongst scientists and

practitioners. However the trade-off between the fixed spectral, spatial and temporal resolution does not always allow for certain applications, such as perhaps the fine-scale macrophyte mapping demonstrated in the last chapter. For instance Landsat-8, one of the most popular satellites for remote sensing, would provide multispectral data in 30m pixel resolution, which is too coarse for fine scale habitat mapping. WV-2 on the other hand, the satellite with the finest spatial resolution for commercial use, would lack the temporal resolution of Landsat as the surface coverage potential of the satellite is too small to overpass the same area in regular intervals.

Sentinel-2 is a twin-satellites mission for supporting the Copernicus programme developed by ESA. The open access and free of charge policy adapted for the data products is anticipated to foster the use of remotely sensed data for routine environmental applications. The satellites will offer a high spatial resolution in the spectral domain 443 – 2190 nm for land monitoring services (part of which wetlands are) and the first satellite is planned to be launched in June 2015. Enhanced specifications include the high spatial resolution up to 10m for selected bands and the integration of narrowband channels in the red-edge region (ESA 2012). One of the main advantages of Sentinel-2, which makes the satellite highly suitable for monitoring and inventorying purposes, is the combination of the wide swath and the frequent revisiting time.

The developed provisions of Sentinel-2 in comparison to satellites already in orbit will potentially deliver new capabilities in natural habitats mapping. For example, Hedley et al. (2012) in a study simulating Sentinel-2 data report an increased performance in comparison to Landsat ETM+ when mapping tropical coral reefs. Richter et al. (2011) test the potential of Sentinel-2 in estimating LAI of three contrasting agricultural crops and suggest that Sentinel-2 can deliver quality biophysical parameter estimation through the PROSPECT_SAILH model.

In a similar manner, it is important to investigate well in advance of the launch of Sentinel-2 the potential of the output product in order to assess the capabilities, examine the compatibility with satellites already in orbit, ensure continuity of image provision with similar specifications and accelerate the operational use of the forthcoming imagery. New sensors such as the Sentinel-2 are equipped with super spectral resolution, trying to bridge this gap. It is yet to be seen whether the addition of extra bands in combination with the very high spatial resolution suffices for fine scale aquatic vegetation mapping.

This study aims to evaluate the potential of the forthcoming Sentinel-2 satellite in mapping lakeshore vegetation at fine scale. The simulation of the high spatial resolution (i.e. 10m and 20m) bands of Sentinel -2 was presented at the VNIR (Visible and Very Near InfraRed) region of the spectrum from the airborne hyperspectral imagery acquired concurrently with AISA Eagle and Hawk instruments over the east part of Bozsai bay. The spectral and spatial aggregation are derived separately as well as the final Sentinel-2 simulated product and the reed bed area in the main thematic categories of vegetation and main materials is classified. A comparison of the products with the classification of the original AISA image is revealing the effect of spectral and spatial downscaling and the information lost through this process when mapping lakeshore vegetation.

6.2 Dataset specifications

Sentinel-2 multispectral sensors are recording incoming radiation in the visible and near infrared spectrum at bands designed to provide continuity to pre-existing multispectral satellite missions such as the Landsat. An additional 4 narrow bands in the red-edge region are included and with the aim to provide enhanced capabilities in vegetation studies (e.g. Delegido et al. 2011). The spatial resolution depends on the channel and is set to 10m, 20m and 60m (Table 6.1), the latter being bands for the purposes of atmospheric correction

from information within individual images, step necessary in several vegetation studies deriving biophysical parameters, time series analysis or transferability studies. The bands' resolution at 10m is at a scale where fine pattern information on aquatic vegetation may be achieved (Figure 6.2).

The study area is defined as the east part of the Bozsai bay, presented and classified in the previous chapter (Figure 6.1). The data used for the simulation are the concurrently acquired Eagle and Hawk hyperspectral overlapping stripes over the East part of the bay, also presented in an earlier chapter. Both datasets inherit a higher spectral, spatial and radiometric resolution compared to the Sentinel-2 announced specifications (ESA Sentinel-2 Team 2010) and therefore simulation by spectral and spatial up-scaling is feasible (Table 6.1). The aircraft flying orientation was planned to a north-south bearing analogous to the direction of the polar orbit (inclination 98.5°) of Sentinel-2 satellite. It is worth noting the difference of coverage between the AISA system and Sentinel-2 in Figure 6.1; the area covered by the airborne image is small due to the low altitude of the aircraft; conversely the 290km swath of Sentinel-2 assures a very large coverage where the whole Lake Balaton is included in a maximum of 2 overpasses.

Table 6.1: Simulated bands of Sentinel-2 (greyed) and specifications of instruments.

Band #	Central wavelength	Bandwidth	Spatial resolution	Radiometric resolution
1	443 nm	20 nm	60 m	12-bit
2	490 nm	65 nm	10 m	
3	560 nm	35 nm	10 m	
4	665 nm	30 nm	10 m	
5	705 nm	15 nm	20 m	
6	470 nm	15 nm	20 m	
7	783 nm	20 nm	20 m	
8	842 nm	115 nm	10 m	
8b	865 nm	20 nm	20 m	
9	945 nm	20 nm	60 m	
10	1380 nm	30 nm	60 m	
11	1610 nm	90 nm	20 m	
12	2190 nm	180 nm	20 m	

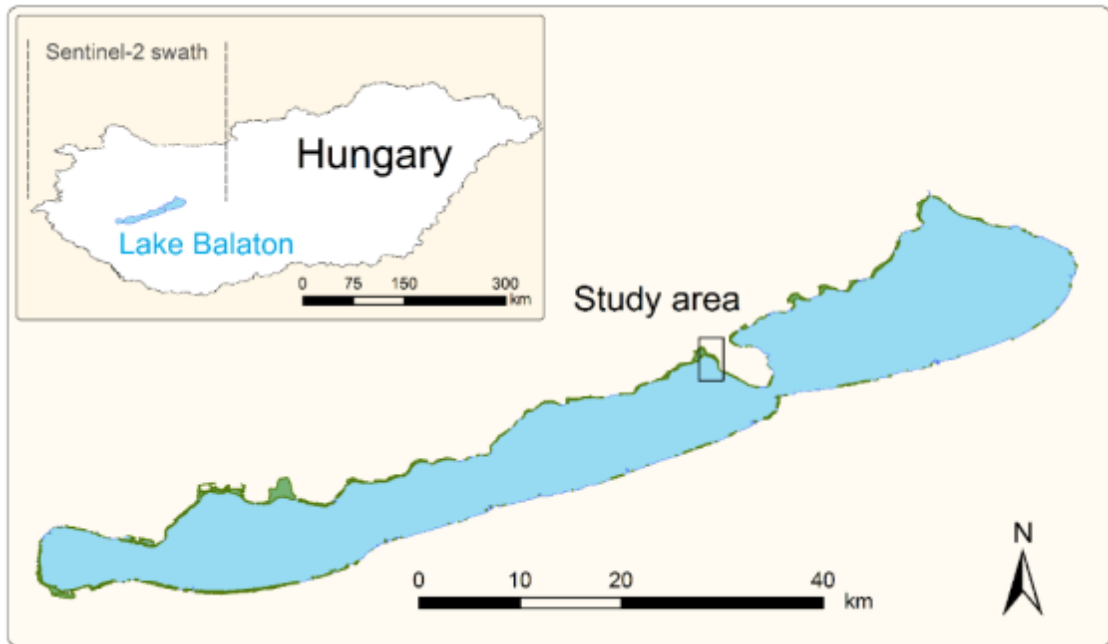


Figure 6.1: Study area in Lake Balaton, Hungary and the wide swath (290 km) of Sentinel-2.

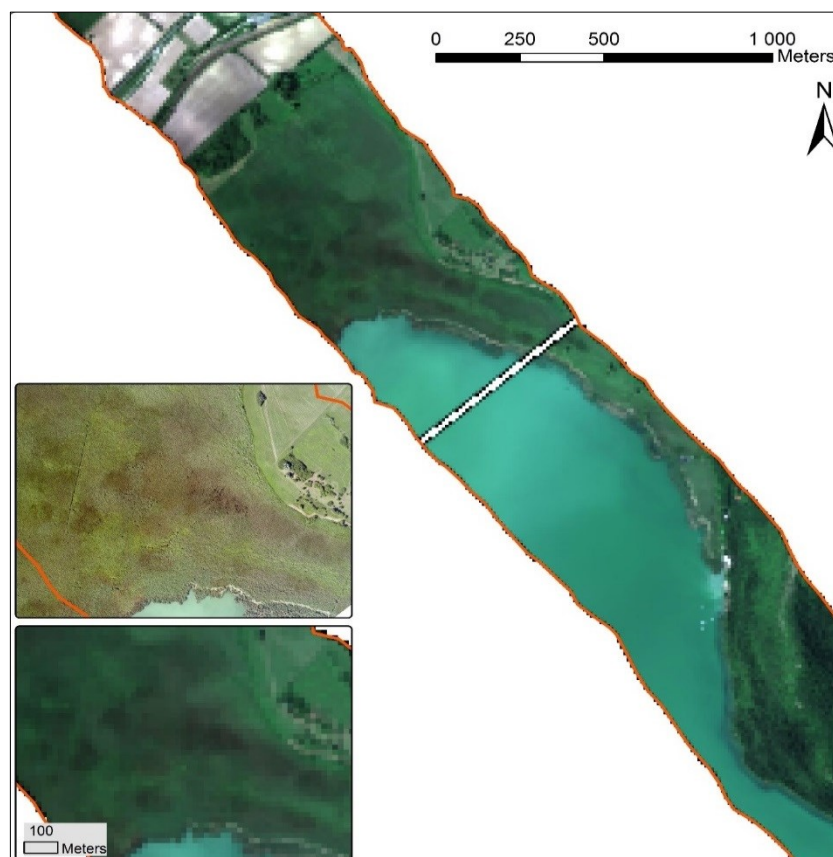


Figure 6.2: RGB representation (665nm, 560nm, 490nm) of the simulated Sentinel-2 image. The white stripe indicates missing data due to systematic dropping lines of the Hawk sensor. Insets: subsets of the central reed bed area of the main image (bottom) and true-colour RGB aerial photo (0.25 m) acquired concurrently with the hyperspectral dataset (top).

6.3 Methodology

The methodology is based on the spectral and spatial aggregation of the airborne hyperspectral dataset in order to synthesize an image with characteristics similar to the Sentinel-2. AISA specifications are superior to Sentinel-2 (Table 6.1) and therefore by downscaling the image specifications a Sentinel-2 image simulation is feasible. The latter product is a suitable ground for testing techniques and methodologies in a pre-operational context.

The AISA dual image (Eagle and Hawk) was first pre-processed as described in chapter 5 by applying radiometric normalization, atmospheric correction and geo-registration. Only one strip covering the east part of the bay was used as the mosaicking of adjacent images introduces artefacts and reduces the radiometric quality of the product. Eagle and Hawk data were merged to produce a single image covering the spectrum 400-2500 nm. Thereafter the bands outside the spectrum covered by Sentinel-2 channels were removed in order to assure comparability between the hyperspectral image and the simulated. Subsequently, the following products were derived (Figure 6.3):

1. The first 10 components of the MNF. This product contains the entire information from the data and is considered representative of the hyperspectral image in this set-up.
2. Spectrally resampled image. The Spectral Response Function (SRF) is convolved with the hyperspectral data for the spectral resampling. The SRF is assumed to be a Gaussian distribution defined by the central wavelength and bandwidth (represented by FWHM) of Sentinel-2 specifications.
3. Spatially aggregated image. The spatial aggregation is performed individually for each narrow band according to the spatial resolution of the corresponding Sentinel-2 band (i.e. 10m or 20m) using bilinear convolution. Bands with coarse resolution (i.e. 20m) are then down-scaled to 10m and merged with the rest of the bands. Subsequently the first 10

components of the inversed MNF transformation were derived to reduce spectral dimensionality.

4. Consecutive spectral and spatial resampling (steps 2 and 3 consecutively). This product represents the simulated Sentinel-2 image, while the individually spectrally and spatially resampled products as described above indicate the loss of information due to the individual or and spectral up-scaling from the hyperspectral airborne data.

The four products are classified using the same parameters and training set. Broader classes than the macrophyte-specific classification scheme that was set-up in the previous chapter were chosen. This decision was taken on the basis that Sentinel-2 products will be more frequently used over large areas and in a more generic lakeshore aquatic environment mapping. Classes of trees and bare soil were included and the classes of *Typha* and *Carex* were excluded as they are not encountered in the east part of the Bozsai bay. The SVM algorithm was employed as it has provided the best results as per chapter 5.

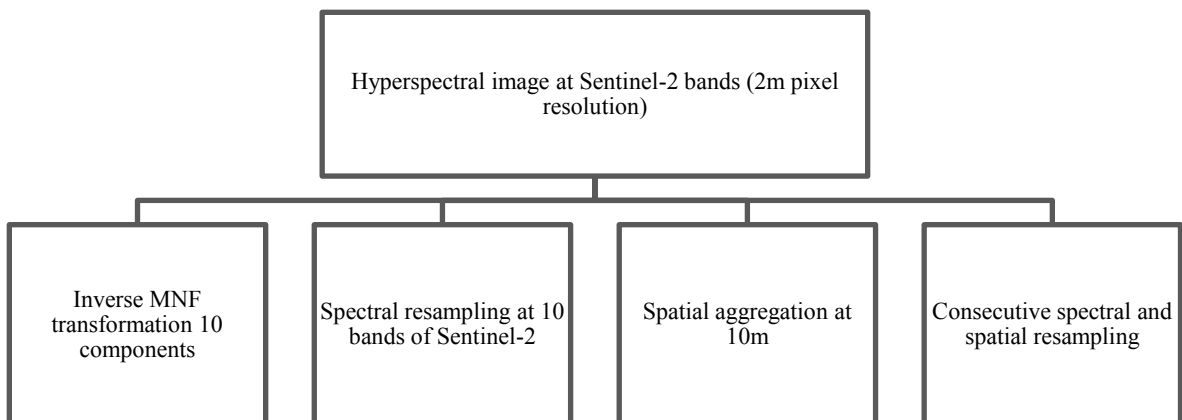


Figure 6.3: Workflow of the methodology, derivation of the four input datasets from the AISA airborne hyperspectral imagery.

6.4 Results and discussion

As demonstrated in Figure 6.4, Sentinel-2 bands with 10m spatial resolution are encountered at the visible and near-infrared spectrum while bands with 20m spatial resolution are concentrated around the red-edge region as well as longer wavelengths at spectral regions encompassing the hyperspectral vegetation spectrum. From the spectral point of view, the 10m bands are placed at wavebands with key information for vegetation studies in the visible domain as is the chlorophyll absorption characteristics and a wide bandwidth covering the near-infrared. 20m bands on the other hand have more diverse characteristics, with wide bands in the near-infrared and 4 narrow bands distributed in the narrow waveband of the red-edge region. It is worth noting that the red-edge bands are as narrow to include only 3-5 measurements from the corresponding hyperspectral data and therefore inherit a spectroscopic nature. Comparing the detail of spectra from the two sources, it becomes apparent that the near infrared bands are averaging the hyperspectral information available over a spectral region, while in the optical and red-edge domain the waveband covered by the Sentinel-2 channels is rather constant, at least for the pure monospecific reed pixel demonstrated in this example.

Table 6.2 presents the Sentinel-2 between-band correlations. The red-edge bands are highly correlated, however not as high to be considered identical. Taking into account that the target material is vegetation, this translates into that the red-edge bands might provide discriminatory information on vegetation condition and stress. For instance, the bands at 705 nm and 783 nm maintain a relatively low value at 0.87. Delegido et al. (2011) have already demonstrated the importance of Sentinel's-2 red-edge bands for the estimation of LAI and Chlorophyll content. However, someone has to take into consideration that the results are weighted averages from the hyperspectral data, and Sentinel-2 sensor might demonstrate different robustness in the way radiation is recorded; hence a real image would be

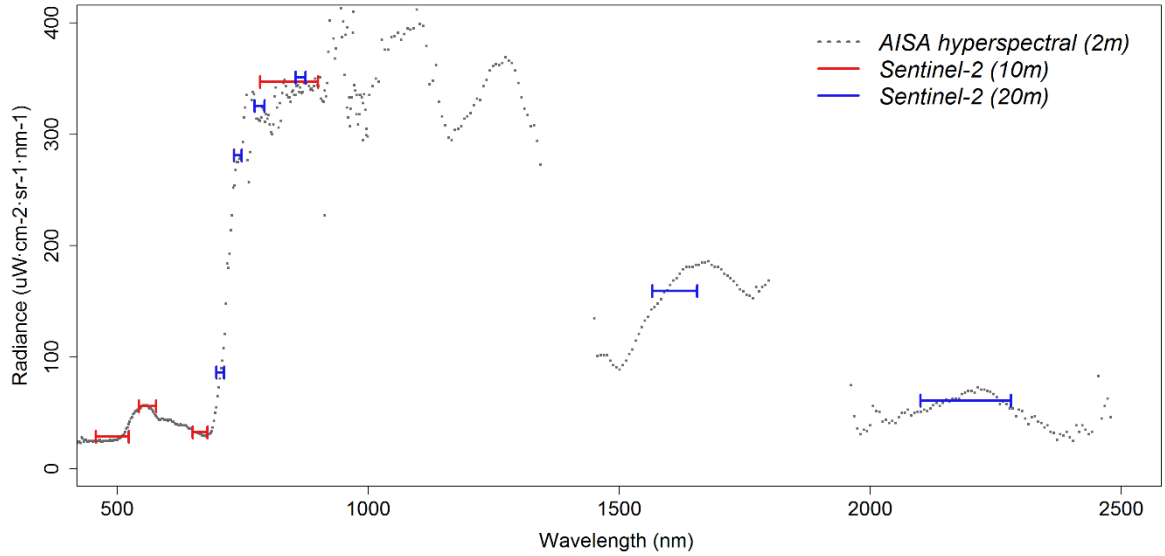


Figure 6.4: A spectral profile from a pixel of pure monospecific reed from the combined Eagle and Hawk data (grey) and the Sentinel-2 simulated image (colour).

Table 6.2: Correlation between the spectral channels of the simulated Sentinel-2 image. Bands in bold numbers are with correlation < 0.9 .

Central band	490	560	665	842	705	740	783	865	1610	2190
490 nm	1.00	0.99	0.92	0.51	0.78	0.54	0.51	0.50	0.60	0.62
560 nm		1.00	0.89	0.56	0.79	0.58	0.56	0.55	0.61	0.60
665 nm			1.00	0.60	0.90	0.64	0.61	0.60	0.79	0.84
842 nm				1.00	0.86	0.99	0.99	0.99	0.90	0.74
705 nm					1.00	0.90	0.87	0.87	0.96	0.92
740 nm						1.00	1.00	1.00	0.93	0.77
783 nm							1.00	1.00	0.91	0.74
865 nm								1.00	0.91	0.75
1610 nm									1.00	0.95
2190 nm										1.00

necessary to judge on the inter-band correlation with confidence. The results from the classification of the 4 input images is presented in Figure 6.5. The intermittent steps of spectral or spatial aggregation present the level of information loss due to reduction of the spectral and spatial dimensionality respectively, as a result from up-scaling from the airborne hyperspectral

image. The consecutive spectral and spatial aggregation is representing the simulated Sentinel-2 image.

Classification of the spectrally aggregated dataset results in a vegetation map very similar to the hyperspectral output. This indicates that the near-complete spectral information inherited by the Sentinel-2 bands contains vital information regarding vegetation targets; indeed in such a classification set-up the superspectral characteristics of Sentinel-2 are sufficient and equally suitable for lakeshore vegetation mapping. However, it is worth noting that in such simulation experiments the effects of the atmospheric path, and how well it can be accounted for if a satellite product is used, can not be simulated. While FLAASH was suitable for hyperspectral data and provided images at-target radiance, the spectral resolution and bandwidth of the satellite channels will not provide adequate information in order to perform such an accurate atmospheric correction; hence someone would expect that the satellite data contain an additional source of error, this of the inadequate atmospheric correction.

At spatial aggregation, macrophyte-specific classes are not as well delineated as in the hyperspectral image and therefore capability of fine scale mapping appears restricted. This may be attributed to the fact that spatial degradation results in larger pixels and therefore more classes are encountered within a single pixel. Consequently, the image is constructed from mixed pixels and the discrimination capability between similar classes is weakened. For instance the road network between the bare soil land parcels on the top of the image is not identifiable since the road which is narrow compared to the pixel size is integrated with the dominant surrounding class.

With regards to the simulated Sentinel-2 image (i.e. lower right inset of Figure 6.5), separability between generic classes as well as vegetation species is maintained and furthermore all classes are present. Nevertheless, class changes occur between macrophytic classes. Thematic consistency in generic

classes such as trees, bare soil and reed is maintained; however, discrimination capability is constrained when mapping classes which inherit higher inter-class spectral variability such as macrophyte associations indicated by misclassified patches. The vegetation classes of reed and trees are well separated, nevertheless sub-dominant reed and grassland are largely confused in the Sentinel-2 simulated image, as a result of the nature of sub-dominant reed which most probably includes grassland at the terrestrial part of the reed bed. This argument indicates that similar classes, such as the aforementioned, are not distinguished as satisfactorily as in the airborne hyperspectral imagery.

Reed die-back is classified correctly as slivers at the waterward edge of the reed bed from the Sentinel-2 data at the 10m resolution and a complete lakeshore vegetation status seems to be feasible based on the simulated data. Vegetation-specific applications based on Sentinel-2 imagery are further supported by the fact that mapping of vegetation vigour requires sound atmospheric correction methods. The 60m bands of Sentinel-2 will provide atmospheric correction from information on water vapour and aerosol derived within the scene and hence Sentinel-2 is especially suited for studying biophysical parameters of vegetation.

Overall, Sentinel-2 performs satisfactorily in classifying wetland ecosystems with high discrimination complexity as judged by qualitative assessment. The 10m spatial resolution allows for detecting fragmented patches at the edge of the reed bed, which are the main manifestation of die-back conditions. Confusion between macrophyte classes and associations is low at the individual spectral aggregation and rather high at the spatial resolution, which indicates that mapping of such classes is feasible with the spectral characteristics of Sentinel-2 but at a finer pixel resolution than the 10m.

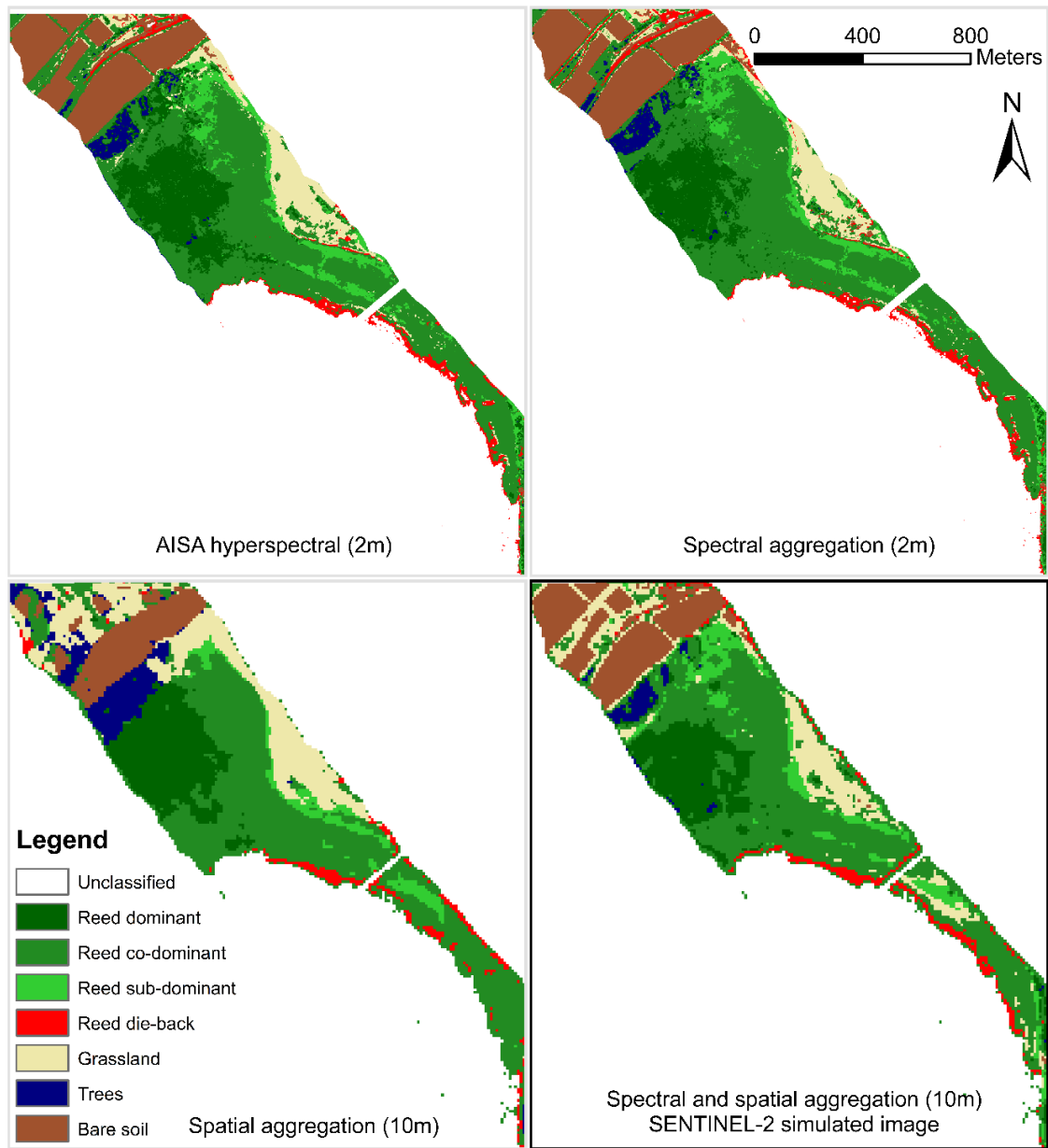


Figure 6.5: Classification of the 4 products; highlighted on the lower right the classification result derived from the Sentinel-2 simulated image.

6.5 Conclusions

Sentinel-2 is the forthcoming satellite with enhanced spectral and spatial capabilities anticipated to provide further potential in habitat mapping and classification of such complex scenes. In the framework of the upcoming satellite launch, simulated data are needed to assess the quality of the expected product and fruitfully exploit the imagery.

In this study a classification from simulated Sentinel-2 imagery was presented, synthesized from hyperspectral airborne data over a nature reserve site in Lake Balaton in order to assess the suitability of the imagery for fine-scale lakeshore vegetation mapping. An SVM supervised classification of Sentinel-2 simulated image in comparison to the MNF transformation of the hyperspectral source image, shows that thematic consistency of generic classes such as trees, bare soil and reed, is maintained; however when mapping classes inheriting higher inter-class spectral variability (e.g. macrophytes associations) the discrimination capability is constrained. The information is well preserved in spectral resample while spatial up-scaling introduces clumping of classes and mixed pixels. The very large swath of Sentinel-2 (i.e. 290 km) provides the opportunity of large scale main categorical mapping of large wetlands. It is foreseeable that the upcoming Sentinel-2 data will enable users to derive frequent products of aquatic vegetation with wide area coverage, high spatial resolution (i.e. 10m) and a thematic consistency. This study adds to the already documented high potential of Sentinel-2 for demanding earth observational needs (Malenovský et al. 2012). Further research on the usefulness of the introduced narrow-width red-edge bands is required to investigate in what degree it can assist in stress mapping and biophysical parameters estimation.

Chapter 7

Contribution to science

7.1 Conclusions

This part presents the findings of the work cumulatively in the framework of the literature review presented in the beginning of the Thesis. This study has been centered on the die-back phenomenon and this document presents, to the author's knowledge, the first investigation of reed stability in general, and hence die-back indications, from the imaging spectroscopy perspective. The results were evaluated with regards to the scientific questions raised and a report on the contribution of the study in the scientific ongoing efforts is given.

Chapter 3 deals with the spectral characteristics of emergent macrophytes from proximate recorded data. The main species at Lake Balaton (i.e. terrestrial reed, aquatic reed, *Typha* and *Carex*) have separating spectra in the 400-1000nm domain at leaf scale; especially reed is differentiated in the red region considerably. Reed die-back samples present a higher reflectance at the visible spectrum at leaf scale; the same observation can be made at canopy scale. However the 95% confidence interval is too wide to draw conclusions, it appears that die-back phenomenon inherits several canopy-related manifestations (mainly illumination geometry) and *Phragmites* in general presents too high heterogeneity at canopy scale to make safe conclusions. The same applied with red-edge inflection point shift, which statistically is important at leaf scale but not at canopy scale. *Phragmites* phenological state is also spectrally diverging at canopy scale according to the dried ramets and inflorescence found in the field of view. Nevertheless, sun and shade leaves do not present any reflectance discrepancies at leaf scale. Finally, a spectral analysis of reed samples collected along a transect perpendicular to the lake shore reveals that spectra are diversifying significantly according to the depth

the ramets are growing in. This is in absolute agreement with the already advocated fact that phenotypic expression depends on bathymetry (Tóth and Szabó, 2012) as well as the genotype (Engloner et al. 2010). This Thesis suggests that these differences pass on the reflectance profile of the leaves in the visible and near-infrared and can be ascribed to the vegetation's stress condition, the microenvironment or even genotypic differences of the species growing in different environments.

The study of the reflectance profiles is the main tool of hyperspectral remote sensing analysis and was investigated in Chapter 3. However the physiological status of the plant is not clearly expressed in the spectral profile. Chapter 4 presents an original idea of using hyperspectral data as a proxy to represent photosynthetic activity, which is directly related to environmental induced stress. It demonstrates the first explicit analysis of coupling *in-situ* hyperspectral data with photophysiological parameters. This allows for detection of spectral indices which can act as a proxy of the parameter under study. A strong correlation between narrowband spectral indices and chlorophyll fluorescence parameters indicates the potential of hyperspectral remote sensing in assessing reed stability. Specifically to the fluorescence parameters, the calculated indices are an indication of plant stability at leaf scale. An application of the findings from the field data analysis to airborne hyperspectral imagery reveals important information about reed condition at the study area. Y(II) values, regarded as a proxy of photosystem activity, have been calculated from high R^2 combination of spectral ratio 612/516 representing F_s and 699/527 representing F_m'. ETR values are estimated based on the calculated Y(II) and the spectral ratio 463/488 for PAR. A comparison with empirical vegetation indices from the literature shows significantly higher R^2 values of the proposed indices for the specific application. Spectral indices at leaf scale were recommended for evaluating reed ecological status based on spectroscopic data to support the

identification of affected vegetation patches and presents R^2 maps that can aid the selection of indices tailored to the specifications of each instrument.

In chapter 5 attention is given to a more holistic approach to the problem on macrophytes mapping in lakeshore environment. Building on the previous chapter and using the indices developed which provide information on the stress conditions, and hence are associated to die-back phenomena, the macrophytic mapping of a reed bed in a nature protected area with high biodiversity is tested with different classifiers and data input scenarios. The ML and SVM algorithms were tested on hyperspectral and LiDAR datasets over a reed bed with high biodiversity. Eagle (400-1000 nm) image classified with SVM presents the most accurate and comprehensible results for most macrophytic classes. The overall accuracy has reached 89%, fact which can be attributed to the high spectral and spatial resolution of the airborne imagery. Co-dominant *Phragmites*, occupying the majority of the reed bed, is classified with 96% producer and 92% user accuracy. Reed die-back is arguably the most challenging class encountered at the edge of the reed bed. It appears that the classifier is categorizing reed die-back mainly according to consequences of the degeneration of the littoral zone (lower density, fragmentation of patches, litter accumulation) which is the aftermath of die-back conditions. As such, several marginal areas of reed (for instance *Typha*) are often categorized as die-back, even if in reality they are another class. The fused hyperspectral and LiDAR data have provided weaker results (overall accuracy 69%); hence it is concluded that the DCM does not assist in macrophytic mapping. Probably another byproduct from the LiDAR such as homogeneity or texture of the DCM may provide useful information. Overall, high spatial resolution hyperspectral data in the visible and near-infrared domain can provide accurate information on vegetation species and associations of reed beds and an indication of areas affected by die-back, however not a direct representation of die-back areas.

Last, in chapter 6 a Sentinel-2 image was synthesized from the airborne data and classified to the main categories in the macrophyte area. The idea behind this study was to investigate to what degree operational mapping of the main classes of the reedbed is feasible with upcoming frequent satellite data. The consistency of generic classes such as bare soil, reed and trees is maintained; however when mapping vegetation association classes with high within-class variability the discrimination capability is lower but still provides useful results. Reed die-back suffers from the same reasoning as the airborne imagery with fragmented fringe areas indicated as such, nevertheless it can be considered as indicated areas affected from die-back conditions. The very wide swath of Sentinel-2 (i.e. 290 km) in combination with the open access policy adopted for the data products could be the ground for operational mapping of reed beds.

7.2 Contribution to knowledge

This work draws from the need to research the spectral characteristics of freshwater emergent vegetation at different spatial scales as it has been proposed by Dekker et al. (2001). Vegetation encountered in lacustrine environments is a challenging mapping case due to the associated dependencies on the heterogeneity of the coverage resulting from the biodiversity, the presence of the water (and absence at the terrestrial side) and the homogeneous structure of the reed beds. Furthermore and for the specific case study, *Phragmites* is an organism with an especially high phenotypic plasticity (i.e. the reaction of the plant to changes of the environment) and therefore can easily acclimatize in the environment it grows.

Under this highly dynamic nature, an attempt to apply imaging spectroscopy on macrophytes encountered at Lake Balaton at leaf and canopy scale was attempted. The most important finding of the research has been the novelty of coupling fluorescence and spectral information from concurrent *in-situ* measurements as described also in Stratoulas et al. (2015). Remote sensing

has long been used to characterize the type, the amount and the spatial distribution of vegetation, however no concrete results have been presented in the literature on the processes of photosynthesis and productivity through remote sensing techniques. Spectral indices have been used to estimate biomass, chlorophyll content, water content and other physiological parameters, nevertheless these vegetation characteristics have no direct link to photosynthetic activity, and hence stress conditions. In chapter 4 narrowband indices are suggested as well as graphs from where case-specific indices can be derived, through which remote sensing can be used to represent the physiology of *Phragmites*. An application of the index on the airborne hyperspectral imagery shows that large scale remote sensing of plant production and possibly detection of plant stress is feasible.

Secondly, comparative proximate-acquired spectra were provided and the variability introduced from several factors was discussed (i.e. species, stress condition, phenology, illumination conditions and inundation level), which affect the spectral response of a plant at leaf and canopy scale. These factors, in the framework of statistical separability, can be taken into account when conducting field measurements and classification of imagery as they introduce considerable variability in the spectral behavior of the macrophytic material. One important aspect of the research has been that bathymetric conditions in which reed grows affect considerably the spectral behavior of the plant, which is probably associated indirectly to different clones encountered across the reed bed.

Finally, a highly accurate map of macrophyte species and associations derived from the classification of hyperspectral airborne imagery was presented. Hyperspectral data at 2m spatial resolution can provide thematic maps with consistency of the vegetation species encountered at reed beds as well as an indication of die-back conditions. However, a message conveyed through the research is that die-back can not be directly projected through airborne, and

thus satellite, imagery but only areas which have been already affected by die-back can be indicatively estimated. A simulation of a Sentinel-2 image shows that main macrophytic classes can be separated at the satellites spectral and spatial resolutions.

Reed die-back is a complex problem that continues to raise concern. In the wider framework of wetland vegetation mapping, remote sensing can provide key knowledge at proximate, local and regional scale. This thesis has attempted to investigate ways hyperspectral information from *in-situ*, airborne and simulated satellite data can aid in the identification of macrophyte species and quantification of biophysical parameters directly associated to reed ecophysiology. The methods and hyperspectral indices proposed in this work can contribute to the monitoring and sustainable management of wetlands with die-back phenomena and diversified macrophytic vegetation. Multi-temporal data and analysis may provide evidence on the peak photosynthetic activity during the growing season and richer information on macrophytes distribution. While the complexity of the problem is large due to the genotypical and phenotypical differences of macrophytes, it appears that proximate hyperspectral reflectance information is well associated to the photosynthetic activity of the plant and airborne imagery is providing evidence on the phenotypical distribution of different clones of *Phragmites*.

Appendix 1: R language script for processing of the field data and production of correlation maps

```
### PROCESSING CHAIN AND PRODUCTION OF FLUORESCENCE GRAPHS

# Install packages
install.packages("gtools")
require(gtools)
install.packages("zoo")
require(zoo)
install.packages("lattice")
require(lattice)
install.packages("grid")
require(grid)
install.packages("gridExtra")
require(gridExtra)
install.packages("RColorBrewer")
require(RColorBrewer)

# !!! set parameter name from excel columns labels
jname <- c("blank", "TEMP", "PAR", "Fs", "Fm", "YII", "ETR", "CHL")

# !!! set reflectance or transmittance values
rad <- "R"

# !!! set working directory when running on WINDOWS
setwd(file.path("C:", "Users", "ds331", "Desktop", "fluorescence", "14 Aug
2012", "field", "exported_reflectance"))

# list the files in the folder (exported from ASD ('reflectance' data format |
'rows' data organisation | 'false' print row title))
readfiles <- list.files(pattern = '*asd.txt')

# read tables and create a list
listoffiles <- lapply(readfiles, read.table, header=TRUE,
colClasses="numeric", sep="\t")

# derive SI and NDSI matrices for each spectrum record (i for observations)
for (i in 1:length(listoffiles))
```

```

{
  # read txt files
  raw <- listoffiles[[i]]

  # subset to spectrum range 400 nm - 1000 nm
  raw <- raw[, c(77:677)]

  # convert table to matrix
  raw = as.numeric(raw)

  # clone rows
  n=length(raw)
  iaxis <- matrix(rep(raw, n), nr=n, byrow = TRUE)

  # transpose raw
  jaxis <- t(iaxis)

  # build Spectral Index (SI) matrix
  SI <- (iaxis/jaxis)

  # build Normalized Difference Spectral Index (NDSI) matrix
  NDSI <- (iaxis-jaxis)/(iaxis+jaxis)

  # write tables to file
  write.table(SI, file = paste("SI", i, ".txt", sep = ""), sep = "\t")
  write.table(NDSI, file = paste("NDSI", i, ".txt", sep = ""), sep = "\t")
}

## BUILD SI AND NDSI DATASETS

# list the files in the folder
readSI <- list.files(pattern = '^SI*')
readNDSI <- list.files(pattern = '^NDSI*')

# package gtools - sort numerically
readSI <- mixedsort(readSI)
readNDSI <- mixedsort(readNDSI)

```

```

# read tables and create a list
SIS <- lapply(readSI, read.table, header=TRUE, sep="\t")
NDSIS <- lapply(readNDSI, read.table, header=TRUE, sep="\t")

## READ IN-SITU MEASUREMENTS

# read in-situ data (from text file)
setwd(file.path("../", "insitu_measurements"))
insitu <- read.table("fldata.txt", sep="\t", header = TRUE, quote = "")

# check if the number of observations is equal with the number of spectra
all.equal(nrow(insitu), length(SIS))

# !!!! SET BAND WINDOW SIZE
maxband <- length(SI[,1])
minband <- 1 #set to 1 to for full spectrum

# set working directory for results
setwd(file.path("../"))

### SI ###

## STATISTICS

# calculate coefficient of determination matrix
# j is the parameter from insitu data: Fv_Fm_ETR_factor_dev_two (1), alpha
(2), ETRmax (3), Ik (4)
for (j in 2:length(jname))
{
  insitu_par <- insitu[,j]
  lmr <- data.frame()
  lmp <- data.frame()

  # calculate correlation for each element in x(px), in y(py) for each
  observation (i)
  for (py in minband:maxband) # in minband:maxband
  {
    for (px in minband:maxband) # in minband:maxband
    {

```

```

obs <- data.frame()

# calculate r ^2 and p values
obs <- as.matrix(obs)
cor <- cor.test(obs[,1], obs[,2], method = "pearson")
lmr <- rbind(lmr, cor[4][[1]]^2)
lmp <- rbind(lmp, cor[3])
}
}

# replace NAs with zeros (0)
lmr[is.na(lmr)] <- 0
lmp[is.na(lmp)] <- 0

# convert to matrix
lmr <- as.matrix(lmr, byrow = TRUE)
lmp <- as.matrix(lmp, byrow = TRUE)

# derive place mark
if (i == 23){
  place = "terrestrial"
} else if(i == 78){
  place = "shallowwater"
} else if(i == 105){
  place = "deepwater"
} else if(i == 122){
  place = "wateredge"
} else if(i == 123){
  place = "fulldata"
} else{
  place = "unknownplacemark"
}

# assign name to use in this session
namer <- paste(rad, "_", "SI", "_", "Rsq", "_", place, "_", jname[j],
".txt", sep = "")
namep <- paste(rad, "_", "SI", "_", "P", "_", place, "_", jname[j], ".txt",
sep = "")

```

```

# write to table
write.table(lmr, namer, sep = "\t")
write.table(lmp, namep, sep = "\t")
}

## PRODUCE Rsquare GRAPH

# iterate for the j parameters of the insitu data, Fv_Fm_ETR_factor_dev_two
(1), alpha (2), ETRmax (3), Ik (4)
for (j in 2:length(jname))
{
  # assign name to use in this session
  namer <- paste(rad, "_", "SI", "_", "Rsq", "_", place, "_", jname[j],
".txt", sep = "")
  namep <- paste(rad, "_", "SI", "_", "P", "_", place, "_", jname[j], ".txt",
sep = "")

  # read the table
  resultr <- as.matrix(read.table(namer, header = TRUE, sep="\t",
row.names=NULL, colClasses = c(rep("NULL", 1), rep("numeric", 1))))
  resultp <- as.matrix(read.table(namep, header = TRUE, sep="\t",
row.names=NULL, colClasses = c(rep("NULL", 1), rep("numeric", 1))))

  # define matrix dimensions
dim(resultr) <- c(sqrt(length(resultr)), sqrt(length(resultr)))
dim(resultp) <- c(sqrt(length(resultr)), sqrt(length(resultr)))

# transpose to fit iaxis in x and jaxis in y
resultr <- t(resultr)
resultp <- t(resultp)

## Plot R with package lattice

# set minimum and maximum values
minr <- min(resultr, na.rm = TRUE)
maxr <- max(resultr, na.rm = TRUE)
minp <- min(resultp, na.rm = TRUE)
maxp <- max(resultp, na.rm = TRUE)

# set diagonal to high values - resulting in white line in graph
diag(resultr) <- NA

```

```

diag(resultp) <- NA

# define data frame for lattice
dr = data.frame(xr=rep(seq(400, 1000, length=nrow(resultr)), ncol(resultr)),
                yr=rep(seq(400, 1000, length=ncol(resultr)),
                each=nrow(resultr)),
                zr=c(resultr))

dp = data.frame(xp=rep(seq(400, 1000, length=nrow(resultp)), ncol(resultp)),
                yp=rep(seq(400, 1000, length=ncol(resultp)),
                each=nrow(resultp)),
                zp=c(resultp))

# create colour palletes
palr <- rev(brewer.pal(10, "RdYlBu"))
palp <- rev(brewer.pal(7, "OrRd"))
breaksr <- c(0.0, 0.1, 0.2, 0.3, 0.4, 0.5, 0.6, 0.7, 0.8, 0.9, 1.0)
breaksp <- c(0, 0.001, 0.01, 0.05, 1)

# save to jpg
tiff(file = paste(rad, "_", "SI", "_", place, "_", jname[j], ".tif", sep =
""), antialias = "cleartype",
      res = 200, pointsize = 1/30, width = 2000, height = 1000, units = "px")
plot.new()
par(mfrow=c(1,2), omd=c(1,0.2,0.4,0.2))
print(
  rplot <- levelplot(zr~xr*yr, data=dr, col.regions= palr,
                    cuts = 10, at = breaksr,
                    #main = paste("r-squared value: ", rad, "Spectral Ratio
Index - ", jname[j]),
                    xlab = paste("Wavelength", parse(text="Ri"), "(nm)",
sep = " "),
                    ylab = paste("Wavelength", parse(text="Rj"), "(nm)",
sep = " "),
                    scales = list(draw = TRUE, tick.number = 7),
                    colorkey = list(space = "right", col=palr, at =
breaksr,
                    labels
c("0.0","0.1","0.2","0.3","0.4","0.5","0.6","0.7","0.8","0.9","1.0")))
)
print(
  pplot <- levelplot(zp~xp*yp, data=dp, col.regions=palp,
                    cuts=3, at=breaksp,

```

```

", jname[j]),          #main = paste("P-value: ", rad, "Spectral Ratio Index -
sep = " "),           xlab = paste("Wavelength", parse(text="Ri"), "(nm)",
sep = " "),           ylab = paste("Wavelength", parse(text="Rj"), "(nm)",
scales = list(draw = TRUE, tick.number = 7),
colorkey = list(space = "right", col=palp, at = c(0.00,
0.10, 0.25, 0.50 ,1),
labels = c("0.000", "0.001", "0.010",
"0.050", "1.000")))
)
# requires gridExtra
grid.arrange(rplot,pplot, nrow=1, ncol = 2)
grid.text(expression("R  ^2"), y=unit(0.1, "npc"), rot=0, x=unit(0.45,
"npc"))
grid.text(expression("p"), y=unit(0.1, "npc"), rot=0, x=unit(0.933, "npc"))
grid.text(expression("(a)"), y=unit(0.045, "npc"), rot=0, x=unit(0.07,
"npc"))
grid.text(expression("(b)"), y=unit(0.045, "npc"), rot=0, x=unit(0.57,
"npc"))
dev.off()
}

### NDSI ###

## STATISTICS

# calculate coefficient of determination matrix
# j is the parameter from insitu data: Fv_Fm_ETR_factor_dev_two (1), alpha
(2), ETRmax (3), Ik (4)
for (j in 2:length(jname))
{
  insitu_par <- insitu[,j]
  lmr <- data.frame()
  lmp <- data.frame()

  # calculate correlation for each element in x(px), in y(py) for each
observation (i)
  for (py in minband:maxband) # in minband:maxband
  {
    for (px in minband:maxband) # in minband:maxband
    {

```

```

obs <- data.frame()

# calculate r ^2 and p values
obs <- as.matrix(obs)
cor <- cor.test(obs[,1], obs[,2], method = "pearson")
lmr <- rbind(lmr, cor[4][[1]]^2)
lmp <- rbind(lmp, cor[3])
}
}

# replace NAs with zeros (0)
lmr[is.na(lmr)] <- 0
lmp[is.na(lmp)] <- 0

# convert to matrix
lmr <- as.matrix(lmr, byrow = TRUE)
lmp <- as.matrix(lmp, byrow = TRUE)

# derive place mark
if (i == 23){
  place = "terrestrial"
} else if(i == 78){
  place = "shallowwater"
} else if(i == 105){
  place = "deepwater"
} else if(i == 122){
  place = "wateredge"
} else if(i == 123){
  place = "fulldata"
} else{
  place = "unknownplacemark"
}

# assign name to use in this session
namer <- paste(rad, "_", "NDSI", "_", "Rsq", "_", place, "_", jname[j],
".txt", sep = "")
namep <- paste(rad, "_", "NDSI", "_", "P", "_", place, "_", jname[j],
".txt", sep = "")

```

```

# write to table
write.table(lmr, namer, sep = "\t")
write.table(lmp, namep, sep = "\t")
}

## PRODUCE Rsquare GRAPH

# iterate for the j parameters of the insitu data, Fv_Fm_ETR_factor_dev_two
(1), alpha (2), ETRmax (3), Ik (4)
for (j in 2:length(jname))
{
  # assign name to use in this session
  namer <- paste(rad, "_", "NDSI", "_", "Rsqr", "_", place, "_", jname[j],
".txt", sep = "")
  namep <- paste(rad, "_", "NDSI", "_", "P", "_", place, "_", jname[j],
".txt", sep = "")

  # read the table
  resultr <- as.matrix(read.table(namer, header = TRUE, sep="\t",
row.names=NULL, colClasses = c(rep("NULL", 1), rep("numeric", 1))))
  resultp <- as.matrix(read.table(namep, header = TRUE, sep="\t",
row.names=NULL, colClasses = c(rep("NULL", 1), rep("numeric", 1))))

  # define matrix dimensions
  dim(resultr) <- c(sqrt(length(resultr)), sqrt(length(resultr)))
  dim(resultp) <- c(sqrt(length(resultr)), sqrt(length(resultr)))

  # transpose to fit iaxis in x and jaxis in y
  resultr <- t(resultr)
  resultp <- t(resultp)

  ## Plot R with package lattice

  # set minimum and maximum values
  minr <- min(resultr, na.rm = TRUE)
  maxr <- max(resultr, na.rm = TRUE)
  minp <- min(resultp, na.rm = TRUE)
  maxp <- max(resultp, na.rm = TRUE)

  # set diagonal to high values - resulting in white line in graph
  diag(resultr) <- NA

```

```

diag(resultp) <- NA

# define data frame for lattice
dr = data.frame(xr=rep(seq(400, 1000, length=nrow(resultr)), ncol(resultr)),
                yr=rep(seq(400, 1000, length=ncol(resultr)),
                each=nrow(resultr)),
                zr=c(resultr))

dp = data.frame(xp=rep(seq(400, 1000, length=nrow(resultp)), ncol(resultp)),
                yp=rep(seq(400, 1000, length=ncol(resultp)),
                each=nrow(resultp)),
                zp=c(resultp))

# create colour palletes
palr <- rev(brewer.pal(10, "RdYlBu"))
palp <- rev(brewer.pal(7, "OrRd"))
breaksr <- c(0.0, 0.1, 0.2, 0.3, 0.4, 0.5, 0.6, 0.7, 0.8, 0.9, 1.0)
breaksp <- c(0, 0.001, 0.01, 0.05, 1)

# save to jpg
tiff(file = paste(rad, "_", "NDSI", "_", place, "_", jname[j], ".tif", sep =
""), antialias = "cleartype",
      res = 200, pointsize = 1/30, width = 2000, height = 1000, units = "px")
plot.new()
par(mfrow=c(1,2), omd=c(1,0.2,0.4,0.2))
print(
  rplot <- levelplot(zr~xr*yr, data=dr, col.regions= palr,
                    cuts = 10, at = breaksr,
                    #main = paste("r-squared value: ", rad, "Normalized
Difference Vegetation Index - ", jname[j]),
                    xlab = paste("Wavelength", parse(text="Ri"), "(nm)",
sep = " "),
                    ylab = paste("Wavelength", parse(text="Rj"), "(nm)",
sep = " "),
                    scales = list(draw = TRUE, tick.number = 7),
                    colorkey = list(space = "right", col=palr, at =
breaksr,
                    labels
c("0.0","0.1","0.2","0.3","0.4","0.5","0.6","0.7","0.8","0.9","1.0")))
)
print(
  pplot <- levelplot(zp~xp*yp, data=dp, col.regions=palp,
                    cuts=7, at=breaksp,

```

```

#main = paste("P-value: ", rad, "Normalized Difference
Vegetation Index - ", jname[j]),
xlab = paste("Wavelength", parse(text="Ri"), "(nm)",
sep = " "),
ylab = paste("Wavelength", parse(text="Rj"), "(nm)",
sep = " "),
scales = list(draw = TRUE, tick.number = 7),
colorkey = list(space = "right", col=palp, at = c(0.00,
0.10, 0.25, 0.50 ,1),
labels = c("0.000", "0.001", "0.010",
"0.050", "1.000"))
)
# requires gridExtra
grid.arrange(rplot,pplot, nrow=1, ncol = 2)
grid.text(expression("R  ^2"), y=unit(0.1, "npc"), rot=0, x=unit(0.45,
"npc"))
grid.text(expression("p"), y=unit(0.1, "npc"), rot=0, x=unit(0.933, "npc"))
grid.text(expression("(a)"), y=unit(0.045, "npc"), rot=0, x=unit(0.07,
"npc"))
grid.text(expression("(b)"), y=unit(0.045, "npc"), rot=0, x=unit(0.57,
"npc"))
dev.off()
}
# END

```

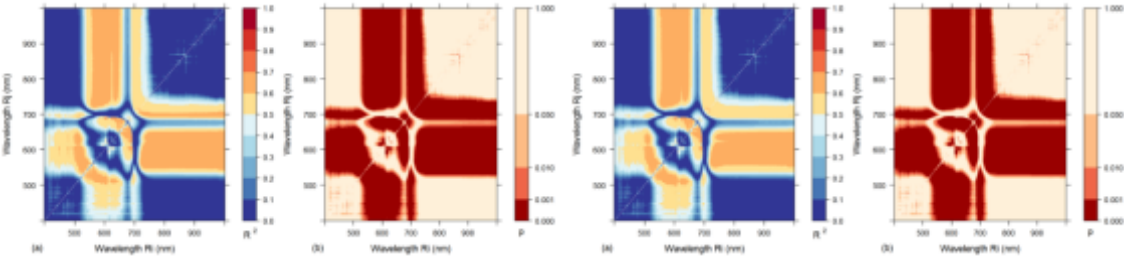
Appendix 2: Correlation of *in-situ* fluorescence parameters and leaf hyperspectral reflectance

DEEPWATER

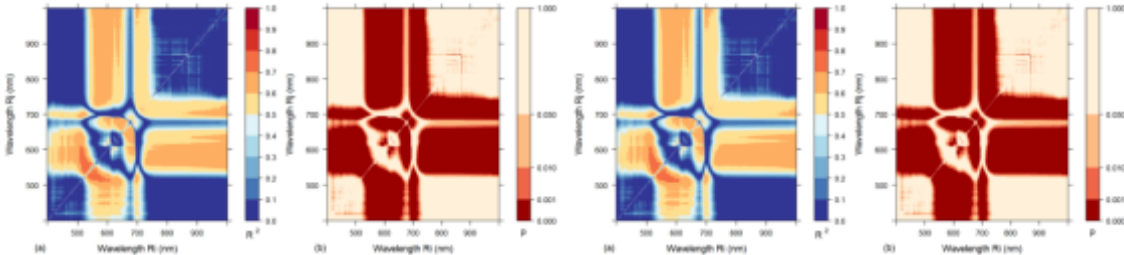
SI

NDSI

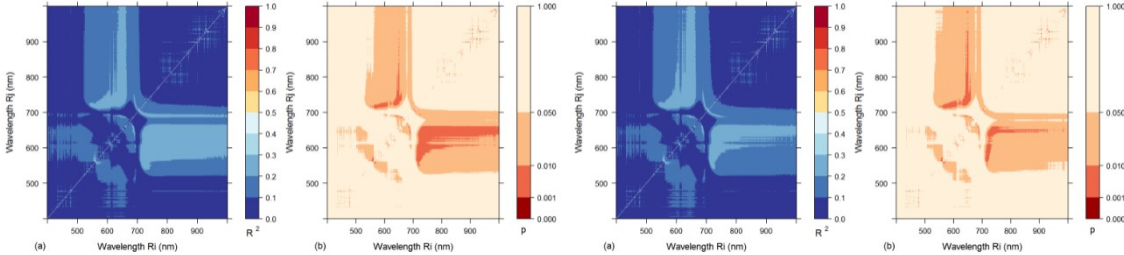
F_s



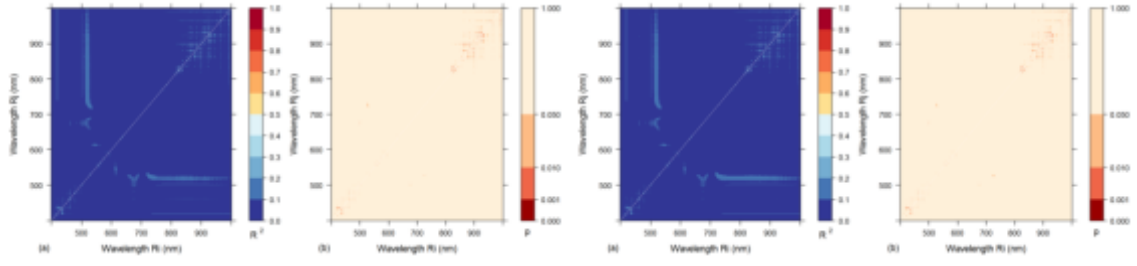
F_m'



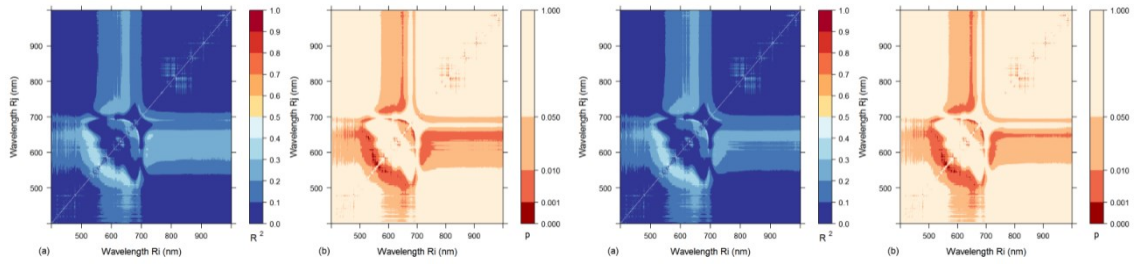
Y(II)



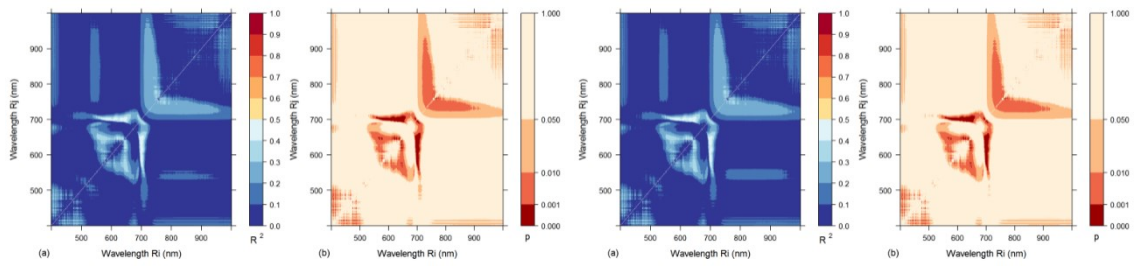
PAR



ETR



CHL



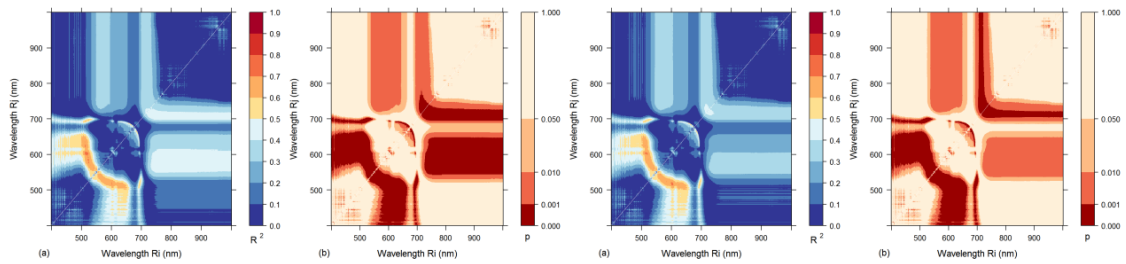
Appendix 3: Correlation of *in-situ* fluorescence parameters and leaf hyperspectral transmittance

DEEPWATER

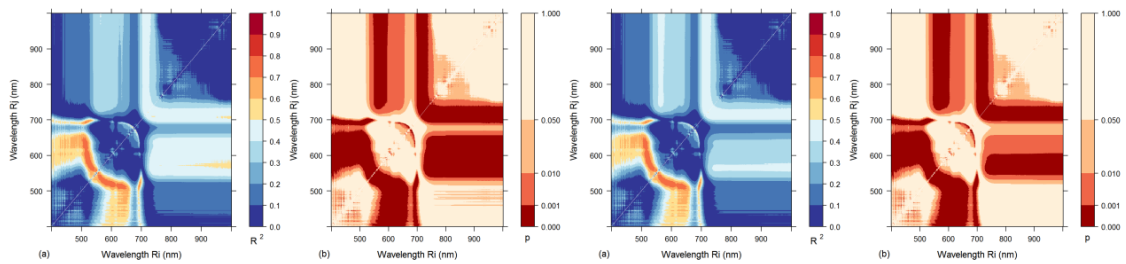
SI

NDSI

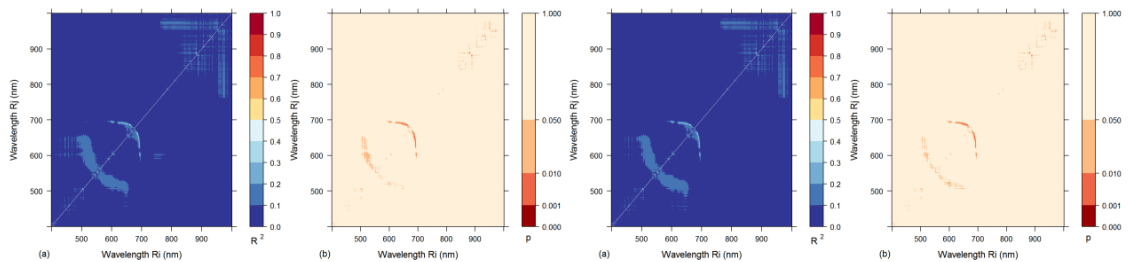
F_s



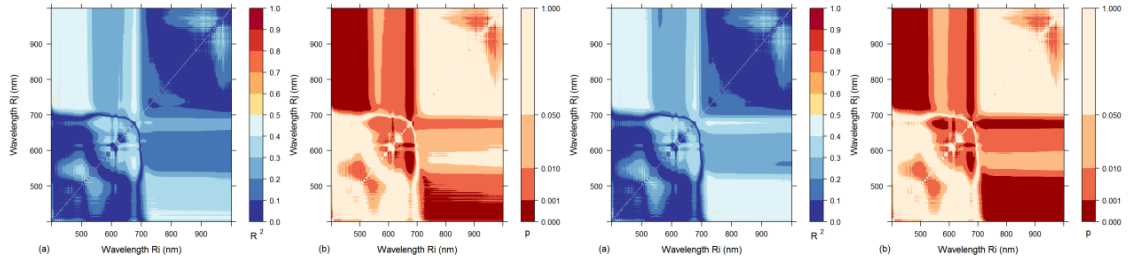
F_m'



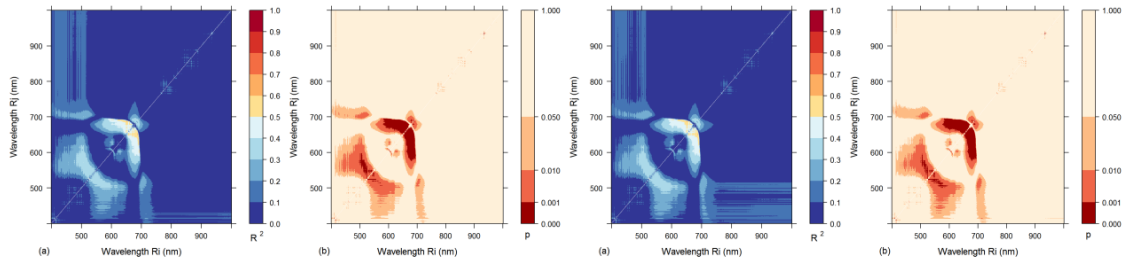
Y(II)



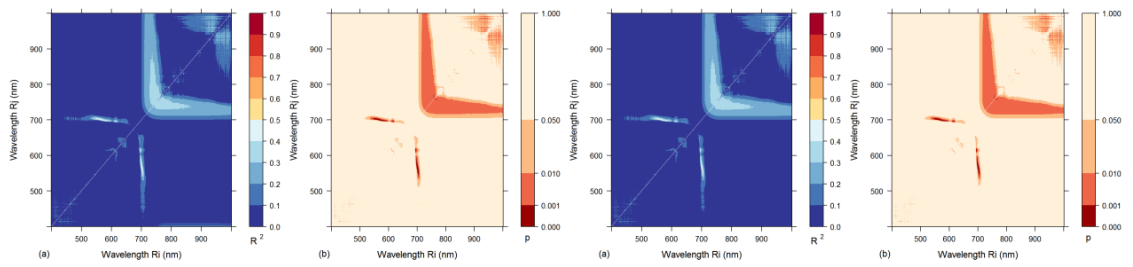
PAR



ETR



CHL



Appendix 4: Atmospheric correction input parameters

Parameter	Value	Notes	Variable
Input radiance Image	xxxxxxx1b.bil	16-bit unsigned integer	x
Scale factor	1000	[1]	
Output reflectance file	xxxxxxx2.bil	Level 2 product	x
Output directory for FLAASH files	\level2\		x
Rootname for FLAASH files	FLAASH		
Sensor type	Hyperspectral-AISA		
Lat		Centre of each scene	x
Lon		Centre of each scene	x
Sensor altitude (km)		Flight log file	x
Ground elevation (km)	0.11		
Pixel size (m)	2	Adjacency effect correction	
Flight date		Day of August 2010	x
Flight time GMT (HH:MM:SS)		Flight log file	x
Atmospheric model	Mid-Latitude Summer	Surface temperature	
Water retrieval	Yes		
Water absorption feature	820 nm for Eagle 1135 nm for Hawk	1135 nm is recommended	x
Aerosol model	Maritime	Non critical for high visibility	
Aerosol retrieval	None		
Initial visibility (km)	50		
Spectral polishing	Yes	[2]	
Width (number of bands)	9 (minimum 2)		
Wavelength recalibration	No		
Hyperspectral settings		Based on AISA specifications	
Spectrograph definition file	-		
Aerosol scale height (km)	1.50	For adjacency scattering range	
CO2 mixing ratio (ppm)	404	[3]	
Use square slit function	No		
Use adjacency correction	Yes		
Reuse MODTRAN calculations	No		
Modtran resolution	5cm-1		
Modtran multiscatter model	Scaled DISORT		

Number of DISORT streams	8		
Zenith angle	180	For nadir-viewing sensors	
Azimuth angle		(Dir – 180°) [4]	x
Use tiled processing	No		
Tile size (Mb)	-	75% of available RAM	
Radiance image	-		
Re-define scale factors for r.i.	-		
Output reflectance scale factor	1000	Reflectance scale factor in .hdr	
Automatic save template file	Yes		
Output diagnostic files	No		

[1] The measurement unit of the data provided is $\mu\text{W} \cdot \text{cm}^{-2} \cdot \text{sr}^{-1} \cdot \text{nm}^{-1}$, however the data in the files includes a x1000 scaling factor. This is included to avoid floating-point numbers, making calculations quicker, avoiding rounding errors and reducing file sizes. Therefore, in essence the data values in the files are effectively $\text{nW} \cdot \text{cm}^{-2} \cdot \text{sr}^{-1} \cdot \text{nm}^{-1}$, and a division by 1000 is required to represent units in $\mu\text{W} \cdot \text{cm}^{-2} \cdot \text{sr}^{-1} \cdot \text{nm}^{-1}$.

[2] Spectral polishing is a correction method used to reduce spectral artifacts (e.g. residual “saw-tooth” instrument noise) by applying a uniform linear transformation.

[3] Carbon mixing ratio exhibits a clear seasonal pattern with lower values corresponding to late summer. According to the Mauna Loa Observatory, CO₂ concentration has an annual growth rate of approximately 2 ppmv for the years 1998 – 2008 (<http://cdiac.ornl.gov/trends/co2/sio-mlo.html>). By extrapolating the data a summer value of 384 ppmv for late summer 2010 when the data were collected was calculated. By adding 20 ppmv to the actual value according to FLAASH user’s guide recommendation for best results, an input value 404 ppmv was considered.

[4] The sensor heading is measured east from north in degrees (0 – 360). FLAASH required as input the angle between the line-of-sight and due north, hence it is between -180 and +180.

References

- Adams, J.B., Smith, M.O. and Johnson, P.E. (1986). Spectral Mixture Modeling - a new analysis of rock and soil types at the Viking Lander-1 Site. *Journal of Geophysical Research-Solid Earth and Planets*, 91, 8098-8112.
- Adam, E., Mutanga, O. and Rugege, D. (2010). Multispectral and hyperspectral remote sensing for identification and mapping of wetland vegetation: a review. *Wetlands Ecology and Management*, 18(3), 281-296.
- Amoros-Lopez, L., Gomez-Chova, L., Vila-Frances, J., Alonso, L., Calpe, J., Moreno J. and del Valle-Tascon, S. (2008). Evaluation of remote sensing of vegetation fluorescence by the analysis of diurnal cycles. *International Journal of Remote Sensing*, 29(17-18), 5423-5436.
- Anderson, K., Bennie, J. and Wetherelt, A. (2010). Laser scanning of fine scale pattern along a hydrological gradient in a peatland ecosystem. *Landscape Ecology*, 25, 477-492.
- Anker, Y., Hershkovitz, Y., Ben Dor, E. and Gasith, A. (2014). Application of aerial digital photography for macrophyte cover and composition survey in small rural streams. *River Research and Applications*, 30(7), 925–937.
- Armstrong, J., Armstrong, W., Armstrong, I.B. and Pittaway, G.R. (1996). Senescence, and phytotoxin, insect, fungal and mechanical damage: factors reducing convective gas-flows in *Phragmites australis*. *Aquatic Botany*, 54(2–3), 211-226.
- Artigas, F.J. and Yang, J.S. (2005). Hyperspectral remote sensing of marsh species and plant vigour gradient in the New Jersey Meadowlands. *International Journal of Remote Sensing*, 26(23), 5209-5220.
- Azaria, I., Goldshleger, N., Ben-Dor, E. and Hamburger, R.B. (2009). Detection of cannabis plants by hyper-spectral remote sensing means. Proceedings of the 6th EARSeL Imaging Spectroscopy SIG Workshop.

Imaging spectroscopy: Innovative tool for scientific and commercial environmental applications, Tel Aviv, Israel, March 16-18, 2009.

Bahria, S., Essoussi, N. and Limam, M. (2011). Hyperspectral data classification using geostatistics and support vector machines. *Remote Sensing Letters*, 2, 99-106.

Baker N. R. (2008). Chlorophyll fluorescence: a probe of photosynthesis in vivo. *Annual Review of Plant Biology*, 59, 89-113.

Bange, J., Esposito, M., Lenschow, D. H., Brown, P. R. A., Dreiling, V., Giez, A., Mahrt, L., Malinowski, S. P., Rodi, A. R., Shaw, R. A., Siebert, H., Smit, H. and Zöger, M. (2013). Measurement of aircraft state and thermodynamic and dynamic variables. In: *Airborne measurements for environmental research: methods and instruments* (eds. Wendisch, M. and Brenguier, J. -L.), Wiley-VCH Verlag, GmbH & Co., Weinheim, Germany.

Barker, R. and King, D.J. (2012). Blanding's Turtle (*Emydoidea blandingii*) Potential Habitat Mapping Using Aerial Orthophotographic Imagery and Object Based Classification. *Remote Sensing*, 4, 194-219.

Barnsley, M.J. and Barr, S.L. (1996). Inferring urban land use from satellite sensor images using Kernel-based spatial reclassification. *Photogrammetric Engineering and Remote Sensing*, 62(8), 949-958.

Bartlett, D.S. and Klemas, V. (1980). Quantitative assessment of tidal wetlands using remote sensing. *Environmental management*, 4(4), 337-345.

Bastlová, D., Čížková, H., Bastl, M. and Květ, J. (2004). Growth of *Lythrum salicaria* and *Phragmites australis* plants originating from a wide geographical area: response to nutrient and water supply. *Global Ecology and Biogeography*, 13(3), 259–271.

Ben-Dor, E., Schläpfer, D., Plaza, A. J. and Malthus, T. (2013). Hyperspectral remote sensing. In *Airborne measurements for environmental research:*

methods and instruments. Eds. Wendisch, M. and Brenguier, J. –L. Wiley-VCH Verlag, GmbH and Co., Weinheim, Germany.

Bengtsson, L. and Hellström, T. (1992). Wind-induced resuspension in a small shallow lake. *Hydrobiologia*, 241(3), 163-172.

Blaschke, T. and Strobl, J. (2001). What's wrong with pixels? Some recent developments interfacing remote sensing and GIS. *GIS - Zeitschrift für Geoinformationssysteme*, 14(6), 12-17.

Blaschke, T. and Hay, G.J. (2001). Object-oriented image analysis and scale-space: Theory and methods for modeling and evaluating multi-scale landscape structure. *International Archives of Photogrammetry and Remote Sensing*, 34(Part 4/W5), 22-29.

Blaschke, T. (2010). Object based image analysis for remote sensing. *ISPRS Journal of Photogrammetry and Remote Sensing*, 65, 2-16.

Boar, R.R., Crook, C.E. and Moss, B. (1989). Regression of *Phragmites australis* reedswamps and recent changes of water chemistry in the Norfolk Broadland, England. *Aquatic Botany*, 35(1), 1-4.

Boorman, L.A., Sheail, J. and Fuller, R.M. (1977). "The *Phragmites* die-back problem." Progress Report. Institute of Terrestrial Ecology Project, no. 539.

Boyd, D., Sanchez-Hernandez, C. and Foody, G. (2006). Mapping a specific class for priority habitats monitoring from satellite sensor data. *International Journal of Remote Sensing*, 27(13), 2631-2644.

Brennan, R. and Webster, T.L. (2006). Object-oriented land cover classification of lidar-derived surfaces. *Canadian Journal of Remote Sensing*, 32(2), 162-172.

- Bresciani, M., Stroppiana, D., Fila, G., Montagna, M and Giardino, C. (2009). Monitoring reed vegetation in environmentally sensitive areas in Italy. *Italian Journal of Remote Sensing*, 41(2), 125-137.
- Bresciani, M., Sotgia, C., Fila, L. G., Musanti, M. and Bolpagni, R. (2011). Assessing common reed bed health and management strategies in Lake Garda (Italy) by means of Leaf Area Index measurements. *Italian Journal of Remote Sensing*, 43(2), 9-22.
- Brix, H. (1999a). The European research project on reed die-back and progression (EUREED). *Limnologica - Ecology and Management of Inland Waters*, 29(1), 5-10.
- Brix, H. (1999b). Genetic diversity, ecophysiology and growth dynamics of reed (*Phragmites australis*). *Aquatic Botany*, 64, 179-184.
- Brix, H., Sorrell, B.K. and Lorenzen, B. (2001). Are *Phragmites*-dominated wetlands a net source or net sink of greenhouse gases? *Aquatic Botany*, 69, 313–324.
- Brown, M., Lewis, H.G. and Gunn, S.R. (2000). Linear Spectral Mixture Models and Support Vector Machines for Remote Sensing, *IEEE Transactions on Geoscience and Remote Sensing*, 38(5), 2346-2360.
- Burai, P., Lövei, G.Z., Csaba, L., Nagy, I. and Enyedi, P. (2010). Mapping aquatic vegetation of the Rakamaz-Tiszanagyfalui Nagy-morotva using hyperspectral imagery. *AGD Landscape and Environment*, 4(1), 1-10.
- Burazerović, D., Heylen, R., Geens, B., Sterckx, S. and Scheunders, P. (2013). Detecting the adjacency effect in hyperspectral imagery with spectral unmixing techniques. *IEEE Journal of Selected Topics in Applied Earth Observations and Remote Sensing*, 6(3), 1070-1078.
- Butera, K.M. (1983). Remote Sensing of Wetlands. *IEEE Transactions on Geoscience and Remote Sensing*, GE-21(3), 383-392.

- Camps-Valls, G., and Bruzzone, L. (2005). Kernel-based methods for hyperspectral image classification. *IEEE Transactions on Geoscience and Remote Sensing*, 43, 1351-1362.
- Carleer, A. and Wolff, E. (2004). Exploitation of very high resolution satellite data for tree species identification. *Photogrammetric Engineering and Remote Sensing*, 70(1), 135-140.
- Carter, G.A. (1994). Ratios of leaf reflectances in narrow wavebands as indicators of plant stress. *International Journal of Remote Sensing*, 15(3), 697-703.
- Caylor, J. (2000). Aerial photography in the next decade. *Journal of Forestry*, 98(6), 17-19.
- Csaplovics, E. and Schmidt, J. (eds.) (2011). International symposium on advanced methods of monitoring reed habitats in Europe. Technische universitat Dresden, Rhombos-Verlag.
- Chen, B., Li, S.-K., Wang, K.-R., Wang, J., Wang, F.-Y., Xiao, C.-H., Lai, J.-C. and Wang, N. (2008). Spectrum characteristics of cotton canopy infected with verticillium wilt and applications. *Agricultural sciences in China*, 7(5), 561-569.
- Chen, D.M. and Stow, D. (2002). The effect of training strategies on supervised classification at different spatial resolutions. *Photogrammetric Engineering and Remote Sensing*, 68(11), 1155-1161.
- Chen, Q., Zhang, Y., Ekroos, A. and Hallikainen, M. (2004). The role of remote sensing technology in the EU water framework directive (WFD). *Environmental Science and Policy*, 7, 267-276.
- Cherrill, A. and McClean, C. (1999). Between-observer variation in the application of a standard method of habitat mapping by environmental consultants in the UK. *Journal of Applied Ecology*, 36(6), 989-1008.

- Chi, M., Feng, R., and Bruzzone, L. (2008). Classification of hyperspectral remote-sensing data with primal SVM for small-sized training dataset problem. *Advances in Space Research*, 41(11), 1793-1799.
- Christian, R.R. (2008). The Global Observation System of Systems (GEOSS). Inventory, assessment and monitoring of Mediterranean wetlands: Mapping wetlands using earth observation techniques, Fitoka, E. and Keramitsoglou, I. (eds.). EKBY and NOA, MedWet publication.
- Čížková-Končalová, H., Kvet, J. and Thompson, K. (1992). Carbon Starvation: A key to reed decline in eutrophic Lakes. *Aquatic Botany*, 43(2), 105–13.
- Čížková, H., Istvánovics, V., Bauer, V. and Balázs, L. (2001). Low levels of reserve carbohydrates in reed (*Phragmites australis*) stands of Kis-Balaton, Hungary. *Aquatic Botany*, 69(2–4), 209-216.
- Congalton, R.G. (1991). A review of assessing the accuracy of classifications of remotely sensed data. *Remote Sensing of Environment*, 37(1), 35-46.
- Convention on Wetlands of International Importance especially as Waterfowl Habitat. Ramsar (Iran), 2 February 1971. UN Treaty Series No. 14583. As amended by the Paris Protocol, 3 December 1982, and Regina Amendments, 28 May 1987.
- Crawley, M.J. (ed) (1997). *Plant Ecology* - 2nd ed. USA: Blackwell Science.
- Cserny, T. and Nagy-Bodor, E. (2000). Limnogeology of Lake Balaton (Hungary), chapter 58, in: Gierlowski-Kordesch, E.H. and Kelts, K.R. (eds), *Lake basins through space and time*. Tulsa, Oklahoma, U.S.A.: The American Association of Petroleum Geologists (AAPG) *Studies in geology*, 46, 605-618.
- Dalponte, M., Bruzzone, L., and Gianelle, D. (2008). Fusion of hyperspectral and LIDAR remote sensing data for classification of complex forest areas. *IEEE Transactions on Geoscience and Remote Sensing*, 46(5), 1416-1427.

- Dalponte, M., Bruzzone, L., Vescovo, L. and Gianelle, D. (2009). The role of spectral resolution and classifier complexity in the analysis of hyperspectral images of forest areas. *Remote Sensing of Environment*, 113(11), 2345-2355.
- Deegan, B.M., White, S.D. and Ganf, G.G. (2007). The influence of water level fluctuations on the growth of four emergent macrophyte species. *Aquatic Botany*, 86(4), 309-315.
- Dekker, A.G., Brando, V.E., Anstee, J.M., Pinnel, N., Kutser, T., Hoogenboom, E.J., Peters, S., Pasterkamp, R., Vos, R., Olbert, C. and Malthus, T.J.M. (2001). Imaging spectrometry of water (chapter 11). In: *Imaging spectrometry: basic principles and prospective applications*, van der Meer, F.D. and de Jong, S.M. (eds.), Springer.
- Delegido, J., Verrelst, J., Alonso, L. and Moreno, J. (2011). Estimation of Sentinel-2 red-edge bands for empirical estimation of green LAI and Chlorophyll content. *Sensors*, 11, 7063-7081.
- Den Hartog, C., Květ, J. and Sukopp, H. (1989). Reed. A common species in decline. *Aquatic Botany*, 35(1), 1-4.
- Dixon, B. and Candade, N. (2008). Multispectral landuse classification using neural networks and support vector machines: one or the other, or both? *International Journal of Remote Sensing*, 29(4), 1185-1206.
- Dulai, S., Horváth, F., Pécsváradi, A., Bondár, M., Molnár, I. and Erdei, L. (2002). Does increased photorespiration protect the leaves of common reed living in fragmented patches from excess light? *Acta Biologica Szegediensis* 46(3-4), 155–156.
- Engloner, A. I. (2009). Structure, growth dynamics and biomass of reed (*Phragmites australis*) – A review. *Flora – Morphology, Distribution, Functional Ecology of Plants*, 204(5), 331-346.

- Ehlers, M., Gähler, M. and Janowsky, R. (2003). Automated analysis of ultra high resolution remote sensing data for biotope type mapping: new possibilities and challenges. *ISPRS Journal of Photogrammetry and Remote Sensing*, 57(5-6), 315-326.
- Elatawneh, A., Kalaitzidis, C., Petropoulos, G.P. and Schneider, T. (2012). Evaluation of diverse classification approaches for land use/land cover mapping in a Mediterranean region utilizing Hyperion data. *International Journal of Digital Earth*, 1-23.
- Engloner, A.I. (2009). Structure, growth dynamics and biomass of reed (*Phragmites australis*) – A review. *Flora - Morphology, Distribution, Functional Ecology of Plants*, 204(5), 331-346.
- Engloner, A. I., Major, Á. and Podani, J. (2010). Clonal diversity along a water depth gradient in a declining reed stand as detected by three different genetic methods. *Aquatic Botany*, 92(1), 1-8.
- Engloner, A.I. and Major, Á. (2011). Clonal diversity of *Phragmites australis* propagating along water depth gradient. *Aquatic Botany*, 94, 172–176.
- Erwin, K.L. (2009). Wetlands and global climate change: the role of wetland restoration in a changing world. *Wetlands Ecology and Management*, 17, 71-84.
- ESA (2012). Sentinel-2: ESA's optical high-resolution mission for GMES operational services. ESA SP-1322/2, ESA Communications. https://sentinel.esa.int/documents/247904/349490/S2_SP-1322_2.pdf
- ESA Sentinel-2 Team (2010). GMES Sentinel-2 Mission Requirements Document. EOP-SM/1163/MR.dr, issue 2.1. http://esamultimedia.esa.int/docs/GMES/Sentinel-2_MRD.pdf
- Felföldy, L., Muszkalay, L., Rakoczi, L. and Szesztay, K. (1969). Origin and movement of sediment in Lake Balaton, 287.

- Ferguson, R.L., Wood, L.L. and Graham, D.B. (1993). Monitoring spatial change in seagrass habitat with aerial photography. *Photogrammetric Engineering and Remote Sensing*, 59, 1033-1038.
- Fernandez-Prieto, D., Arino, O., Borges, T., Davidson, N., Finlayson, M., Grassl, H., MacKay, H., Prigent, C., Pritchard, D. and Zalidis, G. (2006). The Glob Wetland Symposium: Summary and way forward. Proceedings of the first International Symposium on GlobWetland: Looking at Wetlands from Space, Frascati, Italy, 19-20 October 2006. ESA SP-634.
- Findlay, S.E.G., Dye, S. and Kuehn, K.A. (2002). Microbial growth and nitrogen retention in litter of *Phragmites australis* compared to *Typha angustifolia*. *Wetlands*, 22(3), 616-625.
- Finlayson, C.M., Davidson, N.C., Spiers, A.G. and Stevenson, N.J. (1999). Global wetland inventory – current status and future priorities, *Marine and Freshwater research*, 50(8), 717-727.
- Finlayson, C.M., D'Cruz, R. and Davidson, N. (2005). Ecosystem services and human well-being: water and wetland, synthesis. *A report of the Millennium Ecosystem Assessment*.
- Fitoka, E. and Keramitsoglou, I. (eds) (2008). Inventory, assessment and monitoring of Mediterranean wetlands: Mapping wetlands using earth observation techniques. EKBY and NOA. MedWet publication. (Scientific reviewer Nick J Riddiford).
- Fogli, S., Marchesini, R. and Gerdol, R. (2002). Reed (*Phragmites australis*) decline in a brackish wetland in Italy. *Marine environmental research*, 53(5), 465-479.
- Fryer, M. J., Andrews, J. R., Oxborough, K., Blowers, D. A. and Baker, N. R. (1998). Relationship between CO₂ assimilation, photosynthetic electron

transport, and active O₂ metabolism in leaves of maize in the field during periods of low temperature. *Plant Physiology*, 116, 571-580.

Gamon, J. A., Serrano, L. and Surfus, J.S. (1997). The photochemical reflectance index: an optical indicator of photosynthetic radiation use efficiency across species, functional types and nutrient levels. *Oecologia*, 112, 492-501.

Gamon, J.A. and Surfus, J. (1999). Assessing leaf pigment content and activity with a reflectometer. *New Phytologist*, 143(1), 105-117.

Gausman, H.W. (1977). Reflectance of leaf components. *Remote Sensing of Environment*, 6(1), 1-9.

Genty, B., Briantais, J. M. and Baker, N. R. (1989). The relationship between the quantum yield of photosynthetic electron transport and quenching of chlorophyll fluorescence. *Biochimica et Biophysica Acta (BBA) – General Subjects*, 990(1), 87-92.

Gilmore, M.S., Civco, D.L., Wilson, E.H., Barrett, N., Prisloe, S., Hurd, J.D. and Chadwick, C. (2009). Remote Sensing and In Situ Measurements for Delineation and Assessment of Coastal Marshes and Their Constituent Species. In Y. Wang (Ed.), *Remote Sensing of Coastal Environments*, 261-280. Boca Raton, Florida: CRC Press.

Gitelson, A. A. and Merzlyak, M. N. (1994). Spectral reflectance changes associated with autumn senescence of *Aesculus Hippocastanum* L. and *Acer Platanoides* L. leaves. Spectral features and relation to chlorophyll estimation. *Journal of Plant Physiology*, 143, 286-292.

Gitelson, A. A. and Merzlyak, M. M. (1996). Signature analysis of leaf reflectance spectra: algorithm development for remote sensing of chlorophyll. *Journal of Plant Physiology*, 148(3-4), 494-500.

- Gitelson, A. A., Merzlyak, M. N. and Chivkunova, O. B. (2001). Optical properties and nondestructive estimation of anthocyanin content in plant leaves. *Photochemistry and Photobiology*, 71, 38-45.
- Gitelson, A. A., Zur, Y., Chivkunova, O. B. and Merzlyak, M. N. (2002). Assessing carotenoid content in plant leaves with reflectance spectroscopy. *Photochemistry and Photobiology*, 75, 272-281.
- Gong, P. and Howarth, P.J. (1990). The use of structural information for improving land-cover classification accuracies at the rural-urban fringe. *Photogrammetric Engineering and Remote Sensing*, 56(1), 67-73.
- Gong, P., Marceau, D.J. and Howarth, P.J. (1992). A comparison of spatial feature extraction algorithms for land-use classification with SPOT HRV data. *Remote Sensing of Environment*, 40(2), 137-151.
- Granéli, W. (1990). Standing Crop and Mineral Content of Reed, *Phragmites australis* (Cav.) Trin. ex Steudel, in Sweden: Management of Reed Stands to Maximize Harvestable Biomass. *Folia Geobotanica & Phytotaxonomic*, 25(3), 291-302.
- Green, A.A., Berman, M., Switzer, P., and Craig, M.D. (1988). A transformation for ordering multispectral data in terms of image quality with implications for noise removal. *IEEE Transactions on Geoscience and Remote Sensing*, 26, 65-74.
- Griffin, M.K. and Burke, H.-H.K. (2003). Compensation of hyperspectral data for atmospheric effects. *Lincoln laboratory journal*, 14, 1.
- Hansen, D.L., Lambertini, C., Jampeetong, A. and Brix, H. (2007). Clone-specific differences in *Phragmites australis*: Effects of ploidy level and geographic origin. *Aquatic Botany*, 86(3), 269-279.
- Harris, S.W. and Marshall, W.H. (1963). Ecology of water-level manipulations on a northern marsh. *Ecology*, 44(2), 331-343.

- Haslam, S. M. (1969). The development of shoots in *Phragmites communis* Trin. *Annals of Botany*, 33(4), 695-709.
- Hay, G.J. and Castilla, G. (2006). Object-based image analysis: strengths, weaknesses, opportunities and threats (SWOT). 1st International Conference on Object-based Image Analysis, XXXVI-4/C42.
- Hedley, J., Roelfsema, C., Koetz, B. and Phinn, S. (2012). Capability of the Sentinel 2 mission for tropical coral reef mapping and coral bleaching detection. *Remote Sensing of Environment*, 120. Special issue: The Sentinel Missions – New Opportunities for Science, 145-155.
- Herodek, S. (1984). Eutrophication of Lake Balaton: Measurements, Modeling and Management. *Verhandlung Internationale Vereinigung Limnologie*, 221087.
- Herodek, S. (1988a). Limnology of Lake Balaton, in *Lake Balaton, research and management*, Misley, K. (Ed), NEXUS, Hungary.
- Herodek, S. (1988b). Eutrophication of Lake Balaton, in *Lake Balaton, research and management*, Misley, K. (Ed), NEXUS, Hungary.
- Hoffer, R.M. (1978). Biological and physical considerations in applying computer-aided analysis techniques to remote sensor data. In: Swain, P.H. and Davis, S.M. (eds.), *Remote Sensing – The Quantitative Approach*. New York: McGraw-Hill International Book Co., chapter 5.
- Huete, A., Didan, K., Miura, T. Rodriguez, E. P., Gao, X. and Ferreira, L. G. (2002). Overview of the radiometric and biophysical performance of the MODIS vegetation indices. *Remote Sensing of Environment*, 83, 195-213.
- Hufkens, K., Scheunders, P. and Ceulemans, R. (2009). Ecotones on vegetation ecology: methodologies and definitions revisited. *Ecological Research*, DOI 10.1007.

Hughes, G. (1968). On the mean accuracy of statistical pattern recognizers. *IEEE Transactions on Information theory*, 14(1), 55-63.

Hunter, P.D., Gilvear, D.J., Tyler, A.N., Willby, N.J. and Kelly, A. (2010a). Mapping macrophytic vegetation in shallow lakes using the Compact Airborne Spectrographic Imager (CASI). *Aquatic Conservation-Marine and Freshwater Ecosystems*, 20(7), 717-727.

Hunter, P.D., Tyler, A.N., Carvalho, L., Codd, G.A. and Maberly, S.C. (2010b). Hyperspectral remote sensing of cyanobacterial pigments as indicators for cell populations and toxins in eutrophic lakes. *Remote Sensing of Environment*, 114(11), 2705-2718.

Hürlimann, H. (1951). Zur Lebensgeschichte des Schilfs an den Ufern der Schweizer Seen. *Beiträge zur geobotanischen Landesaufnahme der Schweiz*, 30, 1-232. In German.

Husson, E., Hagner, O. and Ecker, F. (2014). Unmanned aircraft systems help to map aquatic vegetation. *Applied Vegetation Science*, 17, 567-577.

Inoue, Y., Peñuelas, J., Miyata, A., and Mano, M. (2008). Normalized difference spectral indices for estimating photosynthetic efficiency and

capacity at a canopy scale derived from hyperspectral and CO₂ flux measurements in rice. *Remote Sensing of Environment*, 112, 156–172.

Inoue, Y., Sakaiya, E., Zhu, Y., and Takahashi, W. (2012). Diagnostic mapping of canopy nitrogen content in rice based on hyperspectral measurements. *Remote Sensing of Environment*, 126, 210-221.

ITT Visual Information Solutions (2009). Atmospheric Correction Module: QUAC and FLAASH User's Guide, Version 4.7, August, 2009 Edition. ESRI, ENVI.

Jensen, J.R., Hodgson, M.E., Christensen, E., Mackey, H.E. and Tinney, L.R. (1986). Remote sensing inland wetlands: a multispectral approach. *Photogrammetric Engineering and Remote Sensing*, 52, 87-100.

Jensen, R., Mausel, P., Dias, N., Gonser, R., Yang, C., Everitt, J. and Fletcher, R. (2007). Spectral analysis of coastal vegetation and land cover using AISA+ hyperspectral data. *Geocarto International*, 22(1), 17-28.

Johansen, K., Tiede, T., Blaschke, T., Phinn, S., and Arroyo, L.A. (2010). Automatic geographic object based mapping of streambed and riparian zone extent from lidar data in a temperate rural urban environment, Australia. GEOBIA 2010 Geographic Object-Based Image Analysis Conference Proceedings, XXXVIII-4/C7.

Johnsson, K. (1994). Segment-based land use classification from SPOT satellite data. *Photogrammetric Engineering and Remote Sensing*, 60(1), 47–53.

Jones, T.G., Coops, N.C. and Sharma, T. (2010). Assessing the utility of airborne hyperspectral and LiDAR data for species distribution mapping in the coastal Pacific Northwest, Canada. *Remote Sensing of Environment*, 114, 2841-2852.

Jordan, C. F. (1969). Derivation of leaf area index from quality of light on the forest floor. *Ecology*, 50, 663-666.

- Jordan, G., Van Rompaey, A., Szilassi, P., Csillag, G., Mannaerts, C. and Woldai, T. (2005). Historical land use changes and their impact on sediment fluxes in the Balaton basin (Hungary). *Agriculture, Ecosystems and Environment*, 108(2), 119-133.
- Kaufman, Y.J., Tanré, D and Boucher, O. (2002). A satellite view of aerosols in the climate system. *Nature*, 219, 215-223.
- Keramitsoglou, I., Kontoes, C., Sifakis, N., Mitchley, J. and Xofis, P. (2005). Kernel based re-classification of earth observation data for fine scale habitat mapping. *Journal for Nature Conservation*, 13, 91-99.
- Keramitsoglou, I., Sarimveis, H., Kiranoudis, C., Kontoes, C., Sifakis, N. and Fitoka, E. (2006). The performance of pixel window algorithms in the classification of habitats using VHSR imagery. *ISPRS Journal of Photogrammetry and Remote Sensing*, 60(4), 225-238.
- Kerr, J.T. and Ostrovsky, M. (2003). From space to species: ecological applications for remote sensing. *Trends in Ecology and Evolution*, 18(6), 299-305.
- Kitajima, M. and Butler, W.L. (1975). Quenching of chlorophyll fluorescence and primary photochemistry in chloroplasts by dibromothymoquinone. *Biochimica et Biophysica Acta (BBA)-Bioenergetics*, 376, 105–115.
- Klemas, V. (2011). Remote sensing of wetlands: case studies comparing practical techniques. *Journal of Coastal Research*, 27(3), 418-427.
- Koetz, B., Morsdorf, F., Curt, T., van der Linden, S., Borgniet, L., Odermatt, D., Alleaume, S., Lampin, C., Jappiot, M. and Allgöwer, B. (2007). Fusion of imaging spectrometer and LIDAR data using Support Vector Machines for land cover classification in the context of forest fire management. The 10th International Symposium on Physical Measurements and Signatures in Remote Sensing (ISPMSRS), March 12-14, 2007, Davos, Switzerland.

- Koppitz, H. (1999). Analysis of genetic diversity among selected populations of *Phragmites australis* world-wide. *Aquatic Botany*, 64(3), 209-221.
- Kovács, M., Turcsányi, G., Tuba, Z., Wolcsanszky, S. E., Vasarhelyi, T., Dely-Draskovits, A., Toth, S., Koltay, A., Kaszab, L. and Szoke, P. (1989). The decay of reed in Hungarian lakes. *Symposia Biologica Hungarica*, 38, 461–471.
- Korponai, J., Braun, M., Buczkó, K., Gyulai, I., Forró, L., Nédli, J. and Papp, I. (2010). Transition from shallow lake to a wetland: a multi-proxy case study in Zalavári Pond, Lake Balaton, Hungary. *Hydrobiologia*, 641(1), 225-244.
- Kotta, J., Remm, K., Vahtmäe, e., Kutser, T. and Orav-Kotta, H. (2014). In-air spectral signatures of the Baltic Sea macrophytes and their statistical separability. *Journal of Applied Remote Sensing*, 8(1), 083634.
- Kovács, M., Turcsányi, G., Tuba, Z., Wolcsanszky, S. E., Vasarhelyi, T., Dely-Draskovits, A., Tóth, S., Koltay, A., Kaszab, L. and Szoke, P. (1989). The decay of reed in Hungarian lakes. *Symposia Biologica Hungarica*, 38, 461–471.
- Krause, G. H. and Weis, E. (1991). Chlorophyll fluorescence and photosynthesis: The Basics. *Annual Review of Plant Physiology and Plant Molecular Biology*, 42, 313-349.
- Krumscheid, P., Stark, H. and Peintinger, M. (1989). Decline of reed at Lake Constance (Obersee) since 1967 based on interpretations of aerial photographs. *Aquatic Botany*, 35(1), 57-62.
- Kruse, F.A., Keirein-Young, K.S. and Boardman, J.W. (1990). Mineral Mapping at Cuprite, Nevada with a 63-channel Imaging Spectrometer. *Photogrammetric Engineering & Remote Sensing*, 56, 83-92.
- Kuo, B.-C., Huang, C.-S., Hung, C.-C., Liu, Y.-L. and Chen, I.-L. (2010). Spatial information based support vector machine for hyperspectral image classification. Proceedings of the 2010 IEEE International Geoscience and

Remote Sensing Symposium (IGARSS), July 25-30, 2010, Honolulu, Hawaii, U.S.A., 832-835.

Kühl, H., Koppitz, H., Rolletschek, H. and Kohl, J. G. (1999). Clone specific differences in a *Phragmites australis* stand: I. Morphology, genetics and site description. *Aquatic Botany*, 64(3), 235-246.

Kühl, H. and Zemlin, R. (2000). Increasing the efficiency of reed plantations on stressed lake and river shores by using special clones of *Phragmites australis*. *Wetlands Ecology and Management*, 8(6), 415-424.

Küshl, H. and Kohl, J.-G. (1992). Nitrogen accumulation, productivity and stability of reed stands (*Phragmites australis* (cav.) trin. ex steudel) at different lakes and sites of the lake districts of Uckermark and Mark Brandenburg (Germany). *Internationale Revue der gesamten Hydrobiologie und Hydrographie*, 77(1), 85–107.

Lang, S. and Blaschke, T. (2006). Bridging remote sensing and GIS - what are the main supportive pillars? *Proceedings of the 1st International Conference on Object-based Image Analysis*.

Lang, M.W. and McCarty, G.W. (2009). Lidar intensity for improved detection of inundation below the forest canopy. *Wetlands*, 29(4), 1166-1178.

Lausch, A., Pause, M., Merbach, I., Zacharias, S., Doktor, D., Volk, M. and Seppelt, R. (2013). A new multiscale approach for monitoring vegetation using remote sensing-based indicators in laboratory, field, and landscape. *Environmental Monitoring and Assessment*, 185, 1215–1235.

Leckie, D.G., Tinis, S., Nelson, T., Burnett, C., Gougeon, F.A., Cloney, E. and Paradine, D. (2005). Issues in species classification of trees in old growth conifer stands. *Canadian Journal of Remote Sensing*, 31(2), 175-190.

Leithead, H.L., Yarlett, L.L. and Shiflett, T.N. (1976). 100 native forage grasses in 11 southern states. USDA SCS.

- Liira, J., Feldmann, T., Mäemets, H. and Peterson, U. (2010). Two decades of macrophyte expansion on the shores of a large shallow northern temperate lake - A retrospective series of satellite images. *Aquatic Botany*, 93(4), 207–215.
- Lissner, J. and Schierup, H.-H. (1997). Effects of salinity on the growth of *Phragmites australis*. *Aquatic Botany*, 55(4), 247-260.
- Lu, D. and Weng, Q. (2007). A survey of image classification methods and techniques for improving classification performance. *International Journal of Remote Sensing*, 28(5), 823-870.
- Maheu-Giroux, M. and de Blois, S. (2005). Mapping the invasive species *Phragmites australis* in linear wetland corridors. *Aquatic Botany*, 83(4), 310-320.
- Malenovský, Z., Rott, H., Cihlar, H., Schaepman, M.E., García-Santos, G., Fernandes, R. and Berger, M. (2012). Sentinels for science: potential of Sentinel-1, -2 and -3 missions for scientific observations of ocean, cryosphere, and land. *Remote Sensing of Environment*, 120, 91-101. Special issue: The Sentinel Missions – New Opportunities for Science.
- Malthus, T.J.M., Best, E.P.H. and Dekker, A.G. (1987). An assessment of the importance of emergent and floating-leaved macrophytes to trophic status in the Loosdrecht lakes (The Netherlands). *Hydrobiologia*, 191, 257-263.
- Malthus, T.J. and George, D.G. (1997). Airborne remote sensing of macrophytes in Cefni Reservoir, Anglesey, UK. *Aquatic Botany*, 58, 317-333.
- Manjunath, K.R., Ray, S.S. and Sushma, P. (2011). Discrimination of spectrally-close crops using ground-based hyperspectral data. *Journal of the Indian Society of Remote Sensing*, 39(4), 599-602.
- Matthew, M.W., Adler-Golden, S.M., Berk, A., Richtsmeier, S.C., Lenive, R.Y., Bernstein, L.S., Acharya, P.K., Anderson, G.P., Felde, G.W., Hoke, M.P., Ratkowski, A., Burke, H.H., Kaiser, R.D. and Miller, D.P. (2000). Status of atmospheric correction using a MODTRAN4-based algorithm. *SPIE*

Proceedings, Algorithms for multispectral, hyperspectral, and ultraspectral imagery VI, 4049, 199-207.

Mauchamp, A., Blanch, S. and Grillas, P. (2001). Effects of submergence on the growth of *Phragmites australis* seedlings. *Aquatic Botany*, 69(2-4), Special issue on *Phragmites*-dominated wetlands, their functions and sustainable use, 147-164.

Mauchamp, A. and Méthy, M. (2004). Submergence-induced damage of photosynthetic apparatus in *Phragmites australis*. *Environmental and experimental botany*, 51(3), 227–235.

Maxa, M. and Bolstad, P. (2009). Mapping northern wetlands with high resolution satellite images and LiDAR. *Wetlands*, 29(1), 248-260.

Maxwell, K. and Johnson, G. N. (2000). Chlorophyll fluorescence – a practical guide. *Journal of Experimental Botany*, 51, 659-668.

McCormick, M.K., Kettenring, K.M., Baron, H.M. and Whigham, D.F. (2010). Spread of invasive *Phragmites australis* in estuaries with differing degrees of development: genetic patterns, Allee effects and interpretation. *Journal of Ecology*, 98(6), 1369–1378.

McDonald, M.E. (1955). Cause and effects of a die-off of emergent vegetation. *The Journal of Wildlife Management*, 19(1), 24-35.

McGwire, K., Minor, T. and Fenstermaker, L. (2000). Hyperspectral mixture modeling for quantifying sparse vegetation cover in arid environments. *Remote Sensing of Environment*, 72(3), 360-374.

Meinesz, A. (1999). Killer algae: the true tale of a biological invasion. University of Chicago Press, Chicago, 360.

- Melgani, F., and Bruzzone, L. (2004). Classification of hyperspectral remote sensing images with support vector machines. *Geoscience and Remote Sensing, IEEE Transactions on*, 42, 1778-1790.
- Meroni, M., Rossini, M., Picchi, V., Panigada, C., Cogliati, S., Nali, C. and Colombo, R. (2008). Assessing steady-state fluorescence and PRI from hyperspectral proximal sensing as early indicators of plant stress: the case of ozone exposure. *Sensors*, 8(3), 1740-1754.
- Merzlyak, M. N., Gitelson, A. A., Chivkunova, O. B. and Rakitin, V. Y. (1999). Non-destructive optical detection of pigment changes during leaf senescence and fruit ripening. *Physiologia Plantarum*, 106(1), 135-141.
- Mewes, T., Franke, J. and Menz, G. (2011). Spectral requirements on airborne hyperspectral remote sensing data for wheat disease detection. *Precision Agriculture*, 12(6), 795-812.
- Miller, C. (2001). Fusion of high resolution LIDAR elevation data with hyperspectral data to characterize tree canopies. *Algorithms for multispectral, hyperspectral and ultraspectral imagery*, Vii, 4381, 246-252.
- Mitsch, W.J. and Wu, X. (1995). Wetlands and global change. In: Soil Management and greenhouse effect. Lal, R., Kimble, J., Levine, E. and Stewart, B.A. (eds). *Advances in soil science*. CRC Press.
- Mitsch, W.J. and Gosselink, J.G. (2000). The value of wetlands: importance of scale and landscape setting. *Ecological Economics*, 35(200), 25-33. Special issue: The values of wetlands: landscapes and institutional perspectives.
- Morris, E.P., Caballero, I., Benavente, J., Navarro, G., Bouma, T.J. and Peralta, G. (2015). Coastal macrophytes contribute to the long term geomorphological stability of Cadiz Bay. Aquatic Sciences Meeting. Aquatic Sciences: Global And Regional Perspectives — North Meets South. Moses, W. J., Bowles, J. H., Lucke, R. L. and Corson, M. R. (2012). Impact of signal-

to-noise ratio in a hyperspectral sensor on the accuracy of biophysical parameter estimation in case II waters. *Optics Express*, 20(4), 4309-4330.

Mountrakis, G., Im, J. and Ogole, C. (2011). Support vector machines in remote sensing: A review. *ISPRS Journal of Photogrammetry and Remote Sensing*, 66(3), 247-259.

Mucsi, L., Tobak, Z., van Leeuwen, B., Kovács, F. and Szatmári, J. (2008). Analyses of spatial and temporal changes in the urban environment using multi- and hyperspectral data. In: *Remote Sensing – New Challenges of high resolution*, Jürgens, C. (ed.), Bochum, 275-284.

Myneni, R.B., Ross, J and Asrar, G. (1989). A review on the theory of photon transport in leaf canopies. *Agricultural and Forest Meteorology*, 45, 1-153. Elsevier Science Publishers, B.V., Amsterdam, The Netherlands.

NASA Land Processes Distributed Active Archive Center (LP DAAC) (2001). ASTER L1B. USGS/Earth Resources Observation and Science (EROS) Center, Sioux Falls, South Dakota.

Naumann, J.C., Anderson, J.E. and Young, D.R. (2008). Linking physiological responses, chlorophyll fluorescence and hyperspectral imagery to detect salinity stress using the physiological reflectance index in the coastal shrub, *Myrica cerifera*. *Remote Sensing of Environment*, 112, 3865-3875.

Niering, W. (1985). *Wetlands: The Audubon Society Nature Guides*, Alfred. A. Knopf, New York.

Nguyen, L.X., Lambertini, C., Sorrell, B.K., Eller, F., Achenbach, L. and Brix, H. (2013). Photosynthesis of co-existing *Phragmites* haplotypes in their non-native range: are characteristics determined by adaptations derived from their native origin? *AoB Plants*, 5, plt016.

- Onojeghuo, A. O. and Blackburn, G. A. (2011). Optimising the use of hyperspectral and LiDAR data for mapping reedbed habitats. *Remote Sensing of Environment*, 115(8), 2025-2034.
- Oommen, T., Misra, D., Twarakavi, N.K.C., Prakash, A., Sahoo, B. and Bandopadhyay, S. (2008). An objective analysis of support vector machine based classification for remote sensing. *Mathematical Geosciences*, 40(4), 409-424.
- Oosting, H.J. (1933). Physical-chemical variables in a Minnesota lake. *Ecological Monographs*, 3(4), 493-533.
- Ostendorp, W. (1989). 'Die-back' of reeds in Europe - a critical review of literature. *Aquatic Botany*, 35(1), 5-26.
- Ostendorp, W. (1999). Susceptibility of lakeside *Phragmites* reeds to environmental stresses: examples from Lake Constance-Untersee (SW-Germany). *Limnologica*, 29(1), 21-27.
- Padisák, J. and Reynolds, C.S. (1998). Selection of phytoplankton associations in Lake Balaton, Hungary, in response to eutrophication and restoration measures, with special reference to the cyanoprokaryotes. *Hydrobiologia*, 384(1), 41-53.
- Paillisson, J.-M. and Marion, L. (2011). Water level fluctuations for managing excessive plant biomass in shallow lakes. *Ecological Engineering*, 37(2), 241-247.
- Pal, M. and Mather, P.M. (2004). Assessment of the effectiveness of support vector machines for hyperspectral data. *Future Generation Computer Systems*, 20, 1215-1225.
- Pal, M. and Mather, M. (2005). Support vector machines for classification in remote sensing. *International Journal of Remote Sensing*, 26(5), 1007-1011.

- Pandey, P.C., Tate, N.L. and Balzter, H. (2014). Mapping tree species in coastal Portugal using statistically segmented Principal Component Analysis and other methods. *IEEE Sensors Journal*, 14(12), 4434-4441.
- Pedergnana, M., Marpu, P.R., Dalla Mura, M., Benediktsson, J.A., and Bruzzone, L. (2011). Fusion of Hyperspectral and LiDAR Data Using Morphological Attribute Profiles. *Image and Signal Processing for Remote Sensing Xvii*, 8180, 81801G.
- Peñuelas, J., Filella, I., Biel, C., Serrano, L. and Save, R. (1993). The reflectance at the 950-970 nm region as an indicator of plant water status. *International Journal of Remote Sensing* 14(10), 1887-1905.
- Peñuelas, J., Baret, F. and Filella, I. (1995). Semi-empirical indices to assess carotenoids/chlorophyll *a* ratio from leaf spectral reflectance. *Photosynthetica*, 31(2), 221-230.
- Peerbhay, K.Y., Mutanga, O. and Ismail, R. (2013). Commercial tree species discrimination using airborne AISA Eagle hyperspectral imagery and partial least squares discriminant analysis (PLS-DA) in KwaZulu–Natal, South Africa. *ISPRS Journal of Photogrammetry and Remote Sensing*, 79, 19-28.
- Perry, E.M., Foote, H.P., Petrie, G.M., Steinmaus, K.L., Irwin, D.E., and Stephan, A.J. (1998). Exploitation of hyperspectral imagery and lidar for landuse classification. *Geosciences and Remote Sensing Symposium Proceedings, IGARSS 1998*, 2, 1013-1015.
- Pfeifer, N. and Zlinszky, A. (eds) (2014). Proceedings of the International Workshop on Remote Sensing and GIS for Monitoring of Habitat Quality, Vienna, 1-178. <http://rsgis4hq.geo.tuwien.ac.at/proceedings/>
- Plaza, A., Benediktsson, J. A., Boardman, J. W., Brazile, J., Bruzzone, L., Camps-Valls, G., Chanussot, J., Fauvel, M., Gamba, P., Gualtieri, A., Marconcini, M., Tilton, J. C. and Trianni, G. (2009). Recent advances in

techniques for hyperspectral image processing. *Remote Sensing of Environment, Imaging Spectroscopy Special Issue*, 113, Supplement 1, S110-S122.

Plaza, J., Hendrix, E.M.T., García, I., Martín, G. and Plaza A. (2012). On Endmember Identification in Hyperspectral Images Without Pure Pixels: A Comparison of Algorithms. *Journal of Mathematical Imaging and Vision*, 42(2-3), 163-175.

Pomogyi, P. (2013). Remote sensing techniques in applied hydrobotany - Vegetation mapping and classification using aerial photographs (In Hungarian). *RS and GIS*, 1, 5-23.

Puttonen, E., Suomalainen, J., Hakala, T., Raikkonen, E., Kaartinen, H., Kaasalainen, S. and Litkey, P. (2010). Tree species classification from fused active hyperspectral reflectance and LIDAR measurements. *Forest Ecology and Management*, 260(10), 1843-1852.

R Core Team (2013). R: A language and environment for statistical computing. R *Foundation for Statistical Computing*, Vienna, Austria.

Ramsar Convention Secretariat (2013). The Ramsar Convention Manual: a guide to the Convention on Wetlands (Ramsar, Iran, 1971), 6th ed. Ramsar Convention Secretariat, Gland, Switzerland.

Rebelo, L.-M., Finlayson, C.M. and Nagabhatla, N. (2009). Remote sensing and GIS for wetland inventory, mapping and change analysis. *Journal of environmental management*, 90(7), 2144-2153.

Richter, R., Bachmann, M., Dorigo, W. and Müller, A. (2006). Influence of the adjacency effect on ground reflectance measurements. *IEEE Geoscience and Remote Sensing Letters*, 3(4), 565-569.

Richter, K., Atzberger, C., Vuolo, F. and D'Urso, G. (2011). Evaluation of Sentinel-2 spectral sampling for Radiative transfer model based LAI

estimation of wheat, sugar beet and maize. *IEEE Journal of selected topics in Applied Earth Observation and Remote Sensing*, 4(2), 458-464.

Roberts, D., Gardner, M., Church, R., Ustin, S., Scheer, G. and Green, R. (1998). Mapping chaparral in the Santa Monica Mountains using multiple endmember spectral mixture models. *Remote Sensing of Environment*, 65, 267-279.

Roberts, D. A. and Herold, M. (2004). Imaging spectrometry of urban materials. Available online at: http://www.geogr.uni-jena.de/~c5hema/spec/imaging_spectrometry_of_urban_materials.pdf (accessed 29 March 2011).

Rosso, P.H., Ustin, S.L. and Hastings, A. (2005). Mapping marshland vegetation of San Francisco Bay, California, using hyperspectral data. *International Journal of Remote Sensing*, 26(23), 5169-5191.

Rosso, R.H., Ustin, S.L. and Hastings, A. (2006). Use of lidar to study changes associated with *Spartina* invasion in San Francisco Bay marshes. *Remote Sensing of Environment*, 100(3), 295-306.

Rouse, J. W., Haas, R. H. Schell, J. A. and Deering, D. W. (1974). Monitoring vegetation systems in the Great Plains with ERTS. *Proc. Third ERTS-1 Symposium*, NASA Goddard, NASA SP-351, 309-317.

Rutchev, K. and Vilchek, L. (1999). Air photointerpretation and satellite imagery analysis techniques for mapping cattail coverage in a northern Everglades impoundment. *Photogrammetric Engineering and Remote Sensing*, 65, 185-191.

Saltonstall, K. (2002). Cryptic invasion by a non-native genotype of the common reed, *Phragmites australis*, into North America. *Proceedings of the National Academy of Sciences*, 99, 2445.

- Sanders, L.C., Schott, J.R. and Raqueño, R. (2001). A VNIR/SWIR atmospheric correction algorithm for hyperspectral imagery with adjacency effect. *Remote Sensing of Environment*, 78(3), 252-263.
- Santer, R. and Schmechtig, C. (2000). Adjacency effects on water surfaces: primary scattering approximation and sensitivity study. *Applied Optics*, 39(3), 361-375.
- Schaepman-Strub, G., Schaepman, M.E., Painter, T.H., Dangel, S., Martonchik, J.V. (2006). Reflectance quantities in optical remote sensing – definitions and case studies. *Remote Sensing of Environment*, 103, 27-42.
- Schmidt, K.S. and Skidmore, A.K. (2003). Spectral discrimination of vegetation types in a coastal wetland. *Remote Sensing of Environment*, 85, 92-108.
- Seinfeld, J.H. and Pandis, S.N. (2006). Atmospheric chemistry and physics: From air pollution to climate change. John Wiley and Sons. Second Edition.
- Shafri, H.Z.M. and Hamdan, N. (2009). Hyperspectral imagery for mapping disease infection in oil palm plantation using vegetation indices and red-edge techniques. *American Journal of Applied Sciences*, 6(6), 1031-1035.
- Shive, J.P., Pilliod, D.S., and Peterson, C.R. (2010). Hyperspectral analysis of columbia spotted frog habitat. *Journal of Wildlife Management*, 74, 1387-1394.
- Sims, D. A. and Gamon, J. A. (2002). Relationships between leaf pigment content and spectral reflectance across a wide range of species, leaf structures and developmental stages. *Remote Sensing of Environment*, 81(2-3), 337-354.
- Somlyódy, L. (1998). Eutrophication modeling, management and decision making: The Kis-Balaton case. *Water Science and Technology*, 37(3), 165-175.
- Spanhove, T., Vanden Borre, J., Delalieux, S., Haest, B. and Paelinckx, D. (2012). Can remote sensing estimate fine-scale quality indicators of natural habitats? *Ecological Indicators*, 18, 403-412.

- Staenz, K., Secker, J., Gao, B.-C., Davis, C. and Nadeau, C. (2002). Radiative transfer codes applied to hyperspectral data for the retrieval of surface reflectance. *ISPRS Journal of Photogrammetry and Remote Sensing*, 57(3), 194-203.
- Stagakis, S., Markos, N., Sykioti, O. and Kyparissis, A. (2010). Monitoring canopy biophysical and biochemical parameters in ecosystem scale using satellite hyperspectral imagery: An application on a *Phlomis fruticosa* Mediterranean ecosystem using multiangular CHRIS/PROBA observations. *Remote Sensing of Environment*, 114(5), 977-994.
- Sterckx, S., Knaeps, E. and Ruddick, K. (2011). Detection and correction of adjacency effects in hyperspectral airborne data of coastal and inland waters: the use of the near infrared similarity spectrum. *International Journal of Remote Sensing*, 32(21), 6479-6505.
- Strand, V.V. and Weisner, S.E.B. (2002). Interactive effects of pressurized ventilation, water depth and substrate conditions on *Phragmites australis*. *Oecologia*, 131(4), 490-497.
- Stratoulas, D., Balzter, H., Zlinszky, A. and Tóth, V.R. (2015). Assessment of ecophysiology of lake shore reed vegetation based on chlorophyll fluorescence, field spectroscopy and hyperspectral airborne imagery. *Remote Sensing of Environment*, 157, 72-84.
- Swatantran, A., Dubayah, R., Roberts, D., Hofton, M., and Blair, J.B. (2011). Mapping biomass and stress in the Sierra Nevada using lidar and hyperspectral data fusion. *Remote Sensing of Environment*, 115, 2917-2930.
- Szilassi, P. (1999). Possibilities of country development from the point of view of tourism - An investigation in the Káli Basin (West Hungary). *Geographica Pannonica*, 3, 30-32.

- Thenkabail, P. S., Smith R. B. and Pauw E. D. (2000). Hyperspectral vegetation indices and their relationships with agricultural crop characteristics. *Remote Sensing of Environment*, 71, 158-182.
- Thenkabail, P. S., Lyon J. G. and Huete A. (2012). Hyperspectral remote sensing of vegetation. ISBN 9781439845370, XXXV, p. 705, CRC Press.
- Tóth, L. (1972). Reed controlled eutrophication of Balaton Lake. *Water Research*, 6(12), 1533.
- Tóth L., Felföldy L. and Szabó E. (1961). A Balatoni nádas-termelés mérésének néhány problémájáról. *Annales Instituti Biologici (Tibany) Hungariae Academiae Scientiarum*, 28, 168-179, in Hungarian.
- Tóth, V. R. and Szabó, K. (2012). Morphological structural analysis of *Phragmites australis* stands in Lake Balaton. *Ann. Limnol.- Int. J. Lim.*, 48, 241-251.
- Tucker, C. J. (1979). Red and photographic infrared linear combinations for monitoring vegetation. *Remote Sensing of the Environment*, 8, 127-150.
- Tucker, G. C. (1990). The Genera of Arundinoideae (Gramineae) in the Southeastern United-States. *Journal of the Arnold Arboretum*, 71(2), 145-177.
- Turner, W., Spector, S., Gardiner, N., Fladeland, M., Sterling, E. and Steininger, M. (2003). Remote sensing for biodiversity science and conservation. *Trends in Ecology and Evolution*, 18(6), 306-314.
- Uhler, F.M. (1944). Control of undesirable plants in waterfowl habitats. *Transactions of the North American Wildlife Conference*, 9, 295-303.
- Üveges, V., Vörös, L., Padisák, J. and Kovács, A. (2011). Primary production of epipsammic algal communities in Lake Balaton (Hungary). *Hydrobiologia*, 660(1), 17-27.

- Van der Meer, F.D. (2001). Basic physics of spectrometry (chapter 1). In: Imaging spectrometry: basic principles and prospective applications, Van der Meer, F.D. and de Jong, S.M. (eds.), Springer.
- Van der Meer, F.D. and de Jong, S.M. (2002). Imaging spectrometry: basic principles and prospective applications. Remote Sensing and Digital Image Processing, 4, XXIII.
- Van der Putten, W. H. (1997). Die-back of *Phragmites australis* in European wetlands: an overview of the European Research Programme on Reed Die-Back and Progression (1993-1994). *Aquatic Botany*, 59(3-4), 263-275.
- Vapnik, V.N. (1995). The Nature of Statistical Learning Theory. New York: Springer
- Velikova, V. and Loreto, F. (2005). On the relationship between isoprene emission and thermotolerance in *Phragmites australis* leaves exposed to high temperatures and during the recovery from a heat stress. *Plant, Cell and Environment*, 28(3), 318–327.
- Villa, P., Laini, A., Bresciani, M. and Bolpagni, R. (2013). A remote sensing approach to monitor the conservation status of lacustrine *Phragmites australis* beds. *Wetlands Ecology and Management*, DOI 10.1007/s11273-013-9311-9.
- Virág, Á. (1988). Engineering and pollution control on Lake Balaton, in *Lake Balaton, research and management*, Miskey, K. (Ed), NEXUS, Hungary.
- Virág, Á. (1997). A Balaton múltja és jelene. Egri Nyomda Rt., Eger. (In Hungarian).
- Vretare, V., Weisner, S.E.B., Strand, J.A. and Granéli, W. (2001). Phenotypic plasticity in *Phragmites australis* as a functional response to water depth. *Aquatic Botany*, 69(2-4), 127-145. Special issue on phragmites-dominated wetlands, their functions and sustainable use.

- Vogelmann, J. E., Rock, B. N. and Moss, D. M. (1993). Red-edge spectral measurements from sugar maple leaves *International Journal of Remote Sensing*, 14(8), 1563-1575.
- Warren, M.A., Taylor, B.H., Grant M.G. and Shutler, J.D. (2014). Data processing of remotely sensed airborne hyperspectral data using the Airborne Processing Library (APL): Geocorrection algorithm descriptions and spatial accuracy assessment. *Computers & Geosciences*, 64, 24-34.
- Weisner, S.E.B. (1987). The relation between wave exposure and distribution of emergent vegetation in a eutrophic lake. *Freshwater Biology*, 18, 537-544.
- Weisner, S.E.B. (1991). Within-lake patterns in depth penetration of emergent vegetation. *Freshwater Biology*, 26, 133-142.
- Weisner, S.E.B. and Granéli, W. (1989). Influence of substrate conditions on the growth of *Phragmites australis* after a reduction in oxygen transport to below ground parts. *Aquatic Botany*, 35(1), 71-80.
- Weisner, S.E.B. and Strand, J.A. (1996). Rhizome architecture in *Phragmites Australis* in relation to water depth: implications for within-plant oxygen transport distances. *Folia Geobotanica and Phytotaxonomica*, 31(1, Adaptation Strategies in Wetland Plants: Links between Ecology and Physiology. Proceedings of a Workshop), 91-97.
- Wilcox, D.A. (1995). Wetland and aquatic macrophytes as indicators of anthropogenic hydrologic disturbance. *Natural Areas Journal*, 15, 240-248.
- Xu, J. and Wu, Z. (2012). Research on geometric and radiometric correction order and its impact for remote sensing image. Proceedings of the XXII Congress of the International Society for Photogrammetry and Remote Sensing, 25 August – 1 September 2012, Melbourne, Australia.

- Yang, C., Goolsby, J.A., Everitt, J.H. and Du, Q. (2008). Applying six classifiers to airborne hyperspectral imagery for detecting giant reed. *Geocarto International*, 27(5), 413-424.
- Yang, J. and Artigas, F.J. (2009). Mapping salt marsh vegetation by integrating hyperspectral and LiDAR remote sensing. In: Remote sensing of coastal environments, ed. Wang Y. CRC Press.
- Zarco-Tejada, P. J., Miller, J. R., Mohammed, G. H., Noland T.L. and Sampson, P. H. (2002). Vegetation stress detection through chlorophyll a+b estimation and fluorescence effects on hyperspectral imagery. *Journal of Environmental quality*, 31(5), 1433-1441.
- Zarco-Tejada, P. J., Miller, J. R., Noland, T. L., Mohammed, G. H. and Sampson, P. H. (2001). Scaling-up and model inversion methods with narrow-band optical indices for chlorophyll content estimation in closed forest canopies with hyperspectral data. *IEEE Transactions on Geoscience and Remote Sensing*, 39(7), 1491-1507.
- Zarco-Tejada, P. J., Berjón, A., López-Lozano, R., Miller, J. R., Martín, P., Cachorro, V., González, M. R., and de Frutos, A. (2005). Assessing vineyard condition with hyperspectral indices: Leaf and canopy reflectance simulation in a row-structured discontinuous canopy. *Remote Sensing of Environment*, 99, 271-287.
- Zhang, X. (1998). On the estimation of biomass of submerged vegetation using satellite thematic mapper (TM) imagery: a case study of the Honghu, PR China. *International Journal of Remote Sensing*, 19, 11-20.
- Zhang, H., Zhu, L. F., Hu, H., Zheng, K. F. and Jin, Q. Y. (2011). Monitoring Leaf Chlorophyll Fluorescence with Spectral Reflectance in Rice (*Oryza sativa* L.). *Procedia Engineering*, 15, 4403-4408.

Zlinszky, A., Tóth, V.R., Pomogyi, P. and Timár, G. (2011). Initial report of the AIMWETLAND project: simultaneous airborne hyperspectral, LiDAR and photogrammetric survey of the full shoreline of Lake Balaton, Hungary. *Geographia Technica*, 1, 101-117.

Zlinszky, A., Mücke, W., Lehner, H., Briese, C. and Pfeifer, N. (2012). Categorizing wetland vegetation by airborne laser scanning on Lake Balaton and Kis-Balaton, Hungary. *Remote Sensing*, 4(6), 1617-1650.

Zlinszky, A. (2013). Mapping and conservation of the reed wetlands on Lake Balaton. Dept. of Plant Systematics, Ecology and Theoretical Biology. Budapest, Eötvös Loránd University. PhD: 1-217.

Zlinszky, A., Tóth, R.V. and Herodek, S. (2013). Aerial surveying of reed die-back and regeneration on Lake Balaton. XXVII SIL Congress Budapest aug. 4-9 2013, In: Tóth et al. (ed.) Abstracts, Balaton Limnological Institute, Tihany, 215.